Highly Flexible Dual and Tri Band Impedance Transformation Techniques and Their Applications in Advanced Passive and Active Circuits

BY

DEEPAYAN BANERJEE

A THESIS

SUBMITTED IN PARTIAL FULFILLMENT OF THE REQUIREMENTS FOR THE DEGREE OF

DOCTOR OF PHILOSOPHY

ELECTRONICS AND COMMUNICATION ENGINEERING
INDRAPRASTHA INSTITUTE OF INFORMATION TECHNOLOGY DELHI

NEW DELHI- 110020

December 2020

Highly Flexible Dual and Tri Band Impedance Transformation Techniques and Their Applications in Advanced Passive and Active Circuits

BY

DEEPAYAN BANERJEE

Under the Supervision of Dr. Mohammad S. Hashmi

A THESIS

SUBMITTED IN PARTIAL FULFILLMENT OF THE REQUIREMENTS FOR THE DEGREE OF

DOCTOR OF PHILOSOPHY

ELECTRONICS AND COMMUNICATION ENGINEERING
INDRAPRASTHA INSTITUTE OF INFORMATION TECHNOLOGY DELHI

NEW DELHI- 110020

December 2020

THESIS CERTIFICATE

This is to certify that the thesis titled "Highly Flexible Dual and Tri Band Impedance Transformation Techniques and Their Applications in Advanced Passive and Active Circuits" being submitted by Mr. Deepayan Banerjee to the Indraprastha Institute of Information Technology Delhi, for the award of the degree of Doctor of Philosophy, is an original research work carried out by him under my supervision. In my opinion, the thesis has reached the standards fulfilling the requirements of the regulations relating to the degree.

The results contained in this thesis have not been submitted in part or full to any other university or institute for the award of any degree/diploma.

Dr. Mohammad S. Hashmi
Thesis Supervisor
Associate Professor
Deptt. of Electronics and Comm.
Indraprastha Institute of Information
Technology Delhi
New Delhi 110020

Place: New Delhi

Date: Wednesday 5th May, 2021

This page is intentionally left blank

ACKNOWLEDGEMENTS

First of all, my heartfelt gratitude to the Almighty- the Supreme intelligence behind the unknown mechanisms of the Universe. Without His blessings and mercy, it would be impossible for me to pursue a career in research.

I am deeply indebted to my thesis supervisor Dr. Mohammad S. Hashmi for his guidance, endless encouragement and immense support in many aspects of my life. I have been continuously learning from him since the early days of our contact.

I would like to take this opportunity to thank my doctoral committee members Prof. Anand Srivastava, Dr. Vivek Bohara and Dr. Sujay Deb for evaluating my work and advising me on every step of my research.

I have no words to express gratitude to my family- my grandparents, parents, and wife. It is all because of my mother who has spent her entire life on educating her students, and my father, who has never compromised on anything to provide me with good education, that I could be in a position to conduct research. I have seen hard days when nobody stands by your side, and then you know you have your parents- the ultimate resort of love and acceptance. My heartfelt thanks to my wife *Antra*, who has also co-authored many papers along with me, for providing her helping hand constantly and supporting me in all aspects of my life. Thanks, especially for tolerating me with a smile! I am also thankful to my in-laws for their constant support and encouragement in all my career ventures.

Many thanks to the Advanced High-Speed Electronics Research Group members, the guys who made my time cheerful and happy. You all are fantastic! They say, "You are the average of the five people you spend the most time with". Those five people are undoubtedly my close friends- Dr. Dinesh Rano (*Dinu da*), Dr. Hemanta Kumar Mondal, Dr. Rahul Gangopadhyay, Dr. Nalla Anandakumar and Mr. Amit Chauhan. I would never forget those *Friday Night Parties* and the fun trips around the city, sudden late-night outings, and deep discussions with you guys. Being the junior-most member,

I was always on the receiving end of valuable guidance and support from all of you. I miss those days so much! Thanks to Mr. Soumallya Chattopadhyay (the smart banker), my best friend for your company. From friendship to brotherhood, you have validated the transformation!

I would never forget the time I spent at the *iRadio Lab.*, University of Calgary, Canada, as a Visiting Researcher. I am thankful to Prof. Fadhel Ghannouchi and Dr. Mohamed Helaoui for guiding and supervising me. I have learned a lot from the meetings and technical discussions. Special thanks to Mr. Yulong Zhao and Dr. Sagar Kumar Dhar to regularly assist me in my learning process. I can never forget your support and guidance. I am also grateful to have a friend like Dr. Mohsin Aziz (*Mohsin Bhai*), a fantastic person with a big heart. Thanks to Dr. Tushar Sharma, Dr. Abubaker Abdelhafiz, Dr. Ahmed Abounemra, Dr. Xuekun Du (Jonathan), Dr. Chao Gai and Dr. Xiang Li. I feel rich to have friends like you.

I would never forget Mrs. Edith (Edie) and Mr. Sieg Koslowski for their immense care and love. I always enjoyed those Saturday Church gatherings, dinner parties, and road trips that I had with you. I would never forget those days. My housemates Jian Liu (the guy who could run 40 kilometers in one go!) and Ahmadreza Motaqi (the mountain hiker) were fantastic people. I learned a lot from them during my days in Canada.

I would also thank the IIITD academic office for their constant toil towards excellence. Ms. Priti Patel, Ms. Sheetu Ahuja, and Mr. Ashutosh Brahma are amongst the few fantastic members that constitute this group. Besides, there are many other people across the globe whom I have come in contact with and they have helped in some way or the other in many aspects of my life. The list goes long, and it would be tough for me to thank each one of them individually. However, if I have made an inch of progress in my life, it's because of important lessons taught by unnamed people.

Lastly, remembering the famous quote by Prof. Albert Einstein, "I am thankful to all those who said NO. It's because of them, I did it myself."

Dedicated to the patient readers of this thesis

ABSTRACT

KEYWORDS: Impedance Transformers, Power Dividers, Power Amplifiers

The proliferation of multi-band and multi-standard wireless systems has led to frequent advancements in their design techniques and schemes. In essence, the multi-band devices ensure a reduction in the resources required for the development of a multi-frequency transceiver, considering that individual components can be utilized to achieve the desired functionalities at multiple frequencies. Furthermore, the operation of one device at different frequencies of interest increases the re-usability of the same. For example, for a tri-band power divider, a single device can split power at three different frequencies of interest, without other additional supporting circuitry.

However, the design of multi-band circuits has been found to be extremely challenging. The key constraints are the achievable frequency ratios (or band separation) and the achievable impedance transformation ratios (or impedance gradient). The designs reported in the literature are limited in frequency ratio, which limits their usefulness in applications having widely separated frequency bands. For example, the design of a device to operate at GSM downlink (900MHz) and WiFi-LTE (5.8GHz) is not practically realizable using current techniques due to wide band separation. Another vital factor for multi-band devices is the requirement of "per-band bandwidth" according to the wireless standards. It has been accepted that for closely separated bands, the per-band bandwidth is either too low or too-high (essentially making it wideband), and this is another pressing issue requiring attention. The other key challenge of impedance transformation ratio or "Impedance Gradient", when appropriately addressed, can be potentially useful for numerous applications, including RF Energy Harvesting, Buttler Matrix in Beamforming, etc. Once again, the existing designs and schemes are pretty good for lower transformation ratios but are extremely limited for a wide range of impedance variations.

The literature is replete with dual-band architectures, but the reports on tri-/quad- and other higher-bands are still in infancy. There have been proposals of some generalized designs, but these have definite limitations. The major limitation of such designs is extremely tedious design procedures and very complicated mathematical formulations when extended to tri-band and above applications. Moreover, most of these generalized techniques rely on convergence technique or graphical approach requiring optimization, thereby essentially leading to a hit-and-trial approach. This issue can be attributed to the absence of closed-form design equations. In addition, most of the existing design techniques are limited in frequency and impedance transformation ratio.

The doctoral research, therefore, envisages addressing some of the most important concerns mentioned above. This necessitates the determination of closed-form design equations for proposed circuits, development of simplified design procedures, and miniaturization of the proposed designs. All of these developments include various aspects such as enhancement in frequency and impedance transformation ratios, increased bandwidth per frequency band, and inherent DC blocking ability at all the selected frequencies. In the context of active circuits, the additional directions that are envisaged are the design, optimization, and linearization. For example, multi-band RF Power Amplifiers in IoT applications within an indoor environment need to operate at low power, but it may often require optimization and linearization techniques to achieve decent performance (PAE, IIP3, etc.) at all the frequencies simultaneously.

The application focus of this research work is commercial communication, satellite and military, and the upcoming IoT. In all of these applications, the RF front-end modules are one of the key players, and therefore the planned objective of this research work has the potential to significantly advance the current state-of-the-art that may eventually lead to a paradigm shift in the design of such applications.

TABLE OF CONTENTS

ACKNOWLEDGEMENTS **2**

ABSTRACT **5**

LIST OF TABLES **11**

LIST OF FIGURES **16**

ABBREVIATIONS **17**

NOTATION **19**

1 INTRODUCTION **1**

1.1 Motivation 1

1.1.1 Drones- A Brief Note 2

1.1.2 A "Swarm" of Drones! 3

1.2 Energy Harvesting Applications 6

1.3 A Multi-Frequency Perspective 8

1.4 Thesis Objectives 12

1.5 Research Contributions 13

1.6 Thesis Outline 14

2 A Review of the Literature **17**

2.1 Impedance Transformers/Matching Networks 17

2.2 Dual-Band Impedance Matching Networks 19

2.2.1 Real to Real Transformers 19

2.2.2 Real to Complex Transformers 21

2.2.3 Tri-Band Impedance Transformers 24

2.2.4 Wilkinson Power Dividers 25

2.2.5 Power Amplifiers: A Brief Survey 28
2.2.6 A Summary of the Review 31

3 Transformation Ratio Flexibility and Bandwidth Enhancement of Dual-Band Impedance Transformers 33

3.1 Behavior of All-Pass Coupled Lines (APCL) 34
3.2 Floating-Arm APCLs as Dual-Band FDCL to Complex Conjugate Converter 39
3.3 $\lambda/4$ Meandered Line APCL Configuration 41
3.4 APCL-Based Dual-Band Impedance Transformer for Enhanced Frequency Ratio in FDCL Systems 42
3.4.1 Mathematical Formulation 43
3.4.2 Simulation Examples and Measured Results 45
3.5 Bandwidth Enhancement of Dual-Band Transformers by APCL-based Wave Slowing Method 48
3.5.1 The Proposed Transformer and Mathematical Deductions . . 48
3.5.2 Simulation and Design Example 51
3.6 APCL-Based Transformers with Super Flexible Transformation Ratios 54
3.7 The Proposed Impedance Transformer 54
3.7.1 The Complex-Conjugate Generator $[Z_{e1}, Z_{o1}, \theta_1]$ 55
3.7.2 Conductance Matching Line $[Z_{e2}, Z_{o2}, \theta_2]$ 57
3.7.3 Dual-Band Susceptance Cancellation Stub 58
3.8 Design Example and Case Studies 58
3.9 Applications in Dual-Band TPD 64
3.10 Conclusion 68

4 An Enhanced Frequency-Ratio Coupled-Line Dual-Frequency Wilkinson Power Divider 69

4.1 Introduction 69
4.2 Structure and Design 70
4.2.1 Even-Mode Analysis 71
4.2.2 Odd-Mode Analysis 73
4.3 Simulation Examples 75

4.4 Prototype and Measurements 76
4.5 Discussion and Conclusion 78

5 Tri-Frequency Circuits on Perspective of Matching Networks and Power Dividers 81

5.1 Introduction 82
5.2 The Proposed Impedance Matching Network 82
5.3 Mathematical formulation 83
5.3.1 FDCL-to-Real Transforming Network 84
5.3.2 Section-A: An L-Section Dual-Band Transformer 85
5.3.3 Section-B: L-Section Dual-Band Transformer 87
5.3.4 Virtual Impedance 88
5.4 Design flow 88
5.5 Case Studies and Design Example 88
5.6 The Impedance Bridge: An Analytical Study 93
5.7 Mathematical Formulation 94
5.7.1 Section-A: The Dual-Band Transformer 94
5.7.2 Section-B: Another Dual-Band Transformer 96
5.7.3 The Impedance Bridge 97
5.8 Simulation and Measurement 97
5.9 A Versatile Tri-Frequency Wilkinson Power Divider 99
5.10 The Proposed Tri-Band WPD 100
5.10.1 Even Mode Analysis: 101
5.10.2 Odd Mode Analysis: 104
5.11 Design Examples and Experimental Validation 105
5.12 DC Isolated Tri-Band WPD 107
5.12.1 Even-mode Analysis 108
5.12.2 Odd-mode Analysis 109
5.13 DC Isolated WPD: Case-Studies and Examples 110
5.14 Conclusion 113

6 A 2-Port Harmonic Tuning Output Network for Efficiency Enhanced RF Power Amplifiers 115

6.1 Background and Motivation 115
6.2 PA Design Basics 120
6.3 Harmonic-Tuned Amplifiers- A Brief Introduction 126
6.4 The Proposed Theory 127
6.5 Measurement Results 130
6.6 A Three-Port Output Network-Based Harmonic Tuned PAs (Ongoing) 134
6.7 Conclusion 135

7 Conclusion and Future Work **137**

A Fabrication of Transmission Lines **142**

B Losses Incurred During Measurements **144**

LIST OF TABLES

3.1 Case Studies For Different Loads and Frequencies 46
3.2 Design Parameters for Table-3.1 46
3.3 Simulation & Measured Results 46
3.4 Comparison With the State-of-The-Art 48
3.5 Case Studies For Different Real Loads at Different Frequencies . . . 51
3.6 Design Parameters for Table-3.5 52
3.7 Fractional Bandwidth for the Case Study in Table-3.5 (Ideal Lines) . 52
3.8 EM-Simulated & Measured Results 53
3.9 Comparison With the State-of-The-Art 54
3.10 Case Studies for Various Frequency and Impedance Transformation Ratios 61
3.11 Comparison with a Few State-of-the-Art Designs 68

4.1 Parameters for Various Band Ratios 75
4.2 Final Dimensions of the Prototypes 76
4.3 Performance Comparison with Some Previous Designs 80

5.1 Design parameters for the three sections 89
5.2 Simulation & Measured Results 91
5.3 Comparison with the Current State-of-the-Art 93
5.4 Design Parameters for the Prototype 98
5.5 Simulation & measured results 98
5.6 Comparison with a Few State-of-the-Art Designs 99
5.7 Comparison with the State-of-the-Art 113

6.1 Impedances Obtained from Load-Pull 126
6.2 Performance Comparison of the Designed PA With the State-of-the-Art 133

LIST OF FIGURES

1.1 A Typical Drone Communication System [1] 2

1.2 Fixed Wing Drone (left) and Rotor-Craft Drone (right) 3

1.3 Drone Swarm (left) [2], Square Squadron by Swarm (right) [3] . . . 4

1.4 Frequency Plans for UAV 5

1.5 Communication Scheme between Drones in a Swarm 6

1.6 General Scenario of an Energy Harvester Exposed to a Typical Radiation Environment 8

1.7 Impedance Transformation Ratio 9

1.8 Per-Band Bandwidth (shaded area) 10

1.9 Swarming Radius Based on the Effective Power Delivered 11

1.10 Simple Illustration of Power Added Efficiency 11

2.1 A Simple Single Band Quarter-Wave Impedance Transformer 18

2.2 Output Impedance of Wolfspeed GaN HEMT: An Example of FDCL 22

3.1 General Structure of Microstrip Coupled Lines with Design Parameters 35

3.2 Coupled Line Structure with Superposed Even and Odd-Mode Currents 36

3.3 Floating-Arm All-Pass Coupled-Line Configuration 38

3.4 Floating-Arm APCL Configuration for Dual-Band FDCL to Complex Conjugate Generation 39

3.5 A Meandered Line APCL Unit Cell 41

3.6 A Meandered Line APCL Unit Cell 42

3.7 Proposed Dual-Band Matching Network 43

3.8 Section-A: Coupled-Line in All-Pass Configuration 43

3.9 Section-B: Susceptance Cancellation Dual-Band Stub 44

3.10 Section-C: $\lambda/4$ Meandered Coupled-Line 45

3.11 Simulation Results of The Case Studies in Table-3.1 47

3.12 The Fabricated Prototype 47

3.13 EM-Simulation and Measured Results 47

3.14 Block Diagram of the Proposed Impedance Transformer 48

3.15 Circuit Representation of the Proposed Design 49

3.16 Design Flow of the Proposed Matching Network 51

3.17 Cases for Different Impedances and Frequencies 52

3.18 The Fabricated Prototype 53

3.19 EM Simulation and Measurement Results 53

3.20 The Proposed Dual-Band Impedance Transformer 55

3.21 The Floating Arm All-Pass Coupled Line 55

3.22 Limits of Impedance Transformation Ratio for Different Values of Z_{e1} and Z_{o1} for Different Source Impedances 59

3.23 (A) Maximum Possible Values of *r* for *k* = 7, and Corresponding Line Impedances for the Set (B) Maximum Possible Values of *r* for *k* = 9, and Corresponding Line Impedances for the Set 59

3.24 (A) Maximum Possible Values of *r* for *k* = 0.4, and Corresponding Line Impedances for the Set (B) Maximum Possible Values of *r* for *k* = 0.2, and Corresponding Line Impedances for the Set 59

3.25 Design Parameter Values for Ultra-Low *k* and Ultra-Low *r* (Denoting Lower Limits of Transformation Ratios: (A) Minimum Possible Values of *r* for *k* = 9, and Corresponding Line Impedances for the Set (B) Minimum Possible Values of *r* for *k* = 0.2, and Corresponding Line Impedances for the Set 60

3.26 Simulation Results for the Various Case Studies 61

3.27 Measurement Setup for the Impedance Transformer and their Dimensions in terms of Guided Wavelength (A) For *r* = 1.33, *k* = 6.0, (W1 = $2.65\lambda_g$; L1 = $4.12\lambda_g$)@$1.8GHz$ (B) For *r* = 9, *k* = 0.3, (W2 = $1.22\lambda_g$; L2 = $3.36\lambda_g$)@$800MHz$ (C) For *r* = 15, *k* = 9, (W3 = $1.25\lambda_g$; L3 = $1.35\lambda_g$)@$400MHz$. Here (L1, W1), (L2, W2) and (L3, W3) are the Lengths and Widths of the Fabricated Prototypes in (A), (B) and (C) respectively 62

3.28 Case-1: Measured vs EM Results; Fractional Bandwidth (FBW: -15dB reference) = 19.4%@$1.8GHz$ and 16.6%@$2.4GHz$ 63

3.29 Case-2: Measured vs EM Results; Fractional Bandwidth (FBW: -10dB reference) = 125%@$800MHz$ and 5.5%@$7.2GHz$ 63

3.30 Case-5: Measured vs EM Results; Fractional Bandwidth (FBW: -10dB reference) = 50%@$400MHz$ and 5.0%@$6.0GHz$ 63

3.31 Proposed TPD with Ultra-High Transformation Ratio 64

3.32 S-Parameter Simulation Results of the TPD (for $k = 0.2$ and $r = 1.33$) 65

3.33 S-Parameter Simulation Results of the TPD (for $k = 5$ and $r = 1.33$) 65

3.34 S-Parameter Simulation Results of the TPD (for $k = 0.2$ and $r = 15$) 65

3.35 S-Parameter Simulation Results of the TPD (for $k = 5$ and $r = 15$) . 66

3.36 Measurement Setup for the T-Junction Power divider (A) For *r* = 6.25, (W1 = 1.39λ_g; L1 = 6.71λ_g)@$900MHz$ (B) For *r* = 15, (W2 = 0.80λ_g; L2 = 2.94λ_g)@$500MHz$. Here (L1, W1) and (L2, W2) are the Lengths and Widths of the Fabricated Prototypes in (A) and (B) respectively 66

3.37 Measured Results vs EM for *r* = 6.25, Fractional Bandwidth (FBW) = 61.1%@$900MHz$ and 12%@$5.0GHz$ 67

3.38 Measured Results vs EM for *r* = 15, Fractional Bandwidth (FBW) = 100%@$500MHz$ and 8%@$7.5GHz$ 67

4.1 General Architecture of the Proposed Dual-Band WPD 70

4.2 Even Mode Equivalent Circuit of the WPD 71

4.3 Odd Mode Equivalent Circuit of the WPD 73

4.4 Variation of line impedances with frequency-ratio for (A) $Z_{ev} = 78\Omega$, (B) $Z_{ev} = 120\Omega$ and (C) $Z_{ev} = 170\Omega$ 74

4.5 Simulated Results of the Proposed WPD for r = 2 76

4.6 Simulated Results of the Proposed WPD for r = 5 and r = 7 77

4.7 The fabricated prototypes for r = 2 (top) and r = 7 (bottom) and their measurement using a VNA. Dimensions are in mm/mm 78

4.8 The fabricated prototypes for r = 2 (top) and r = 7 (bottom) and their measurement using a VNA. Dimensions are in mm/mm 79

5.1 Schematic of the Proposed Tri-Band Impedance Matching Network 83

5.2 Circuit Representation of the Proposed Tri-Band Impedance Matching Network using Microstrip Transmission Lines 83

5.3 FDCL-to-Real Load Conversion: Considering Only the Impedances- Z_{L1} and Z_{L3} @ f_1 and f_3 Respectively 84

5.4 Section-A: Admittance property of two section transmission line used to match $Z_{in,real}$ with Z_V at f_1 and f_3 86

5.5 The Tri-Band Impedance Transformer Design Flow 89

5.6 The Output Impedance of the 10W Wolfspeed GaN HEMT 89

5.7 The Variation in Z_V for Different Values of $Z_{in,real}$. For Realizable Design, Z_V and hence, $Z_2 \in$ [30-150]Ω, with the Assumption that $Z_1 = Z_{in,real}$ 90

5.8 Variation of Z_4 with Z_V for a 50Ω source 90

5.9 The Dependence of Frequency Ratio r_{31} on Z_V 91

5.10 The Dependence of Frequency Ratio r_{21} on Z_V 92

5.11 The Fabricated Prototype of the Proposed Impedance Transformer . 92

5.12 EM Simulation vs Measured Results 92

5.13 Schematic of the Proposed Tri-Band Impedance Transformer 93

5.14 Dual-Band Matching using a Meandered APCL 94

5.15 Extension of Frequency Ratio r_{32} for Various Virtual Impedances Z_{V1}. All Units of Impedances are in Ohm (Ω) 95

5.16 Behavior of Both Frequency Ratio and Impedance Transformation Ratio for Various Virtual Impedances. All Impedance Units are in Ohm (Ω) 96

5.17 Impedance Bridging with a $\lambda/4$ Transformer at Common Frequency f_2 97

5.18 The Fabricated Prototype Along with Dimensions 98

5.19 EM Simulation vs Measured Results 98

5.20 General Architecture of the Proposed Tri-Band WPD 100

5.21 Even Mode Half-Circuit 101

5.22 Odd-Mode Half-Circuit 104

5.23 WPD Designed at 0.8GHz, 1.8GHz and 3.4GHz; $Z_1 = Z_S = 51.16\Omega, Z_0 = 50\Omega, \theta_0 = 8.7°\theta_1 = 55.38°, Z_P = 47.64\Omega, Z_Q = 100\Omega, Z_X = 74.64\Omega, Z_Y = 156.67\Omega, R_1 = 100\Omega, R_2 = 25\Omega$ (Optimized) 105

5.24 The Measurement Setup (top) and the Fabricated Prototype (bottom). L = $0.17\lambda_g$; W = $0.12\lambda_g$ 106

5.25 Measured, Simulated and EM Results of the Fabricated Prototype . 107

5.26 DC Isolated Tri-Band WPD 108

5.27 Even Mode Half-Circuit 108

5.28 Odd Mode Half-Circuit 110

5.29 WPD Designed at 0.8GHz, 1.8GHz and 3.4GHz; $Z_e = 59\Omega, Z_o = 24.4\Omega, Z_S = 70.5\Omega, \theta_0 = 3.5°, \theta_1 = 55.4°, \theta_2 = 110.7°, Z_X = 56.6\Omega, Z_Y = 118.8\Omega, R_1 = 100\Omega, R_2 = 15\Omega$ 111

5.30 The Measurement Setup (top) and the Fabricated Prototype (bottom) of the DC Isolated WPD. All Units in Millimeter (mm) L = $0.37\lambda_g$; W = $0.32\lambda_g$ 112

5.31 Measured, Simulated and EM Results of the DC Isolated Variant of the Fabricated WPD Prototype 112

6.1 Classes of Operation of RFPAs and their Corresponding Transistor Bias States w.r.t Conduction Angle [4] 117

6.2 Ideal Case of Zero I-V Overlap Leading to 100% Efficiency 118

6.3 Practical Case where I-V Overlap Occurs leading to Power Dissipation (Yellow Shaded Region) and $< 100\%$ Efficiency 118

6.4 Classical Example of Class-F PA with Harmonic Load Conditions . 119

6.5 Mapping of Harmonic Impedances from the Intrinsic to the Packaged Drain Plane of the Transistor 120

6.6 The RFPA Design Flow 121

6.7 Determining DC I-V Q-Point in Keysight ADS 122

6.8 Example Setup- Setting up the Transistor for Unconditional Stability 123

6.9 Stability Analysis Results 124

6.10 Load-Pull Analysis for Determining Z_{opt} 125

6.11 Fundamental and Harmonic Load-Pull Contours for Power Delivered and Power Added Efficiency 125

6.12 Parasitic Model of the Transistor used for Modelling Drain Impedances from the Intrinsic Plane to the Packaged Plane 127

6.13 The Proposed Two-Port Harmonic Tuning Network 128

6.14 (a) Impedance Points of the Proposed Amplifier at the Packaged Drain Plane (b) Corresponding Impedance Points in the Intrinsic (Current Generator) Plane [Mentioned at the Design Frequency of 2.4GHz] . 130

6.15 Fabricated 2-Port Network with Measured S-Parameter Results (Units in cm and default width = 0.6cm) 131

6.16 The Fabricated PA with all Dimension are in Centimeter (cm) and Default Line-Width of the PA is 0.6cm unless Otherwise Mentioned . . 132

6.17 The Measurement Chain with Schematic Representation 132

6.18 Simulated and Measured Results with IV Waveforms 133

6.19 Schematic of the Hypothetical Harmonic Tuned PA 134

6.20 Circuit Under Investigation 135

7.1 Substrate Integrated Waveguide Technology (Basic Structure) [5] . . 140

ABBREVIATIONS

4G	4th Generation Wireless Standard
5G	5th Generation Wireless Standard
ADS	Advanced Design System
APCL	All Pass Coupled Lines
BLoS	Beyond Line of Sight
CAD	Computer Aided Design
CATV	Cable Television
CW	Continuous Wave
DBA	Dual-Band Antenna
DC	Direct Current
DE	Drain Efficiency
DPD	Digital Pre-Distortion
EM	Electromagnetic Momentum
FDCL	Frequency Dependent Complex Load
FET	Field Effect Transistor
FOM	Figure of Merit
GaN	Gallium Nitride
GDT	Ground Data Terminal
GSM	Global System for Mobile Communications
HEMT	High Electron Mobility Transistor
IIP3	Input 3rd Order Intercept Point
IoT	Internet of Things
ISM	Industrial Scientific and Medical Band
IV	Current-Voltage
LDMOS	Laterally Diffused Metal Oxide Semiconductor
LNA	Low Noise Amplifier
LoS	Line of Sight
LTE	Long Term Evolution

mMIMO	massive Multiple Input Multiple Output
MATLAB	Matrix Laboratory
OC	Open Circuit
OIP3	Output 3rd Order Intercept Point
P1dB	1dB Compression Point
PAE	Power Added Efficiency
PCB	Printed Circuit Board
RF	Radio Frequency
RFPA	Radio Frequency Power Amplifier (also PA)
SAR	Synthetic Aperture Radar
SC	Short Circuit
SIW	Substrate Integrated Waveguide
SMD	Surface Mounted Devices
SWS	Slow Wave Structure
TPC	T-Junction Power Combiner
UAV	Unmanned Aerial Vehicle
UHF	Ultra High Frequency
VHF	Very High Frequency
VNA	Vector Network Analyzer
WCDMA	Wideband Code Division Multiple Access
WiFi	Wireless Fidelity
WiMAX	Worldwide Interoperability for Microwave Access
WPD	Wilkinson Power Divider

NOTATION

ϵ_r	Dielectric Constant of Material
$\tan\delta$	Loss Tangent
λ_g	Guided Wavelength
Z_L	Load Impedance
Z_S	Source Impedance
R_L	Resistive Load

CHAPTER 1

INTRODUCTION

1.1 Motivation

The proliferation of wireless standards has necessitated the advancements in RF-front end and the associated peripheral circuit components, devices, and systems. It is also a well-accepted fact the advancement in circuit design technology generally lags the evolution in wireless standards by a few years. The outcome of this lag has culminated in a scenario where the RF circuit design community is still trying to address the circuit design schemes for currently employed standards such as WCDMA, WiMAX, WiFi, etc. In this context, the scientific community has been actively engaged in the development of multi-frequency circuits, components, and devices for RF front-end utilized in radio systems such as Software Defined Radio System [6–9], Cognitive Radio System [10–12], WCDMA Systems [13–16], and IoT Systems [17–24].

The design of multi-frequency circuits and components readily available in literature is focused around dual-frequency designs [25–65], with some recent reports of tri-band and beyond [66–80]. The significant challenges in these designs are circuit complexity, frequency ratio, impedance transformation ratio, circuit size, complicated design procedure, optimization technique, etc. Keeping these into perspectives, this thesis aims to address some of the issues pertaining to the current wireless standards, which could also be applied in the realms of upcoming futuristic wireless standards such as 5G, RF energy harvesting, low power IoT applications, and surveillance strategy adopted in civil and defense applications.

In perspective of military applications, the advent of latest technology in the past few years has redefined fighting machines than those used in the wars in history. The advent of “non-human” involvement, or more specifically, robotic warfare has gained

attention since they involve no loss of human lives and additional tech-precision that has the edge over humans [22–24]. Drones or Unmanned Aerial Vehicles (UAV) are aerial robots that can be either autonomous or manually controlled by a ground operator. Besides military applications, drones also find a wide variety of usage in other day-to-day affairs like agricultural field monitoring, disaster relief missions, and rescue missions where human intervention is not possible. Depending upon the nature of the task being performed, drones can have a wide range of specifications- from dynamic range to peer-handling throughput, etc.

1.1.1 Drones- A Brief Note

Drones or Unmanned Aerial Vehicles (UAV) are aerial robots that can be either autonomous or manually controlled by a ground operator. Fig. 1.1 describes the essential parts in a typical drone communication system:

- UAV
- Ground control (UAV Ground Station)
- Mobile GDT (Command and Control + Support Equipment + Display Terminal)
- Payload inside UAV (Camera / SAR / Missile etc.)

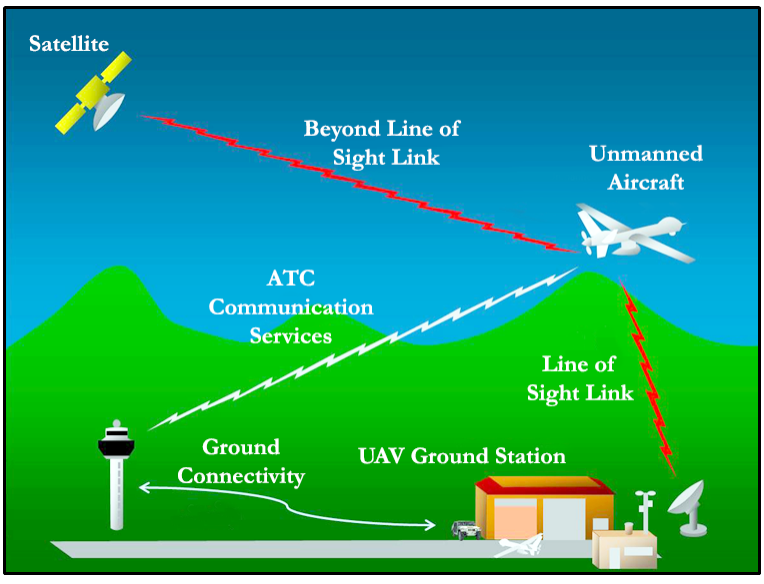

Figure 1.1: A Typical Drone Communication System [1]

The “flying” counterpart falls into two categories- the fixed wing and the rotor-craft, as are illustrated in Fig. 1.2 [81].

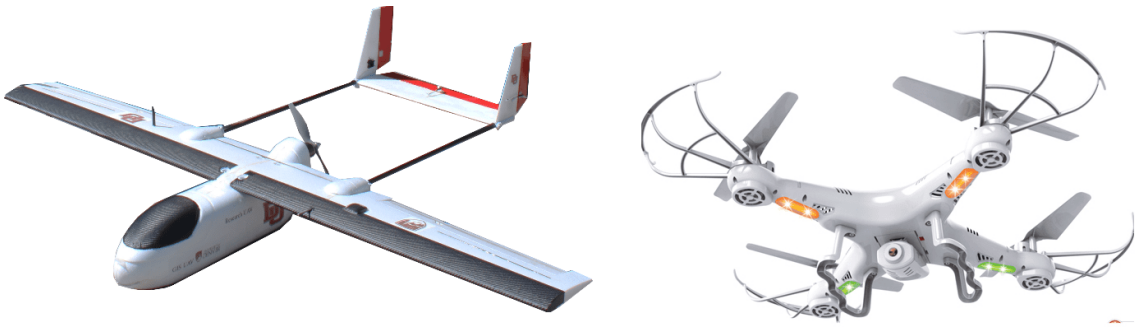

Figure 1.2: Fixed Wing Drone (left) and Rotor-Craft Drone (right)

While the fixed-wing drones have an advantage of high “on-air” time, that increases their flight efficiency, but they lack the ability to hover around a particular area of interest. On the other hand, rotor-craft drones (mostly quad-copters) can hover around a fixed location, making them suitable for military stealth missions. While the type of drones to be used mostly depends on the purpose of using it, there are still some factors that determine their efficiency. These are listed as follows:

- Flight time
- Payload efficiency
- Operating range
- Privacy and security

Research all around the globe is being carried out to address the concerns of a very long operating range and Privacy and Security. Operating range and Security come hand in hand and happens to be of the utmost importance when not only one but many drones fly up in the sky. Those are called drone swarms and are discussed in the next section.

1.1.2 A "Swarm" of Drones!

Drone swarms are collection or aggravation of many drones (typically 60-100) flying together, controlled as a whole, by a ground operator. Instead of controlling a single

drone, the operator collectively controls the entire swarm. This has a significant advantage in bottleneck attacks when the enemy shoots down a single or a couple of drones without noticeable damage to the swarm as a whole, thus proving to be cost-effective.

Drone-swarm warfare is still in the nascent phase, with the US and China investing much money in their research. The US "Avatar" project by DARPA [82] was successfully deployed, where several fixed wing micro-drones were launched from an F-16 fighter at 430 miles/hour. The project calls for the Pentagon to pair "high-tech 5th generation" fighter jets like the F-22 Raptor and F-35 Joint Strike Fighter with unmanned versions of older jets like the F-16 Falcon or F/A-18 Hornet, targeted to be flown without a pilot for the first time.

In the Asian front, the China Electronics Technology Group Corporation (CETC) claimed to have made a world record of flying 67 drones together [83], shattering the previous record of the US-based Advanced Robotic Systems Engineering Laboratory (ARSENL) who launched 50 drones successfully at Monterey, California [84]. Fig. 1.3 illustrates the idea of drone swarms.

Figure 1.3: Drone Swarm (left) [2], Square Squadron by Swarm (right) [3]

There are two types of communications possible for a UAV, namely:

1. Line of Sight (LoS)

2. Beyond Line of Sight (BLoS)

As evident from the names, the former requires the UAV to have a line of sight from the control station, thus limiting the capabilities within a fixed range (segregated or non-segregated airspace). On the other hand, the BLoS communication scheme does not require the UAV to be in the line of sight with its control station. The vehicle is

controlled via satellite links and thus provides the advantage of increased range over its former counterpart. The frequency plan of UAVs are discussed in Fig. 1.4.

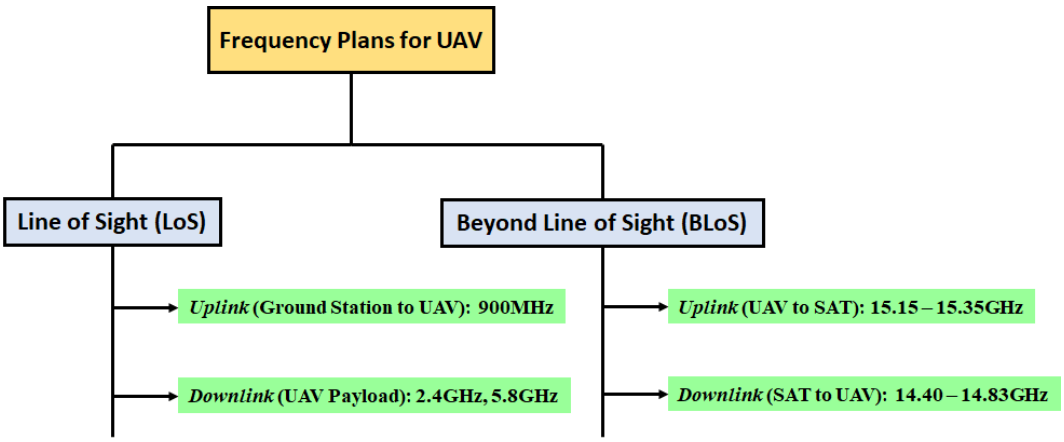

Figure 1.4: Frequency Plans for UAV

The above-described frequencies are for ground control with a UAV or a swarm. Apart from this, in a swarm, the UAVs are required to talk with one another. As this inter-drone duplex communication is LoS, thus it would mostly use 1.2, 2.4, and 5.8GHz for communication. This would include flight control and payload data, requiring multi-band devices to facilitate two things together.

The communication system is the backbone of a swarm. To have a successful operation, a swarm should have strong contact with its ground station (if manually controlled) and amongst its peers. The operating range for a manually controlled swarm can be defined in two perspectives:

- Range from the Ground: This defines the maximum distance the swarm can fly collectively and yet be controlled securely from the ground.
- Maximal spread: This defines the maximum distance that each drone can stay from one another for functional operation. Considering the swarm to be lined up in a circle, it can be defined as the maximum length of the arc between each drone along the circumference of the circle.

The range depends on the amount of power that the transmitter spits out with other factors remaining reliable and robust. Thus, at the circuit level, a High-Efficiency Power Amplifier is required to do the same. The scheme is illustrated in Fig. 1.5.

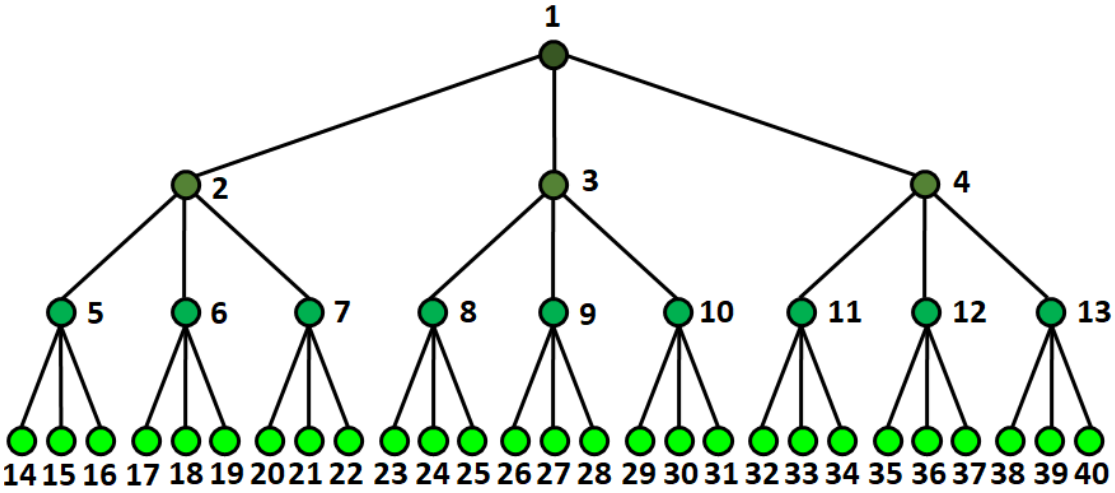

Figure 1.5: Communication Scheme between Drones in a Swarm

For a swarm to be operationally successful, it is of utmost necessity that each member can talk to each other in a non-colliding fashion. An exponential communication scheme proves to be efficient. In this scheme, a single drone can communicate with three other drones, each of which can communicate with three others and so on. This creates a swarm of 40 interconnected drones in the 3rd generation itself. To practically implement this type of wireless transceiver architecture, multi-band (tri-band in this case) RF devices are necessary. To be more specific, a tri-band RF Power Amplifier (RFPA) that has a viable high Delivered Output Power, linear over the range of operation (at the three bands), and a considerably high Power Added Efficiency, is required. In addition to it, several other components, such as Power Dividers/Combiners, Couplers, and Impedance Matching Networks, are also required for facilitating the process. The upcoming chapters elaborate various research works on multi-band Impedance Matching Networks and their applications in various RF components like Power Dividers/Combiners and Power Amplifiers.

1.2 Energy Harvesting Applications

It is a common fact that nowadays, the performance-based development and deployment of efficient wireless protocols have made it necessary to develop efficient circuitry to implement the same. Recently, there has been an increased research interest in RF energy harvesting/scavenging techniques. Energy harvesting is a technique uti-

lized to generate electricity from ambient RF radiation sources, thus proving useful in energy-constrained RF systems like wireless sensor networks. Typical applications of RF energy harvesting are in wireless body area networks, wireless power transfer, and wireless charging of cell-phones/smart-watches. Apart from that, energy harvesters are increasingly gaining demands in home automation IoT systems as well that tend to "recharge themselves" from the available radio-energy in the surroundings.

With the recent practical implementation of the 5G standards, there has been an abrupt broadening of the spectrum in which wireless devices used to operate [85]. It is a fact worth noting that crowded localities [86], establishments, communities, and even IoT-automated homes [87] are drowned in a "radiation tsunami" much of which can be attributed to various gadgets of daily use operating at different frequency bands. That being said, developing an efficient RF energy harvester capable of harvesting energy from sources at different frequency bands has gained research interests [88–91]. The only challenge that hinders the implementation of such a network is that the bands might be widely separated across the radio spectrum. This essentially limits the operation of the underlying passive components of the system, mainly the impedance matching networks, and the power dividers. Existing architectures [86] have reported usage of separate harvesting chains for addressing this problem, but with the prime disadvantage being redundancy and bulkiness of the harvester. These limitations can be addressed by proposing architectures that can operate simultaneously at frequencies of interest that are widely spaced apart in the spectrum.

Fig. 1.6 illustrates a typical scenario in which an energy harvester is exposed to a radiation environment. It is important to note that in this case, only ambient radiation from the communication devices have been considered as it comprises a maximum share of the available radiated power. The figure shows that the environment addresses the frequency range of 400MHz to 8.0GHz, and the associated RF energy is targeted for harvesting. The energy harvester consists of an antenna, an impedance matching network, a voltage multiplier, and an energy storage sector. To facilitate dual-band operation at the existing 4G/LTE and the new sub-6GHz 5G bands, it is necessary that the harvester's internal circuit modules also operate at the said frequencies. A dual-band impedance transformer with a flexible frequency ratio is primarily necessary to match both closely and distantly separated frequency bands. Depending on the loading

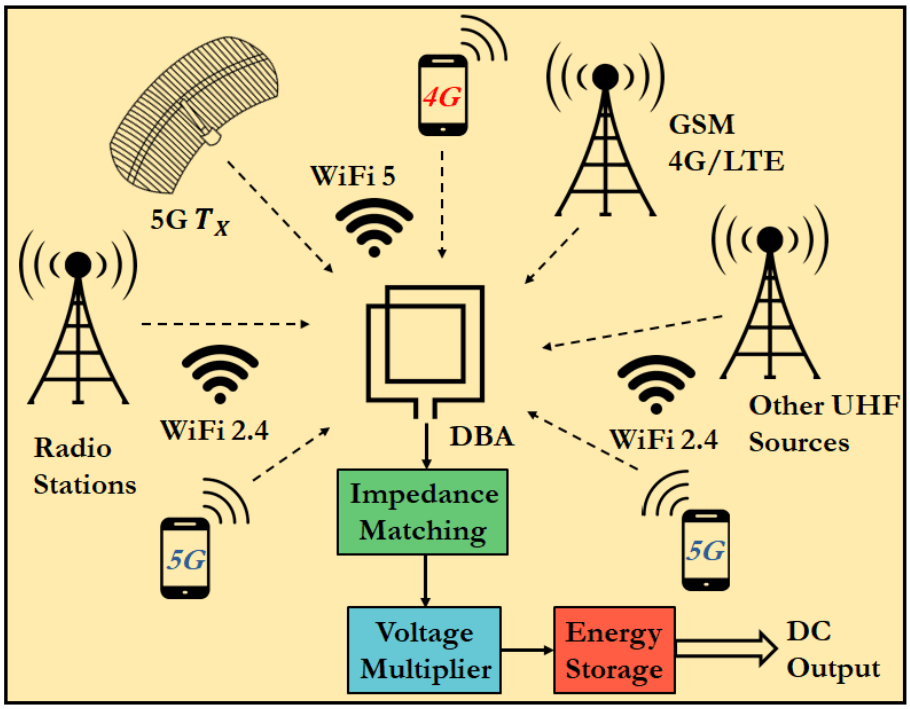

*DBA: Dual-Band Antenna; WiFi 2.4 and WiFi 5: 2.4GHz and 5.0GHz WiFi Standard

Figure 1.6: General Scenario of an Energy Harvester Exposed to a Typical Radiation Environment

condition, the desired impedance matching network should be able to accommodate a wide range of load values from very high to very low, hence making the impedance transformation ratio an important design parameter. Apart from that impedance transformers and power dividers also report usage in commercial Cable Television (CATV) broadcasts [92], wireless sensor nodes [93], cellular base stations [94], satellite communications [95] etc. The application domain being huge, a flexible and robust dual-band transformer architecture that addresses the above-stated limitations are necessary.

1.3 A Multi-Frequency Perspective

The basic building blocks of all the multi-band modern wireless systems that we discussed are multi-band active and passive devices. In practice, certain metrics are used to characterize the performance/Figures of Merits (FoM) of the designed device. These are important because based on the performance parameters, the devices are chosen for a particular application. They are discussed in detail as:

1. Frequency Ratio: This is a vital performance measuring metric in any multi-band circuit and essentially defines the maximum obtainable band separation without degrading other measuring parameters. For instance, a specific application might require a power divider to operate at two widely separated frequencies, such as 900MHz, and 5.8GHz. The design of such a device is challenging owing to the distant separation of the frequencies of interest. There have been reports of frequency-based designs that consider the case of operation at discrete frequencies. This limits the design flexibility as the same structure cannot be reused for other sets of frequencies having the same frequency ratio. In other words, a flexible design signifies that a device operating on 1 and 4 GHz should be able to operate successfully at 1.5 and 6 GHz also (for a frequency ratio-based design).

2. Impedance Transformation Ratio: Another important performance measuring metric for multi-band devices is the impedance transformation ratio or the impedance gradient. This is simply the ratio of the load impedance at the device's output port to the source impedance at its input port. From Fig. 1.7, transformation ratio, $Z_T = Z_L/Z_S$. In most conventional designs reported in the literature, the load impedance does not differ from the source impedance by a large value. This parameter is of importance, especially in inter-stage matching networks, as designing the same becomes challenging when the input impedance of the next stage is very high compared to the output impedance of the preceding stage.

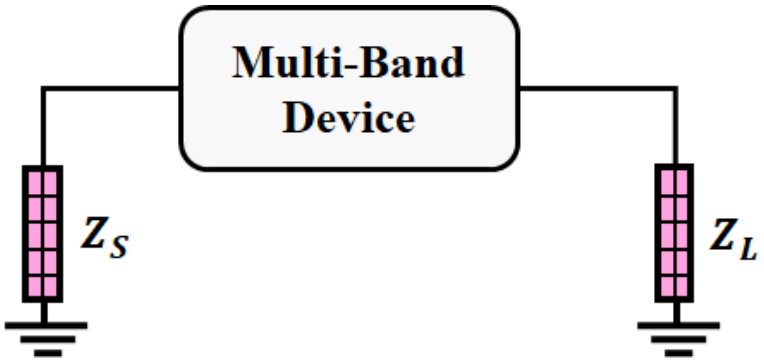

Figure 1.7: Impedance Transformation Ratio

3. Per-Band Bandwidth: For a device operating at multiple frequencies, it is essential to determine the bandwidth attainable at each of the bands of interest. This parameter is not absolute as the bandwidth requirement per band depends upon the application the device is serving. As an example, for a highly selective military radio, operating at three bands of interest, the bandwidth per-band needs to be narrow in order to make it highly selective (with a high Q-factor). On the other hand, in high-speed transceiver systems, the bandwidth requirement per operating band is very high. Generally, the bandwidth is specified below a particular level of reflection coefficient, mostly -10, -15, or -20dB. The shaded part in Fig. 1.8 denotes the same.

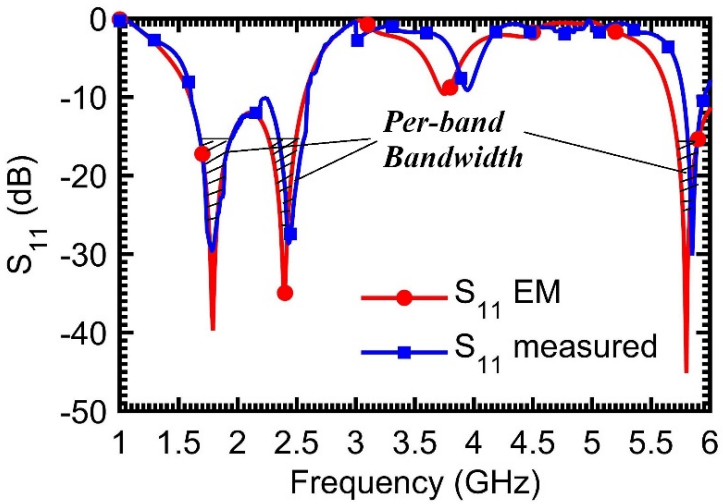

Figure 1.8: Per-Band Bandwidth (shaded area)

4. Effective Power Delivered: In active devices such as power amplifiers, the effective power delivered is one of the critical parameters that essentially determine the operating range of the device in which it is deployed. This can vary over a broad range depending upon the application in which the Power Amplifier is used. For example, in the case of drone swarms, high output power is necessary to increase the swarming range/radius.

   Fig. 1.9 depicts the swarming radius comparison based on the effective delivered power from the transmitter of each drone. The small circular balls denote the position of each drone. It is intuitive that when the Effective Power Delivered is

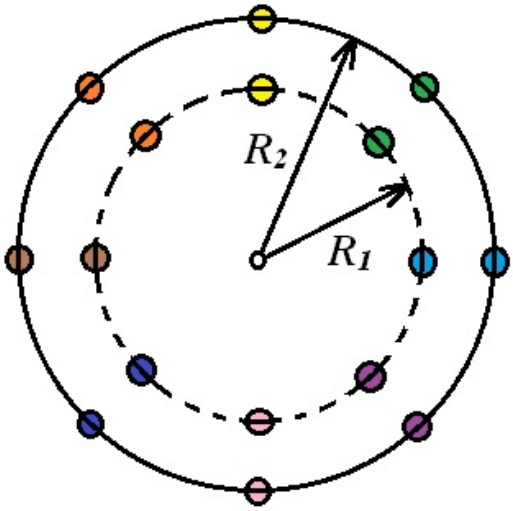

Figure 1.9: Swarming Radius Based on the Effective Power Delivered

less, the swarming radius (R1) is less as compared to when the Effective Delivered Power is more (thus providing a greater swarming radius of R2). On the other hand, in many indoor IoT applications, the delivered output power needs to be low, especially in sensor nodes, and hence, the design has to be made accordingly.

5. Power Added Efficiency: A performance determining metric in Power Amplifiers, the Power Added Efficiency (PAE) is a measure of how much extra power is added to the system by the amplifying block. Essentially, it gives an idea about the amount of DC power that gets converted into RF power by the amplifying device. This is illustrated in Fig. 1.10 where a feeble RF input power is boosted up to an amplified RF output, but in the process, DC power is consumed. A high value of PAE is always desirable in Power Amplifier applications.

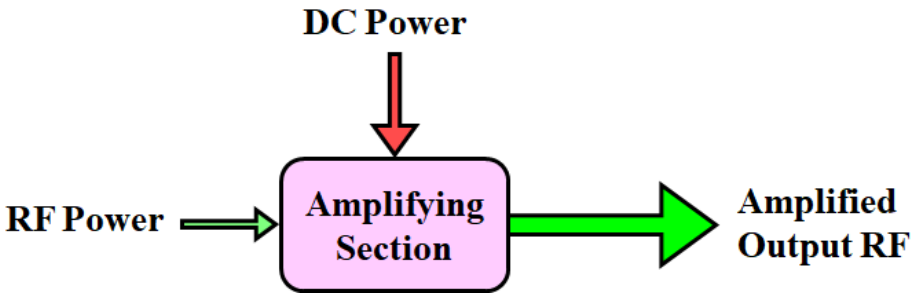

Figure 1.10: Simple Illustration of Power Added Efficiency

1.4 Thesis Objectives

The main objectives of the thesis are to design dual and tri- band impedance matching architectures with enhanced frequency ratios and validate their applications in passive components like power dividers as well as active devices like power amplifiers. They are elaborated point-wise as.

1. Frequency Ratio Extension of Dual-Band Components: The existing literature is replete with dual-band impedance transforming topologies. However, most of them are severely restricted in frequency ratio, operating mostly on frequencies that are not widely spaced apart. Moreover, most of the designs find it difficult to operate smoothly between the minimum and maximum limits of achievable frequency ratios. This work emphasizes on designing frequency ratio enhanced dual-band networks.

2. Transformation Ratio Flexibility: Although some existing works focus on extending the transformation ratios, they lack flexibility. This signifies that an increase in frequency transformation ratio, as well as impedance transformation ratio, cannot be achieved at the same time. Apart from that, it is also observed that the existing architectures are limited in matching two very closely spaced frequencies. This thesis targets simultaneous flexibility in frequency ratio as well as impedance transformation ratio in both the upper and the lower limits.

3. Designing Tri-Band Components: Although there has been many reports of dual-band components in literature, the design of tri-band circuits is still in its infancy. This thesis targets providing new tri-frequency impedance matching techniques and their applications in circuit components like power dividers. This includes proper characterization of the upper and lower frequency ratios f_3/f_1 and f_2/f_1, respectively, their limits and implementation based on design parameters.

4. Design of an Efficiency Enhanced RF Power Amplifier: High-efficiency classes of power amplifiers, namely Class- B, C, D, E, F/F^{-1}, and the more sophisticated ones like Continuous Class-F, Class-B/J, Class-X etc. are harmonically

tuned with specific harmonic terminations. In each of them, the fundamental impedance point is heavily dependent on the harmonics due to the transistor's internal parasitics. This thesis targets developing a passive network to control the fundamental as well as the harmonic loads at three frequencies independently.

1.5 Research Contributions

The defined objectives have been accomplished, and several contributions have been made in the community. These are briefly listed below and are elaborated in the thesis.

- Microstrip coupled-lines have been investigated in detail. Especially, the all-pass coupled line configuration has been studied from scratch, their properties with respect to dual-band matching have been identified and deployed to design dual-band impedance transformers and power dividers. The immense potential of the all-pass configuration in transformation ratio flexibility has been discovered. In addition, another all-pass coupled-line configuration- the meandered-line slow-wave structure has also been reported. It proves to be a fantastic candidate for bandwidth increment in dual-band RF circuits and has adequate potential to be used in energy harvesters.

- A coupled-line core dual-band Wilkinson Power Divider has also been developed that operates on enhanced frequency ratios. The structure is simple, compact, and robust in performance. Previously reported power divider structures either included intensive mathematical analysis, were limited in frequency ratio, or were bulky. The dual-band power divider presented in this thesis addresses the said limitations and proves to be a novel contribution in the domain of passive circuits.

- A new concept of Virtual Impedance has been proposed for tri-band impedance matching networks. A detailed mathematical model has been developed with the characterization of the network with respect to limits of the upper and lower frequency ratios, choice of impedances, and implementation. Variants of the concept

have also been derived in order to enhance the frequency transformation ratios. The proposed theory results in a simple design flow and hence, easy prototyping for commercial uses.

- A tri-frequency Wilkinson Power Divider has been proposed based on the tri-band extension principal of a dual-band transformer. The design strategy is generic to the sense that one can choose from a variety of impedance transformers depending on the applications the device is meant to serve. Therefore, based on the same structure, one can develop a wideband/DC isolated/spurious band suppressed power divider, without changing the entire design model. This generic and versatile behavior has been verified by designing a DC isolated Wilkinson Power Divider on the same framework.

- An efficiency enhanced RF power amplifier has been designed at the WiFi/Bluetooth frequency of 2.4GHz. A passive two-port output network has been proposed that makes the fundamental load independent from the harmonic loads. This essentially controls the drain impedances at three frequencies- fundamental, the second and the third harmonics. Thus, a proper choice of reactive harmonic terminations can be made from the lot that corresponds to efficiency enhanced performance. In other words, the proposed amplifier behaves as a special case of Class-X. A simple mathematical model has been formed with the necessary design criteria.

1.6 Thesis Outline

This doctoral thesis has three major sectors of research. Firstly the frequency and transformation ratio limitations of dual-band transformers are discussed and addressed. Following that, a new tri-band impedance transforming topology is proposed and analyzed in detail. The final section proposes a novel output network for high-efficiency RF power amplifiers. These concepts are further elaborated in the respective chapters according to the following line.

Chapter 2 presents a comprehensive literature survey of the topics discussed in this thesis. There are three major sub-sections that elaborate the study on dual-band impedance transformers, tri-band impedance transformers, Wilkinson Power Dividers, and RF power amplifiers. The prime design strategy in each report is discussed, and limitations are identified in each case.

Chapter 3 discusses in detail about the less-studied properties of All-Pass Coupled-Lines. Two major configurations, namely the floating-arm type and the meandered line type, have been analyzed in detail. Finally, their proper usage to design dual-band impedance transformers and the ability to increase the per-band bandwidth has also been explored. Another highly flexible dual-band impedance transformer configuration has been proposed that has the property to extend the limits of frequency and impedance transformation ratios simultaneously. A detailed mathematical model has been proposed along with closed-form equations and a design flow for easy prototyping. The proposed impedance transformer is utilized to design a T-junction Power Divider exhibiting high-frequency ratios of operations. This would indeed prove advantageous in the design of RF energy harvesters for the upcoming 5G standard.

In **chapter 4**, a new methodology to design WPDs using coupled-line core has been discussed. Detailed mathematical analysis has been provided with various simulation examples. The design scheme enhances the frequency ratio to 7 for the first time.

Chapter 5 introduces a new design concept of tri-band impedance matching networks. A variant of the design strategy has also been analyzed, and its ability to extend frequency ratios have also been explored. A generic tri-band WPD has also been developed that serves a multitude of purposes based on a proper choice of its constituent impedance transformer. A coupled-line-based DC isolated variant of the design has also been designed and tested to validate its generic behavior.

In **chapter 6**, a power amplifier architecture consisting of a specially designed output network has been proposed. The proposed network isolates the fundamental and harmonic impedance dependencies, thus providing a broader reactive design space to the harmonics. The proposed amplifier behaves as a special case of Class-X amplifiers. As has been discussed early, this doctoral thesis targets the design of a dual/tri-band framework addressing the frequency and transformation ratio limitations, targeting

drone swarm applications. In this regard, the relevance and importance of power amplifiers have been mentioned. Moreover, the two-port network mentioned is a perfect example of the ability of passive control on harmonic impedances. Apart from that, the chapter also provides a brief introduction about an ongoing project that targets utilizing the proposed concept to develop a three-port output network for PAs. The advantages would include increased bandwidth and efficiency. Therefore this chapter proves to be a perfect fit in this dissertation.

Chapter 7 concludes the thesis with a brief highlights of the contributions and provides future directions for research in this domain.

CHAPTER 2

A Review of the Literature

Outline

This chapter presents a comprehensive review of the existing literature with respect to multi-band RF passive devices (especially impedance matching networks and power dividers) and RF power amplifiers. The design strategies are briefly discussed with key points and novelty. The limitations of the reported designs, if any, are also identified. It must be noted that the existing literature is reviewed till June 2020. Anything after the said date is beyond the scope of this thesis.

2.1 Impedance Transformers/Matching Networks

Impedance transformers are one of the essential elements of an RF circuit. In fact, it is omnipresent in apparently all passive as well as active devices. The function of an impedance transformer is to convert a given impedance into another. The impedance to be converted is termed as the load (denoted mostly by the notation Z_L), and the target impedance value is called the source (denoted mostly by Z_S). Either the load or the source or both can be a real or a complex value- fixed or frequency-dependent. The terms "impedance transformer" and "impedance matching network" are used invariably, and they both point to the same network. While an impedance transformer "transforms" a given load impedance Z_L into a particular value Z_S, an impedance matching network "matches" the load impedance Z_L with a given source impedance Z_S. The latter is mostly used in the context of circuits where two different modules with varying impedances need to be connected together for minimum transmission loss (hence maximum power transfer). At high frequencies, designing impedance matching networks require transmission lines as lumped component theory fails to respond. The simplest

single-band impedance transforming device is a $\lambda/4$ transmission line [96] that matches two arbitrary real impedances at a desired frequency, as depicted in Fig. 2.1.

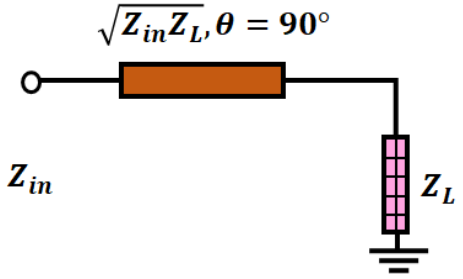

Figure 2.1: A Simple Single Band Quarter-Wave Impedance Transformer

This technique, though the simplest, is limited in a number of ways. Firstly, the process applies only to a single frequency, which is the most trivial solution. Modern-day communication devices are multi-band owing to space compression, resource utilization and robust operation. Thus, research interest in multi-band impedance transformation networks are very high. Secondly, the $\lambda/4$ transformer matches only real loads (Z_L in the figure is real). Most active devices, like PA, LNA, Active Filters etc. have a complex input/output impedance (may or may not be frequency-dependent) that has to be matched to another real/complex impedance. Thus, the $\lambda/4$ transformer fails to serve the purpose. Owing to these shortcomings of the $\lambda/4$ transformer, researchers started showing great interest in networks that can provide matching at more than one frequency of interest. If that could be the case, then several applications can be carried out within a single device.

Impedance transformers can be functionally categorized into three main types, depending upon their source and load impedances, namely:

- Real Source and Load Impedances Transformer: Here, both the load and the source impedances are real-valued. These find applications in power dividers, couplers, crossovers etc.

- Complex to Real Impedances Transformer: In this case, either of the load or the source is a complex impedance, and the other is a real impedance. They find applications in RF amplifiers, active mixers etc.

- Complex to Complex Impedances Transformer: This is a case in which both the load and source impedances are complex-valued. These types of transformers mostly find use as a part of inter-stage matching networks in RF systems.

In the upcoming section, we will be reviewing the literature comprehensively based on the mentioned categorization.

2.2 Dual-Band Impedance Matching Networks

2.2.1 Real to Real Transformers

The run for dual-band networks started with the 2002 paper authored by *Chow et. al.* [26], who proposed a dual-band impedance matching technique for the first time. This method used a two-section 1/3rd wavelength transmission line, cascaded in series, which could provide matching at a particular frequency of interest and its harmonics. Matching was obtained between a 50Ω port impedance (Z_0) with a load equals to KZ_0, where *K* is a constant, mainly known as the transformation ratio of the transformer. The input impedance was forced to be real and equal to KZ_0, the simplification of which leads to transcendental equations of the 4th order. This was followed by a CAD solution for a particular case of $K = 2$. The solution was satisfied for the choice of $Z_1 = K^{2/3}R_L$, $Z_2 = K^{1/3}R_L$, $\theta_1 = \theta_2 = 60^\circ$. The major limitation of this design was that the analysis was not exact, and the design equations were not closed-form. In addition to it, another shortcoming of this design was that the second frequency was always a harmonic of the fundamental. i.e, it could not be chosen arbitrarily. However, this design theory was an important report to start with.

Monzon [27] in 2003, addressed a simple dual-band transformer in two sections, which addressed the limitations of the *Chow* transformer, including the problem of harmonic matching. The Monzon transformer was a simple cascaded two-section transmission line structure, similar to that of *Chow*. The difference lied in the electrical lengths of the transmission lines, which *Monzon* assumed to be $\theta_A = \theta_B = \theta$, which was indeed dependent on the frequency ratio f_2/f_1. This modified transformer had

a reduced design variable count and could provide dual-band impedance matching at any two arbitrary frequencies of interest. Although very promising and widely used, the *Monzon* transformer does not consider the practical limits of the line impedance $[20\Omega - 160\Omega]$ for fabrication in microstrip technology (see Appendix- A). There are several instances, which make the design theoretically perfect but rather practically impossible. In addition to that, the *Monzon* transformer is also limited in terms of the achievable transformation ratio.

A two-section dual-band Chebyshev impedance transformer was reported in [97], establishing the fact that *Monzon* transformer is a special case of the same. The proposed theory, a more generalized *Monzon* transformer, established a trade-off between the out-of-band reflection coefficient and the achievable bandwidth. Another modification of the design was proposed in [98], with an even number of transmission lines.

A dual-band L-network was reported in [58]. The design fascinates owing to its simplicity in structure and the fact that the dual-band stub can be placed in either the load or the source side, facilitating conventional design. In addition to it, the stub has its own design flexibility as it can be either open or short circuited. This proves advantageous over a wide range of susceptances that are generated in the matching process. However, the frequency ratio and impedance transformation ratio of the presented design scheme is even limited compared to the *Monzon* transformer. It also fails to provide a strong mathematical background behind the transformer operation.

A coupled-line based L-section dual-band impedance transformer was reported in [99]. The two configurations proposed in the design scheme prove to be flexible and caters to match a fair range of real loads. An important feature of this design is the inherent DC block property due to the use of coupled lines. Though proving to be useful in the design of a power amplifier output stage, this scheme has a few limitations. However, the "per-band" bandwidth obtained for each frequency is quite low. Moreover, the range of loads that could be matched are also limited by the difference between the even and odd arm impedances of the coupled line. Certain values can lead to very low spacing between the coupled line arms, hence hindering fabrication.

An interesting dual frequency admittance property of two-section transmission line was reported in [100]. The proposed design scheme resembles the *Monzon* transformer

with an additional susceptance cancellation stub. It was however, demonstrated that the *Monzon* transformer is a special case of the proposed theory with the limitations properly addressed. A T-junction power divider was also developed using the proposed theory to demonstrate practical utility. Similar architecture was used to develop two-section transmission line based L and T networks for dual-band matching. The designs could solve many of *Monzon* transformer's problems but still, were limited in transformation ratios. The maximum frequency ratio from the simulations did not exceed 4 and the maximum impedance transformation ratio was around 8 (for a 50Ω source). One major drawback of this design is the inter-dependence of the frequency and impedance transformation ratio. This signifies that an increase in frequency ratio would correspond to a lower impedance transformation ratio and vice versa.

2.2.2 Real to Complex Transformers

In many applications like power amplifiers, low noise amplifiers, mixers, antennae etc. often a complex load has to be matched with a real source or vice versa. Here comes the utility of real to complex transformers. Designing these transformers are a bit more challenging as the load has two distinct complex values at two frequencies of interest. Such loads are called **F**requency **D**ependent **C**omplex **L**oads or FDCL. Fig. 2.2 illustrates the output impedance of a 10W Wolfspeed GaN HEMT for power amplifier applications. It is evident from the figure that the real as well as the imaginary part of the impedance vary with frequency. Thus in this scenario, matching has to be obtained at the two frequencies of interest where loads are different complex values.

There have been many architectures of a transformer matching complex loads to real impedances with early reports in [101]. The structure, based on multiple transmission line sections and two parallel stubs employed CAD approximations to solve a fourth-degree equation. The results obtained from this method point more towards a wideband transformation rather than dual-band. A more generalized version of this design [102] considered complex source as well as load impedances and provided a detailed analytical methodology for the design process. However, the major limitation of the design scheme is that it does not consider the frequency dependent behavior of the load.

A three-section dual-band impedance transformer [46] reported matching of FDCLs

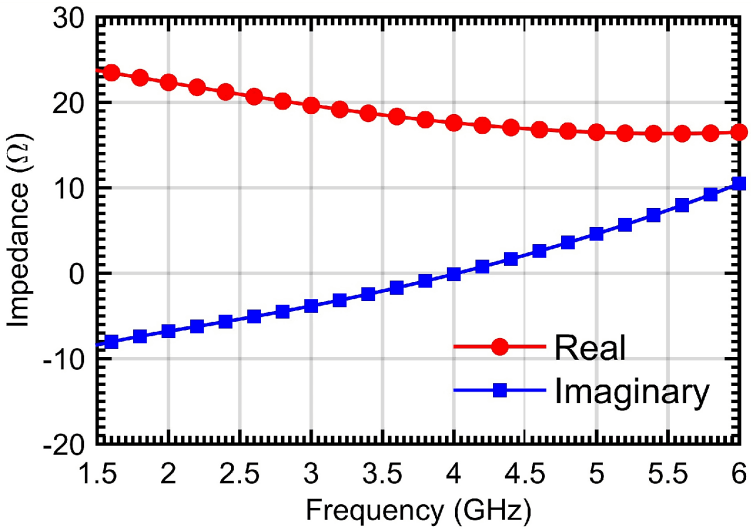

Figure 2.2: Output Impedance of Wolfspeed GaN HEMT: An Example of FDCL

with a real source at two arbitrary frequencies of interest. The first section would transform the complex load into an intermediate impedance that have same resistive part and conjugate reactances. The next two sections are utilized to cancel out the conjugate reactances and match the real part with the real source at the two frequencies of interest. The proposed design scheme supported by very complicated analytical equations, however, does not clarify in detail the matching of complex conjugates with the real source. A generalized version of the same was reported in [103]. The design consisted of four cascaded transmission line sections. The additional section on the source side was used to transform the real source impedance into complex conjugates, similar to the load side. Then the intermediate two sections would match both the complex conjugate impedances at two frequencies of interest. This scheme also had similar limitations as that of the three-section transformer in [46].

A two-section transformer incorporating shunt stubs was reported in [104]. The limitations included transcendental equations that could only be solved by numerical optimization techniques. A simple T-structure dual-band impedance transformer was reported in [25]. The design operated on the principle of complex conjugate generation similar to [46], canceling the susceptance using a dual-band stub and matching the real part to the source. However, the design was limited in the achievable frequency ratio and physical realizability for certain impedance values.

Often it is observed that dual-band transformers have a very limited choice of loads

over which they operate [25]. Especially in cases of complex loads, the choices narrow down severely. A systematic methodology to address this problem was reported in [32]. It uses an additional section of transmission line/stub, called the "load healer" to shift the unrealizable impedance value to a realizable one. Thorough mathematical derivations were presented and a simple design flow was provided.

A dual-frequency phase offset line based dual-band transformer was proposed in [105]. The transmission lines had unequal characteristic impedances and the design strategy was graphical and complicated. Similarly a $\Pi-$ section dual-band transformer was reported in [30] but the design process was mostly iteration based. A modified version of a T-network based dual-band impedance transformer was reported in [106] that used the *Monzon* transformer as one of its arms. It is due to this reason that the reported architecture is limited in frequency ratio. Two distinct loads have been converted into complex conjugates and then a filter transformation is used to match it to the source in [107]. However, this design strategy does not have any analytical background and does not exhibit a wide bandwidth performance. An interesting dual-frequency admittance property of commensurate transmission lines has been reported in [48]. The proposed theory targeted frequency ratio improvement but could only attain a maximum of around 3.5. Another two-section transmission line based transformer for matching FDCLs to real impedances was reported in [48]. Detailed analysis was provided along with closed-form design equations but was limited in frequency ratio.

Several coupled-lines based dual-band impedance transformers have been reported in the literature [28, 108, 109]. Incorporating coupled-lines in the designs has been a motivation because of the fact that besides compactness, coupled-lines provide an extra design parameter (because of even and odd characteristic impedances) adding to its degree of freedom. Apart from that coupled-lines are inherently DC isolated, which proves to be advantageous in applications like amplifiers, obliterating the requirement of coupling capacitors. A dual-band impedance matching network with inherent DC block characteristic was reported in [28] and a T-junction power divider based on matching network using coupled-lines in the all-pass configuration in [108]. The limitations of these designs were in maintaining the matching for both the real and imaginary parts of the impedance at the two frequencies of interest, which can be difficult at times, more often with coupled-lines having unequal even/odd mode phase velocities. A com-

pact DC isolated coupled-line based dual-band impedance transformer was reported in [109]. The idea is based on loading the two opposite arms of the coupled-lines with short or open circuit stubs. The design however, is severely restricted in frequency ratio, proving to be useful only at closely spaced frequencies. A T-section dual-band transformer using coupled lines was reported in [29]. The design employed complex conjugate generation using a series transmission line, susceptance cancellation by a dual-band stub and matching of the real impedance to the source using a coupled-line section. The design methodology is simple but is limited in frequency ratio as well as bandwidth provided by each band of interest. Similar concepts using dual-band $\lambda/4$ lines were reported in [49] with similar bandwidth and frequency ratio limitations. Another impedance transformer reported in [34] utilizes dual transmission line approach to achieve high values of transformation ratios. Ladder networks proposed in [36] also facilitate multi-band matching but at the cost of increased circuit bulkiness and design complexities. A coupled-line cascaded with planar transmission line architecture has been reported in [37]. The proposed design facilitates an impedance transformation ratio range from 0.1 till 10 at frequency ratios between 2 to 7. The circuit is limited by its non-simultaneous behavior in which improvement of one transformation ratio (frequency or impedance) degrades the other. Recently [110] reported a cross-coupled architecture for impedance transformers capable of handling extreme load values. The design claims an ultra-wide impedance transformation ratio of 0.1 till 40, but limited to single band operation only along with moderate design flexibility.

Examples of lumped-element based dual-band impedance matching network like that of [111] have also been reported in the literature. The major limitation with lumped elements is that they lose their ideal behavior at high frequencies due to package parasitics. Thus maintaining a constant value over a frequency range is impossible.

2.2.3 Tri-Band Impedance Transformers

A step up from the dual-band devices, researchers lately have started exploring the domain of tri-band RF circuits that operate concurrently on three desired frequencies of interest. Needless to explain their importance in the reduction of circuit redundancy, tri-band networks play an important role in reducing the circuit form factor, thus proving to be promising for high-end applications. Early reports of tri-band devices include

[66], which is specific to a Wilkinson Power Divider and uses curve fitting techniques. Lumped components were used in [112] to facilitate tri-band matching with limitations in high-frequency operations. Moreover the technique used brute force method and lacked closed-form design equations for sequential design. A tri-band impedance transformer using stubbed coupled-line was reported in [70]. The design scheme consists of two sets of coupled-lines one behaving as a stub and the other in all-pass configuration. The limitations include performance degradation in microstrip technology due to differential even-odd velocities and complicated layout process. A generalized, systematic design process for tri-band impedance matching networks was reported in [113] for the first time. The design strategy is mathematically sound and presents a comprehensive analysis on the tenets of tri frequency matching. However, the three bands of interests are not too widely spaced apart leading to limited second and third frequency ratios r_{21} and r_{31} respectively. Very recently, a tri-band impedance transforming power divider was reported in [73]. The design used the architecture presented in [113] as a component of its arms and claimed controllable power division ability and bandwidth. Though increment of frequency ratios has been claimed, it is observed that at elevated frequency ratios, the line impedances become practically unrealizable. The bandwidths at each band of interest also tend to reduce at the higher frequency end.

2.2.4 Wilkinson Power Dividers

Wilkinson Power Dividers (WPD) are an important component in almost all RF and Microwave circuits. As evident from the name, WPDs split power supplied at their input into two equal or unequal halves depending upon the configuration. In addition to that, WPDs are known for providing good isolation between the output ports such that there is no power leakage between them. Depending upon the ratio of powers at their output ports, they can be equal-split, dividing the input power equally between the two ports, or unequal-split, in which the input power is split in a fixed ratio as designed. There has been many reports of WPDs in literature, with the most common being the equal-split type. On this regard, it is important to note that the basic building block of a WPD is an impedance matching network. Most architectures proposed in literature make use of a systematically designed impedance matching network for designing WPDs.

Due to the overwhelming research in multi-band RF circuits, dual-band WPDs have

emerged over the last few years. Early reports of a dual-band WPD was made in [114], which utilized a dual-band $\lambda/4$ transformer to match the output and the input ports. Though compact in form factor, the design lacked explanation about the determination of the value of the isolation resistor and was limited in frequency ratio of operation. Several architectures were proposed by *Park et. al.*- T-section matching network based, port extension based [115], [116], coupled-line based [40] and some are unequal split [59]. All of these designs are supported by closed-form equations and a sequential design flow but fail to achieve high frequency ratio of operation. As discussed previously in the impedance transformer section, coupled-lines have been widely used as a part of multi-band circuits, a lot of their usage has also been reported in designing WPDs. A coupled-line based dual-band WPD was reported in [41] that employed two cascaded coupled-line sections and two-isolation resistors. The design scheme is mathematically intensive but limited to a maximum obtainable frequency ratio of 3. A generalized two-way two-section dual-band WPD was reported in [117]. The design strategy presented a detailed analysis and synthesis procedure but still, lacked in the extent of frequency ratio beyond 3. A three-section dual-band WPD was reported in [63] with ratio limitations and operation at harmonic frequencies. A performance enhanced equal-split port extended dual-band WPD was proposed in [50]. The design utilized port extension principle and demonstrated frequency ratio extension till 4. This was the first design approach that made the isolation resistor value independent of the frequency ratio of operation, and hence the extension of the same possible. The design provided closed-form equations for easy prototyping and was compact in size. A compact size design theory targeting arbitrary transmission line ratio was reported in [118]. The design approach was generic but used lumped inductors and resistors as a part of its isolation network, thus limiting its operation in higher frequencies.

Many solutions are based on the conventional transmission lines [39], composite right-left material [42], or are with embedded filtering function [119]. The coupled-line based dual-band designs are considered very exciting due to several advantages such as the inherent possibility of miniaturization, and due to the additional degree of freedom in terms of even- and odd-mode impedances. The isolation in such designs is limited due to the physical closeness of the output ports, but it is still possible to achieve $> 20dB$ isolation, which is usually adequate in most applications. Further-

more, the earlier reported designs have either limited frequency-ratio (f_2/f_1) or uses complex isolation to improve performance [43, 44]. A higher frequency-ratio is important while incorporating two widely separated frequency bands. In complex isolation architectures, often, the lumped elements are continuous function of frequency-ratio. However, isolation element independent of frequency-ratio is important as the non-standard value of isolation element are not available commercially and would require added optimization during the design phase. Furthermore, lesser number of lumped elements are preferred at higher frequencies [45] considering that more isolation elements would add more parasitic and would necessitate extensive optimization to achieve the target isolation level and port matching.

A majority of the WPD architectures present is literature lack high-frequency ratio operation, which is a very important aspect for the upcoming 5G circuits. Later in this thesis a coupled-line core dual-band WPD would be proposed that extends the frequency ratio till 7 with the isolation element independent of band ratio [64].

With the focus now shifting towards designing of tri-band WPDs [66–73], a lot of reports have come up in the last few years. A tri-band WPD was proposed for the first time utilizing a three-section transmission line transformer [66]. This architecture consists of cascaded transmission lines of different impedances and electrical lengths and uses analytical methods to numerically solve for the line parameters. No closed-form design equations were provided, and the design becomes complicated for widely spaced frequencies. Dual- and tri-band power divider architectures proposed in [67] utilizes composite left- and right-handed transmission lines. Analysis of the proposed design scheme is complicated in terms of mathematical implementation and the use of lumped components severely restricts its operation at higher frequencies, hence limiting the operating band ratio. A tri-band WPD design incorporating coupled lines was proposed in [68]. In this, the core of the WPD was replaced by a coupled line $\lambda/4$ transformer with cascaded transmission lines of different lengths and impedances at either side. This design achieves tri-band matching conditions at the ports and provides associated design equations. However, it is limited in operation at the third frequency, with the power division and isolation parameters deteriorating with increased frequency. An unequal split WPD was proposed in [69] by incorporating a circular coupling power divider and a triple-band resonator. The design ensures compactness and matching at three arbitrary

frequencies of interest. Another interesting tri-band WPD architecture was reported in [70]. It demonstrates the usefulness of coupled-line stubs and its importance in tri-band matching. The design was backed by closed-form equations with its limitations being mathematical complexity and fabrication constraint for certain values of design parameters. Quarter-wave open stub based slow wave structures and tri-band filters have been utilized in [71] to implement a tri-frequency WPD. The design methodology is mostly analytical with the replacement of conventional WPD structure with quarter-wave stubs operating at multiple frequencies. The limitations include excessive dependence on tuning rather than closed-form design equations.

2.2.5 Power Amplifiers: A Brief Survey

The domain of RF power amplifiers is massive with lot of different architectures serving different sets of applications. While the basic functionality of RF power amplifiers is to amplify the power at their input, the ways to characterize them lead to many topologies. Typically amplifiers are targeted to have high efficiency, high gain, and good linearity. Achieving all the three simultaneously, is rather impossible due to the contradicting requirements and practical effects like device parasitics at higher frequencies. Researchers over the world, therefore make a trade-off between these three figures of merits depending upon the target application. The chapter on power amplifier in this thesis focuses only on efficiency enhancement in switched-mode operation. The literature survey is thereby limited to switched-mode harmonic tuned amplifiers only. Other architectures and methodologies are beyond the scope of this dissertation.

The simplest form of power amplifiers, Class-A has a theoretically maximum efficiency of 50% with both sinusoidal voltage and current waveforms. To increase efficiency, the conduction angle was reduced, and all the harmonics were shorted, thereby reshaping the waveforms for minimum current-voltage overlap. Class-B, AB and C amplifiers were formulated in this consideration. Waveform engineering has been one of the important ways for efficiency enhancement where the drain current is shaped while maintaining a perfect sinusoidal drain voltage. An interesting solution for efficiency enhancement in PAs is by Harmonic Tuning [120–127], which incorporates waveform reshaping by terminating all the harmonic impedances into purely reactive loads. Although it is theoretically possible to attain 100% efficiency through this method, it is

only possible to control the first three harmonics in practice, thereby limiting the maximum achievable efficiency up to around 85%. Generally, harmonically tuned PAs consist of a family of PA operating modes targeted for a constant performance specification [128]. Best examples include Class-J amplifiers in which the drain waveform was reshaped to include the 2nd harmonic component without any sacrifice of efficiency and output power [129–132]. Class-B/J wideband PAs were also developed using mode transferring technique. They offer a promising performance over a wide range of frequencies. Similar harmonic tuning architectures were implemented with Class-F/F^{-1} PAs where the drain voltage/current waveforms were engineered to include more harmonic components. Design of broadband PAs using second harmonic manipulation was presented in [126]. The proposed design scheme considers Class-F^{-1} mode of operation and extends it to operate as a family of specifications that exhibit better performance than Class-B operating mode in terms of output power and drain efficiency. The advantage of the design is that it provides a broader design space for implementing broadband PAs. Another similar topology was reported in [123] that generalizes the Class-F operation theory to model their operation for above-pinch-off gate bias voltages. The conduction angle is swept from $180^\circ - 360^\circ$ and a new shifted design space for the fundamental and an expanded design space for the second harmonic. An important inference from this design scheme is that the required input power of the device is dependent upon its bias conditions. A comprehensive study about the effect of input and output harmonics on designing PAs was reported in [125]. Both the input and output harmonics have been taken into consideration concurrently. The intrinsic drain I-V waveforms are computed as a function of conduction angle, and the output performance parameters- power delivered and drain efficiency are calculated as a function of the input non-linearity and output loading conditions of the device. This scheme also investigates the design sensitivity of the device to input non-linearity and its resulting effect on the fundamental design space. An application of the theory in designing continuous Class-F^{-1} PAs was investigated in [133]. Possible ways to exploit the input non-linearity of devices to improve the performance in a broadband perspective has been explored. The proposed design theory also proposes a new second harmonic design space that reduces the complexity of input matching network design. Very recently, a comprehensive analytical study was reported in [134] that investigates the

effects of device's input non-linearity on performance and broadband operation of continuous mode Class-F amplifiers. Design equations were provided demonstrating that the fundamental load design space of continuous Class-F PAs need to be re-assessed in presence of second harmonic input non-linearity. A Doherty PA was also designed based on the findings to demonstrate broadband operation for a modulated signal input. Often, during second harmonic load-pull, it is observed that in a particular region of the Smith Chart, there is a significant performance degradation. Several reports are found in literature that present theories behind this efficiency degradation [125, 135–137]. This effectively narrows down the second harmonic design space by creating a significant challenge in the selection of second harmonic impedances. A proper explanation for this strange behavior was first reported and experimentally validated in [138]. The investigation also derived a closed-form design equation to determine the location of the efficiency null for any device and frequency of operation. The equation also provides an insight about the determination of the output capacitance of the device and the optimum impedance at the intrinsic plane. An extended version of this investigation was used to design a Class-F^{-1} PA without any prior knowledge of the parasitic elements [139]. Several architectures were also proposed to extend the design space of harmonic tuned PAs. Simultaneous tuning of the first three harmonic impedances in Class-F was reported in [140]. Resistive second harmonic tuning for bandwidth increment at the cost of output power was investigated in [141, 142]. In fact, numerical optimization techniques with arbitrary harmonic terminations were implemented in [143]. A multi-harmonic tuned PA was introduced in [144] with the limitation that only the amplitude of the fundamental and the harmonics are tunable while the phase is fixed. As reported in [128], the optimal fundamental load trajectory is dependent on the output current level and the harmonic load impedances for Class-X PAs. Unlike Class-F/F^{-1} PAs with fixed open/short harmonic loads, Class-X provides a larger degree of freedom in practical design as the designer can chose from a wide range of reactive harmonic loads pertaining to optimum performance.

From the literature survey on harmonic tuned PAs, it is clear that the design space of the second harmonic plays a crucial role in the performance of the amplifier. A proper second harmonic load boosts the efficiency to a great extent whereas certain second harmonic load values can drastically degrade the same. In light of this thesis, it is very

important to study the possibilities to control and tune the second harmonic impedance from a circuits perspective and is presented in the chapter on Power Amplifiers [145].

2.2.6 A Summary of the Review

It is indeed worth mentioning that the existing literature in the domain of multi-band passive networks as well as power amplifiers is vast and diverse. With a variety of design schemes targeting a broad range of applications, many existing limitations have been addressed over the years. However, after an intensive study of the literature, we have identified some shortcomings of the existing designs that need addressal in order to cope up with the fast pace of developing wireless standards. They are listed as follows.

1. Limitation in Frequency Ratio: A primary limitation of a majority of the proposed design schemes is their limited operating frequency ratio. This inadvertently hampers their ability to operate at distantly separated frequency bands. This is a potent problem especially with the deployment of the 5G standards where the usable bands might be wide apart across the frequency spectrum. The initial chapters of the thesis involve an in-depth analysis of coupled transmission lines in their all-pass configuration and their role in frequency ratio improvement. A robust mathematical model has been developed in this regard that provides a deeper insight into the network behavior, the ratio bounds and the design parameter values.

2. Limitation in Impedance Transformation Ratio: Another important aspect missing in the existing literature is the ability of the multi-band networks to operate at a fairly high impedance gradient. In other words, the ratio to the load impedance to the source impedance is quite limited, which often reduces the utility of the design at high impedance applications. One of the important contributions of this thesis is the improvement in impedance transformation ratios of dual-band networks. In fact, we have obtained simultaneous flexibility in frequency ratio as well as impedance transformation ratio at both their higher and lower ends.

3. Lack of a Simple Tri-Band Transformation Technique: While dual-band networks have widely been researched upon, the development of tri-band networks has not yet reached its full potential. The existing design strategies are either mathematically intensive or depend heavily upon optimization algorithms, which often lead to false positives. This makes the design unduly complicated. This thesis contributes towards the development of a design technique for tri-band impedance transformation using a combination of mathematical and optimization methods. The proposed method has a simple design flow and ensures fast prototyping.

4. Harmonic Control Network in Power Amplifiers: After an intensive survey of the RF Power Amplifier literature, it is worth mentioning that a critical step towards efficiency improvement lies in output wave-shaping, which directly depends upon the control of the harmonic impedances at the output drain of the transistor. This has led to a broad variety of amplifier operating classes. In this thesis, we have designed an output network that facilitates independence between the fundamental and harmonic impedances. This ensures proper harmonic tuning without disturbing the fundamental match- a necessary condition to maintain high efficiency.

CHAPTER 3

Transformation Ratio Flexibility and Bandwidth Enhancement of Dual-Band Impedance Transformers

This chapter is based on the following research papers-

- **D. Banerjee**, A. Saxena, M.S. Hashmi and F.M. Ghannouchi, "A Compact Dual-Band Impedance Matching Network Based on All-Pass Coupled Lines", *Proc. on IEEE 61st Intt. Midwest Symp. on Circuits and Systems (MWSCAS)*, p.p. 937 - 939, Aug. 5 - 8, 2018, Windsor, Canada

- **D. Banerjee**, A. Saxena and M.S. Hashmi, "A Novel Design of a Bandwidth Enhanced Dual-Band Impedance Matching Network With Coupled Line Wave Slowing", *Proc. on IEEE 69th Electronic Components and Technology Conference (ECTC)*, p.p. 1770 - 1773, May 28 - 31, 2019, Las Vegas, USA *(Best Paper Award)*

- **D. Banerjee**, M.S. Hashmi and F.M. Ghannouchi, "A Flexible Ultra-High Transformation Ratio Based Dual-Band Impedance Transformer and its Applications in a T-Junction Power Divider", *IET Microwaves, Antennas and Propagation (Accepted: May 2021)*

Outline

This chapter introduces the concept of an All-Pass Coupled-Line (APCL) for dual-band transformers. The proposed theory highlights the use of APCLs in dual-band impedance transformers for both simple as well as Frequency Dependent Complex Loads (FDCL). It also addresses the lower bandwidth problem for each operating bands in a dual-band network. Three different architectures have been proposed that addresses the problem of frequency ratio extension for FDCLs, use of APCL-based Slow Wave Structures (SWS) for bandwidth enhancement and flexibly extending the frequency ratio as well as impedance transformation ratio simultaneously. Prototypes have been fabricated for each case and measurement results have been provided.

IMPEDANCE TRANSFORMERS are ubiquitous in all RF front ends and play an important role in lossless power transmission from one operating circuit stage to the other. Depending on situations an impedance transformer can be used for inter-stage matching between two RF modules or as a standalone component that matches two unequal source and load impedances. Over the past few years, a lot of research has been done on dual-band impedance transformers and the literature is replete with dual-band matching architectures serving various purposes. Two most common limitations of these architectures are non-flexible frequency ratios and narrow bandwidth, for FDCLs. This simply means that the dual-band networks are strict in the two frequencies of operation and the bandwidth obtained at the two desired frequencies is small. This chapter introduces an analytical approach to demonstrate the possibility of making the frequency ratio flexible and increasing the "per-band bandwidth" of the dual-band network under consideration.

3.1 Behavior of All-Pass Coupled Lines (APCL)

Before investigating the frequency flexibility operations, it is important to understand the behavior of coupled lines. Fig. 3.1 illustrates a microstrip coupled line structure fabricated on a PCB laminate.

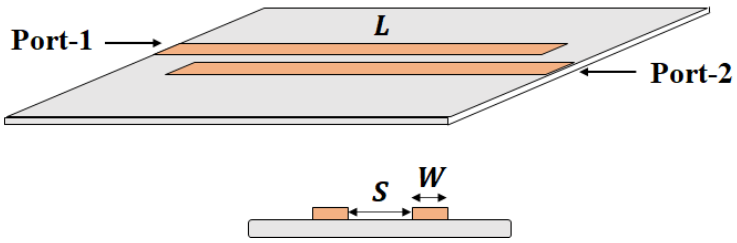

Figure 3.1: General Structure of Microstrip Coupled Lines with Design Parameters

Coupled lines can be a very good candidate for a matching network, depending on the applications to be served. As an example for the case of DC isolation, the all-pass coupled line cannot be used as there is no DC discontinuity between the input and output ports. On the other hand, designing ordinary impedance transformers with band-pass coupled lines can be challenging as not all the design parameters are fabricable. Practically there are three design parameters for a coupled line, as illustrated in Fig. 3.1, namely the length of the coupled line L, the width W and the distance separating the two coupled lines S. Especially the separation parameter S determines the amount of coupling and thereby, the overall behavior of the coupled line section. For a very small value of S, we can say that the lines are "tightly" coupled and if the value of S is considerably large, it can be said that there is "loose coupling" between the two lines.

To develop a mathematical model for the all pass coupled line, it is primarily essential to derive the open-circuit impedance matrix of the coupled line 4-port network. A simplistic schematic representation with even and odd-mode excitations are depicted in Fig. 3.2. The final impedance matrix is obtained by superposing the even and odd mode excitations [96]. The currents i_1 and i_3 drive the coupled line in even mode while the currents i_2 and i_4 drive it in odd mode. By superposition theorem, the total port currents at the 4 ports can be expressed in (3.1) as:

$$I_1 = i_1 + i_2 \tag{3.1a}$$

$$I_2 = i_1 - i_2 \tag{3.1b}$$

$$I_3 = i_3 - i_4 \tag{3.1c}$$

$$I_4 = i_3 + i_4 \tag{3.1d}$$

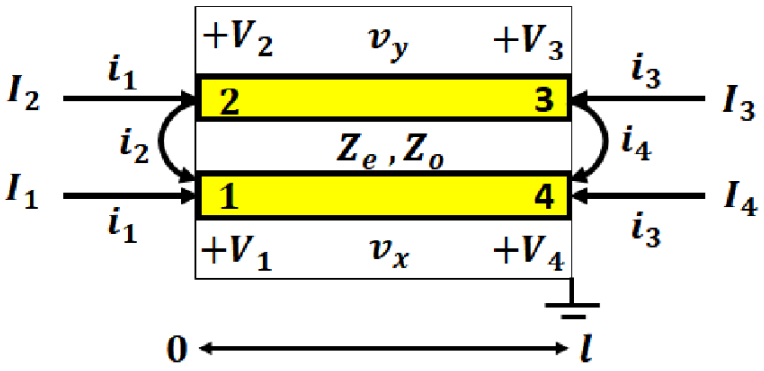

Figure 3.2: Coupled Line Structure with Superposed Even and Odd-Mode Currents

Firstly, considering the line driven by the i_1 current sources, if all other ports are open-circuited, the impedance seen at port 1 or 2 is given in (3.2).

$$Z_{in}^{e} = -jZ_e \cot \beta l \tag{3.2}$$

Here the length of the coupled lines l is considered to be along the $+z$ axis. The voltage on either of the conductors can be expressed in (3.3) as:

$$\begin{aligned} v_x^1(z) = v_y^1(z) &= V_e^+[e^{-j\beta(z-l)} + e^{j\beta(z-l)}] \\ &= 2V_e^+ \cos \beta(l-z) \end{aligned} \tag{3.3}$$

Therefore, the voltage at port 1 or 2 is given in (3.4) as:

$$v_x^1(0) = v_y^1(0) = 2V_e^+ \cos \beta l = i_1 Z_{in}^e \tag{3.4}$$

(3.3) can be rewritten in terms of i_1 using (3.4) and (3.2) as expressed in (3.5).

$$v_x^1(z) = v_y^1(z) = -jZ_e \frac{\cos \beta(l-z)}{\sin \beta l} i_1 \tag{3.5}$$

Similarly, the voltages due to current sources i_3, driving the coupled line in even mode can be obtained in (3.6) as:

$$v_x^3(z) = v_y^3(z) = -jZ_e \frac{\cos \beta z}{\sin \beta l} i_3 \tag{3.6}$$

Now considering the coupled line being driven in odd mode by current i_2 and all other

ports are open-circuited. The impedance seen at port 1 or 2 is given in (3.7).

$$Z_{in}^{o} = -jZ_o \cot \beta l \tag{3.7}$$

and the voltage on either of the conductors can be expressed in (3.8) as:

$$\begin{aligned} v_x^2(z) = -v_y^2(z) &= V_o^+[e^{-j\beta(z-l)} + e^{j\beta(z-l)}] \\ &= 2V_0^+ \cos\beta(l-z) \end{aligned} \tag{3.8}$$

Thus, the voltage at port 1 or 2 is given in (3.9):

$$v_x^2(0) = -v_y^2(0) = 2V_0^+ \cos\beta l = i_2 Z_{in}^0 \tag{3.9}$$

Rewriting (3.8) in terms of i_2 by using (3.7) and (3.9), we obtain (3.10).

$$v_x^2(z) = -v_y^2(z) = -jZ_o \frac{\cos\beta(l-z)}{\sin\beta l} i_2 \tag{3.10}$$

Similarly the voltages due to current i_4 driving the coupled line in odd mode are given in (3.11).

$$v_x^4(z) = -v_y^2(z) = -jZ_o \frac{\cos\beta z}{\sin\beta l} i_4 \tag{3.11}$$

From (3.5), (3.6), (3.10) and (3.11), the total voltage at port 1 is written in (3.12) as:

$$\begin{aligned} V_1 &= v_x^1(0) + v_x^2(0) + v_x^3(0) + v_x^4(0) \\ &= -j(Z_e i_1 + Z_o i_2)\cot\theta - j(Z_e i_3 + Z_o i_4)\csc\theta \end{aligned} \tag{3.12}$$

where $\theta = \beta l$ is the electrical length of the coupled line section. Solving (3.1) for i_j in terms of I_T, we obtain (3.13).

$$i_1 = \frac{1}{2}(I_1 + I_2) \tag{3.13a}$$

$$i_2 = \frac{1}{2}(I_1 - I_2) \tag{3.13b}$$

$$i_3 = \frac{1}{2}(I_3 + I_4) \tag{3.13c}$$

$$i_4 = \frac{1}{2}(I_4 - I_3) \tag{3.13d}$$

Substituting (3.13) in (3.12), we obtain (3.14).

$$\begin{aligned} V_1 = &\frac{-j}{2}(Z_e I_1 + Z_e I_2 + Z_o I_1 - Z_o I_2)\cot\theta \\ &+ \frac{-j}{2}(Z_e I_3 + Z_e I_4 + Z_o I_4 - Z_o I_3)\csc\theta \end{aligned} \tag{3.14}$$

(3.14) determines the top row of the open-circuit impedance matrix of the coupled lines. All the other elements of the matrix can be determined from (3.14) through symmetry. They are summarized in (3.15).

$$Z_{11} = Z_{22} = Z_{33} = Z_{44} = \frac{-j}{2}(Z_e + Z_o)\cot\theta \tag{3.15a}$$

$$Z_{12} = Z_{21} = Z_{34} = Z_{43} = \frac{-j}{2}(Z_e - Z_o)\cot\theta \tag{3.15b}$$

$$Z_{13} = Z_{31} = Z_{24} = Z_{42} = \frac{-j}{2}(Z_e - Z_o)\csc\theta \tag{3.15c}$$

$$Z_{14} = Z_{41} = Z_{23} = Z_{32} = \frac{-j}{2}(Z_e + Z_o)\csc\theta \tag{3.15d}$$

Now, for the case of the floating-arm all-pass coupled line configuration as shown in Fig. 3.3, ports 2 and 3 are open-circuited. This simplifies obtaining the impedance matrix of this structure as the parameters for port 2 and 3 are all zero.

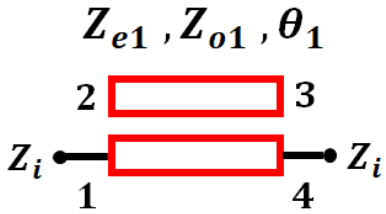

Figure 3.3: Floating-Arm All-Pass Coupled-Line Configuration

The impedance parameters for this structure are reiterated in (3.16).

$$Z_{11} = Z_{44} = \frac{-j}{2}(Z_{e1} + Z_{o1})\cot\theta \tag{3.16a}$$

$$Z_{14} = Z_{41} = \frac{-j}{2}(Z_{e1} + Z_{o1})\csc\theta \tag{3.16b}$$

In Fig. 3.3, Z_i is the image impedance of the coupled line section and is obtained from the impedance matrix from (3.17).

$$Z_i = \sqrt{Z_{11}^2 - \frac{Z_{11}Z_{14}^2}{Z_{44}}} \tag{3.17}$$

Substituting the values of (3.16) in (3.17), Z_i is obtained in (3.18).

$$Z_i = \frac{Z_{e1} + Z_{o1}}{2} \tag{3.18}$$

The floating-arm coupled line section can be utilized in a variety of applications such as FDCL to real transformer and frequency ratio extender, each of which are demonstrated in detailed in the upcoming sections.

3.2 Floating-Arm APCLs as Dual-Band FDCL to Complex Conjugate Converter

In this section we will be investigating about the ability of the floating-arm APCL to transform FDCLs into real loads at two frequencies. From [46] we can infer that a $\lambda/4$ transmission line operating at two frequencies can convert an FDCL into a set of complex conjugate impedances. At this point it must be noted that an APCL can be enforced to behave like a dual-band conjugate generator like a simple transmission line. The advantage lies in that fact that it makes high impedance lines physically implementable. Fig. 3.4 illustrates the equivalence between the APCL and a quarter-wave transmission line.

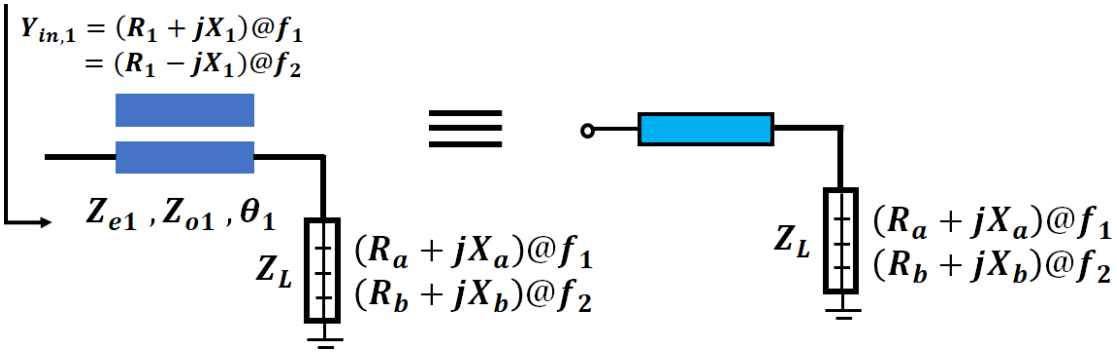

Figure 3.4: Floating-Arm APCL Configuration for Dual-Band FDCL to Complex Conjugate Generation

For a single line FDCL to real transformer, $[Z_1, \theta_q]$ are given in (3.19) [46]:

$$Z_1 = \sqrt{R_a R_b + X_a X_b + \frac{X_a + X_b}{R_b - R_a}(R_a X_b - R_b X_a)} \tag{3.19a}$$

$$\theta_q = \frac{n\pi + \arctan \frac{Z_1(R_a - R_b)}{R_a X_b - R_b X_a}}{(m+1)} \tag{3.19b}$$

where *m* is the frequency ratio $m = f_2/f_1$.

Now, the equivalence of the APCL with that of the dual-band $\lambda/4$ transformer is expressed in (3.20).

$$Z_1 = Z_i = \frac{Z_{e1} + Z_{o1}}{2} \tag{3.20}$$

Thus, the design parameters of an APCL behaving like a dual-band $\lambda/4$ transformer are obtained in (3.21).

$$Z_{e1} = \frac{2\sqrt{R_a R_b + X_a X_b + \frac{X_a + X_b}{R_b - R_a}(R_a X_b - R_b X_a)}}{1 + M} \tag{3.21a}$$

$$\theta_q = \frac{n\pi + \arctan \frac{Z_{e1}(1+M)(R_a - R_b)}{2(R_a X_b - R_b X_a)}}{(1+m)} \tag{3.21b}$$

here, $M = Z_{o1}/Z_{e1}$

The minimum transmission line thickness (and arm separation in case of coupled lines) in microstrip technology that can be fabricated in general commercial facilities do not go below 8.0mils or 0.2mm. This also takes into consideration the dielectric constant and the substrate thickness of the laminate selected for prototyping. However, the typical least count is 8.0mils. The main advantage of using a floating-arm APCL as a dual-band conjugate generator is the possibility of frequency ratio extension. In the case of a simple transmission line, the maximum achievable ratio is quite limited because of the fabrication limitations. However, this constraint can be relaxed by using APCLs as the impedance is equally distributed between the even-half and the odd-half arms. On this regard, it must be noted that a very crucial design parameter for APCLs is M, or, the ratio between the even and odd-arm impedances. This determines the distance of separation between the two arms, and hence, the amount of coupling between them. To ensure this, the value of *M* should always be chosen within the range $M \in [0.6 - 0.8]$. This keeps the values of Z_{e1} and Z_{o1} close to each other with the condition $Z_{o1} < Z_{e1}$

being unconditionally satisfied, making the APCL section fabricable. In some cases it can be seen that the spacing between the arms of the APCL are quite high. In-fact, if the spacing is greater than five times the substrate thickness [146] the coupling can be considered loose. Beyond the limits of loose coupling, the APCL can be considered to behave like a simple transmission line without any change in behavior.

3.3 $\lambda/4$ Meandered Line APCL Configuration

Another important configuration of using a coupled-line section in all-pass configuration is a meandered line. As the name suggests, a meandered line is a transmission line that has been bent so closely that the bends give rise to mutual-coupling. The amount of coupling is determined by the separation of the bent arm. Fig. 3.5 illustrates a meandered line APCL unit cell.

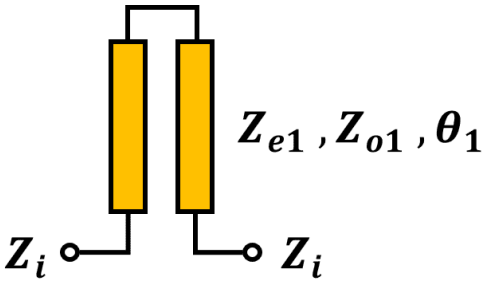

Figure 3.5: A Meandered Line APCL Unit Cell

From the equations (3.15), it can be obtained that the image impedance Z_i of the meandered line APCL configuration is (3.22).

$$Z_i = \sqrt{Z_e Z_o} \tag{3.22}$$

For a $\lambda/4$ meandered line to behave as a real-to-real transformer, the characteristic impedance of the same should be equated with that of the latter.

From Fig. 3.6, the equivalence can be expressed in (3.23).

$$Z_1 = Z_i = \sqrt{R_L R_S} \tag{3.23}$$

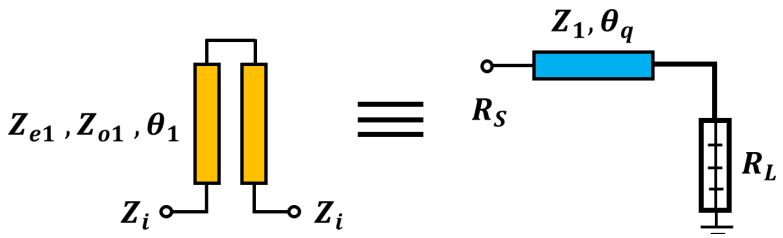

Figure 3.6: A Meandered Line APCL Unit Cell

Therefore, the design parameters for the meandered line are calculated in (3.24) as:

$$Z_{e1} = Z_i \tan\theta_q \tag{3.24a}$$

$$Z_{o1} = Z_i / \tan\theta_q \tag{3.24b}$$

and $\theta_1 = \theta_q = 90^\circ$ for a quarter-wave transformer.

Applications of the APCL in both the floating-arm and meandered line configurations are discussed in the next sections.

3.4 APCL-Based Dual-Band Impedance Transformer for Enhanced Frequency Ratio in FDCL Systems

Now that we know that an APCL can behave as a complex-conjugate generator at two desired frequencies of interest and a meandered line can behave as a real-to-real impedance transformer, we can use both of these properties to design a dual-band impedance matching network and study the extent to which the frequency ratio can be extended. Fig. 3.7 illustrates the proposed dual-band matching network architecture.

Section-A and C comprises of coupled-lines in their all-pass configuration and Section-B is a susceptance cancellation dual-band stub. The impedances and electrical lengths of all the transmission line sections are as depicted in Fig. 3.7. The load is an FDCL defined as $Z_L = (R_a + jX_a)@f_1$ and $(R_b + jX_b)@f_2$. Section-A converts the complex load Z_L into a real value with two conjugate susceptances at f_1 and f_2, right of node-*n*. This conjugate susceptance is cancelled by the dual-band stub (Section-B), to leave a real impedance value. A $\lambda/4$ meandered coupled-line (Section-C) matches the real value with the source Z_S.

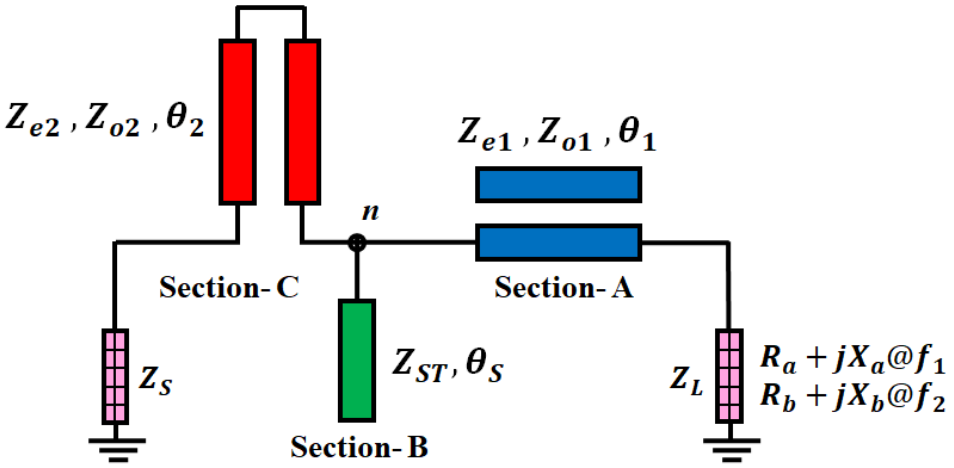

Figure 3.7: Proposed Dual-Band Matching Network

3.4.1 Mathematical Formulation

Section-A consists of a coupled-line in its all-pass configuration, as depicted in Fig. 3.8.

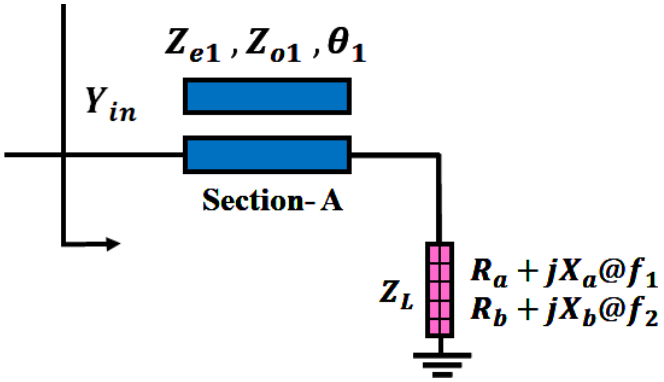

Figure 3.8: Section-A: Coupled-Line in All-Pass Configuration

Considering $M = Z_{o1}/Z_{e1}$, the design parameter, $[Z_{e1}, \theta_1]$ are defined in (3.21a) and (3.21b) and are reiterated here in (3.25).

$$Z_{e1} = \frac{2\sqrt{R_aR_b + X_aX_b + \frac{X_a+X_b}{R_b-R_a}(R_aX_b - R_bX_a)}}{1+M} \tag{3.25a}$$

$$\theta_1 = \frac{n\pi + \tan^{-1}[\frac{Z_{e1}(1+M)(R_a-R_b)}{2(R_aX_b-R_bX_a)}]}{1+r} \tag{3.25b}$$

where, $r = f_2/f_1$ is the frequency ratio. The input admittance, Y_{in} can be represented as $Y_{in} = G_{in} + jB_{in}@f_1$ and $G_{in} - jB_{in}@f_2$, where,

$$G_{in} = \frac{R_1}{R_1^2 + X_1^2} \tag{3.26a}$$

$$B_{in} = \frac{X_1}{R_1^2 + X_1^2} \tag{3.26b}$$

and, R_1 and X_1 are expressed in (3.27) and (3.28) respectively.

$$R_1 = \frac{R_a Z_{e1}^2 (1+M)^2 \sec^2\theta_1}{Z_{e1}^2(1+M)^2 - 8(1+M)Z_{e1}X_a \tan\theta_1 + 4(R_a^2 + X_a^2)\tan^2\theta_1} \tag{3.27}$$

$$X_1 = \frac{[Z_{e1}^2(1+M)^2 - 4R_a^2 - 4X_a^2]Z_{e1}(1+M)\tan\theta_1 + 2Z_{e1}^2(1+M)^2(1-\tan^2\theta_1)}{2[Z_{e1}^2(1+M)^2 - 8(1+M)Z_{e1}X_a\tan\theta_1 + 4(R_a^2+X_a^2)\tan^2\theta_1]} \tag{3.28}$$

Section-B consists of a dual-band susceptance cancellation stub, as depicted in Fig. 3.9.

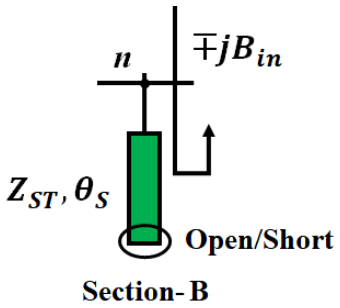

Figure 3.9: Section-B: Susceptance Cancellation Dual-Band Stub

The dual-band stub offers admittance equal to $-jB_{in}@f_1$ and $+jB_{in}@f_2$, thereby, cancelling the conjugate susceptance, generated post Section-A. The impedances of the stubs are given in (3.29).

$$Z_{ST|short} = \cot\theta_S / B_{in} \tag{3.29a}$$

$$Z_{ST|open} = -\tan\theta_S / B_{in} \tag{3.29b}$$

for short and open circuit stub respectively. The type of stub depends upon the sign of the susceptance generated. Electrical length θ_S is expressed in (3.30) as:

$$\theta_S = \frac{n\pi}{1+r} \tag{3.30}$$

where, $n \in [1, 2, 3...]$.

Post susceptance cancellation, the node-*n* is left with only a real impedance value ($= 1/G_{in}$), that needs to be matched to Z_S at two frequencies f_1 and f_2.

Section-C, illustrated in Fig. 3.10, consists of a $\lambda/4$ meandered coupled-line section that matches the real value $R_{in} = 1/G_{in}$ with the source Z_S at f_1 and f_2.

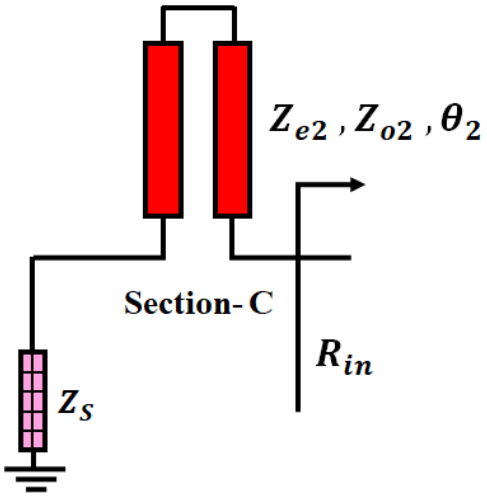

Figure 3.10: Section-C: $\lambda/4$ Meandered Coupled-Line

The design parameters for the meandered line in Fig. 3.10 are obtained in (3.24) and are iterated here in (3.31) for convenience.

$$Z_{e1} = \sqrt{R_{in} Z_S} \tan\theta_2 \tag{3.31a}$$

$$Z_{o1} = \sqrt{R_{in} Z_S} / \tan\theta_2 \tag{3.31b}$$

where, $\theta_2 = \theta_S$ and is expressed in (3.30).

3.4.2 Simulation Examples and Measured Results

A few examples have been considered in Table-3.1, verifying the proposed theory. The design parameters for Table-3.1 are listed in Table-3.2 along with the simulation results in Fig. 3.11. It is observed from Table-3.1 that although the design parameters for the APCL theoretically match the FDCLs at the two desired frequencies but may not always be within the physically realizable limits. For example, the lower limit to the obtainable frequency ratio is 1.2, below which the mathematical model fails to generate practical design parameter values for the transmission lines. As previously discussed, the factor

that determines physical realizability is *M*, or the even-odd ratio. It is advised that for an APCL to be fabricable, the value of *M* should be within 0.6 to 0.8, i.e. $M \in [0.6, 0.8]$.

Table 3.1: Case Studies For Different Loads and Frequencies

	f_1(GHz)	f_2(GHz)	$Z_{L\|f_1}$	$Z_{L\|f_2}$
Case-I	2.4	3.5	104.56+j19.81	110.46+j30.3
Case-II	2.4	4.0	19.83-j4.89	24.41+j62.51
Case-III	2.4	5.0	20.18+j5.28	19.77-j1.31

Table 3.2: Design Parameters for Table-3.1

	Section-A	**Section-B**	**Section-C**
Case-I	$Z_{e1} = 190.78\Omega$ $Z_{o1} = 95.39\Omega$ $\theta_1 = 56.65^\circ$	$Z_{ST} = 106.87\Omega$ $\theta_S = 366.1^\circ$ (open)	$Z_{e2} = 331.63\Omega$ $Z_{o2} = 30.15\Omega$ $\theta_2 = 73.22^\circ$
Case-II	$Z_{e1} = 175.07\Omega$ $Z_{o1} = 87.53\Omega$ $\theta_1 = 58.53^\circ$	$Z_{ST} = 82.84\Omega$ $\theta_S = 202.5^\circ$ (open)	$Z_{e2} = 381.72\Omega$ $Z_{o2} = 65.49\Omega$ $\theta_2 = 67.5^\circ$
Case-III	$Z_{e1} = 54.54\Omega$ $Z_{o1} = 27.27\Omega$ $\theta_1 = 56.04^\circ$	$Z_{ST} = 203.02\Omega$ $\theta_S = 58.38^\circ$ (open)	$Z_{e2} = 97.06\Omega$ $Z_{o2} = 36.79\Omega$ $\theta_2 = 58.38^\circ$

As a design example, a prototype has been fabricated in RO5880 substrate ($\epsilon_r = 2.2$, 1oz copper) and measured. The load is an FDCL defined as $Z_L = (91.06 - j31.81)@2.4GHz$ and $(106.61 - j6.66)@5.8GHz$. The fabricated prototype along with the measured results are illustrated in Figs. 3.12, 3.13 and Table-3.3 respectively. Table-3.4 compares the proposed design with a few other recent works.

Table 3.3: Simulation & Measured Results

Parameters	**Simulation Results**		**Measured Results**	
Frequency (GHz)	2.4	5.8	2.39	5.81
S_{11} (dB)	-46.79	-46.98	-34.72	-30.96

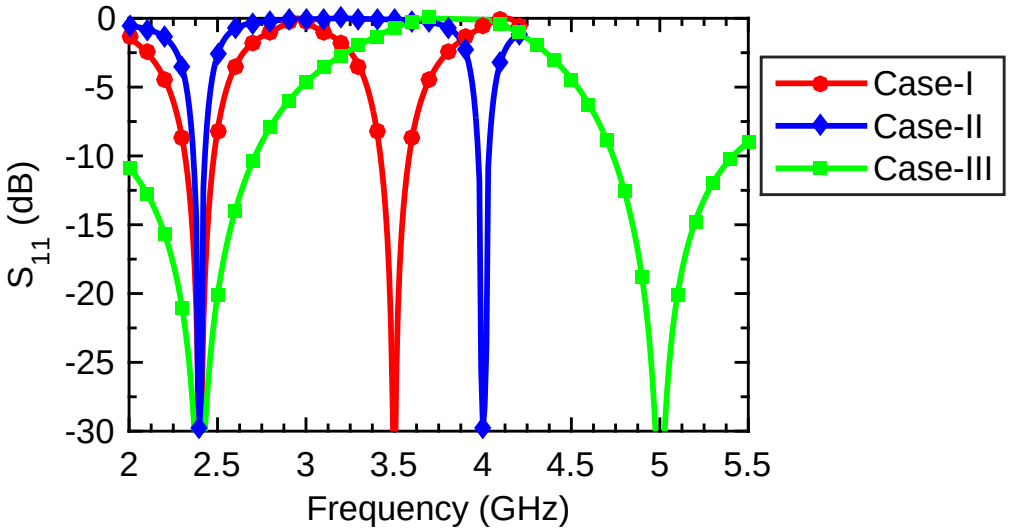

Figure 3.11: Simulation Results of The Case Studies in Table-3.1

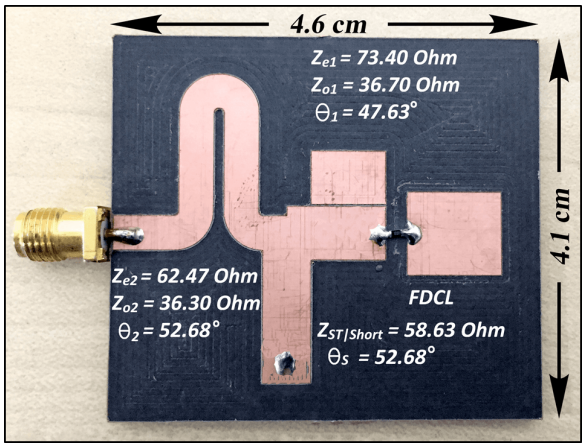

Figure 3.12: The Fabricated Prototype

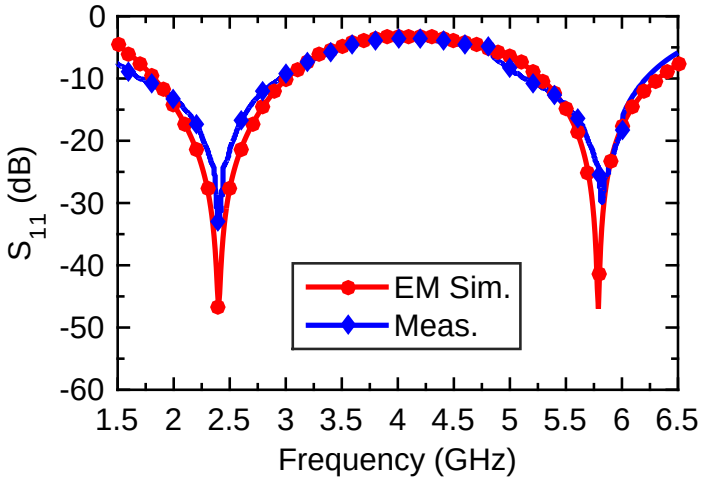

Figure 3.13: EM-Simulation and Measured Results

Table 3.4: Comparison With the State-of-The-Art

Ref., Year	Venue	Method used	Design Procedure	Load type	Frequency Ratio
[30], (2015)	MWCL	Pi-model	tedious	Complex	1.5
[25], (2011)	IET-EL	T-model	simple	FDCL	Tested till 2.0
[46], (2009)	MWCL	Three-Section TL	tedious	FDCL	2.42
This work	———	**All-Pass Coupled-Lines**	**simple**	**FDCL**	2.42

3.5 Bandwidth Enhancement of Dual-Band Transformers by APCL-based Wave Slowing Method

It is often observed that the architectures available in literature operating particularly at lower frequencies (GSM and WiFi as example), have limited bandwidth for the operating band, which indeed limits the effective data rate over the channel. With increasing demands for high data rates and for low-latency applications like satellite communication and wireless non-ad-hoc medical surgeries, this is a significant limitation. The desire is always for high bandwidth such that sophisticated data multiplexing schemes can be incorporated to effectively enhance the system efficiency. As for the best of the authors' knowledge, the existing architectures have not addressed this issue. We have utilized meandered APCLs for the first time to develop a dual-band impedance matching network that provides a substantial "per-band" bandwidth increment over the GSM and WiFi bands. The network, being generalized, applies for both real as well as FDCL and the same has been verified with fabricated prototypes (tested with real load).

3.5.1 The Proposed Transformer and Mathematical Deductions

The schematic representation of the proposed dual-band impedance matching network is depicted in Fig. 3.14.

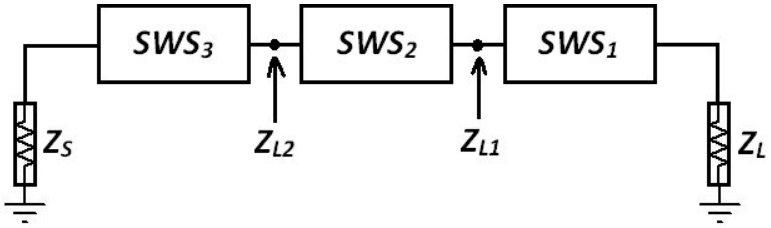

Figure 3.14: Block Diagram of the Proposed Impedance Transformer

The load Z_L can be of real or FDCL type and is matched to the conventional 50Ω

real source Z_S using three Slow Wave Structures (SWS_n). Z_{L1} and Z_{L2} are two intermediate impedance values. The matching is obtained in a step-wise fashion using symmetrical $\lambda/4$ meanders. Firstly Z_L is matched to Z_{L1} using SWS_1, followed by Z_{L1} with $_{L2}$ using SWS_2, and finally, Z_{L2} with the source Z_S using SWS_3. This essentially slows down the group velocity of the travelling wave in the bands of interest, thereby enhancing the bandwidth. For implementing the SWS, we have used APCLs, considering the electrical length relationship for dual-band matching, their additional advantage being compact size.

The design is based on recursive blocks of wave slowing structures- in this case quarter-wave meandered lines. The circuit representation of the network is presented in Fig. 3.15. Sections- A, B and C are the SWSs, implemented using $\lambda/4$ meandered lines with even/odd impedance values and electrical lengths as depicted in Fig. 3.15.

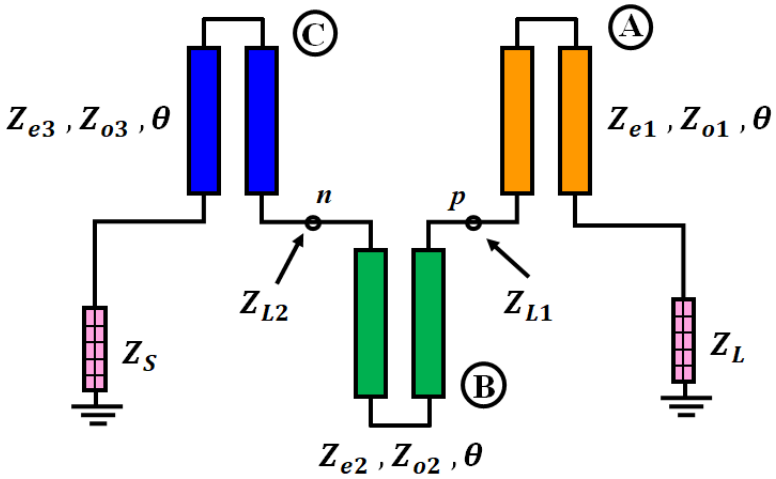

Figure 3.15: Circuit Representation of the Proposed Design

The design is based on correct determination of the values of Z_{L1} and Z_{L2} to facilitate the step-matching criteria. The choice can be made such that the impedances lie equidistant to one another linearly, as provided in (3.32).

$$Z_{L1} = Z_L - \frac{Z_L - Z_S}{3} \tag{3.32a}$$

$$Z_{L2} = Z_S + \frac{Z_L - Z_S}{3} \tag{3.32b}$$

This essentially means that the impedance difference $(Z_L - Z_{L1})$ is equal to the impedance difference $(Z_{L1} - Z_{L2})$, which indeed equals the impedance difference $(Z_{L2} - Z_S)$. Fol-

lowing that, the determination of the meandered line parameter values is quite straightforward and are provided in (3.33) [96].

$$Z_{e1} = \sqrt{Z_L.Z_{L1}}\tan\theta \tag{3.33a}$$

$$Z_{o1} = \frac{\sqrt{Z_L.Z_{L1}}}{\tan\theta} \tag{3.33b}$$

where θ is given in (3.34) as:

$$\theta = \frac{m\pi}{1+r} \tag{3.34}$$

and *r* is the frequency ratio, denoted by $r = f_2/f_1$ and *m* $\in [1, 2, 3, ...]$.

The design of sections- B and C are similar as the SWSs are symmetric. Thus, the design parameters Z_{e2}, Z_{o2}, Z_{e3}, and Z_{o3} can be determined as given in (3.35)-(3.36).

$$Z_{e2} = \sqrt{Z_{L1}.Z_{L2}}\tan\theta \tag{3.35a}$$

$$Z_{o2} = \frac{\sqrt{Z_{L1}.Z_{L2}}}{\tan\theta} \tag{3.35b}$$

and

$$Z_{e3} = \sqrt{Z_{L2}.Z_S}\tan\theta \tag{3.36a}$$

$$Z_{o3} = \frac{\sqrt{Z_{L2}.Z_S}}{\tan\theta} \tag{3.36b}$$

The proposed scheme is applicable for frequency dependent complex loads as well. The only addition to the existing architecture would be a complex to real impedance transformation network at two frequencies [53]. The same can be a pi-, L- or T- network and are available quite easily in literature. The conversion network would be placed between the load and Section-A (from Fig. 3.15), and would transform the complex load impedance $Z_{complex}$ into real load Z_L. While choosing the complex to real impedance transformer it is recommended to select a network that offers high bandwidth. As this would be the first stage in the matching network, a slight bandwidth crunch at this stage

would decrease the overall bandwidth of the network. The rest circuit operation would follow as discussed. The design flow for the theory is illustrated in Fig. 3.16.

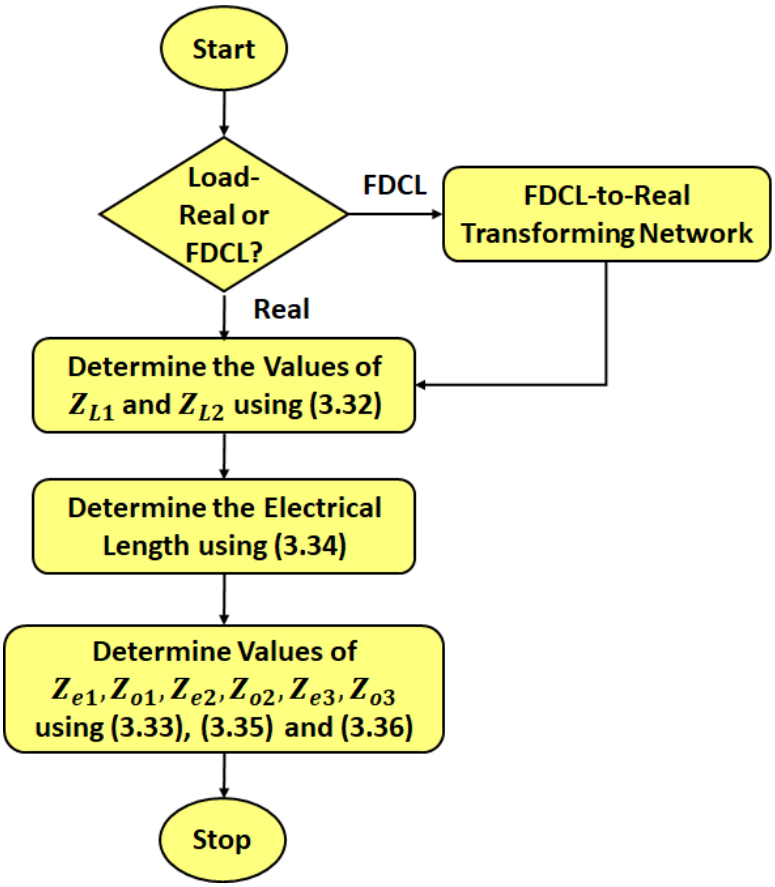

Figure 3.16: Design Flow of the Proposed Matching Network

3.5.2 Simulation and Design Example

Based on the theory, CAD simulations have been performed and listed in Table-3.5.

Table 3.5: Case Studies For Different Real Loads at Different Frequencies

	f_1 **(GHz)**	f_2 **(GHz)**	Z_L
Case-I	0.9	1.8	200
Case-II	0.9	2.4	100
Case-III	0.9	3.5	80

Three cases have been considered for three different real loads at three different sets of frequencies. The design parameters are listed in Table-3.6 and the corresponding simulation results are provided in Fig. 3.17. Fractional Bandwidth is defined as the bandwidth achieved at a particular band of interest, i.e. $(\Delta f / f_{desired}) X 100\%$. Table-3.7 illustrates the same for all the cases considered here. It is evident that as the band

separation ($\Delta f = f_2 - f_1$) increases, the fractional bandwidth increases, which is obvious. The interesting point to note is that even when the bands are closely spaced (as in Case-I), the fractional bandwidth is still above 30%, considering a -15dB reference level. In general, bandwidth calculation uses a -10dB reference level but we have chosen -15dB as a reference intentionally in order to record the worst case scenario.

Table 3.6: Design Parameters for Table-3.5

	Section-A	**Section-B**	**Section-C**
Case-I	Z_{e1} = 300	Z_{e2} = 212.13	Z_{e3} = 122.47
	Z_{o1} = 100	Z_{o2} = 70.71	Z_{o3} = 40.82
	$\theta = 60°$	$\theta = 60°$	$\theta = 60°$
Case-II	Z_{e1} = 96.55	Z_{e2} = 74.78	Z_{e3} = 63.21
	Z_{o1} = 72.49	Z_{o2} = 56.16	Z_{o3} = 47.46
	$\theta = 49.09°$	$\theta = 49.09°$	$\theta = 49.09°$
Case-III	Z_{e1} = 56.02	Z_{e2} = 48.52	Z_{e3} = 41.00
	Z_{o1} = 99.96	Z_{o2} = 86.57	Z_{o3} = 73.16
	$\theta = 36.82°$	$\theta = 36.82°$	$\theta = 36.82°$

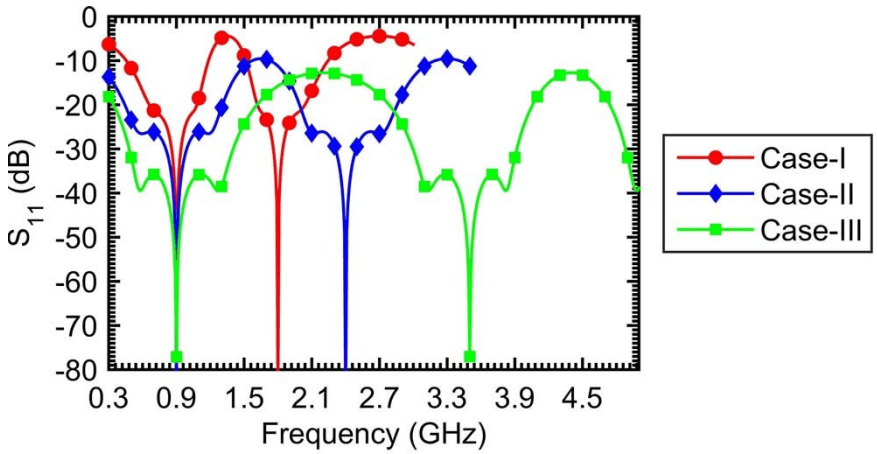

Figure 3.17: Cases for Different Impedances and Frequencies

The fact that lower the S_{11}, better is the match, is well known. For a high bandwidth, the S_{11} should be lower for a larger band of frequencies. If the reference level is brought down to -15dB, this would mark a worst case consideration for bandwidth. A better performance at -15dB reference would assure even higher bandwidth at -10dB.

Table 3.7: Fractional Bandwidth for the Case Study in Table-3.5 (Ideal Lines)

	$(\Delta f/f_1)$**X100**	$(\Delta f/f_2)$**X100**
Case-I	62%	31%
Case-II	122%	46%
Case-III	153%	48%

Based on the proposed theory, we have fabricated a prototype (Fig. 3.18) operating on 900MHz and 2.4GHz (Case-II) on RO5880 substrate. The simulated and the measured results are provided in Fig. 3.19 and Table-3.8. To illustrate the relevance of the research, we have also provided a comparison of the design with the current state-of-the-art in Table-3.9.

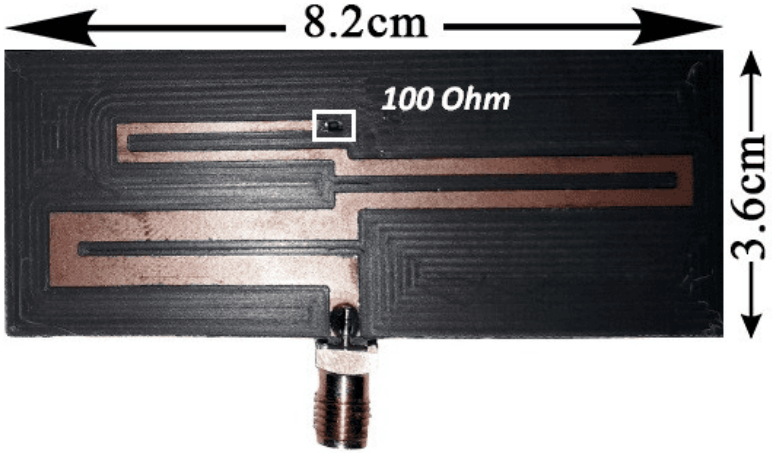

Figure 3.18: The Fabricated Prototype

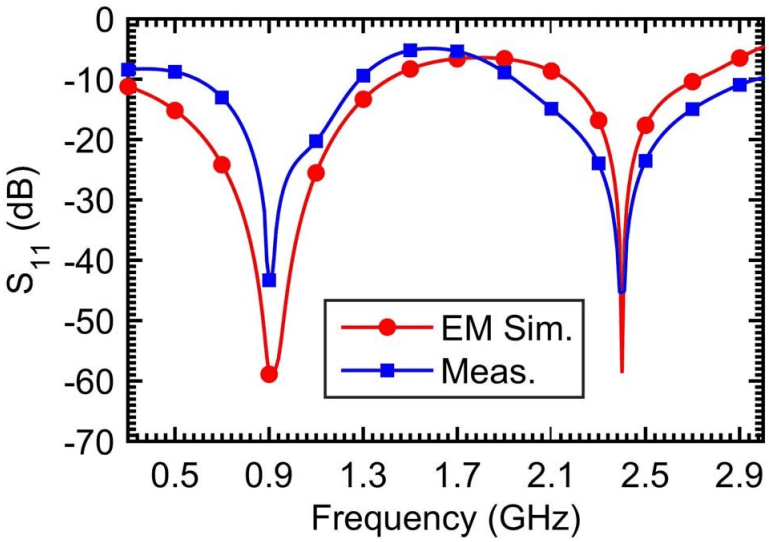

Figure 3.19: EM Simulation and Measurement Results

Table 3.8: EM-Simulated & Measured Results

Results	**Fractional Bandwidth**	
Simulated	85.56%@f_1	23.43%@f_2
Measured	50%@f_1	25%@f_2

Table 3.9: Comparison With the State-of-The-Art

Ref., Year	**Venue**	**Method Used**	**Design Procedure**	$^{*}(\Delta f/f_1)X100$	$^{+}(\Delta f/f_1)X100$
[25], 2011	IET-EL	T-model	simple	4%	3.6%
[30], 2015	MWCL	Pi-model	tedious	6%	4%
[46], 2009	MWCL	Three-Section TL	tedious	8%	6%
This Work	**——-**	**Coupled-Line Wave Slowing**	**simple**	**50%**	**25%**

*fractional BW at f_1, $^{+}$fractional BW at f_2

3.6 APCL-Based Transformers with Super Flexible Transformation Ratios

It has been an essential requirement that existing wireless architectures are compatible with the modern wireless standards that uses a considerably higher frequency band than the previously existing ones. Apart from that, a high impedance transformation ratio enables a wide range of impedances at the higher and lower ends to match with the standard 50Ω terminal impedance. We proposed a floating-arm APCL-based dual-band impedance transformer address these limitations. Rigorous mathematical models have been developed that expand the limits of frequency ratio from 1.2 till 15 and impedance transformation ratio from 0.2 till 9. We have also provided four-dimensional space plots to visualize the maximum limits to which the network can operate with the stated properties. Moreover, the extension range of these ratios are mutually independent, where increasing/decreasing one ratio do not have an effect on the other. This aspect is being reported for the first time in literature and is one of the most important contributions of this thesis. The proposed theoretical, analytical and graphical deductions are backed up by experimental results comprising of fabricated prototypes and their measurements. Another important circuit element, the equal-split T-junction power divider, has also been designed with the same specifications. Later we will see that the measured results of the divider validates the design and highlights the utility of the proposed theory.

3.7 The Proposed Impedance Transformer

Fig. 3.20 depicts the schematic of the proposed dual-band impedance transformer.

As discussed previously, the APCL $[Z_{e1}, Z_{o1}, \theta_1]$ transforms the real load Z_L into two complex conjugate admittances namely, $G_1 + jB_1$ and $G_1 - jB_1$ at f_1 and f_2 re-

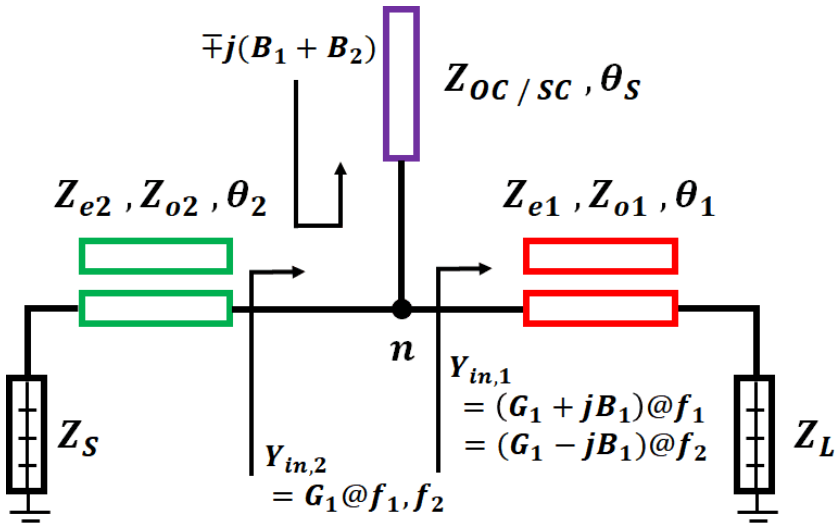

Figure 3.20: The Proposed Dual-Band Impedance Transformer

spectively. $[Z_{OC/SC}, \theta_S]$ is a dual-band stub that cancels the net susceptance $\mp(B_1+B_2)$ at the two frequencies. The stub may be either open or short circuit depending upon the sign of the susceptance generated. After susceptance cancellation, the remaining conductance G_1 is matched to the source Z_S at two frequencies by a similar all-pass coupled line $[Z_{e2}, Z_{o2}, \theta_2]$. The mathematical analysis and derivation of the design parameters are provided in the upcoming sub-sections.

3.7.1 The Complex-Conjugate Generator $[Z_{e1}, Z_{o1}, \theta_1]$

Fig. 3.21 illustrates the APCL structure with ports marked where Z_i is the image impedance. The Z-Parameters, given in (3.37), for this architecture can be obtained by simple current-voltage analysis of the coupled-line [96]. Furthermore, the image impedance Z_i of the all-pass coupled-line structure is expressed in (3.38). Equations (3.37) and (3.38) can be simplified to get the expression of Z_i given in (3.39).

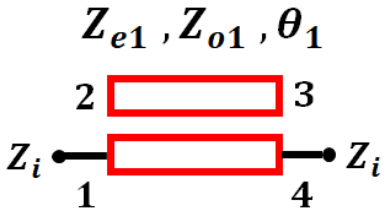

Figure 3.21: The Floating Arm All-Pass Coupled Line

$$Z_{11} = Z_{44} = \frac{-j}{2}(Z_{e1} + Z_{o1}) \cot \theta_1 \tag{3.37a}$$

$$Z_{14} = Z_{41} = \frac{-j}{2}(Z_{e1} + Z_{o1}) \csc \theta_1 \tag{3.37b}$$

$$Z_i = \sqrt{Z_{11}^2 - \frac{Z_{11}Z_{14}^2}{Z_{44}}} \tag{3.38}$$

$$Z_i = \frac{Z_{e1} + Z_{o1}}{2} \tag{3.39}$$

For complex-conjugate generation at f_1 and f_2, the condition in (3.40) must be satisfied. Further simplification gives the expression for Z_{e1} in (3.41). Apparently, value of Z_{o1} within the fabricable limits of $[20 - 160]\Omega$ enables determination of Z_{e1}. It must be noted that the values of Z_{e1} and Z_{o1} should be close to each other with the condition $Z_{o1} < Z_{e1}$ for the coupled-line section to be fabricable. This has already been discussed earlier. The ABCD-parameters are obtained from the transformation relation in (3.42) and are expressed in (3.43).

$$\frac{Z_{e1} + Z_{o1}}{2} = \sqrt{Z_S Z_L} \tag{3.40}$$

$$Z_{e1} = 2\sqrt{Z_S Z_L} - Z_{o1} \tag{3.41}$$

$$\begin{bmatrix} A & B \\ C & D \end{bmatrix} = \begin{bmatrix} Z_{11}/Z_{41} & (Z_{11}Z_{44} - Z_{14}Z_{41})/Z_{41} \\ 1/Z_{41} & Z_{44}/Z_{41} \end{bmatrix} \tag{3.42}$$

$$\begin{bmatrix} A & B \\ C & D \end{bmatrix} = \begin{bmatrix} (\frac{Z_{e1}+Z_{o1}}{Z_{e1}-Z_{o1}}) \cos \theta_1 & \frac{j}{2}(Z_{e1} + Z_{o1}) \sin \theta_1 \\ \frac{2j \sin \theta_1}{(Z_{e1}+Z_{o1})} & (\frac{Z_{e1}+Z_{o1}}{Z_{e1}-Z_{o1}}) \cos \theta_1 \end{bmatrix} \tag{3.43}$$

The admittance $Y_{in,1}$ obtained after the coupled-line stage can be expressed in (3.44). Now, $Y_{in,1}$ in (3.45) can be obtained by simplifying (3.43) and (3.44).

$$Y_{in,1} = \frac{CZ_L + D}{AZ_L + B} \tag{3.44}$$

$$Y_{in,1} = \frac{\frac{(Z_{e1}+Z_{o1})\cos\theta_1}{Z_{e1}-Z_{o1}} + \frac{2jZ_L\sin\theta_1}{Z_{e1}+Z_{o1}}}{\frac{j}{2}(Z_{e1}+Z_{o1})\sin\theta_1 + \frac{Z_L(Z_{e1}+Z_{o1})\cos\theta_1}{Z_{e1}-Z_{o1}}} \tag{3.45}$$

Decomposing $Y_{in,1}$ into real and imaginary parts, $Y_{in,1} = G_1 \pm jB_1$ at f_1 and f_2 respectively can be obtained in (3.46).

$$G_1 = \frac{Z_L\cos^2\theta_1(Z_{e1}+Z_{o1})^2}{(Z_{e1}-Z_{o1})^2\sigma} + \frac{Z_L(Z_{e1}+Z_{o1})\sin^2\theta_1}{(Z_{e1}+Z_{o1})\sigma} \tag{3.46a}$$

$$B_1 = \frac{2Z_L^2\sin\theta_1\cos\theta_1 - \frac{1}{2}(Z_{e1}+Z_{o1})^2\sin\theta_1\cos\theta_1}{\rho} \tag{3.46b}$$

where, $\sigma = \frac{1}{4}(Z_{e1}+Z_{o1})^2\sin^2\theta_1 + \frac{Z_L^2(Z_{e1}+Z_{o1})^2\cos^2\theta_1}{(Z_{e1}-Z_{o1})^2}$ and
$\rho = (Z_{e1}-Z_{o1})[\frac{1}{4}(Z_{e1}+Z_{o1})^2\sin^2\theta_1 + \frac{Z_L^2(Z_{e1}+Z_{o1})^2\cos^2\theta_1}{(Z_{e1}-Z_{o1})^2}]$

For dual-band operation at f_1 and f_2, let us consider electrical lengths at the respective frequencies to be θ and θ_1. $\theta + \theta_1 = n\pi$, where n is an integer. If $\theta = r\theta_1$, where, $r = f_2/f_1$, the expression reduces to $\theta_1 + r\theta_1 = n\pi$. This enables determination of the electrical length of the dual-band L-network in (3.47). Here, $n \in [1, 2, 3...)$.

$$\theta_1 = \frac{n\pi}{1+r} \tag{3.47}$$

The real part of the admittance, $Re\{Y_{in,2}\} = G_1$ at both f_1 and f_2, is matched to Z_S by another APCL section $[Z_{e2}, Z_{o2}, \theta_2]$.

3.7.2 Conductance Matching Line $[Z_{e2}, Z_{o2}, \theta_2]$

For the APCL to operate as a dual-band quarter-wave transformer, the impedance condition in (3.48) must be satisfied. The conditions in (3.39) and (3.48) can be simplified to get the design parameters as expressed in (3.49). Here, $K = Z_{o2}/Z_{e2}$.

$$Z_i = \sqrt{\frac{Z_S}{G_1}} \tag{3.48}$$

$$Z_{e2} = \frac{2\sqrt{\frac{Z_S}{G_1}}}{1+K} \tag{3.49}$$

The susceptance, B_2, generated by this section is calculated from (3.46b) by replacing Z_L with Z_S and $[Z_{e1}, Z_{o1}, \theta_1]$ with $[Z_{e2}, Z_{o2}, \theta_2]$, where $\theta_2 = m\theta_1$ and $m \in [1, 2, 3...)$.

3.7.3 Dual-Band Susceptance Cancellation Stub

The susceptances B_1 and B_2 are added and canceled using a dual-band susceptance cancellation stub, the parameters of which are expressed in (3.50). Here, OC and SC are for Open Circuit and Short Circuit stubs respectively and $\theta_S = p\theta_1$ where $p \in [1, 2, 3...)$.

$$Z_{OC} = \frac{\tan\theta_S}{(B_1 + B_2)} \tag{3.50a}$$

$$Z_{SC} = \frac{-1}{(B_1 + B_2)\tan\theta_S} \tag{3.50b}$$

3.8 Design Example and Case Studies

It is imperative to note that the impedance transformation ratio (k) depends directly on the chosen set of $[Z_{e1}, Z_{o1}]$ of the all-pass coupled line adjoining the load.

Fig. 3.22 illustrates the graphical representation of the maximum value of impedance transformation ratio *(k)* that can be achieved theoretically when varying the design parameters of coupled line section $[Z_{e1}, Z_{o1}]$ within the fabricable limits. This is shown for different values of sources impedances, keeping the case of inter-stage matching into consideration where the output impedance of a stage, being the nominal source impedance of the next stage, can be a non-50Ω real value. It is observed that for standard 50Ω sources, a maximum impedance transformation ratio of 9 can be achieved.

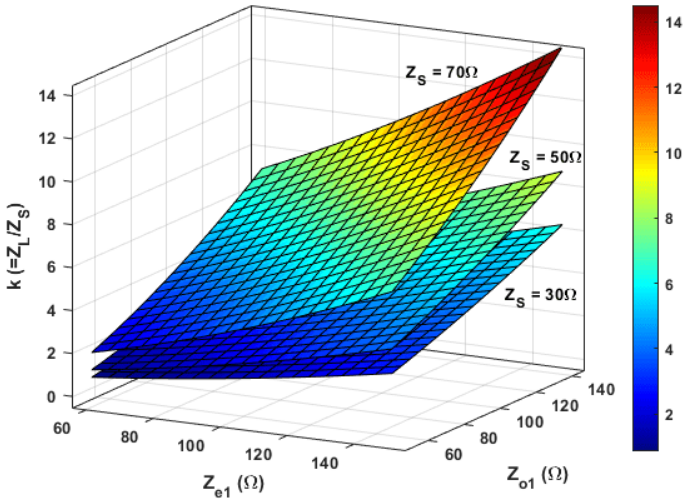

Figure 3.22: Limits of Impedance Transformation Ratio for Different Values of Z_{e1} and Z_{o1} for Different Source Impedances

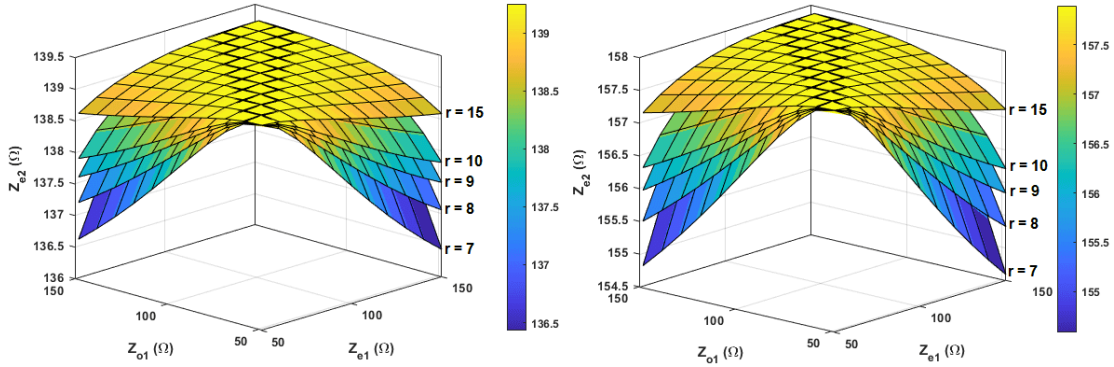

Figure 3.23: (A) Maximum Possible Values of r for k = 7, and Corresponding Line Impedances for the Set (B) Maximum Possible Values of r for k = 9, and Corresponding Line Impedances for the Set

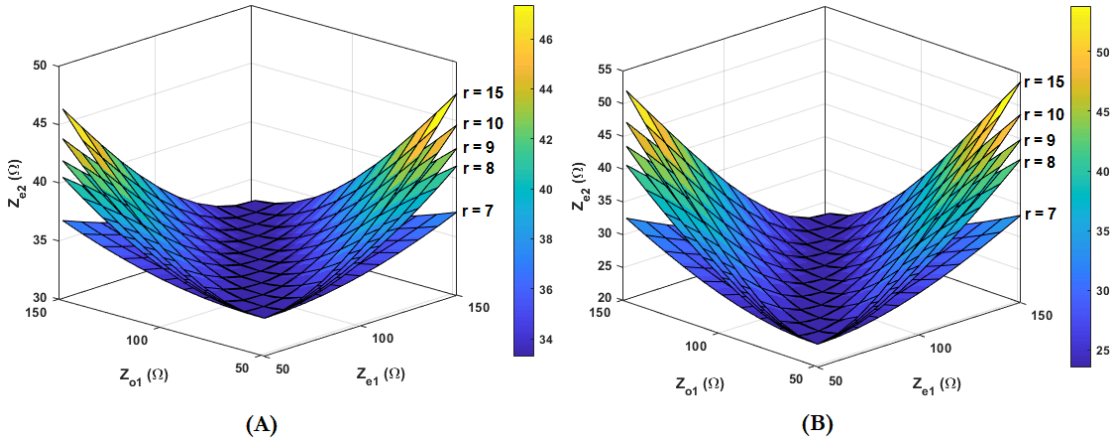

Figure 3.24: (A) Maximum Possible Values of r for k = 0.4, and Corresponding Line Impedances for the Set (B) Maximum Possible Values of r for k = 0.2, and Corresponding Line Impedances for the Set

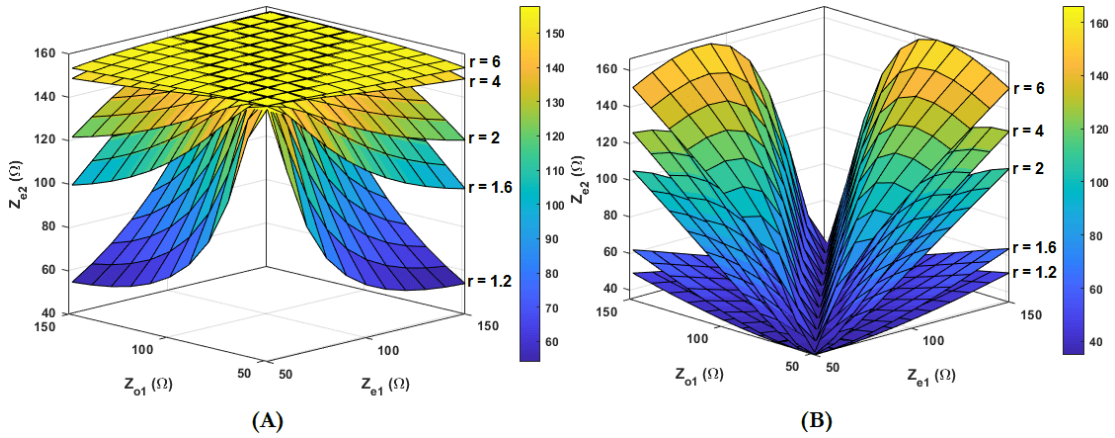

Figure 3.25: Design Parameter Values for Ultra-Low k and Ultra-Low r (Denoting Lower Limits of Transformation Ratios: (A) Minimum Possible Values of r for k = 9, and Corresponding Line Impedances for the Set (B) Minimum Possible Values of r for k = 0.2, and Corresponding Line Impedances for the Set

While the design parameters of the coupled line $[Z_{e1}, Z_{o1}]$ determine the maximum achievable impedance transformation ratio, the maximum achievable frequency ratio depends mostly on the selection of $[Z_{e2}, Z_{o2}]$ and is studied in Figs. 3.23 through 3.25. We observe that with the choice of selection of $[Z_{e1}, Z_{o1}]$ from Fig. 3.22 the impedance surfaces obtained by increasing both the transformation ratios (r and k) are within the fabricable limits of $[20 - 160\Omega]$ in microstrip technology. This directly determines Z_{e2} and hence Z_{o2} from (3.49). It is worth mentioning again that the value of K in (3.49) should be chosen around 0.6 to 0.8 for the coupled line to be physically implementable. Figs. 3.23(A) and (B) illustrate the ability of the network to operate at high impedance transformation ratios at two distantly separated frequency bands (high r). This is clearly denoted by the high impedance surface generated at $r = 15$ for the two extreme values of $k = 7$ and $k = 9$. Figs. 3.24(A) and (B) depict the lower limits of achievable impedance transformation ratio for high values of frequency ratios. The ability of the proposed network to operate at closely spaced frequencies with contrasting load conditions is illustrated in Figs. 3.25(A) and (B) where the former portrays a high impedance transformation ability $(k = 9)$ at two arbitrary closely spaced frequencies while the latter depicts the same with severely low loading conditions $(k = 0.2)$. From these figures it is evident that the proposed network is highly flexible in terms of impedance and frequency transformation, both operating simultaneously. It is also imperative to note that extending any one of the transformation ratios (r or k) towards the upper/lower limit

do not detriment the other transformation ratio and the matching conditions at the frequencies of interest. Subsequently, we have considered few examples that demonstrate simultaneous enhancement of frequency ratio and impedance transformation ratio. The cases and the corresponding design parameters are listed in Table-3.10. The values clearly confirm fabrication-ability for industrial use. Fig. 3.26 illustrates the simulation results for the case studies from Table-3.10.

Table 3.10: Case Studies for Various Frequency and Impedance Transformation Ratios

Cases	r ($= f_2/f_1$)	k ($= Z_L/Z_S$)	Design Parameters							
			$Z_{e1}(\Omega)$	$Z_{o1}(\Omega)$	$\theta_1(^\circ)$	$Z_S(\Omega)$	$\theta_S(^\circ)$	$Z_{e2}(\Omega)$	$Z_{o2}(\Omega)$	$\theta_2(^\circ)$
1	1.3	6	125	120	77.14	126.71 (SC)	231.42	60	51.8	77.14
2	9	0.3	30	24.7	18	15.95 (OC)	18	36.8	23.7	90
3	10	10	160	156.11	16.36	159.5 (SC)	81.82	160	156.11	81.82
4	15	0.1	23.71	21	11.25	22.27 (OC)	33.75	24.94	23	90
5	15	9	151	149	11.25	160.0 (SC)	78.75	151	149	78.75

a) The Source impedance (Z_S) is kept constant at 50Ω, thus different *k* signifies different load impedances (Z_L)

b) Fundamental frequency f_1 is versatile, signifying matching ability at arbitrary frequencies for the corresponding ratio *r*

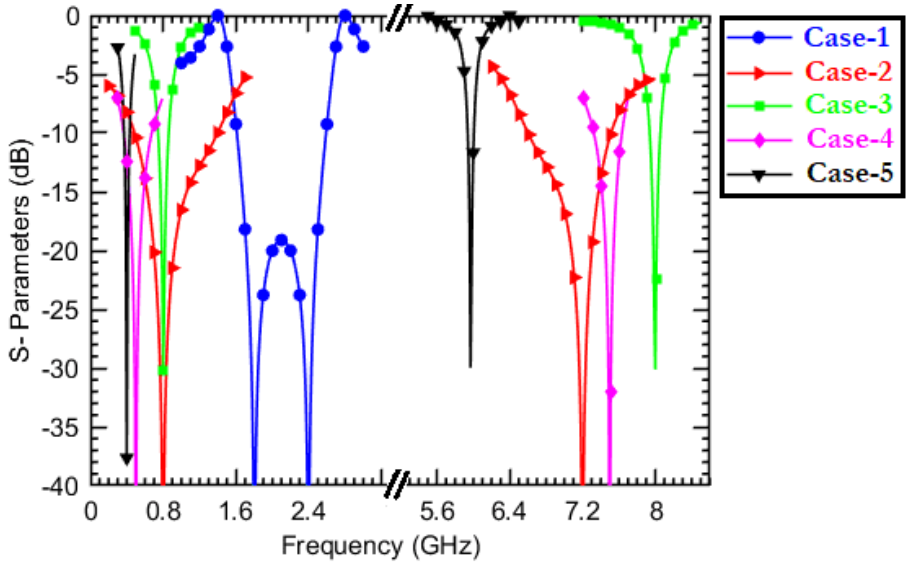

Figure 3.26: Simulation Results for the Various Case Studies

To demonstrate the practical utility of the proposed impedance matching network, we considered Case-1, Case-2 and Case-5 from Table-3.10 for fabrication on RO4350 ($\epsilon_r = 3.68,\ 1oz\ Cu$) and RO5880 ($\epsilon_r = 2.2,\ 1oz\ Cu$) and measurement. Fig. 3.27 illustrates the fabricated prototypes along with the measurement setup for the S-Parameter measurements. It is evident from Figs. 3.28 through 3.30 that the measured results achieve a perfect matching at the two desired frequencies of interest under the specified loading conditions. We should also note that the proposed design scheme

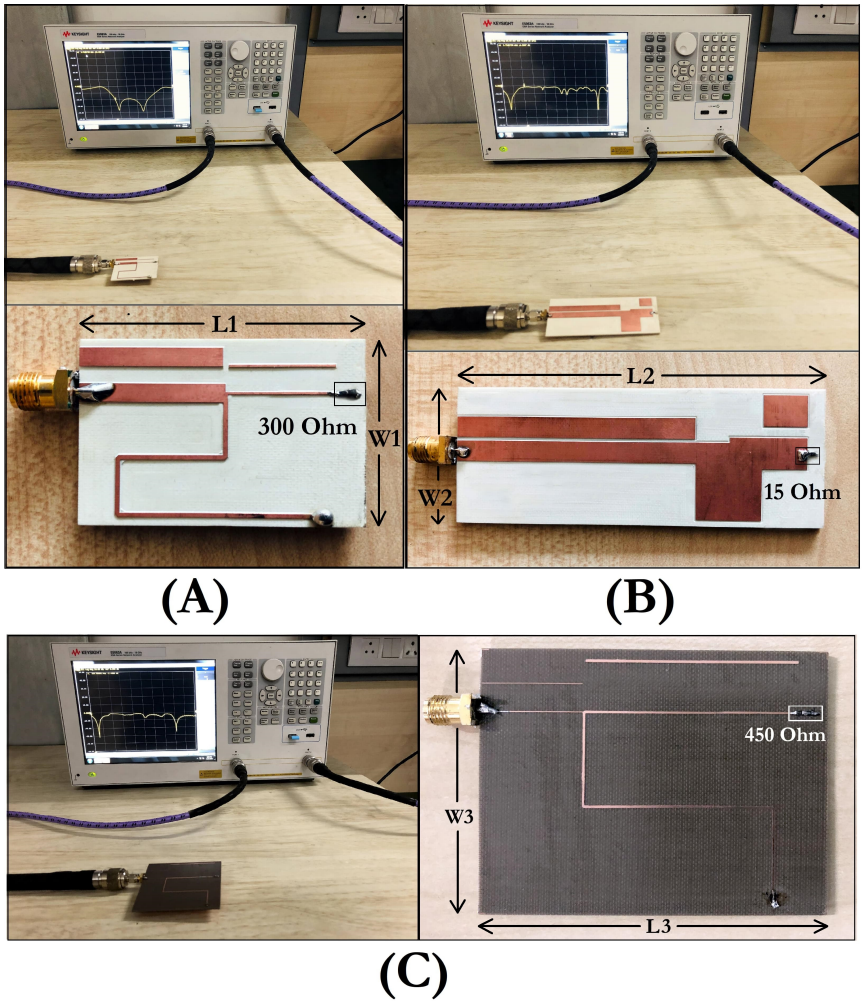

Figure 3.27: Measurement Setup for the Impedance Transformer and their Dimensions in terms of Guided Wavelength (A) For r = 1.33, k = 6.0, (W1 = $2.65\lambda_g$; L1 = $4.12\lambda_g$)@$1.8GHz$ (B) For r = 9, k = 0.3, (W2 = $1.22\lambda_g$; L2 = $3.36\lambda_g$)@$800MHz$ (C) For r = 15, k = 9, (W3 = $1.25\lambda_g$; L3 = $1.35\lambda_g$)@$400MHz$. Here (L1, W1), (L2, W2) and (L3, W3) are the Lengths and Widths of the Fabricated Prototypes in (A), (B) and (C) respectively

is substrate invariant. As evident from the experiment, a frequency-stable substrate (RO5880) has been chosen for demonstration at higher frequencies, and the measured results show a perfect match at the two desired frequencies $(r = 15)$. The circuits are compact in size thus contributing towards a lower form factor in applications like an energy harvester. As per the best of our knowledge, this is the highest obtained frequency ratio till date, for a dual-band transformer. The next section describes the application of the proposed impedance matching topology in designing a T-junction power divider.

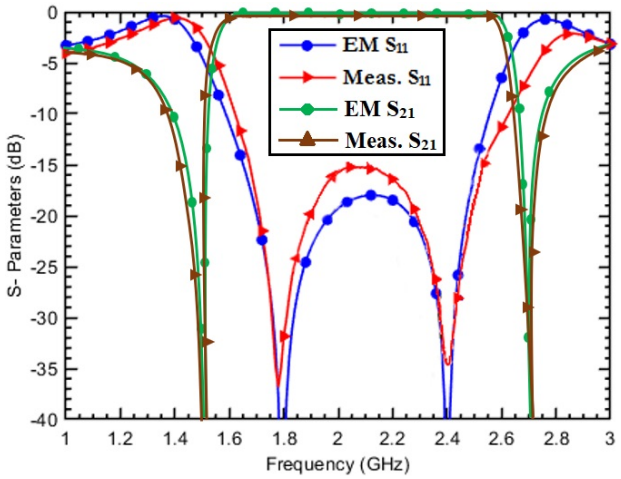

Figure 3.28: Case-1: Measured vs EM Results; Fractional Bandwidth (FBW: -15dB reference) = $19.4\%@1.8GHz$ and $16.6\%@2.4GHz$

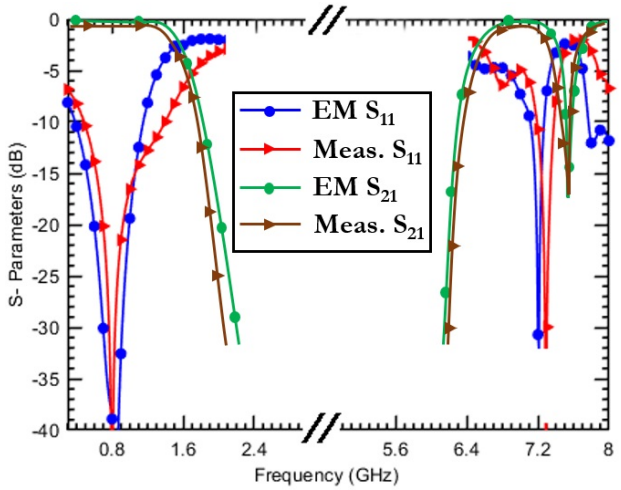

Figure 3.29: Case-2: Measured vs EM Results; Fractional Bandwidth (FBW: -10dB reference) = $125\%@800MHz$ and $5.5\%@7.2GHz$

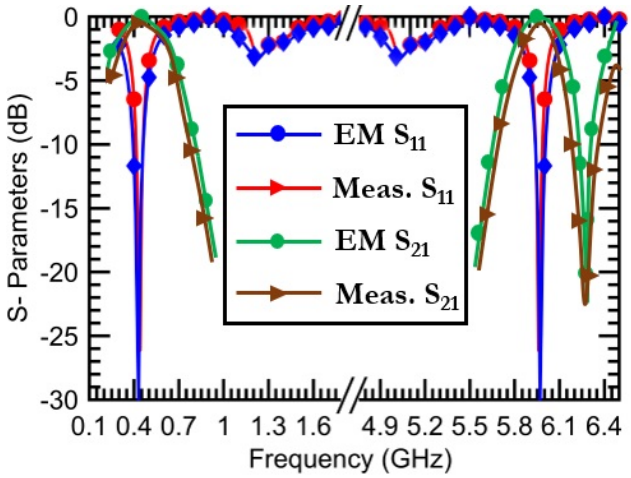

Figure 3.30: Case-5: Measured vs EM Results; Fractional Bandwidth (FBW: -10dB reference) = $50\%@400MHz$ and $5.0\%@6.0GHz$

3.9 Applications in Dual-Band TPD

One of the elementary components of RF and Microwave circuits is a power divider. A T-Junction Power Divider (TPD) differs from the Wilkinson Power Divider functionally in the sense that here, the output ports are not strictly mutually isolated. Isolation is not necessary here because using TPDs, we do not handle any intelligent signal that needs to be preserved for linearity and port leakage. The proposed impedance transformer can be utilized to implement a T-junction TPD that divides the power at two closely/distantly separated frequency bands. An application of this can prove to be suitable for mobile energy harvesting networks for advanced wireless standards.

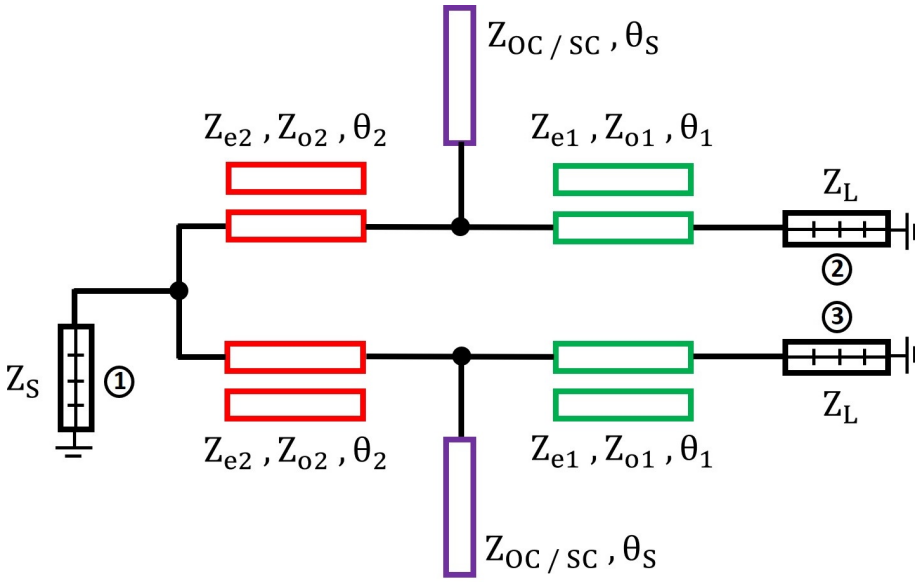

Figure 3.31: Proposed TPD with Ultra-High Transformation Ratio

Fig. 3.31 illustrates the proposed equal-split dual-band TPD featuring ultra-high-frequency ratios developed from the proposed theory. Conventionally the ports of a power divider have standard 50Ω terminations. The design presented here is capable of loading the output ports to a high value. We have done this in order to demonstrate the power division capability, augmented with high impedance transformation at extended frequency ratios. As the even and odd mode half-circuits are same in a TPD, the equations to determine the design parameters are same as discussed previously.

Figs. 3.32 through 3.35 illustrate different S-Parameter responses of the designed TPD under different loading conditions while the frequency ratio (r) is chosen to be as close as 1.2 and extended till 15. It is evident from the case studies that the power

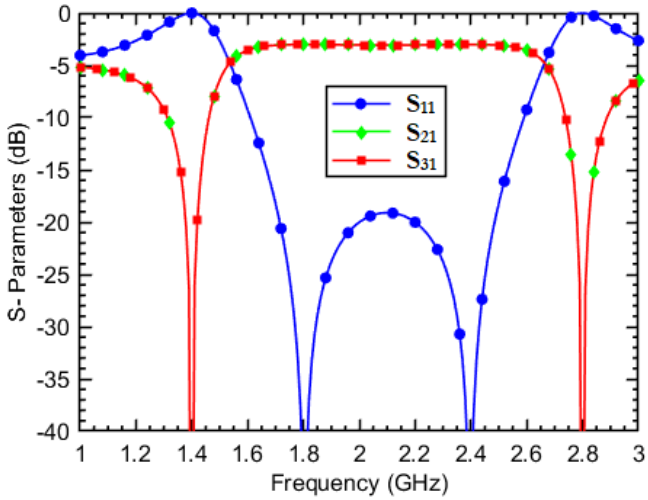

Figure 3.32: S-Parameter Simulation Results of the TPD (for $k = 0.2$ and $r = 1.33$)

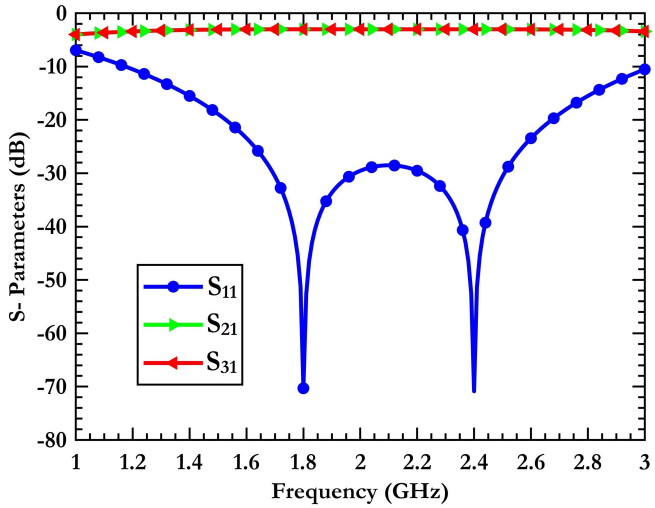

Figure 3.33: S-Parameter Simulation Results of the TPD (for $k = 5$ and $r = 1.33$)

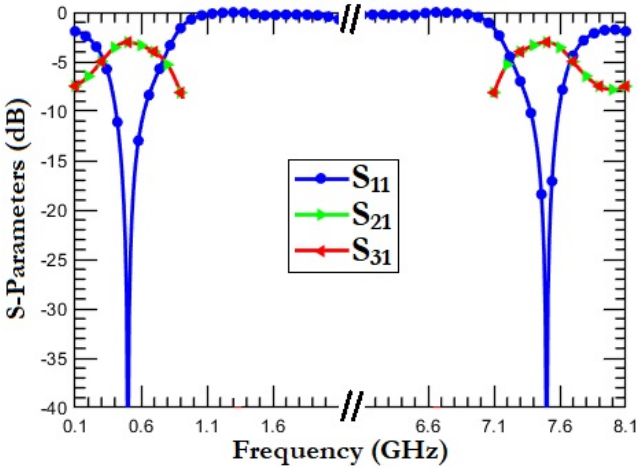

Figure 3.34: S-Parameter Simulation Results of the TPD (for $k = 0.2$ and $r = 15$)

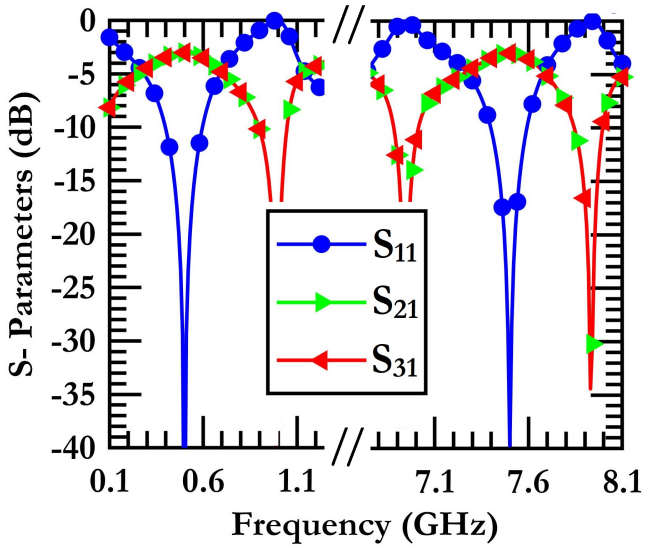

Figure 3.35: S-Parameter Simulation Results of the TPD (for $k = 5$ and $r = 15$)

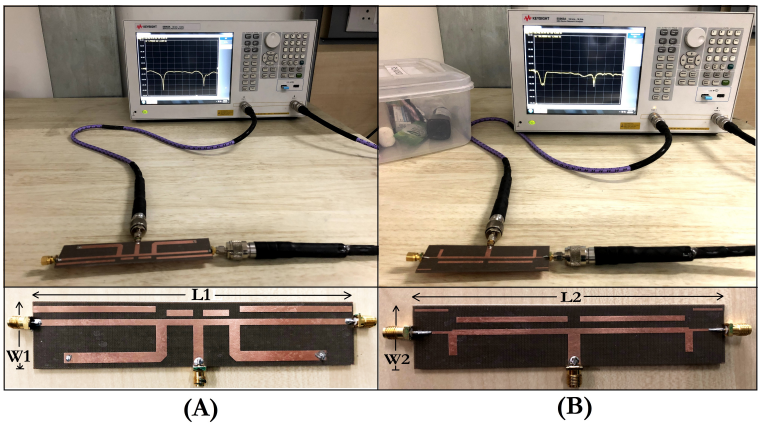

Figure 3.36: Measurement Setup for the T-Junction Power divider (A) For r = 6.25, (W1 = 1.39λ_g; L1 = 6.71λ_g)@900MHz (B) For r = 15, (W2 = 0.80λ_g; L2 = 2.94λ_g)@500MHz. Here (L1, W1) and (L2, W2) are the Lengths and Widths of the Fabricated Prototypes in (A) and (B) respectively

divider equally splits the input power in the two uncorrelated frequencies of interest. To validate the realization of the proposed T-junction power divider, we have fabricated two prototypes on RO5880, as illustrated in Fig. 3.36 performed the measurements. We can infer from Figs. 3.37 and 3.38 that the fabricated dividers show a perfect match at the desired frequencies of interest spread wide apart in the spectrum. The values of the S_{21} and S_{31} parameters being same and equal to -3.07dB, it is also verified that the dividers split power equally from the two ports, at the two frequencies. We note that while a flexible ultra-high transformation ratio can be achieved, the fractional bandwidth is limited at the upper frequency band. This comes as a trade-off for the simultaneous transformation operation for dual-band networks. Although bandwidth increment was not the

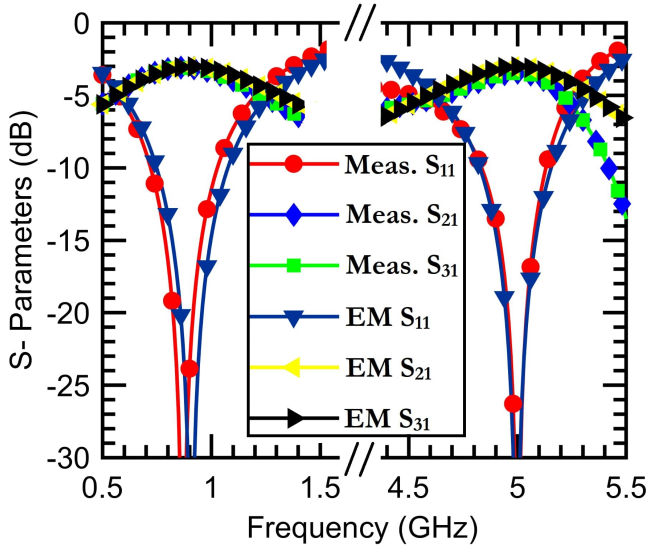

Figure 3.37: Measured Results vs EM for r = 6.25, Fractional Bandwidth (FBW) = $61.1\%@900MHz$ and $12\%@5.0GHz$

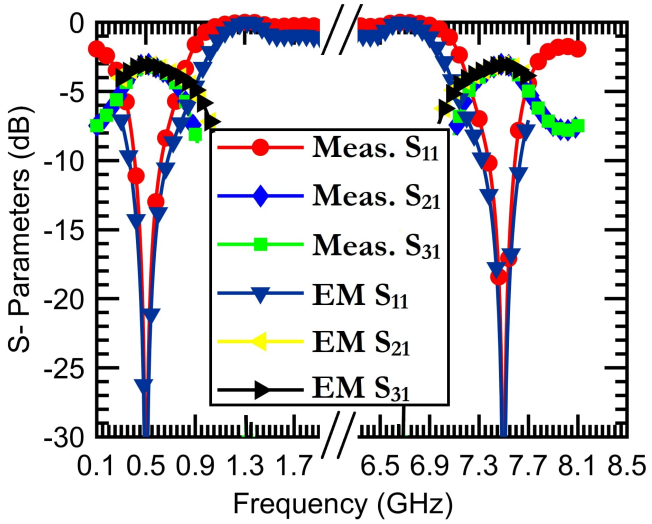

Figure 3.38: Measured Results vs EM for r = 15, Fractional Bandwidth (FBW) = $100\%@500MHz$ and $8\%@7.5GHz$

scope of this research, the proposed design scheme provides commendable bandwidth at the lower band of interest and works perfectly fine for narrow-band applications. Table-3.11 presents a structural and functional comparison of the proposed architecture with a few state-of-the-art designs. We can thereby conclude that this design approach has a potential to serve as an important component in an energy harvester.

Table 3.11: Comparison with a Few State-of-the-Art Designs

Ref. (Year)	Technique Used	Frequency Ratio (r)	Impedance Ratio (k)	Simultaneous r & k Transform.	Design Flexibility	Design Complexity	Approx. Size (λ_g^2) at Corresponding Freq.
[33] 2016	Coupled Lines	N/A (SB*)	20	No	Low	Complex	N/A
[53] 2019	Coupled Lines	3.88	4.0	No	Moderate	Very Simple	$(3.64\lambda_g$ x $1.6\lambda_g)@900MHz$
[37] 2019	Planar TL + Coupled Line	2 - 7	0.2 - 10	No	Low	Moderate	$(1.38\lambda_g$ x $0.55\lambda_g)@400MHz$
[110] 2020	Cross Shaped Structure	N/A (SB*)	0.1 - 40	No	Moderate	Simple	$(0.47\lambda_g$ x $0.42\lambda_g)@2.4GHz$
This Work (2021)	**All-Pass Coupled Lines**	**1.2 - 15**	**0.2 - 9**	**Yes**	**High**	**Very Simple**	**$(\mathbf{2.65}\lambda_g$ x $\mathbf{4.12}\lambda_g)@1.8GHz$; $(\mathbf{1.25}\lambda_g$ x $\mathbf{1.35}\lambda_g)@400MHz$**

λ_g: Guided Wavelength; *SB: Single Band Operation; N/A: Not Available

3.10 Conclusion

In this chapter we learnt about the concept of All-Pass Coupled-Lines, their types- both floating arm and meandered, architectural aspects and advantages. We also derived the relation between the image impedance of APCLs and their even-odd arm impedances. Use of floating-arm APCLs as a dual-band FDCL to complex-conjugate impedance generator has also been discussed and detail. We also learnt the implementation of a meandered line APCL as a dual-band quarter-wavelength line and their advantage in form-factor reduction. The use of APCLs to extend the frequency ratios in FDCLs has been demonstrated by designing a dual-band impedance transformer. Another dual-band transformer has been designed with meandered line based slow-wave structures to demonstrate their ability of bandwidth increment at the two desired frequency bands. We also discussed a new design approach for the development of dual-band impedance matching networks and T-junction Power Dividers that can be used in energy harvesting applications. Rigorous mathematical and graphical analyses have been made to develop a mathematical model for the design process. Three impedance matching network and two power divider prototypes have been fabricated and measured under a wide range of loading conditions over the frequency range spanning 300MHz-8.5GHz. We also demonstrated the generic and substrate-independent behaviour of the proposed model. An excellent agreement between the simulated and the measured results validate the design theory and prove its effectiveness in being an important component for several RF and Microwave circuits.

CHAPTER 4

An Enhanced Frequency-Ratio Coupled-Line Dual-Frequency Wilkinson Power Divider

This chapter is based on the following research papers-

- M.H. Maktoomi, **D. Banerjee**, and M.S Hashmi, "An Enhanced Frequency-Ratio Coupled-Line Dual-Frequency Wilkinson Power Divider", *IEEE Transactions on Circuits and Systems- II: Express Briefs*, Vol. 65, Iss. 7, p.p. 888 - 892, Jul. 2018.

Outline

This chapter presents a novel design of a dual-band equal split Wilkinson Power Divider. It is based around a single coupled line section as core and uses stub-based port matching networks at each of the ports. The structure incorporates only one isolation resistor, which is independent of frequency-ratio, for achieving perfect isolation. Closed-form design equations are developed for the general analysis of the power divider. Design case studies are provided to evaluate the proposed design. Prototypes for frequency-ratios of 2 and 7 have been developed and measurements carried out. A good agreement between the Electromagnetic (EM) simulated and measured results validate the reported theory.

4.1 Introduction

WILKINSON Power Dividers (WPD) are one of the most important building blocks of any RF circuit that performs the task of splitting (or combining in case of combiner) power in a certain ratio defined as per the requirement. A $1:1$

WPD that divides power equally between its two arms are called the equal-split power dividers. Similarly there can be cases where dividers are unequally-split, like $2:1$ or $3:1$, depending upon the amount of power to be supplied to the feeder branch.

In this chapter we have proposed a dual-frequency WPD that includes only one coupled-line section in the core, a single isolation resistor, and a stub-based port matching at each of the ports. A thorough and systematic analysis has been performed and is backed by closed-form design equations to highlight the uniqueness of the design. As per our knowledge, so far, this design provides widest possible frequency ratio (~ 7) achieved in coupled-line dual-band WPD without using complex isolation network. Another key contribution in this work is the presence of the frequency-ratio independent isolation resistor in the proposed WPD.

4.2 Structure and Design

The schematic of the proposed dual-band WPD is shown in Fig. 4.1.

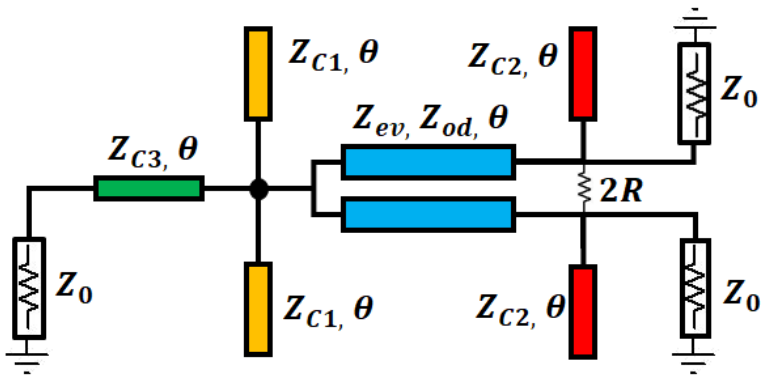

Figure 4.1: General Architecture of the Proposed Dual-Band WPD

It consists of a single coupled-line section as a core with the even- and odd-mode characteristic impedances, Z_{ev} and Z_{od}, and an isolation resistor, R. As shown in the diagram, Z_{C1} and Z_{C3} are characteristic impedances of input side network, whereas Z_{C2} is that of the output side stub. The electrical length, θ, is the same for all the sections and each port is terminated into Z_0. It is evident from Fig. 4.1 that this structure is symmetric and hence can be decomposed into the even- and odd-mode half-circuits. Conditions for port matching and dual-frequency operation are imposed on the half-circuits to obtain the design parameters.

4.2.1 Even-Mode Analysis

The even-mode equivalent half-circuit is shown in Fig. 4.2. For the input port matching of the WPD, the even-mode half circuit's input port should be matched. The terms Y_a,Y_b, Y_c, and Y_d are the respective admittances at the nodes as shown in Fig. 4.2. The terms jY_1 and jY_2 are admittance of the stubs. The admittance of the output port is denoted by g_0 $(= 1/Z_0)$ and characteristic admittance $Y_i = 1/Z_i$, for $i = ev, od, C_3$. Then, in Fig. 4.2:

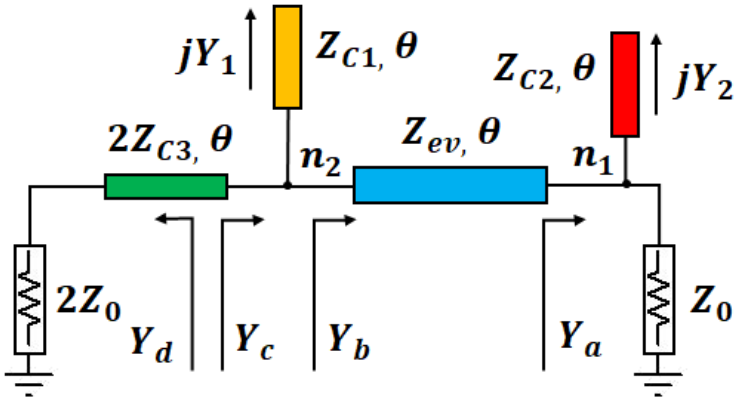

Figure 4.2: Even Mode Equivalent Circuit of the WPD

$$Y_a = g_0 + jY_2 \tag{4.1}$$

$$Y_b = Y_{ev}\frac{Y_a + jY_{ev}\tan\theta}{Y_{ev} + jY_a\tan\theta} \tag{4.2}$$

$$Y_c = Y_b + jY_1 \tag{4.3}$$

$$Y_d = \frac{Y_{C3}}{2}\cdot\frac{\frac{g_0}{2} + j\frac{Y_{C3}}{2}\tan\theta}{\frac{Y_{C3}}{2} + j\frac{g_0}{2}\tan\theta} \tag{4.4}$$

Now, applying complex conjugate matching criteria at the node n_2 yields:

$$Re[Y_c] = Re[Y_d] \tag{4.5a}$$

$$Im[Y_c] = -Im[Y_d] \tag{4.5b}$$

Where, the real and imaginary parts of Y_c and Y_d are formulated in (4.6) and (4.7):

$$Re[Y_c] = \frac{(1+\tan^2\theta)g_0 Y_{ev}^2}{(g_0^2+Y_2^2)\tan^2\theta - 2Y_2Y_{ev}\tan\theta + Y_{ev}^2} \tag{4.6a}$$

$$Im[Y_c] = \frac{Y_1(g_0^2+Y_2^2)\tan^2\theta - Y_{ev}(g_0^2+Y_2(2Y_1+Y_2))\tan\theta + A}{(g_0^2+Y_2^2)\tan^2\theta - 2Y_2Y_{ev}\tan\theta + Y_{ev}^2} \tag{4.6b}$$

where $A = Y_{ev}^2(Y_1 - Y_2(\tan^2\theta - 1)) + Y_{ev}^3\tan\theta$

$$Re[Y_d] = \frac{(1+\tan^2\theta)g_0 Y_{C3}^2}{2(\tan^2\theta g_0^2 + Y_{C3}^2)} \tag{4.7a}$$

$$Im[Y_d] = \frac{Y_{C3}\tan\theta(Y_{C3}^2 - g_0^2)}{2(g_0^2\tan^2\theta + Y_{C3}^2)} \tag{4.7b}$$

Substituting (4.6a) and (4.7a) in (4.5a) and solving for Y_{C3}, we obtain (4.8). Similarly, substituting (4.6b) and (4.7b) in (4.5b) and solving for Y_1, we get (4.9). Once Y_1 is obtained, the characteristic admittance Y_{C1} can be determined as:

$$Y_{C3} = \pm\frac{g_0\sqrt{2k_1}\tan\theta}{\sqrt{1-2k_1}} \tag{4.8}$$

where $k_1 = \frac{Y_{ev}^2}{(g_0^2+Y_2^2)\tan^2\theta - 2Y_2Y_{ev}\tan\theta + Y_{ev}^2}$

$$Y_1 = \frac{Y_{ev}^2(k_2 - Y_2) + Y_{ev}(g_0^2 - 2k_2Y_2 + Y_2^2 - Y_{ev}^2)\tan\theta + (g_0^2k_2 + Y_2(k_2Y_2 + Y_{ev}^2))\tan^2\theta}{Y_{ev}^2 - 2Y_2Y_{ev}\tan\theta + (g_0^2+Y_2^2)\tan^2\theta} \tag{4.9}$$

where $k_2 = -\frac{Y_{C3}(Y_{C3}^2 - g_0^2)\tan\theta}{2(Y_{C3}^2+g_0^2)\tan^2\theta}$

$$Y_{C1} = Y_1\cot\theta \tag{4.10}$$

4.2.2 Odd-Mode Analysis

The odd-mode half-circuit for the WPD is depicted in Fig. 4.3. For the WPD to be matched at the output port, the odd-mode half-circuit must be matched at the output port. In this figure, the admittance seen looking left of the node n_1 is:

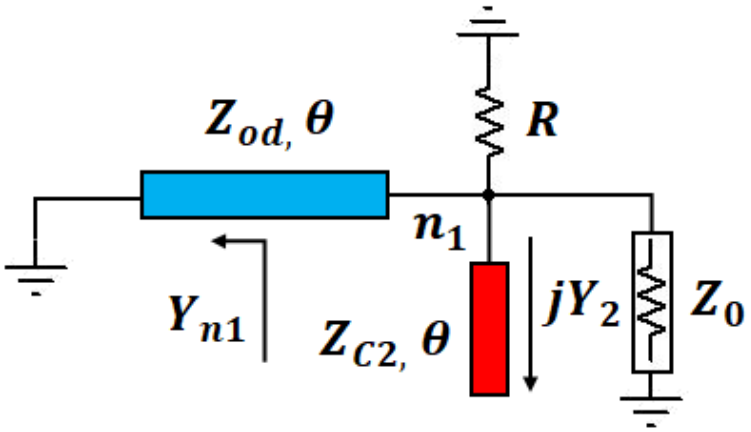

Figure 4.3: Odd Mode Equivalent Circuit of the WPD

$$Y_{n1} = -j\frac{Y_{od}}{\tan\theta} \tag{4.11}$$

Thus, for conjugate matching at node n_1:

$$Y_{n1} + jY_2 = 0 \tag{4.12}$$

$$R = 1/g_0 \tag{4.13}$$

Substituting (4.11) into (4.12) and solving for Y_2 yields:

$$Y_2 = Y_{od}\cot\theta \tag{4.14}$$

Thus, the characteristic admittance Y_{C2} can be obtained as:

$$Y_{C2} = Y_{od}\cot^2\theta \tag{4.15}$$

Now, for dual-frequency operation the electrical length, θ, is chosen as follows [32]:

$$\theta = \frac{m\pi}{1+r} \tag{4.16}$$

where, $r = \frac{f_2}{f_1}$, m is an integer and θ is electrical length at frequency f_1. The values of Z_{od} and Z_{ev} can be chosen independently and is a very advantageous feature of the proposed design. The parameters θ, $Z_{C1} = 1/Y_{C1}$, $Z_{C2} = 1/Y_{C2}$ and $Z_{C3} = 1/Y_{C3}$ are calculated from the above derived equations.

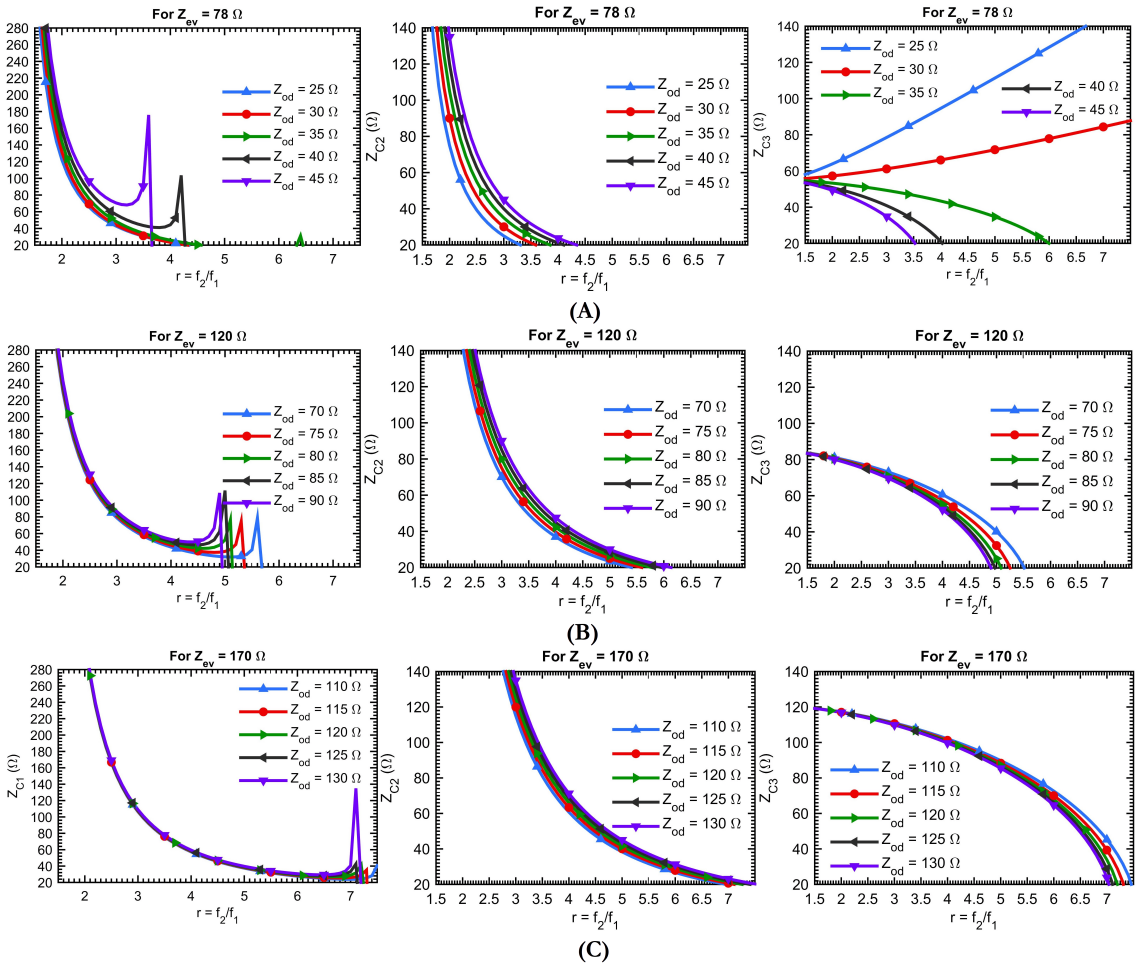

Figure 4.4: Variation of line impedances with frequency-ratio for (A) $Z_{ev} = 78\Omega$, (B) $Z_{ev} = 120\Omega$ and (C) $Z_{ev} = 170\Omega$

Fig. 4.4 shows the variation of the line impedances, Z_{C1}, Z_{C2} and Z_{C3}, with the frequency-ratio, r, considering $20\Omega - 140\Omega$ to be the limit of characteristic impedance. We observe that the two input side stubs, Z_{C1} are in parallel, and can be combined to make one stub with characteristic impedance $Z_{C1}/2$. In Fig. 4.4(A), Z_{ev} is fixed at 78Ω and Z_{od} is swept from 25Ω to 45Ω. It is apparent that for $Z_{od} = 45\Omega$, the achievable

frequency-ratio = (frequency-ratio of Z_{C1}) $\cap$ (frequency-ratio of Z_{C2}) $\cap$ (frequency-ratio of Z_{C3}) =(1.7-3.65) $\cap$ (2.0-4.35) $\cap$ (1.5-3.55) = 2.0-3.55.

Figs. 4.4(B) and (C) show that to enhance the achievable frequency-ratio, different values of Z_{ev} can be chosen. For example, it is apparent from Fig. 4.4(C) that to design a WPD for $r = 7$, $Z_{ev} = 170\Omega$ and $Z_{od} = 120\Omega$ are chosen and the required values of Z_{C1} Z_{C2} and Z_{C3} are still realizable.

4.3 Simulation Examples

In this section, we have provided some simulation based examples to show the working of the proposed WPD. As discussed in previous chapters, it is important to note that for a coupled line structure the ratio of the even- and odd-mode impedances ($\rho = Z_{ev}/Z_{od}$) should be such that the value of the design parameters S and W, that is, the separation and width of the coupled lines should be within the fabrication limits. Keeping this requirement in mind, some design cases are synthesized using the closed-form design equations obtained in Section- 4.2. The values of the design parameters for three frequency-ratios (r = 2, 5 and 7) have been provided in Table-4.1. Figs. 4.5 and 4.6 illustrate the simulation results for r =2, r =5, and r =7, respectively. It is apparent from these figures that the proposed WPD works as intended. Specifically, in each case the plots show good port-match, isolation, transmissions, and phase profile, concurrently at the two design frequencies. This clearly validates the design equations that we obtained in the previous section.

Table 4.1: Parameters for Various Band Ratios

Freq. Ratio (r)	θ	Z_{ev}	Z_{od}	Z_{C1}	Z_{C2}	Z_{C3}
2	60	78	35	144	105	53.27
5	30	120	80	52.4	26.66	25.24
7	22.5	170	120	28.90	20.58	33.82

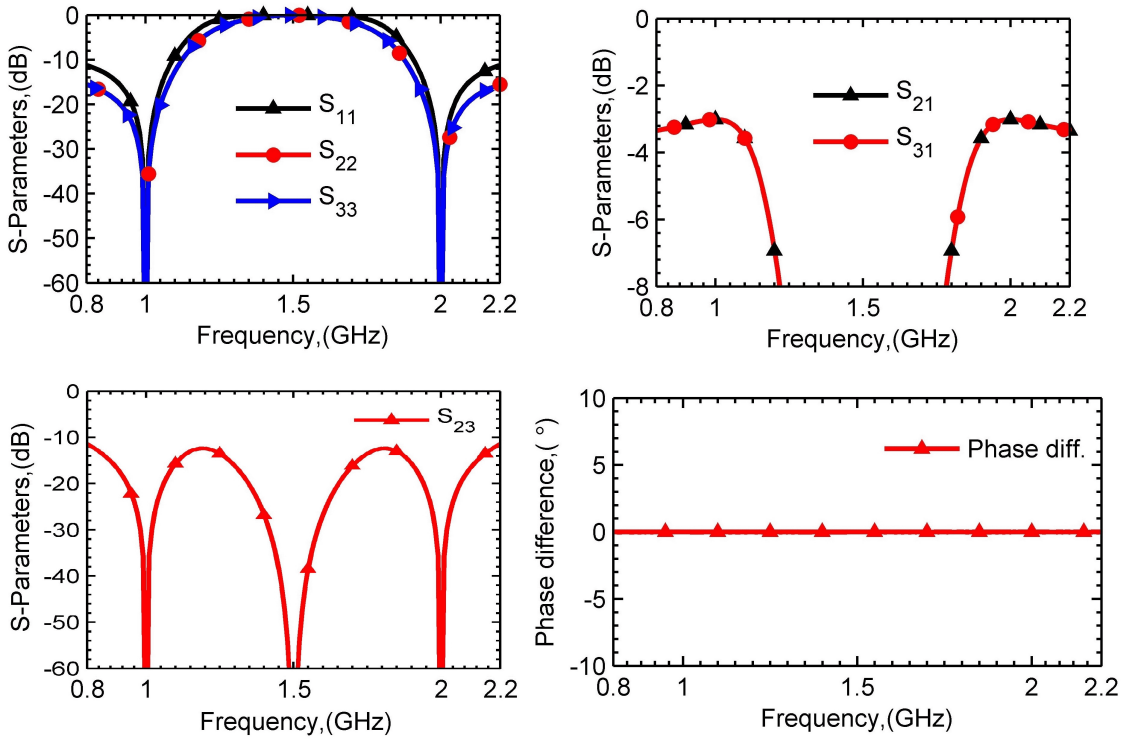

Figure 4.5: Simulated Results of the Proposed WPD for r = 2

4.4 Prototype and Measurements

To validate the proposed theory, we have designed, fabricated and tested two WPD prototypes. The first prototype operates concurrently at f_1=1GHz and f_2=2 GHz with r = 2, whereas the second one operates at f_1=0.5GHz and f_2=3.5 GHz with r = 7. The design parameters are provided in Table-4.1. The devices are fabricated on 62 mil thick Rogers RT/Duroid® 5880 substrate with ϵ_r = 2.2 and $\tan\delta$ = 0.0009. The fabricated prototypes are shown in Fig. 4.7, with the final dimensions given in Table-4.2, and is measured using a Keysight VNA. It should be noted that the final designs were optimized to compensate for the effects of junction discontinuities. In addition, we have combined the input side stubs in the first prototype for the ease of implementation. The measured and EM simulated results are compared in Fig. 4.8.

Table 4.2: Final Dimensions of the Prototypes

r = 2, dimension in mils			**r = 7, dimension in mils**		
L_1 = 1467	W_1=305	W_4=16.5	L_1 = 1314	W_1 = 395	W_5 = 316
L_2 = 1345	L_5 = 330	L_6 = 654	L_2 = 831	W_3 = 483	S = 96.6
W_2 = 158	L_3 = 1375	S = 28.8	W_2 = 292	W_4 = 17.9	L_3 = 1150
W_3 = 18.4	L = 3982	W = 2297	L_4 = 876	L_P = 3830	W_P = 3577
L_4 = 1025					

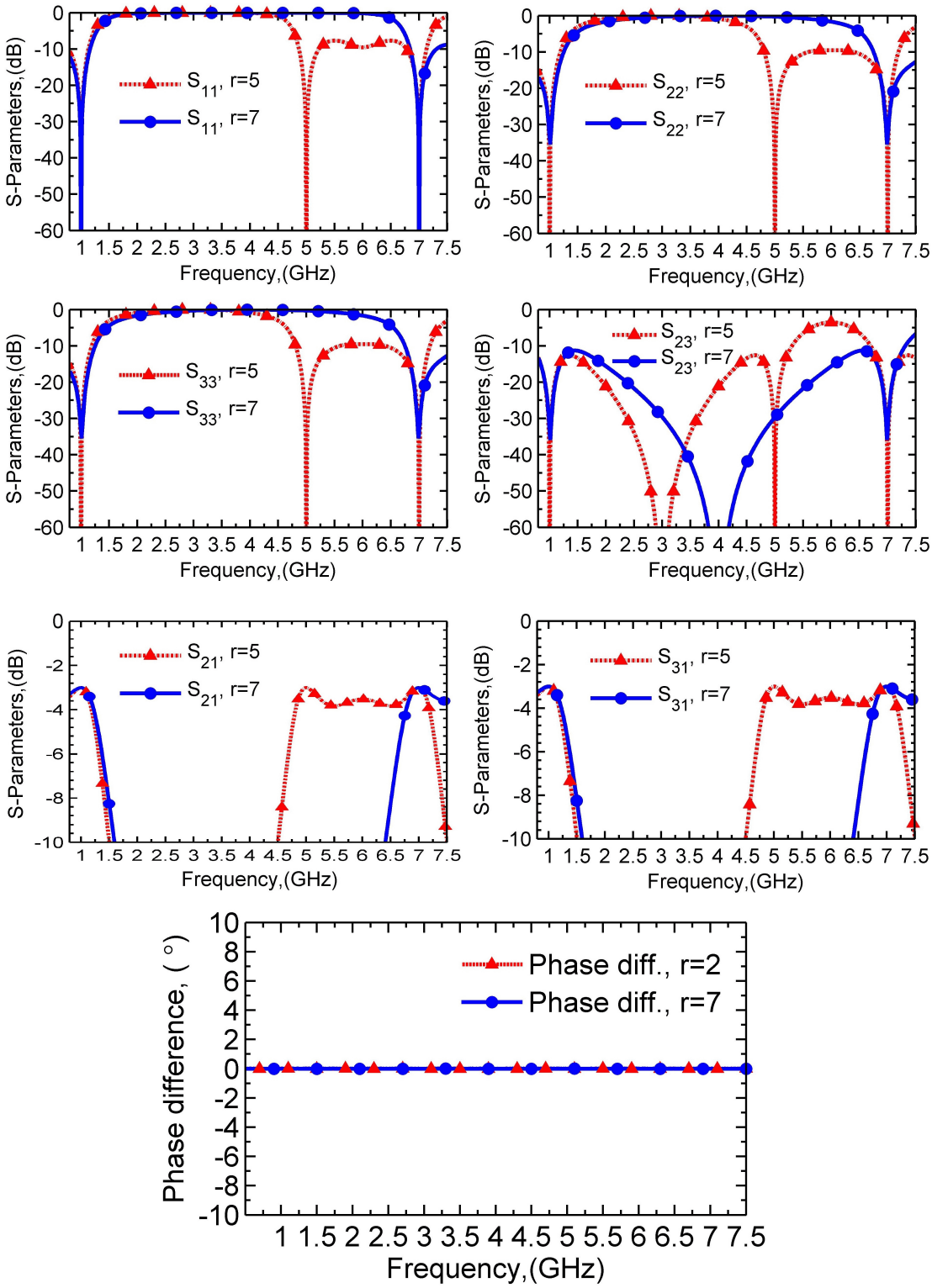

Figure 4.6: Simulated Results of the Proposed WPD for r = 5 and r = 7

For the first prototype, the measured S_{11} are less than -25 dB at f_1 and f_2, transmissions are 3.1 and 3.2 dB, and isolations are more than 32 dB at both the frequencies. In addition, the phase-difference between the output ports are 0.33 and 0.46 degrees at f_1 and f_2, and can be considered very close to the ideal value of 0 degree. For the second

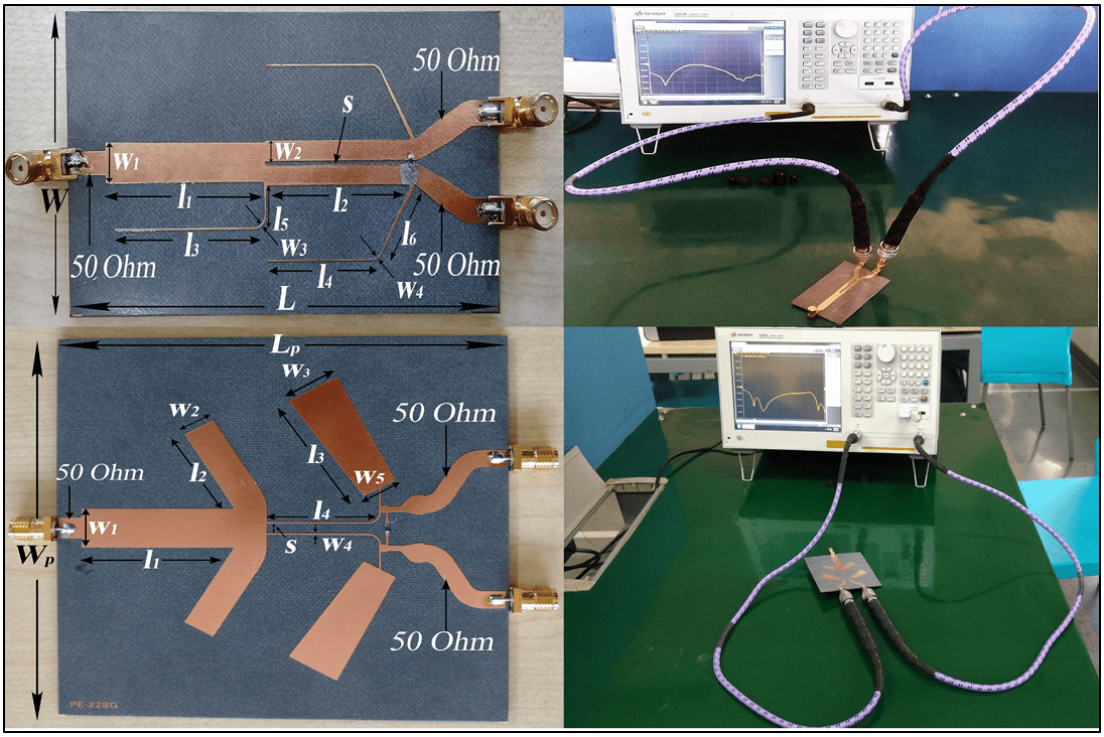

Figure 4.7: The fabricated prototypes for r = 2 (top) and r = 7 (bottom) and their measurement using a VNA. Dimensions are in mm/mm

prototype, the measured S_{11} are less than -30 dB at f_1 and f_2, transmissions are 3.24 and 3.68 dB, and isolations are more than 29 dB at both the frequencies. In addition, the phase-difference between the output ports are 0.9 and 0.8 degrees at f_1 and f_2.

Comparison with some previously reported works have been provided in Table-4.3. In majority of works, the isolation network comprises of more than one lumped element, and often forms complex network with L and C. Moreover, in previously reported designs, the lumped elements of isolation network are mandatorily a continuous function of frequency-ratio. It is apparent from this table that the proposed design presented a dual-frequency WPD that has fairly wide band-ratio with just one element isolation network, and that too, the isolation element is independent of the band-ratio.

4.5 Discussion and Conclusion

In this chapter, we have presented a dual-frequency Wilkinson Power Divider using coupled lines in the core. We discussed in detail the advantages of using such a structure. Analyses, leading to the closed-form design equations were also presented and

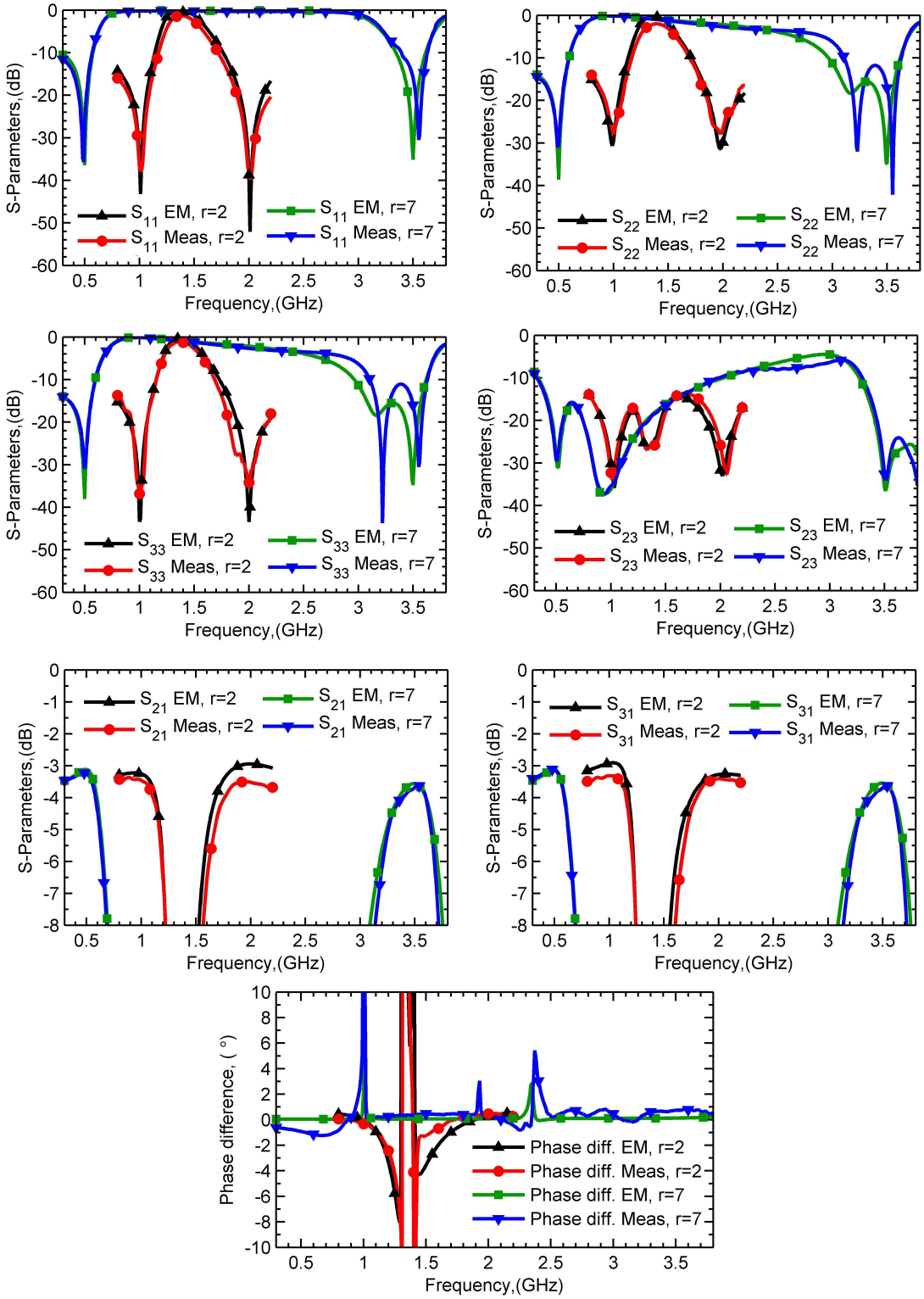

Figure 4.8: The fabricated prototypes for r = 2 (top) and r = 7 (bottom) and their measurement using a VNA. Dimensions are in mm/mm

verified with simulation examples. We discussed the variation of three important design parameters and their effect was represented graphically. Finally, we fabricated and measured the prototypes and demonstrated that the measured results compare well with

Table 4.3: Performance Comparison with Some Previous Designs

Ref.	**Technique used**	**Isolation network**	**I.N.D.B.R***	**Band ratio (r)**	S_{11} @ f_1, f_2 **(dB)**	S_{21}, S_{31}@f_1, f_2 **(dB)**	S_{23}@f_1, f_2 **(dB)**	**Phase diff. @** f_1, f_2 **(deg)**
[39]	Two section cascaded coupled-line	1 Resistor	Yes	1 - 3	-27.5, -26.9	-3.08, -3.08	-33.1, -50.8	NA
[40]	Two section coupled-line	2 Resistor	Yes	1 - 3	-25	-3.1, -3.2	-30	NA
[43]	Port extension with complex isolation	1 Resistor, 1 Capacitor, 1 Inductor	Yes	>(1 - 10)	-47, -26	-3.1, -3.3	-34, -40	NA
[44]	Two section cascaded coupled-line	1 Resistor, 1 Capacitor, 1 Inductor	Yes	1 - 3.5	-40, -26	-3.1, -3.2	-30, -25	NA
This work	**Single section coupled-line**	**1 Resistor**	**No**	**1 - 7**	**r=2 -39, -40** **r=7 -36, -31**	**r=2 -3.1, -3.2** **r=7 -3.24, -3.68**	**r=2 -34, -32** **r=7 -29, -32**	**r=2 0.33, 0.46** **r=7 0.9, 0.8**

$*$Isolation Network Dependency on Band ratio

those obtained from the EM simulations. From the comparison with some previously reported works we can conclude that the proposed design potentially helps solve some limitations of the current state-of-the-art.

CHAPTER 5

Tri-Frequency Circuits on Perspective of Matching Networks and Power Dividers

This chapter is based on the following research papers-

- **D. Banerjee**, A. Saxena, and M.S. Hashmi, "A Novel Concept of 'Virtual Impedance' for High-Frequency Tri-Band Impedance Matching Networks", *IEEE Transactions on Circuits and Systems-II: Express Briefs*, Vol. 65, No. 9, p.p. 1184 - 1188.

- **D. Banerjee**, M.S. Hashmi, and F.M. Ghannouchi, "A Novel Design of a Tri-Band Impedance Matching Network Based on the Concept of an Impedance Bridge", Proc. on the IEEE Asia-Pacific Microwave Conference (APMC), p.p. 318 - 320, Kyoto, Japan, Nov. 6, 2018.

- **D. Banerjee**, and M.S. Hashmi, "Generalized Design Scheme of a Versatile Tri-Frequency Wilkinson Power Divider", *Wiley Intt. Jrnl. RF and Microw. Comp. Aided Engg., Vol. 31, Iss. 5, e22578, May 2021.*

Outline

This chapter introduces a novel concept of a Virtual Impedance for tri-band impedance matching. The proposed mathematical concept when applied in practical realization, simplifies the design of tri-band matching and also enhances the achievable frequency ratios beyond 7.3. A variant of the design scheme based on an "Impedance Bridge" has also been discussed. The design, conceptualization, and validation of a simple generic and versatile tri-band Wilkinson Power Divider (WPD) has also been presented. To demonstrate the generalization of the design approach, a coupled-line based DC isolated WPD is also developed along with the design cases operating at varied specifications.

5.1 Introduction

A TRI-band impedance transformer ensures simultaneous operation at three frequencies of interest. This further reduces circuit redundancy and increases the overall functionality of the circuit of which it is a part. Recently, there have been reports of tri-band matching [70, 113], to facilitate designs of tri-band components and circuits. These designs, although significant advancements, suffer from complicated design strategies and limited frequency ratios. For example, the dual to tri-band transformation based design provides limited frequency ratios [113]. On the other hand, the stubbed coupling line based design is constrained by limited frequency ratios and relies on optimization to account for different even- and odd-mode velocities in addition to the requirement of one frequency being related to the other two in a particular way [70].

This chapter introduces a novel concept of a Virtual Impedance that addresses some of the mentioned concerns. The identification of an appropriate Virtual Impedance enables the development of simplified closed-form design equations and thereby eases the design procedure. In addition, it also aids in the significant enhancement of the achievable frequency ratio. We have also proposed a variant of the concept and presented it with examples, theoretical analysis and design equations. In the next part of the chapter, we have presented the design scheme of a generic and versatile tri-band WPD. Detailed mathematical models along with design flow has been provided. Finally we have provided fabricated and measured prototypes for all the cases to validate the proposed concepts.

5.2 The Proposed Impedance Matching Network

The schematic of the proposed tri-band matching network is depicted in Fig. 5.1. It consists of two dual-band transformers joined by a Virtual Impedance. As a concept, the load Z_L is matched to the Virtual Impedance, Z_V, at two frequencies f_3 and f_1. The combined section-A along with the load Z_L possess an impedance that equals the virtual impedance Z_V. This impedance Z_V, then, must be matched to the source impedance Z_S at frequencies f_2 and f_1 using section-B for achieving the tri-band functionality.

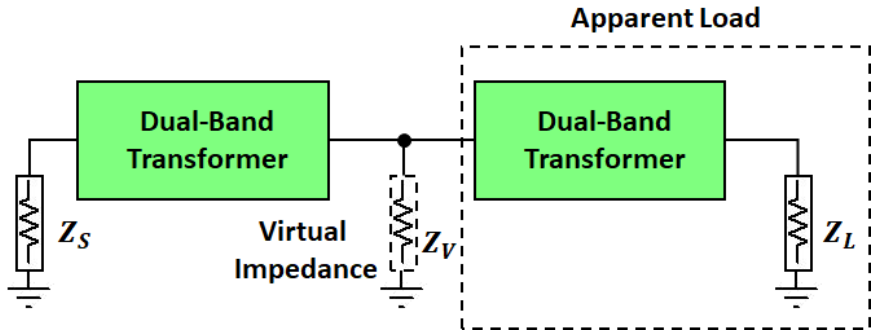

Figure 5.1: Schematic of the Proposed Tri-Band Impedance Matching Network

We have coined the term "Virtual Impedance" because the impedance is just a mathematical concept and does not exist physically. In principle, any dual-band matching architectures can be used as sections-A and B but for the sake of simplicity and compactness, an L-network has been used here.

5.3 Mathematical formulation

The circuit representation of the proposed impedance transformer given in Fig. 5.2 includes an L-section dual-band impedance transformer as section-A that utilizes the interesting admittance property of two section transmission line [48].

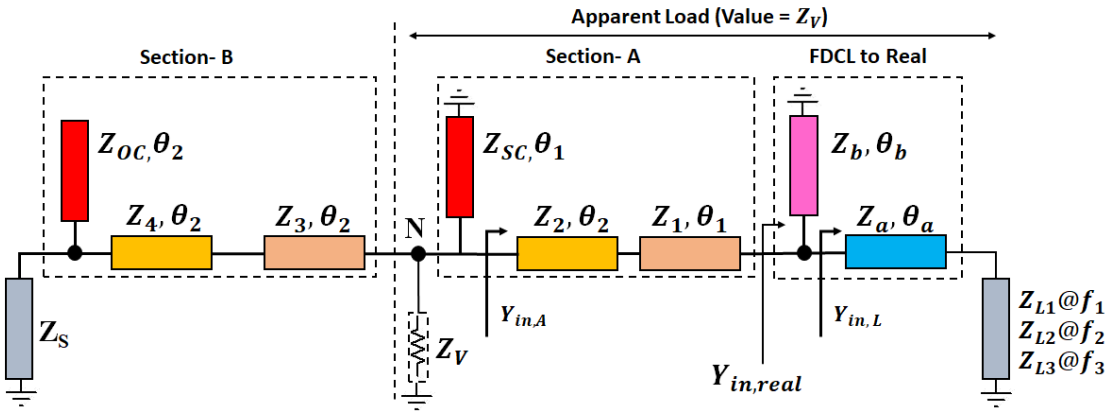

Figure 5.2: Circuit Representation of the Proposed Tri-Band Impedance Matching Network using Microstrip Transmission Lines

Here, Z_1, Z_2, and Z_{SC} are the respective characteristic impedances of the transmission line segments and the shorted stub while all the segments have equal electrical length of θ_1. We have also chosen section-B as an L-section dual-band impedance transformer with an open stub. The corresponding characteristic impedances and the elec-

trical lengths are mentioned in the figure. We have considered a frequency dependent complex load (FDCL) type and an additional L-network preceding section-A converts it to a real value. The virtual impedance Z_V is the conduit between sections-A and B.

5.3.1 FDCL-to-Real Transforming Network

The section-A matches with the Virtual Impedance only at f_1 and f_3, so the impedances Z_{L1} and Z_{L3} are key parameters. The FDCL and the other associated parameters for the real impedance transformation are given in Fig. 5.3. Here, the three FDCLs are $Z_{L1} = R_1 + jX_1@f_1; Z_{L2} = R_2 + jX_2@f_2$, and $Z_{L3} = R_3 + jX_3@f_3$. Now, the transmission line parameters Z_a and θ_a are obtained from (5.1)[46].

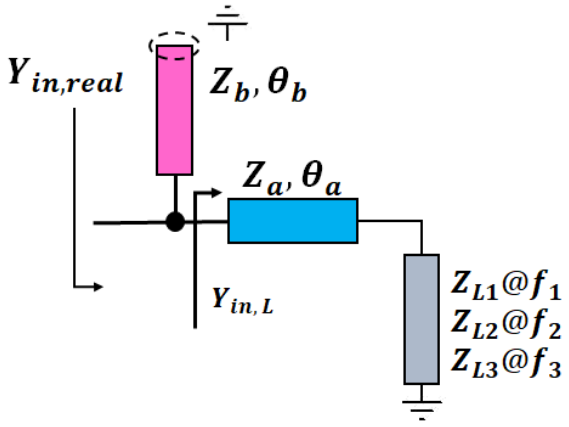

Figure 5.3: FDCL-to-Real Load Conversion: Considering Only the Impedances- Z_{L1} and Z_{L3} @ f_1 and f_3 Respectively

$$Z_a = \sqrt{R_1R_3 + X_1X_3 + \frac{X_1 + X_3}{R_3 - R_1}(R_1X_3 - R_3X_1)} \tag{5.1a}$$

$$\theta_a = \frac{p\pi + \arctan[\frac{Z_1(R_1 - R_3)}{R_1X_3 - R_3X_1}]}{1 + r_{31}} \tag{5.1b}$$

where, $p \in [0, 1, 2, 3, ...]$.

The admittance $Y_{in,L}$ are complex conjugates of each other at frequencies f_1 and f_3, i.e. $Z_{in,L}|_{f_1} = Z^*_{in,L}|_{f_3}$ [3], where, $Z_{in,L} = 1/Y_{in,L} = R_{in,L} + jX_{in,L}@f_1$ and $R_{in,L} - jX_{in,L}@f_3$. The separation of real and imaginary parts gives values for $R_{in,L}$ and $X_{in,L}$ [48].

$$R_{in,L} = \frac{R_1 Z_1^2[1+\tan^2\theta_a]}{Z_a^2 - 2Z_a X_1 \tan\theta_1 + (R_1^2+X_1^2)\tan^2\theta_a} \tag{5.2a}$$

$$X_{in,L} = \frac{(Z_a^2 - R_1^2 - X_1^2)Z_a \tan\theta_a + Z_a^2 X_1[1-\tan^2\theta_a]}{Z_a^2 - 2Z_a X_1 \tan\theta_a + (R_1^2+X_1^2)\tan^2\theta_a} \tag{5.2b}$$

$Y_{in,L}$ can also be represented in terms of conductance and susceptance as: $Y_{in,L} = G_{in,L} + jB_{in,L}$ @ f_1 and $G_{in,L} - jB_{in,L}$ @ f_3, where,

$$G_{in,L} = R_{in,L}/(R_{in,L}^2 + X_{in,L}^2) \tag{5.3a}$$

$$B_{in,L} = X_{in,L}/(R_{in,L}^2 + X_{in,L}^2) \tag{5.3b}$$

A susceptance cancellation dual-band stub is used to negate the term $\pm jX_{in,L}$, and hence, a real impedance, $Z_{in,real}(= 1/Y_{in,real})$ is obtained. The stub parameters can be obtained from (5.4)-(5.6) depending on stub type [48].

$$\theta_b = \frac{(1+m)\pi}{1+r_{31}} \tag{5.4}$$

$$Z_b|_{open} = -\tan\theta_b/B_{in,L} \tag{5.5}$$

$$Z_b|_{short} = \cot\theta_b/B_{in,L} \tag{5.6}$$

where, $m \in [0,1,2,3,...]$ and frequency ratio r_{31} = f_3/f_1. The susceptance $B_{in,L}$ is obtained from (5.3b). The real impedance $Z_{in,real}$ (= $1/Y_{in,real}$), hence obtained, is matched to the virtual impedance Z_V at f_1 and f_3.

5.3.2 Section-A: An L-Section Dual-Band Transformer

Analysis of dual-band section-A, depicted in Fig. 5.4, for tri-band impedance matching applications require elaboration of two distinct situations namely $Z_{in,real} \in$ [30,150] Ω, and $Z_{in,real} \notin$ [30,150] Ω.

Case-I: $Z_{in,real} \in$ **[30, 150]:** For the sake of mathematical simplicity, we have considered the impedance of Z_1 to be same as $Z_{in,real}$. Moreover, this assumption ($Z_1 = Z_{in,real}$) holds only for physically realizable loads, eg. 30-150 Ω. Under this assump-

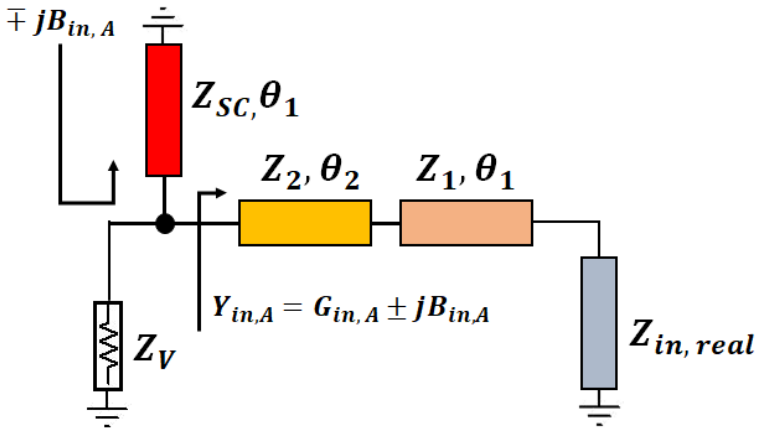

Figure 5.4: Section-A: Admittance property of two section transmission line used to match $Z_{in,real}$ with Z_V at f_1 and f_3

tion, Z_2 can be expressed as [48]:

$$Z_2 = \frac{-b \pm \sqrt{b^2 - 4ac}}{2a} \tag{5.7}$$

$$a = Y_0 Z_L^2 \tan^4\theta_1 + Y_0 Z_1^2 \tan^2\theta_1 \tag{5.8a}$$

$$b = 2Y_0 Z_1^3 tan^2\theta_1 - 2Y_0 Z_L^2 Z_1 tan^2\theta_1 \tag{5.8b}$$

$$c = -Z_L Z_1^2 (1 + \tan^2\theta_1)^2 + Y_0 Z_L^2 Z_1^2 + Y_0 Z_1^4 \tan^2\theta_1 \tag{5.8c}$$

The electrical length, θ_1, is obtained from (5.4) while the admittance, Y_0, in (5.8) corresponds to the virtual impedance, i.e., $Y_0 = 1/Z_V$. The simplification of (5.7) and (5.8) results in two solutions for Z_2 presented in (5.9). The simplified expression for Z_2 in (5.10) is obtained by substituting $Z_{in,real} = Z_1$, as assumed earlier, in (5.7) and (5.8).

$$Z_2 = \frac{Y_0 Z_1 \tan^2\theta_1 (\pm Z_{in,real}^2 \mp Z_1^2) + \sqrt{A}}{Y_0 \tan^2\theta_1 (Z_1^2 + Z_{in,real}^2 \tan^2\theta_1)} \tag{5.9}$$

where, $A = Y_0 Z_1^2 Z_{in,real} \tan^2\theta_1 (1 + \tan^2\theta_1)^2 (Z_{in,real}^2 \tan^2\theta_1 + Z_1^2 (1 - Y_0 Z_{in,real}))$

$$Z_2 = \frac{\sqrt{Y_0 Z_L (\tan^2\theta_1 - Y_0 Z_{in,real} + 1)}}{Y_0 \tan\theta_1} \tag{5.10}$$

The virtual impedance Z_V, and hence Y_0, in (5.11) can then be obtained from the simplified expression of Z_2.

$$Z_V = 1/Y_0 = \frac{Z_{in,real}^2 + Z_2^2 \tan^2\theta_1}{Z_{in,real}(1+\tan^2\theta_1)} \tag{5.11}$$

The dual-band admittance $Y_{in,A}$ at the end of two-section transmission line segment can be written as $Y_{in,A} = G_{in,A} \pm jB_{in,A}$, where $G_{in,A}$ and $B_{in,A}$ are given by (5.12) and (5.13) respectively. Now, the susceptance $jB_{in,A}$ is cancelled at f_3 and f_1 by a dual-band stub to leave only the conductance $G_{in,A}$ that equals $1/Z_V$. The dual-band stub can be open or short, depending upon the sign of susceptance generated, and their design parameters can be deduced by making appropriate replacements in expressions (5.4)-(5.6). The next stage (section-B) requires matching between the source impedance Z_S and $Z_V = 1/G_{in,A}$ at two frequencies f_1 and f_2 for achieving the tri-band matching.

$$G_{in,A} = \frac{Z_{in,real}Z_1^2(1+\tan^2\theta_1)^2}{Z_{in,real}^2(Z_1 - Z_2\tan^2\theta_1)^2 + Z_1^2(Z_1+Z_2)^2\tan^2\theta_1} \tag{5.12}$$

$$B_{in,A} = \frac{Z_{in,real}^2(Z_1 - Z_2\tan^2\theta_1) - Z_1^2(Z_2 - Z_1\tan^2\theta_1)}{Z_{in,real}^2(Z_1 - Z_2\tan^2\theta_1)^2 + Z_1^2(Z_1+Z_2)^2\tan^2\theta_1}(1+\frac{Z_1}{Z_2})\tan\theta_1 \tag{5.13}$$

Case-II: $Z_{in,real} \notin$ **[30, 150]:** In this case, we have chosen $Z_{in,real} \neq Z_1$ in order to physically realize Z_1. The solution for this case can be obtained by choosing Z_1 to be a free variable. This provides an extra design variable and hence an additional degree of freedom for matching $Z_{in,real}$ with Z_V. Considering Z_1 to be a free variable, (5.9) can be used to determine Z_2. The subsequent process is similar to the situation when $Z_{in,real} \in [30, 150]\Omega$.

5.3.3 Section-B: L-Section Dual-Band Transformer

Section-B is a structural replica of section-A except for some minor changes in the transmission line parameters. Here, the design expressions for Z_3 and Z_4 is similar to Z_1 and Z_2 respectively. In these expressions, Z_V is replaced by Z_S, $Z_{in,real}$ by Z_V, θ_1 by θ_2, and r_{31} by $r_{21}(= f_2/f_1)$. The stub parameters are calculated using (5.4)-(5.6) once $B_{in,B}$ is determined.

5.3.4 Virtual Impedance

The Virtual Impedance, Z_V, is the most important element in the entire network as it alone regulates the design in achieving tri-band functionality and also aids in the enhancement of the frequency-ratio. It is an arbitrary, yet wisely chosen impedance value, that acts as a link between the two dual-band impedance transformers of distinct electrical lengths. The value Z_V should be chosen such that the transmission line parameters of the dual-band transformers remain within the limits of 30-150 Ω. If seen from section-B, the Z_V is essentially an equivalent impedance for the rest of the network. The idea in the design of transformer is to ensure that that the value of the Virtual Impedance, Z_V, equals the impedance value of the network to the right of it (i.e., section-A and FDCL combined in this case).

5.4 Design flow

The flow chart in Fig. 5.5 depicts the summary of the design procedure based on the developed mathematical formulations. It is pertinent to note that we have also used optimization using Keysight ADS optimizer to provide good performance at the desired frequencies of interest. The optimization variables usually chosen are the width of the transmission lines that essentially control the line impedances. Moreover, critical line lengths are also chosen to adjust the overall electrical length.

5.5 Case Studies and Design Example

As an example, we have considered the output impedance of a 10W GaN HEMT from Wolfspeed as FDCL to validate the presented tri-band impedance matching concept. The loads at the three chosen frequencies are $Z_{L1} = (22.89 - j6.64)\Omega$ @ 1.8GHz, $Z_{L2} = (21.80 - j5.45)\Omega$ @ 2.4GHz, and $Z_{L3} = (17.66 + j9.89)\Omega$ @ 5.8GHz, and is illustrated in Fig. 5.6. Simulations have been carried out to understand the boundary conditions of each design variables and lastly we have also fabricated a prototype on Rogers RO5880 substrate to substantiate the presented theory and claims.

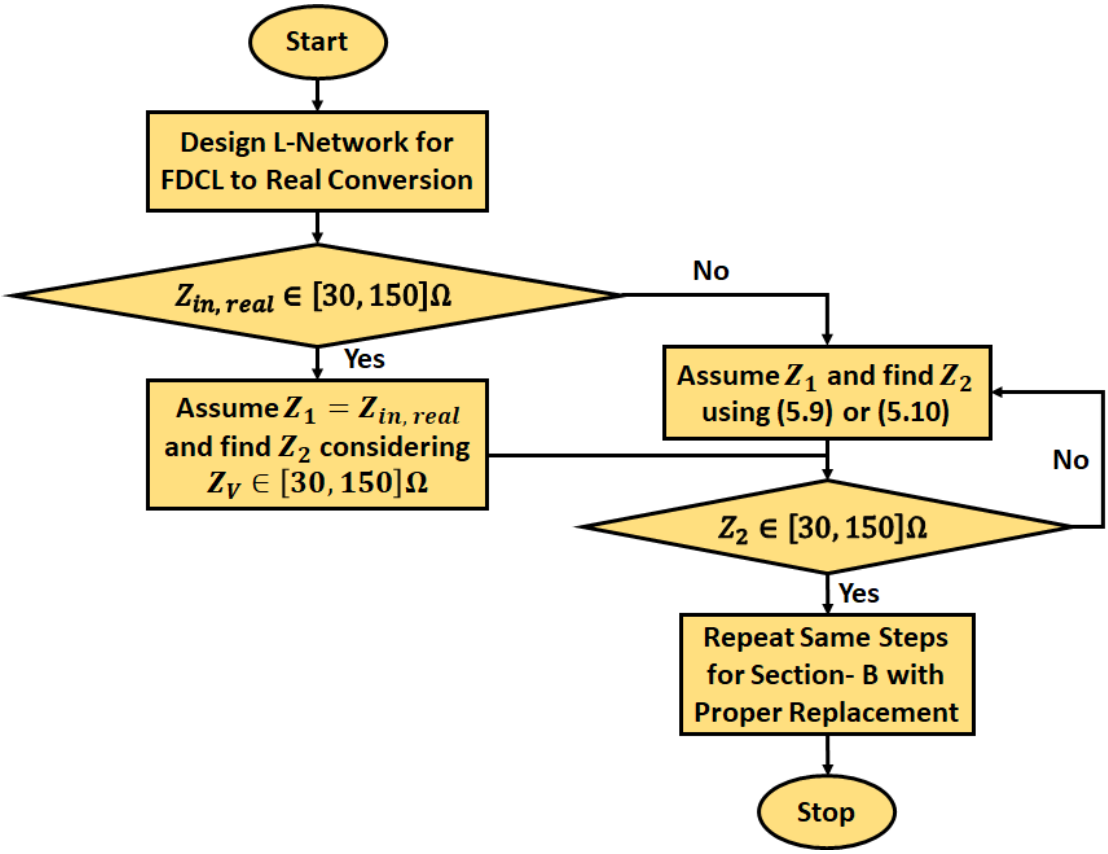

Figure 5.5: The Tri-Band Impedance Transformer Design Flow

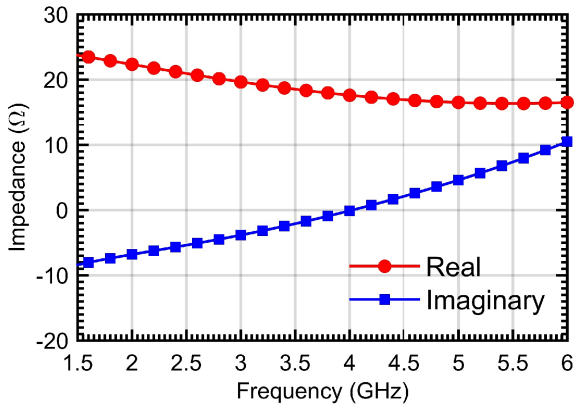

Figure 5.6: The Output Impedance of the 10W Wolfspeed GaN HEMT

Table 5.1: Design parameters for the three sections

FDCL to real	Section-A	Section-B
$Z_a = 53.89\ \Omega$	$Z_1 = 60\ \Omega$	$Z_3 = 40\Omega$
$Z_b = 53.89\ \Omega$	$Z_2 = 48.07\Omega$	$Z_4 = 61.03\Omega$
$\theta_a = 65.43°$	$Z_{SC} = 82.92\Omega$	$Z_{OC} = 68.81\Omega$
$\theta_b = 2.43°$	$\theta_1 = 85.26°$	$\theta_2 = 154.28°$
———————	$r_{31} = f_3/f_1 = 3.22$	$r_{21} = f_2/f_1 = 1.33$

We have obtained the values of the transmission line parameters for each section, provided in Table-5.1, by using the design expressions from last section. The design plots, for the chosen FDCL, are given in Figs. 5.7-5.10. Here, the virtual impedance, Z_V, is the key for tri-band matching and, hence, a prudent choice of Z_V is essential to obtain a physically possible design along with enhanced frequency ratios. The choice of Z_V in any design is regulated by the value of $Z_{in,real}$ obtained at the end of first design stage. The dependence of Z_V on $Z_{in,real}$ is depicted in Fig. 5.7. This implies that for lower $Z_{in,real}$, Z_V should be chosen high enough to maintain the realizability of Z_2 and Z_4 simultaneously as can be deduced from Figs. 5.7 and 5.8.

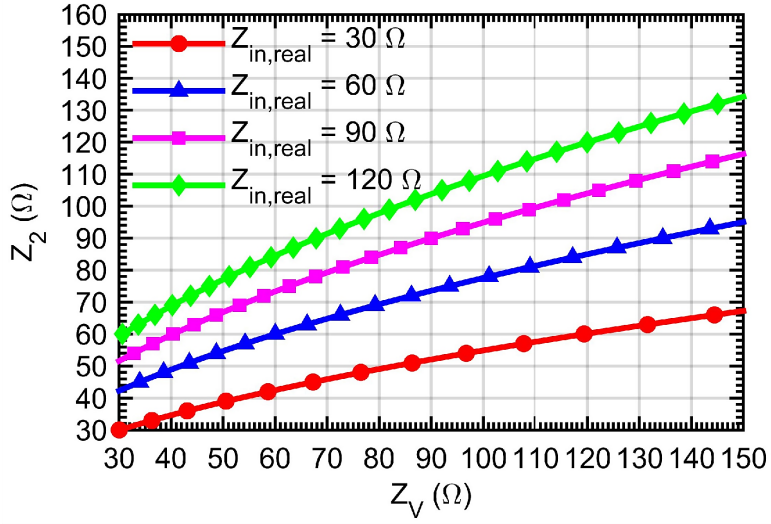

Figure 5.7: The Variation in Z_V for Different Values of $Z_{in,real}$. For Realizable Design, Z_V and hence, $Z_2 \in$ [30-150]Ω, with the Assumption that $Z_1 = Z_{in,real}$

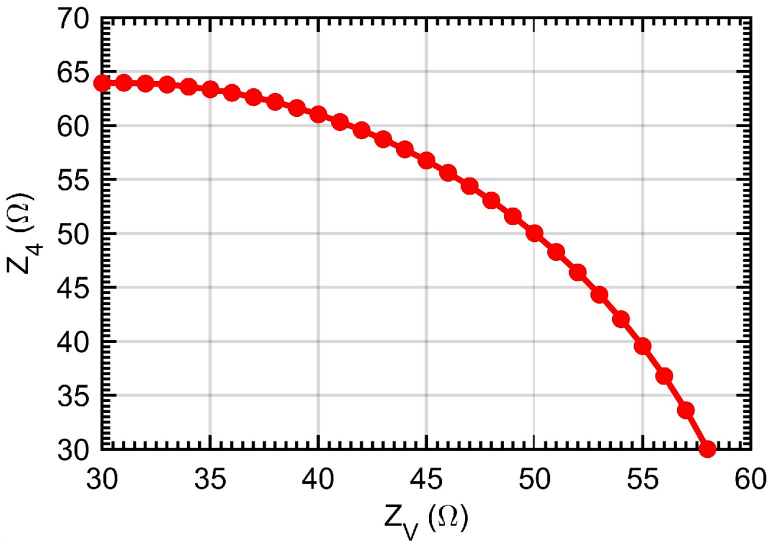

Figure 5.8: Variation of Z_4 with Z_V for a 50Ω source

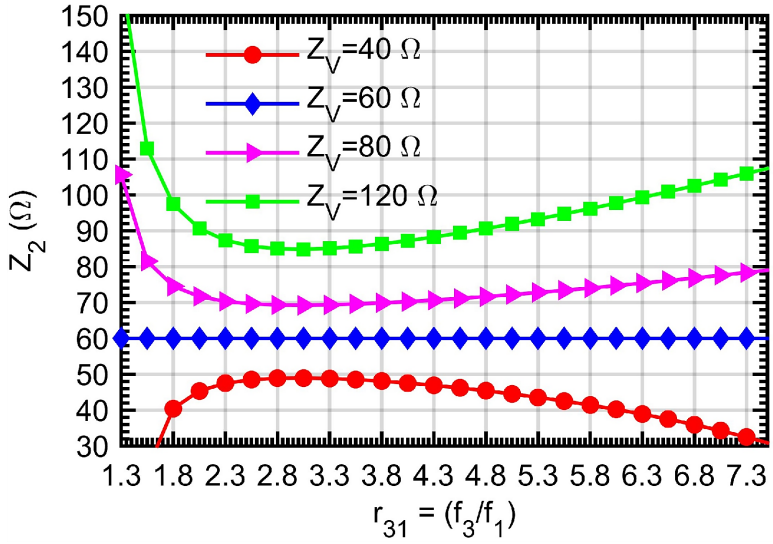

Figure 5.9: The Dependence of Frequency Ratio r_{31} on Z_V

Another important contribution of the presented concept is its ability to enhance both the frequency ratios r_{31} and r_{21} as can be seen in Figs. 5.9 and 5.10. We can obtain the realizable values of Z_2 for different values of Z_V and the corresponding range of frequency ratio r_{31} from Fig. 5.9. Similarly, the achievable values of r_{21} for variable Z_V and realizable values of Z_4 can be deduced from Fig 5.10. We can infer that the choice of Z_V in the moderate range of (40-60Ω) provides all the design parameters that are physically fabricable and the desired frequency ratios can be attained. For validation, we have designed the prototype, in Fig. 5.11, by taking $Z_V = 40\Omega$. The simulated and the measured responses in Fig. 5.12 and Table-5.2 show a good agreement. It is observed that there is a slight anomaly in the measured and simulated values. Especially around 4GHz, there is a minor resonant peak of around -5dB. This is a result of real-time tuning during measurements and could be attributed to fabrication tolerance in the FDCL. Other factors contributing to these minor variations include connector and cable losses (see Appendix B) incurred during the measurement process. However, the value is quite small (-5dB) and can be ignored for any practical considerations.

Table 5.2: Simulation & Measured Results

Parameters	**Simulation Results**			**Measured Results**		
Frequency (GHz)	1.8	2.4	5.8	1.79	2.42	5.83
S_{11} (dB)	-35.00	-32.31	-29.97	-31.86	-30.77	-27.75

A comparison of the proposed technique with the existing state-of-the-art on multi-frequency impedance matching is presented in Table-5.3. Overall, it is apparent that the

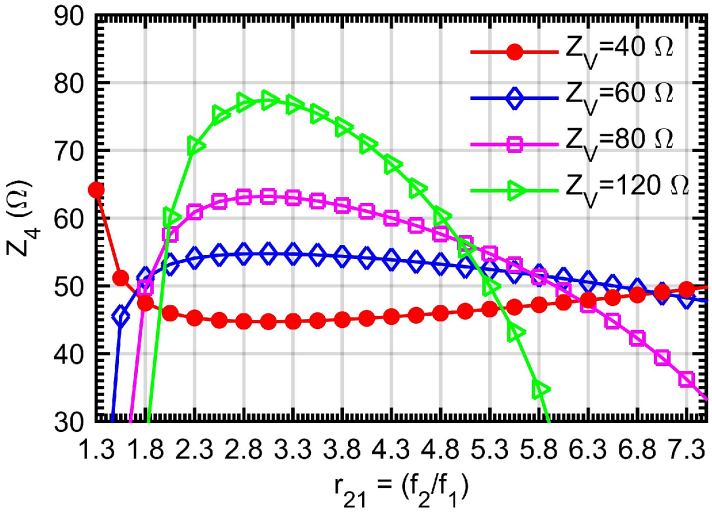

Figure 5.10: The Dependence of Frequency Ratio r_{21} on Z_V

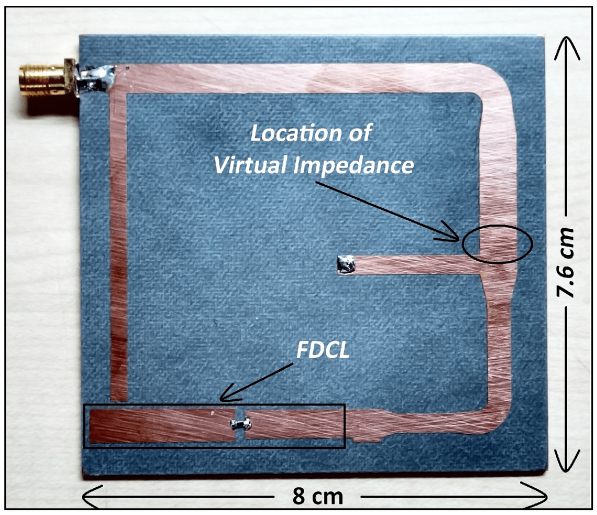

Figure 5.11: The Fabricated Prototype of the Proposed Impedance Transformer

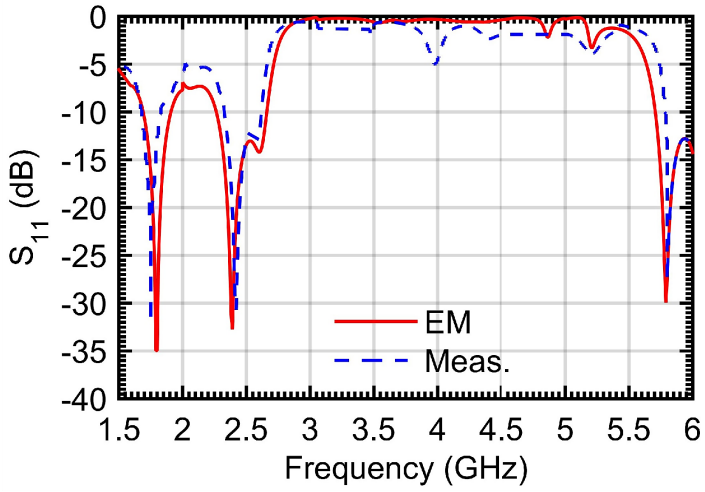

Figure 5.12: EM Simulation vs Measured Results

proposed technique advances the state-of-the-art significantly.

Table 5.3: Comparison with the Current State-of-the-Art

Ref., Year	Venue	Operation	Method used	Load type	Frequency ratios
[32], (2017)	TCAS-II	dual-band	load healer	FDCL	$r_{21} = 2.5$
[35], (2017)	MWCL	dual-band	three shunt stubs	FDCL	$r_{21} = 1.67$
[70], (2013)	JPIER	tri-band	stubbed coupled-lines	real	$r_{31} = 3.55, r_{21} = 2$
[113], (2016)	MWCL	tri-band	dual to tri-band transformation	complex	$r_{31} = 2.5, r_{21} = 2$
This work	————	**tri-band**	**Virtual Impedance**	**FDCL**	**extending 7.3 and beyond**

5.6 The Impedance Bridge: An Analytical Study

Another variant of a virtual impedance is implemented with an impedance bridge. The concept, though similar, differs from the former by a quarter-wave line that joins two APCL-based dual-band transformers. The schematic representation of the proposed design is presented in Fig. 5.13. Sections- A and B consist of two meandered APCLs. A $\lambda/4$ transmission line links the two sections using two variable Virtual Impedances- Z_{V1} and Z_{V2}. The load Z_L is matched to Z_{V1} at f_3 and f_2 by Section- A and Z_{V2} is matched to Z_S at f_2 and f_1. The match between Z_{V1} and Z_{V2} is obtained using the Impedance Bridge at f_2- the frequency common to both sections.

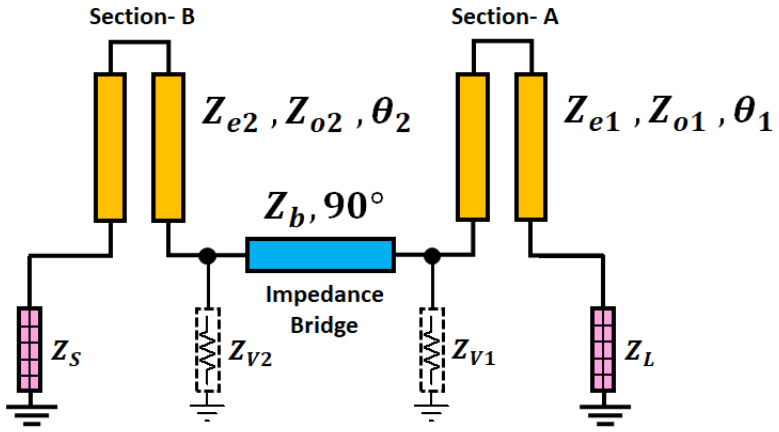

Figure 5.13: Schematic of the Proposed Tri-Band Impedance Transformer

The advantage lies in the fact that each meandered coupled line, in their all-pass configuration present an extra design variable that enhances design flexibility. Moreover, availability of two virtual impedances provide a design space for extending frequency and impedance transformation ratios.

5.7 Mathematical Formulation

The schematic represented in Fig. 5.13 can be decomposed into three blocks, namely Section-A, Section-B and the Impedance Bridge.

5.7.1 Section-A: The Dual-Band Transformer

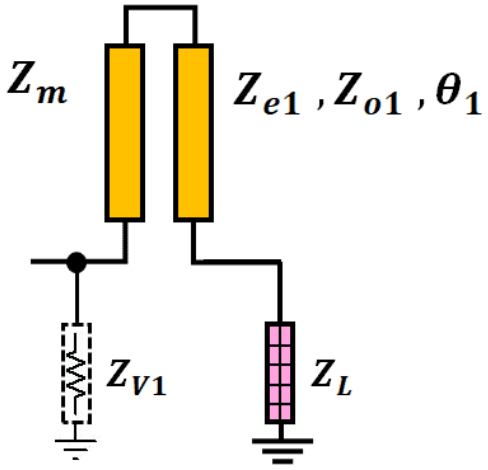

Figure 5.14: Dual-Band Matching using a Meandered APCL

Fig. 5.14 illustrates a meandered APCL, used to match the load, Z_L to a wisely selected value ($Z_{V1} \in [30 - 150]\Omega$) of Virtual Impedance Z_{V1}. This is for the physical realizability of the coupled-line TL-section. The choice of Z_{V1} is very crucial for the frequency ratio $r_{32} = f_3/f_2$ of the network. For a $\lambda/4$ meandered APCL section,

$$Z_m = \sqrt{Z_L Z_{V1}} \tag{5.14}$$

Now, the design parameters, Z_{e1} and Z_{o1} can be obtained as

$$Z_{e1} = Z_m \tan\theta_1 \tag{5.15a}$$

$$Z_{o1} = Z_m / \tan\theta_1 \tag{5.15b}$$

where, Z_{e1} and Z_{o1} are the even and odd arm impedances of the meandered line respectively and θ_1 is the electrical length corresponding to Section-A, given by

$$\theta_1 = \frac{k\pi}{1 + r_{32}} \tag{5.16}$$

where $k \in [1, 2, 3...]$ and $r_{32} = f_3/f_2$.

Substituting (5.14) and (5.16) in (5.15a), we obtain

$$Z_{e1} = \sqrt{Z_L Z_{V1}} \tan \frac{\pi}{1 + r_{32}} \tag{5.17}$$

It is evident from (5.17) that the frequency ratio r_{32} is related to Z_{V1} and they together determine the design parameter Z_{e1}. Fig. 5.15 describes the dependency, thus indicating that a proper choice of Z_{V1} can extend the frequency ratio r_{32} till 10.

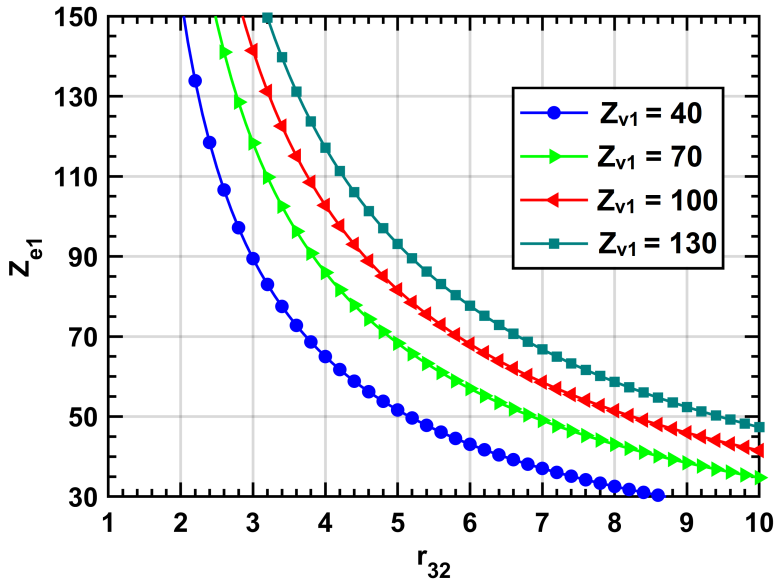

Figure 5.15: Extension of Frequency Ratio r_{32} for Various Virtual Impedances Z_{V1}. All Units of Impedances are in Ohm (Ω)

The selection of a proper Z_{V1} is also necessary for enhancement of the impedance transformation ratio. Defined as the ratio of the load to the source impedance of an impedance transforming network, it determines the maximum limit of impedance that can be scaled using the network. Generally, for a standalone matching network, the source impedance is considered to be a conventional 50Ω resistance, and hence, the transformation ratio $z_t (= Z_L/Z_S)$ can be expressed as:

$$z_t = Z_L/Z_S = Z_{e1}^2/Z_{V1} \tan\theta_1 \tag{5.18}$$

Considering a fixed value of Z_{e1} as 50Ω, Fig. 5.16 illustrates the behavior of both the impedance and the frequency transformation ratios for different values of virtual impedance Z_{V1}. We can see from Figs. 5.15 and 5.16 that obtaining an enhanced frequency and impedance transformation ratio at the same time is impractical. This is because of the fact that a relatively higher Z_{V1} yields an extended frequency ratio but at reduced transformation ratio. Conversely, a lower Z_{V1} increases the impedance transformation ratio at the cost of frequency ratio. Thus we can see that a trade-off has to be made between the performance parameters.

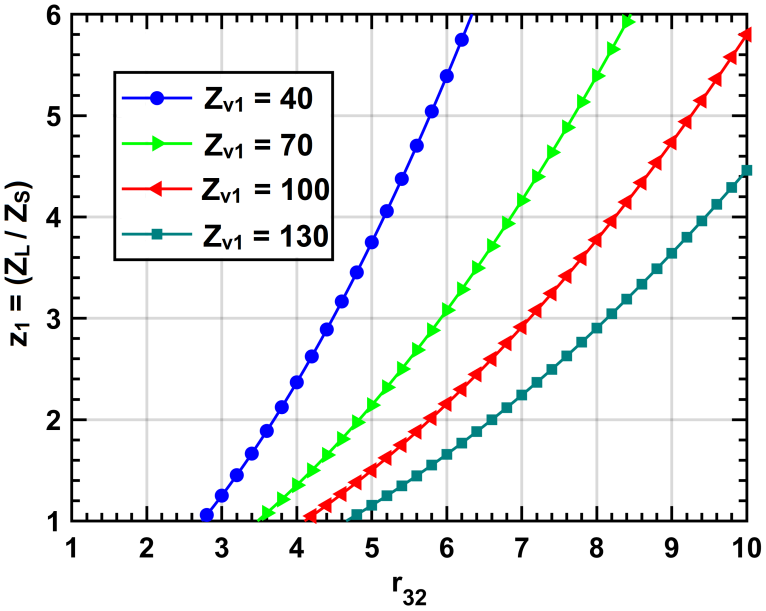

Figure 5.16: Behavior of Both Frequency Ratio and Impedance Transformation Ratio for Various Virtual Impedances. All Impedance Units are in Ohm (Ω)

5.7.2 Section-B: Another Dual-Band Transformer

Section-B is the replica of Section-A, the same being a meandered coupled-line dual-band impedance transforming network, obtaining match between the virtual impedance Z_{V2} and the source Z_S at f_2 and f_1. The design equations for this section are similar to that of section-A with proper replacements of design variables. All the design analysis remains the same. It is intuitive that with a proper selection of Z_{V2}, frequency ratio $r_{21} = f_2/f_1$ can be enhanced. The transformation ratio cannot be defined at this point of the circuit because Z_{V2} is not a physical circuit parameter.

5.7.3 The Impedance Bridge

This is a simple $\lambda/4$ transformer that matches the virtual impedances Z_{V1} and Z_{V2} at the common frequency f_2, as depicted in Fig. 5.17.

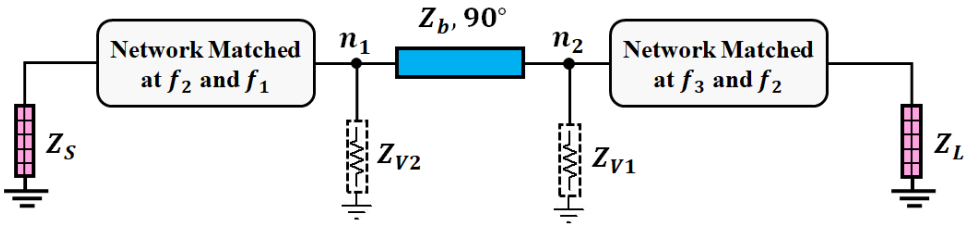

Figure 5.17: Impedance Bridging with a $\lambda/4$ Transformer at Common Frequency f_2

Depending upon the chosen values of Z_{V1} and Z_{V2}, the bridge can be balanced ($Z_{V1} = Z_{V2}$) or unbalanced ($Z_{V1} \neq Z_{V2}$). The design parameter for the bridge is thus $Z_b = \sqrt{Z_{V1}Z_{V2}}$ with an electrical length of $90°$. The significance of the bridge in the entire design is the availability of two free variables Z_{V1} and Z_{V2}, which would otherwise not have been present. Moreover it acts as a conduit between sections-A and B, linking them up on basis of f_2. It must be noted that while connecting the two dual-band transformers at distinctly different frequencies f_3 and f_1, f_2 being the reference, ordinarily there are subsequent losses at f_1 and f_3 due to the unequal even and odd mode velocities of the coupled lines. We have managed this by optimization using CAD tools like Keysight ADS optimizer. The variables chosen for the optimization process are the separation between the coupled-lines and the length of the bridge Z_b.

5.8 Simulation and Measurement

Based on the proposed theory, we have fabricated a prototype on RO4350 that operates on three arbitrary frequencies of 1GHz, 2GHz and 5GHz. A balanced bridge has been demonstrated with $Z_{V1} = Z_{V2} = 80\Omega$. We considered a 100Ω SMD resistor as a real load in the example. The design parameters are listed in Table-5.4. Apparently, the parameters are well within the fabricable limits and a symmetrical design can be obtained for prototyping, as illustrated in Fig. 5.18.

Fig. 5.19 and Table-5.5 depicts a comparison between the EM simulated and the mea-

Table 5.4: Design Parameters for the Prototype

Section-A	**Section-B**
Z_{e1} = 112.16	Z_{e2} = 109.54
Z_{o1} = 71.32	Z_{o2} = 36.51
θ_1 = 51..43	θ_2 = 60
$r_{32} = f_3/f_2$ = 2.5	$r_{21} = f_2/f_1$ = 2.0

*$Z_{V1} = Z_{V2} = 80\Omega$; Bridge Impedance $Z_b = 80\Omega$

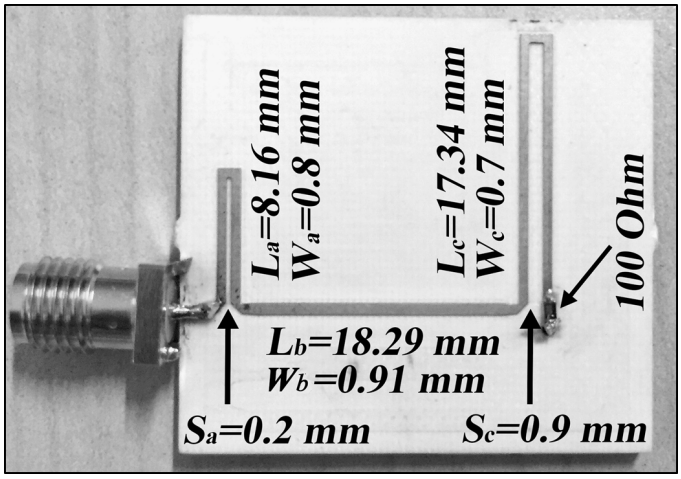

Figure 5.18: The Fabricated Prototype Along with Dimensions

sured results, showing good agreement between the simulated and measured results.

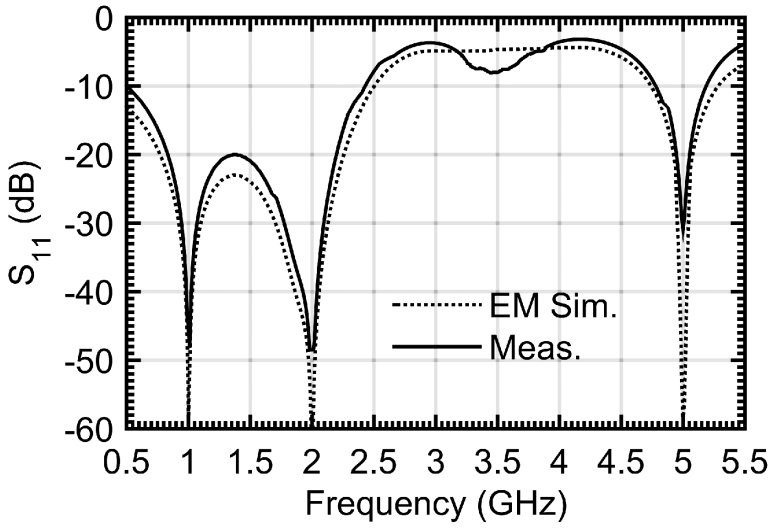

Figure 5.19: EM Simulation vs Measured Results

Table 5.5: Simulation & measured results

Parameters	**Simulation Results**			**Measured Results**		
Frequency (GHz)	1.00	2.00	5.00	1.00	2.01	5.00
S_{11} (dB)	-58.83	-60.01	-59.92	-48.76	-49.37	-32.01

Table 5.6: Comparison with a Few State-of-the-Art Designs

Ref., Year	Journal	Operation	Method used	Imp. Trans. ratio	Frequency ratios
[32], (2017)	TCAS-II	dual-band	load healer	$< 2.0^*$	$r_{21} = 2.5$
[35], (2017)	MWCL	dual-band	three shunt stubs	2.0^*	$r_{21} = 1.67$
[70], (2013)	JPIER	tri-band	stubbed coupling line	2.0	$r_{31} = 3.55, r_{21} = 2.0$
[113], (2016)	MWCL	tri-band	dual to tri-band transformation	0.4	$r_{31} = 2.5, r_{21} = 2.0$
This work	————	**tri-band**	**Impedance Bridge**	**extendable beyond 5.5**	**extendable beyond 10**

*For FDCL and Complex Loads, the magnitude value of load impedance has been considered

5.9 A Versatile Tri-Frequency Wilkinson Power Divider

We have seen that the literature is replete with dual-band architectures and has been deeply explored as of now. With tri-band designs entering the race, interests have inclined towards design of simple, yet effective tri-band Wilkinson Power Dividers. This domain has not yet been fully explored yet some light has been shed over the past few years. Studying the literature we have made some observations and the most common concerns of the reported tri-band WPDs could be summarised as:

- Lack of a Generic Model: Existing Tri-Band WPD design schemes are specific in terms of operating principle and cannot be reconfigured according to the application served. The design strategies discussed do not exhibit a generalized design flow irrespective of its constituent blocks.

- Use of Reactive Lumped Elements: Some existing architectures [57, 60, 67], used lumped reactive components as a part of their design. However, the parasitics present in packaged lumped elements limit their operation at high frequencies. It makes them unsuitable for a broad range of frequencies.

- Complicated Design Procedure: Designs like [70, 147, 148] are complicated and require intensive mathematical rigor to arrive at design equations. A simple step-by-step design procedure is lacking for many existing designs in the literature.

This section of the chapter proposes a generic design scheme of a tri-band WPD, reconfigurable by changing its constituent dual-band impedance transformer. We have achieved tri-band matching by extending the dual band-behavior of a transformer to operate at the third frequency. This is facilitated by addition of an extra transmission line and one (or two) set of open-short stub pairs. Two isolation resistors achieve port isolation at all the three frequencies of operation.

5.10 The Proposed Tri-Band WPD

The schematic of the proposed tri-band WPD is illustrated in Fig. 5.20. The dual-band transformer represented by the block may be chosen from a broad variety of existing designs depending upon the applications to be served. As an example, we can choose the slow-wave-structure based dual-band transformer [53] for a wider bandwith, while a coupled-line based design can be utilized for DC isolation. In this work, firstly, we have considered a simple L-network dual-band transformer, followed by a coupled-line section to demonstrate the versatility of the design scheme. The next section, denoted by dotted boxes, is a tri-band extender consisting of a transmission line of characteristic impedance equal to the impedance of the output port and an open-short circuit stub in parallel. The optional open-short stub combination (dotted) might be necessary depending on certain conditions described later in the article. The function of this block is to extend the dual-band operation to tri-band without disturbing the matching at the other two frequencies. We have performed even and odd mode half-circuit analysis to determine the design parameters of the circuit.

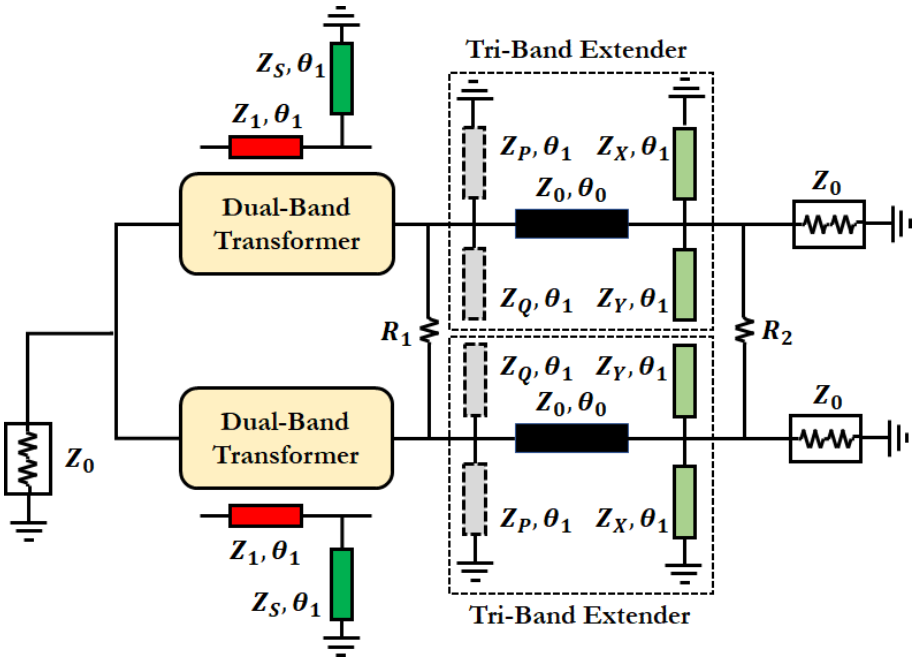

Figure 5.20: General Architecture of the Proposed Tri-Band WPD

5.10.1 Even Mode Analysis:

The even mode-circuit of the proposed WPD is depicted in Fig. 5.21. Here we have considered an L-network consisting of a transmission line $[Z_1, \theta_1]$ and a stub $[Z_S, \theta_1]$ for dual-band operation. The admittance Y_{in1}, given by (5.19), seen after the transmission line $[Z_1, \theta_1]$ can be deduced using standard transmission line formulation. For a short stub $[Z_S, \theta_1]$, the admittance is expressed in (5.20). The impedance transformation from $2Z_0$ to Z_0 at two frequencies f_1 and f_2 is essentially related through $Y_{in,1}|_{f_1,f_2} + Y_S|_{f_1,f_2} = Y_0|_{f_1,f_2}$ and given by (5.21).

$$Y_{in,1} = \frac{1}{Z_1}\frac{Z_1 + 2jZ_0\tan\theta_1}{2Z_0 + jZ_1\tan\theta_1} \tag{5.19}$$

$$Y_S|_{short} = -\frac{j}{Z_S\tan\theta_1} \tag{5.20}$$

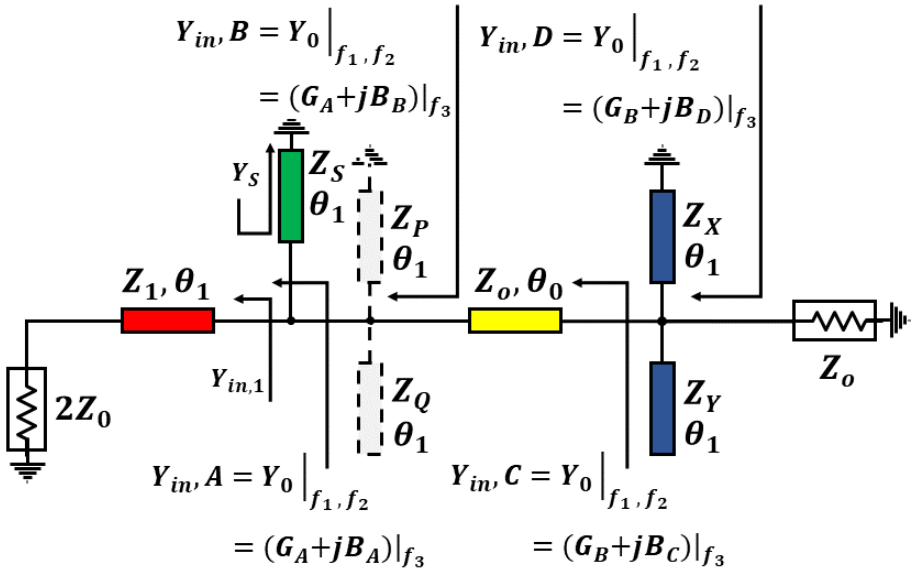

Figure 5.21: Even Mode Half-Circuit

$$\frac{1}{Z_1}\frac{Z_1 + 2jZ_0\tan\theta_1}{2Z_0 + jZ_1\tan\theta_1} + Y_S|_{short} = \frac{1}{Z_0} \tag{5.21}$$

Separating real and imaginary parts and solving for Z_1 and Z_S, we obtain (5.22).

$$Z_1 = \frac{\sqrt{2Z_0^2(1 - 2\cos^2\theta_1)}}{\sin\theta_1} \tag{5.22a}$$

$$Z_S = Z_1 \tag{5.22b}$$

For dual-band operation at f_1 and f_2, considering electrical lengths at the respective frequencies to be θ_1 and θ_2, $\theta_1 + \theta_2 = n\pi$, where n is an integer. If $\theta_2 = r\theta_1$, where $r = f_2/f_1$, the expression reduces to $\theta_1 + r\theta_1 = n\pi$, where $n \in [1, 2, 3...]$. Thus, the electrical length for both the transmission line segment and the shorted stub for dual-band L-network is expressed in (5.23).

$$\theta_1 = \frac{n\pi}{1+r} \tag{5.23}$$

After obtaining a matching at f_1 and f_2, it must be noted that the L-network generates a complex value of admittance at the third frequency f_3, denoted by $Y_{in,A}|_{f_3} = (G_A + jB_A)$, expressed by (5.24a) and (5.24b). Here, $m = f_3/f_1$.

$$G_A = \frac{2Z_0(1 + \tan^2 m\theta_1)}{4Z_0^2 + Z_1^2 \tan^2 m\theta_1} \tag{5.24a}$$

$$B_A = \frac{\tan m\theta_1(4Z_0^2 - 2Z_1^2) - 4Z_0^2 \cot m\theta_1}{Z_1(4Z_0^2 + Z_1^2 \tan^2 m\theta_1)} \tag{5.24b}$$

To achieve tri-band matching, it must be ensured that the matching at f_1 and f_2 is not disturbed and this is facilitated by maintaining $Y_{in,A}|_{f_1,f_2} = Y_{in,B}|_{f_1,f_2} = Y_{in,C}|_{f_1,f_2} = Y_{in,D}|_{f_1,f_2} = 1/Z_0$ as shown in Fig. 5.21 [113]. The transmission line segment after the L-network does not disturb the matching at f_1 and f_2 due to its characteristic impedance being same as the port impedance, i.e. Z_0. The open-short circuit stub combinations $[Z_P, Z_Q, \theta_1]$ and $[Z_X, Z_Y, \theta_1]$ provide infinite impedances, which can be further simplified to obtain the stub parameters given in (5.25a) and (5.25b). The open-short circuit stubs, $[Z_P, Z_Q, \theta_1]$, transform the admittance to a new value of $Y_{in,B}|_{f_3} = (G_A + jB_B)$, the susceptance of which is given in (5.26) while maintaining the match at the frequencies of f_1 and f_2. Furthermore, the cascading of the transmission line $[Z_0, \theta_0]$ maintains the the match at the frequencies of f_1 and f_2 while transforming admittance at f_3 to a new value $Y_{in,C}|_{f_3} = G_B + jB_C$. Here, the terms G_B and B_C are given by (5.27a) and (5.27b) respectively.

$$Z_Q = Z_P \tan^2 \theta_1 \tag{5.25a}$$

$$Z_Y = Z_X \tan^2 \theta_1 \tag{5.25b}$$

$$B_B = B_A + Y_Q(\tan m\theta_1 - \tan^2\theta_1 \cot m\theta_1) \tag{5.26}$$

$$G_B = \frac{G_A(1+\tan^2 m\theta_0)}{(1 - Z_0 B_B \tan m\theta_0)^2 + (Z_0 G_A \tan m\theta_0)^2} \tag{5.27a}$$

$$B_C = \frac{(1 - Z_0 B_B \tan m\theta_0)(Z_0 B_B + \tan m\theta_0) - Z_0^2 G_A^2 \tan m\theta_0}{Z_0[(1 - Z_0 B_B \tan m\theta_0)^2 + (Z_0 G_A \tan m\theta_0)^2]} \tag{5.27b}$$

The open-short circuit stub combination $[Z_X, Z_Y, \theta_1]$ transforms the admittance into $Y_{in,D}|_{f_3} = G_B + jB_D$, the susceptance of which is given in (5.28).

$$B_D = B_C + Y_Y(\tan m\theta_1 - \tan^2\theta_1 \cot m\theta_1) \tag{5.28}$$

To achieve matching at f_3, following conditions in (5.29) need to be satisfied. Subsequently, (5.27a) and (5.29a) can be solved simultaneously to obtain expression for θ_0 given in (5.32). Furthermore, (5.28) and (5.29) can be simplified to deduce the expression for Z_Y given in (5.30). Similarly, the parameter Z_X can be obtained by simplifying (5.23), (5.25b) and (5.30). The remaining parameters Z_Q given in (5.31), and Z_P are obtained by simplifying (5.23), (5.25a), and (5.26).

$$G_B = \frac{1}{Z_0} \tag{5.29a}$$

$$B_D = 0 \tag{5.29b}$$

$$Z_Y = \frac{\tan^2\theta_1 \cot m\theta_1 - \tan m\theta_1}{B_C} \tag{5.30}$$

$$Z_Q = \frac{\tan m\theta_1 - \tan^2\theta_1 \cot m\theta_1}{B_B - B_A} \tag{5.31}$$

To reiterate the fact that in applications where broader bandwidth per band is a requirement, the dual-band transformer marked with dotted lines in Fig. 5.20 should be chosen widely. As an example, utilizing all-pass coupled-line based slow wave structures [53] can be an option to increase the bandwidth at each desired frequency band.

$$\theta_0 = \frac{1}{m}\tan^{-1}\frac{Z_0 B_B \pm \sqrt{(Z_0 B_B)^2 - (1 - Z_0 G_A)(Z_0^2 B_B^2 + Z_0^2 G_A^2 - Z_0 G_A)}}{(Z_0^2 B_B^2 + Z_0^2 G_A^2 - Z_0 G_A)} \tag{5.32}$$

5.10.2 Odd Mode Analysis:

Once the design parameters of L-network and the open-short circuit stub combinations are determined, the next step is to obtain the values of the isolation resistors R_1 and R_2 using the odd-mode half-circuit, Fig. 5.22, of the proposed WPD. It must be noted that to obtain isolation at three frequencies, the impedance conditions must be satisfied concurrently at the three frequencies of interest. The impedances seen after each section of transmission lines and stubs are given in (5.33) through (5.36).

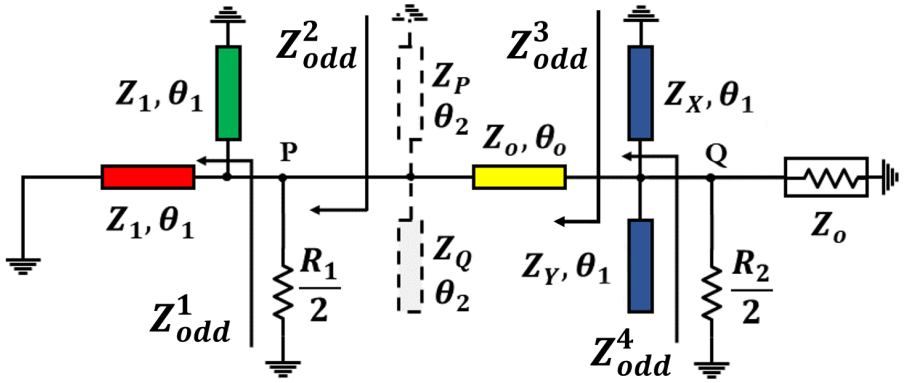

Figure 5.22: Odd-Mode Half-Circuit

$$Z^1_{odd} = j(\frac{Z_1}{2})\tan\theta_1 \tag{5.33}$$

$$Z^2_{odd} = Z^1_{odd}||(\frac{R_1}{2}) \tag{5.34a}$$

$$= \frac{Z^1_{odd}\cdot\frac{R_1}{2}}{Z^1_{odd}+\frac{R_1}{2}} \tag{5.34b}$$

Considering the absence of the open-short stub pair Z_P, Z_Q for mathematical simplicity,

$$Z^3_{odd} = Z_0\frac{Z^2_{odd} + jZ_0\tan\theta_0}{Z_0 + jZ_{odd}\tan\theta_0} \tag{5.35}$$

$$Z^4_{odd} = Z^3_{odd}||(jZ_X\tan\theta_1)||(-jZ_Y\cot\theta_1) \tag{5.36}$$

For perfect port isolation, the condition in (5.37) needs to be satisfied.

$$Z^4_{odd}||(\frac{R_2}{2}) = Z_0 \tag{5.37}$$

By solving (5.37) and separating the real and imaginary part, the resistor values can

$$R_1 = 2Z_0 \tag{5.38a}$$

$$R_2 = \frac{4Z_0(1+\tan^2 m\theta_0)}{2Z_0^2[(1-Z_0B_B\tan m\theta_0)^2+(Z_0G_A\tan m\theta_0)^2]-2(1+\tan^2 m\theta_0)} \tag{5.38b}$$

be obtained in (5.38). The simplification of (5.37) has been carried out in MATLAB and the results are directly presented here. It is worth noting that in cases where the stubs $[Z_P, Z_Q]$ are needed, the impedances provided by them must be considered in the transformation equality.

5.11 Design Examples and Experimental Validation

To demonstrate the effectiveness of the proposed design scheme, we have considered two design examples operating at different sets of frequencies, one of which is fabricated. The cases have been implemented in Keysight Advanced Design System, a full wave solver, that ensures easy schematic to layout and EM simulations in a user-friendly GUI environment.

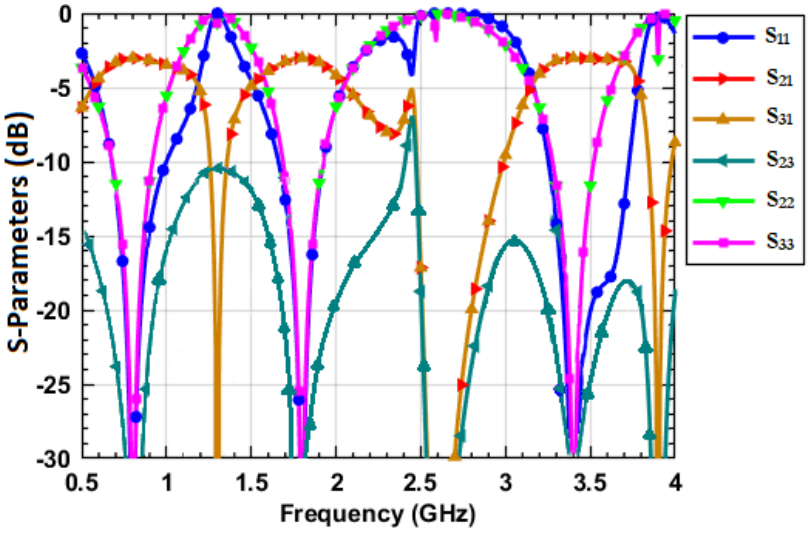

Figure 5.23: WPD Designed at 0.8GHz, 1.8GHz and 3.4GHz; $Z_1 = Z_S = 51.16\Omega, Z_0 = 50\Omega, \theta_0 = 8.7°\theta_1 = 55.38°, Z_P = 47.64\Omega, Z_Q = 100\Omega, Z_X = 74.64\Omega, Z_Y = 156.67\Omega, R_1 = 100\Omega, R_2 = 25\Omega$ (Optimized)

It can be seen in Fig. 5.23 that perfect matching is obtained at all the three desired frequencies. The equal power division, i.e. $S_{21} = S_{31}$, occurs at both the output ports as is evident from these figures. The isolation between the output ports, i.e. S_{23}, is also very good as can be deduced from these plots. Now, in order to demonstrate the

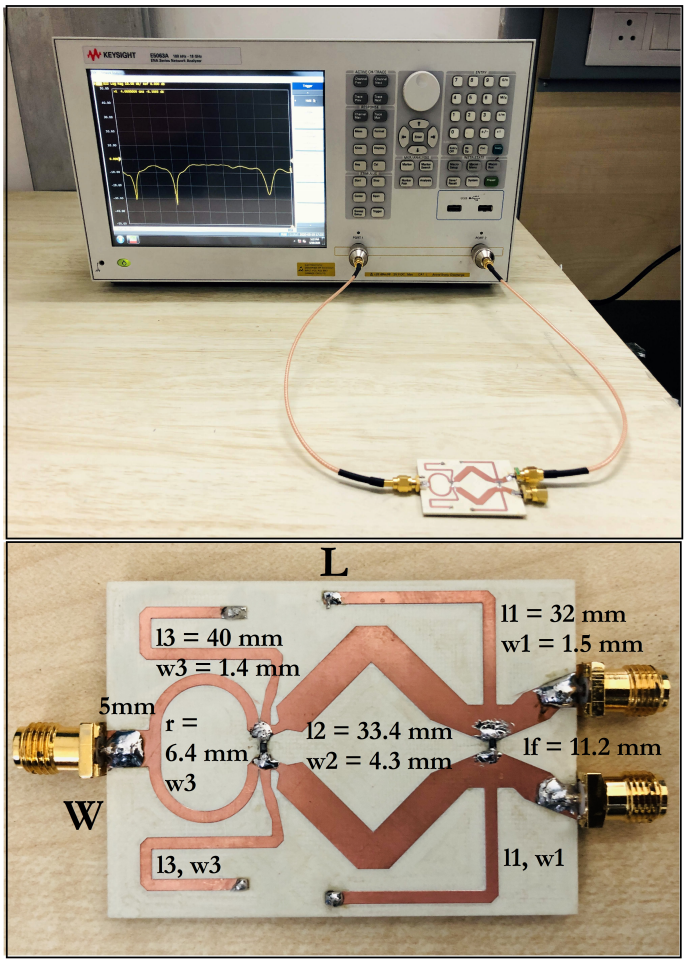

Figure 5.24: The Measurement Setup (top) and the Fabricated Prototype (bottom). L = $0.17\lambda_g$; W = $0.12\lambda_g$

successful operation of the proposed design experimentally, we have realized one of the cases on RO4350B ($\epsilon_r = 3.66$, 1.52mm thickness, 1.0oz Cu) substrate and carried out the measurement as shown in Fig. 5.24. It must be noted that the prototype layout has been simplified with reduced stub count by combining the susceptances generated by the open and short stubs. The measured and the simulated results are illustrated in Figs. 5.25. It is evident that excellent impedance matching at all the ports is obtained at the three desired frequencies of interest. Furthermore, a good power division is also achieved as can be inferred from a very similar output power at both the output ports. However, there is some anomaly between the measured and EM simulated results. This can be attributed to the aging of the measurement cables and ports whose performance generally degrade with time. Finally, the measured isolation values of around 40dB at the three design frequencies demonstrate a good isolation behavior between the output ports. At this point it is imperative to note that providing perfect isolation at the third frequency can be challenging with only two isolation resistors. To overcoming this

phenomenon, the optimization for S_{23} is carried out by considering $[\theta_0, \theta_1, Z_X Z_Y]$ as optimization variables with a fair goal of -40dB.

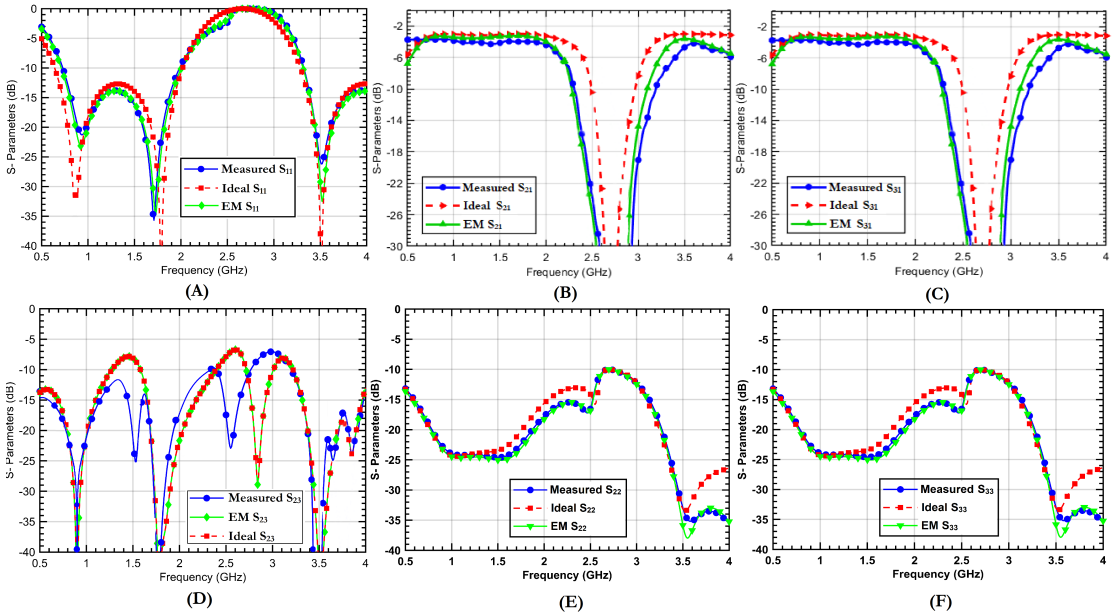

Figure 5.25: Measured, Simulated and EM Results of the Fabricated Prototype

5.12 DC Isolated Tri-Band WPD

There are a number of applications, such as tri-band/multi-band Doherty Power Amplifiers (PA) and Harmonic Injection based PAs, which require WPD with DC isolation capability. This is usually achieved with a DC blocking capacitor before the input matching network stage. However, the use of lumped elements have their own issues and challenges. As per the best of our knowledge, there are no PAs having WPDs with inherent DC isolation feature. The proposed DC isolated WPD design in this section has the potential to fill this gap.

The proposed design of tri-band WPD, in Fig. 5.26, incorporates coupled-line based dual-band matching network and therefore achieves DC isolation behavior. Once again we have carried out the even and odd mode analysis technique to determine the design parameters for the various elements of the circuit.

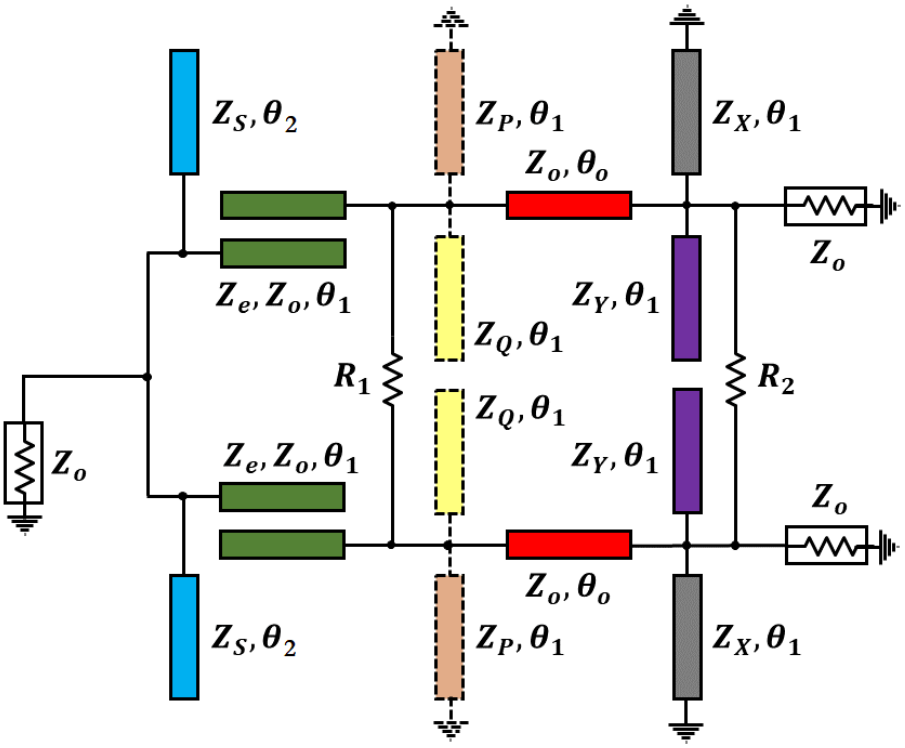

Figure 5.26: DC Isolated Tri-Band WPD

5.12.1 Even-mode Analysis

The even-mode half-circuit of the proposed DC-isolated WPD is illustrated in Fig. 5.27.

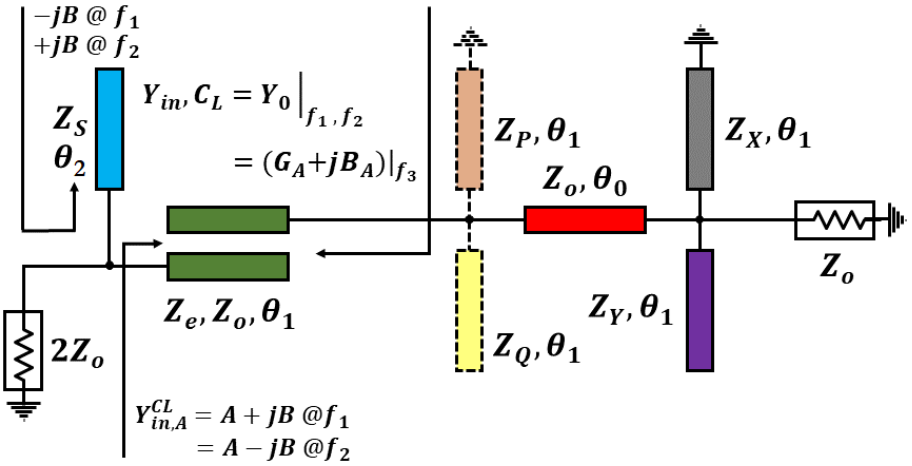

Figure 5.27: Even Mode Half-Circuit

Here, the dual-band coupled line transformer matches the source $(2Z_o)$ with Y_0 at f_1 and f_2 [146]. The coupled-line, $[Z_e, Z_o, \theta_1]$, transforms the impedance looking from right side (here $Y_0@f_1; f_2$) into $Y_{in,A}^{CL}$. Here, $Y_{in,A}^{CL} = (A \pm jB)@f_1, f_2$ respectively, where A and B are given in (5.39a) and (5.39b) respectively and $\sigma = Z_e/Z_o$. The dual-

$$A = \frac{4Z_0(\sigma-1)^2}{4[Z_0^2(\sigma+1)^2 - 2\sigma(\sigma-1)^2Z_o^2]\cos^2\theta_1 + (\sigma-1)^4Z_o^2\sin^2\theta_1 + 16\sigma^2Z_o^2\frac{\cos^4\theta_1}{\sin^2\theta_1}} \tag{5.39a}$$

$$B = \frac{\sigma+1}{Z_o}\frac{[4Z_0^2 - (\sigma-1)^2Z_o^2]\sin 2\theta_1 + 8\sigma Z_o^2\cos^3\theta_1/\sin\theta_1}{4[Z_0^2(\sigma+1)^2 - 2\sigma(\sigma-1)^2Z_o^2]\cos^2\theta_1 + (\sigma-1)^4Z_o^2\sin^2\theta_1 + 16\sigma^2Z_o^2\frac{\cos^4\theta_1}{\sin^2\theta_1}} \tag{5.39b}$$

band stub $[Z_S, \theta_2]$ cancels the imaginary part of this $Y_{in,A}^{CL}$ and provides matching with $2Z_0$. The electrical length θ_2 of the susceptance cancellation stub can be determined using (5.40) in which $p \in [1, 2, 3...)$ is an integer. Depending on the sign of the susceptance (B) generated by the coupled-lines, the stub Z_S, θ_2 can be either a short or an open stub and the impedance Z_S is determined accordingly.

$$\theta_2 = \frac{p\pi}{1+r} \tag{5.40}$$

The coupled-line is designed such that $A = 1/2Z_0$. For a desired value of *r*, θ_1 is obtained from (5.23) and assuming a certain value of Z_o of the coupled-line, the value of σ is obtained from (5.23) and (5.39a). It must be noted that Z_o should be chosen wisely as the coupled-line is realizable only when $\sigma \in [2, 4]$ [70]. Conversely, assuming a value of σ within the prescribed range, Z_o can be obtained using the same equation. Once Z_o (or σ) is obtained, Z_e can be easily determined from the relation $Z_e = \sigma Z_o$. The process is reiterated until the design parameter values are within the fabricable limits of $[20, 160]\Omega$. Once the design parameters of the coupled-line and the stub are determined, the rest can be easily obtained from the equations described earlier.

5.12.2 Odd-mode Analysis

The odd-mode circuit in Fig. 5.28 facilitates the determination of the values of isolation resistors R_1 and R_2. Here, the coupled-line behaves as a short stub with no real part. Impedances seen after every stage of the lines and stubs are presented in (5.41) through (5.44). The remaining circuit after the coupled line section being structurally similar to that described earlier, hence R_1 and R_2 can be obtained from solving (5.45) in MATLAB. Here we have skipped the derivations due to redundancy.

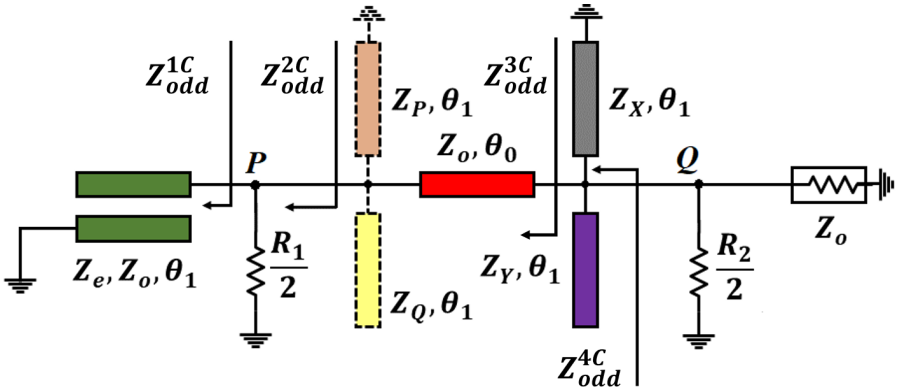

Figure 5.28: Odd Mode Half-Circuit

$$Z_{odd}^{1C} = \frac{\sqrt{Z_e Z_o}\sqrt{(Z_e - Z_o)^2 - (Z_e + Z_o)^2 \cos^2\theta_1}}{(Z_e + Z_o)\sin\theta_1} \tag{5.41}$$

$$Z_{odd}^{2C} = Z_{odd}^{1C} || (\frac{R_1}{2}) \tag{5.42}$$

Considering the absence of the open-short stub pair Z_P, Z_Q for mathematical simplicity,

$$Z_{odd}^{3C} = Z_0 \frac{Z_{odd}^{2C} + jZ_0 \tan\theta_0}{Z_0 + jZ_{odd}\tan\theta_0} \tag{5.43}$$

$$Z_{odd}^{4C} = Z_{odd}^{3C} || (jZ_X \tan\theta_1) || (-jZ_Y \cot\theta_1) \tag{5.44}$$

For perfect port isolation, the condition in (5.45) needs to be satisfied.

$$Z_{odd}^{4C} || (\frac{R_2}{2}) = Z_0 \tag{5.45}$$

Similar to the ordinary WPD discussed in previous sections, it is essential to note that in cases where the stubs Z_P, Z_Q are necessary, the impedances contributed by them should be considered in the calculation.

5.13 DC Isolated WPD: Case-Studies and Examples

Once again we have considered two different sets of frequencies (0.8GHz, 1.8GHz and 3.4GHz) and (1.0GHz, 2.0GHz and 4.0GHz), out of which the later is fabricated. The

detailed performance visualized through S-Parameters of the three cases are depicted in Fig. 5.29 and Figs. 5.31. Apparently the results show perfect tri-band response in terms of matching, power division and isolation. In this case, the power divider consists of coupled lines between the input-output path and hence no input DC component (if any) can get through to the output, thereby proving to be very effective in applications such as tri-band Doherty, Chireix and Balanced PAs.

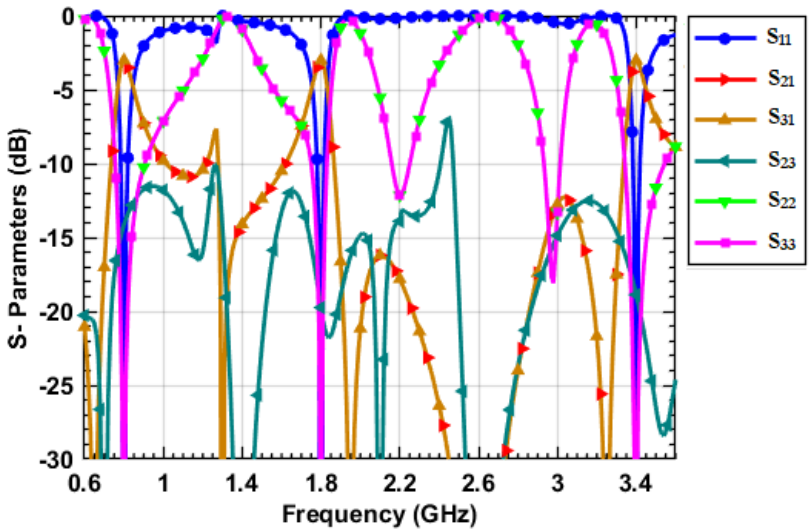

Figure 5.29: WPD Designed at 0.8GHz, 1.8GHz and 3.4GHz; $Z_e = 59\Omega, Z_o = 24.4\Omega, Z_S = 70.5\Omega, \theta_0 = 3.5°, \theta_1 = 55.4°, \theta_2 = 110.7°, Z_X = 56.6\Omega, Z_Y = 118.8\Omega, R_1 = 100\Omega, R_2 = 15\Omega$

We have fabricated a prototype operating at (1.0GHz, 2.0GHz and 4.0GHz) on RO4350B substrate and performed the measurement. The measurement setup and the fabricated prototype of the DC Isolated WPD is illustrated in Fig. 5.30. It is evident from Figs. 5.31 that the fabricated prototype achieves a good impedance matching at the three desired frequencies of interest and divides power equally between the two output ports. It is imperative to note that the DC isolated variant of the tri-band WPD is limited in bandwidth. This is primarily due to the band-limited behavior of coupled lines [146] and design parameter constraints. On the other hand, this finds application in highly selective radio communication circuits. The output port isolations are more than 15dB at the three design frequencies, which are within the industrial standards.

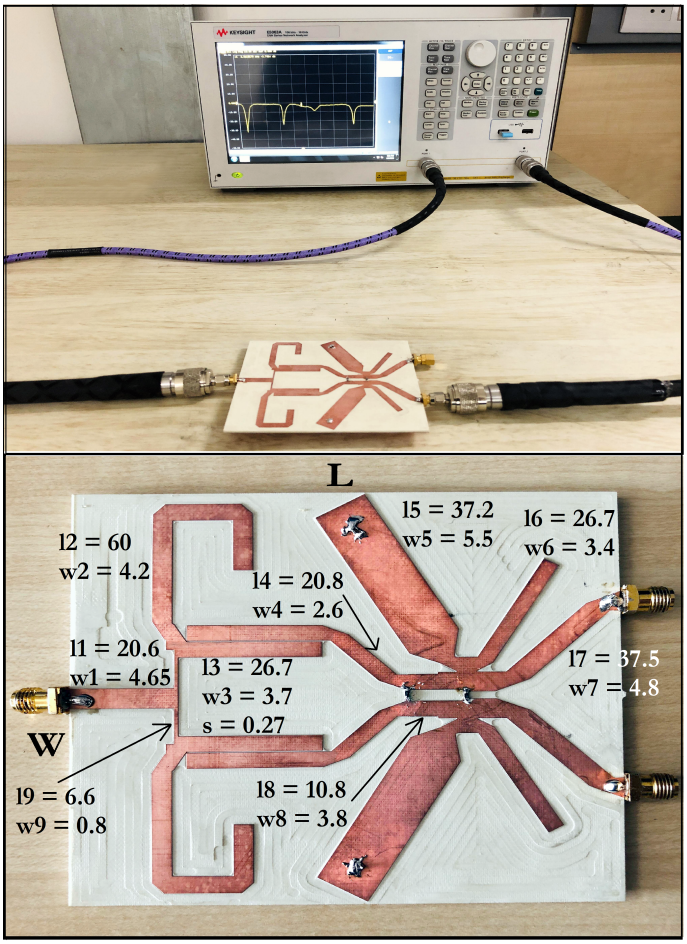

Figure 5.30: The Measurement Setup (top) and the Fabricated Prototype (bottom) of the DC Isolated WPD. All Units in Millimeter (mm) L = $0.37\lambda_g$; W = $0.32\lambda_g$

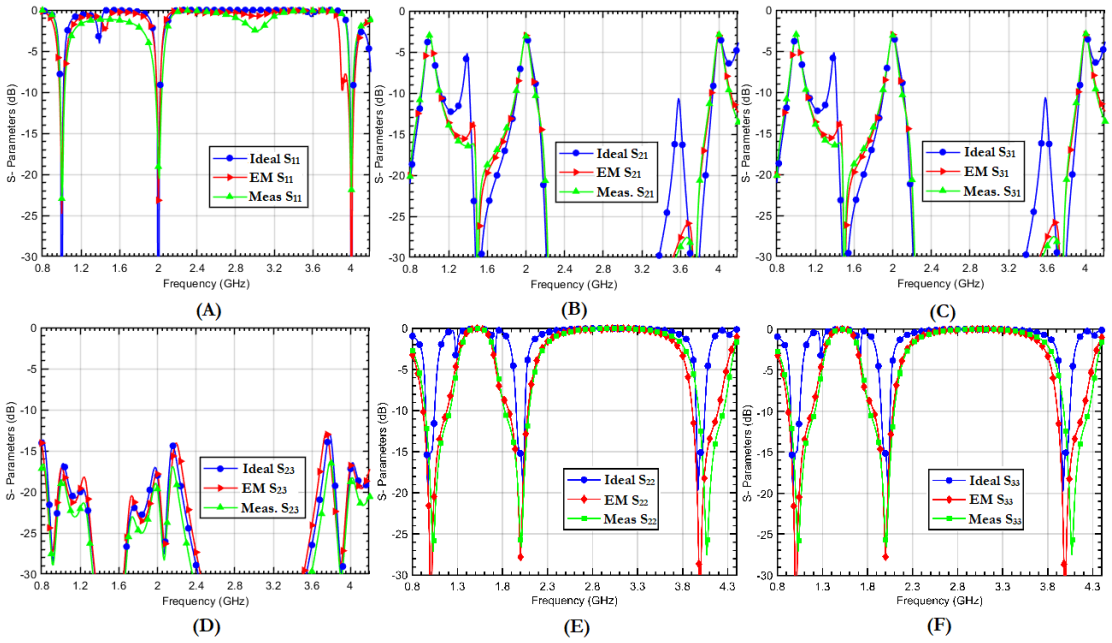

Figure 5.31: Measured, Simulated and EM Results of the DC Isolated Variant of the Fabricated WPD Prototype

Table 5.7: Comparison with the State-of-the-Art

Ref., Year	Freq. (GHz)	Design Method	S_{11} (dB)	S_{21} (dB)	S_{23} (dB)	FBW (%)	Size
[71], 2017	1.5, 1.9, 2.35	$\lambda/4$ Open Stubs	-22, -19.8, -20	-3.3, -3.4, -3.5	-17, -21, -27	40, 10.5, 17.9	$0.28\lambda_g$ X $0.22\lambda_g$
[72], 2018	0.9, 3.15, 5.4	Extended Cross-Shaped Structure	-28.5, -35.5, -32.4	-3.3, -3.1, -3.1	-43.8, -35.2, -37.4	23, 12.6, 5.0 #	$0.12\lambda_g$ X $0.07\lambda_g$
[73], 2019	2.0, 4.4, 5.0	T-Junction Power Divider	-30, -27, -20	-4.4, -3.8 -3.1	-7.4, -11.0, -12.1	23.2, 5.8, 6.6	$0.33\lambda_g$ X $0.33\lambda_g$
This Work	**0.9, 1.8, 3.5**	**Dual- to Tri-**	**-21, -35, -26**	**-3.3, -3.5, -3.5**	**-40, -42, -41**	**40, 22.2, 11.5**	**$0.17\lambda_g$ X $0.12\lambda_g$**
	1.0, 2.0, 4.0	**Band Extension**	**-23, -21, -24**	**-3.1, -3.3, -3.4**	**-19, -17, -16**	**<10%, <10%, <10%**	**$0.37\lambda_g$ X $0.32\lambda_g$**

Approximate Values; FBW (Fractional Bandwidth) = $100X(f_2 - f_1)/f_1$

An observation from the measured results mark the presence of spurious transmissions between stop-bands. In other words, it is difficult to create absolute stop-bands between the three specific bands of interest. One approach to solve this problem is by the utilization of Π-network based dual-band transformers. This has been intensively studied in [34] in which the attainment of large stop-band in between two pass-bands of interest has been demonstrated. It is clear that the proposed design approach is structurally generic. It basically implements a tri-band WPD by extension of the dual-band operation of an impedance matching network. This essentially implies that the design scheme is not strict on the choice of the basic dual-band matching network to be selected. Depending upon the application, any network can be chosen. There can be an impact on various design parameters like bandwidth enhancement [53], extension of operating frequency ratio [54]/impedance transformation ratio [37] and power division ratio [73] or strict spurious transmission suppression [34], as discussed. Table-5.7 presents the performance comparison of the proposed WPD design scheme with some eminent State-of-the-Art designs. It is evident that the proposed design approach exhibits a good performance and advances the State-of-the-Art significantly.

5.14 Conclusion

In this chapter, we introduced a novel concept of a *Virtual Impedance* for implementing tri-band impedance matching networks. We have presented the design theory conceptually, formulated the closed-form design equations and provided a systematic design flow that would aid in easy prototyping. Detailed analysis on the possibility of frequency ratio extension and limitations have been provided. As an example, three arbitrary chosen frequencies were selected to design a test prototype that was fabricated and measured. The second half of the chapter introduces a variant of the virtual impedance concept as an impedance bridge. The design provides flexibility and provisions for frequency

and transformation ratio extension. Thirdly, a simple design scheme of a tri-band WPD using band extension has also been presented. Closed-form design equations backed up with rigorous mathematical analyses facilitate easy prototyping of the proposed design. The design can be readily modified to cater the requirements of DC blocking and it has been demonstrated with design examples and rigorous simulation studies. Lastly, we have fabricated PCB based prototypes and performed their measurements. The measurement results compare well with the simulations and thus addresses a number of limitations associated with the existing state-of-the-art.

CHAPTER 6

A 2-Port Harmonic Tuning Output Network for Efficiency Enhanced RF Power Amplifiers

This chapter is based on the following research papers-

- **D. Banerjee**, A. Saxena, and M.S. Hashmi, "A Novel Independent Harmonic Tuned Two-Port Output Network for Efficiency Enhanced RF Power Amplifiers", *Wiley Microwave and Optical Technology Letters*, Vol. 63, Iss. 2, p.p. 426 - 431, Feb. 2021.

Outline

This chapter introduces a simple two-port harmonic tuned output network-based design of RF Power Amplifiers. The proposed output network facilitates mutual independence between the fundamental, 2^{nd} and 3^{rd} harmonic impedances, which thereby eases the tuning process. The same has been synthesized, fabricated and measured separately to demonstrate the harmonic independence behavior. Thorough graphical and analytical deductions are provided for the design scheme. The proposed design strategy has been validated with a Wolfspeed 10W GaN HEMT based fabricated prototype at 2.4GHz. The measured results show an obtained drain efficiency up to 82.3% and a gain of >11.0dB. A brief idea about an ongoing project which involves extension of the proposed theory for a three-port output network, has also been provided.

6.1 Background and Motivation

THE modern world is unimaginable without wireless devices, the necessity of which has leaped to such an extent that the availability of a smart-phone, tablet or

IoT devices has become quite normal in daily life. High data rates and thereby, the immense volume of data that these devices consume contribute to their "smartness". This has indeed driven a lot of research in investigating various ways to facilitate high data rates and a larger connectivity. The newly deployed fifth generation (5G) wireless standard addresses many of the existing communication constraints like network coverage, reliability, latency and spectral efficiency and brings with it the boon of a "connected environment" through IoT. The extensive and wide arena of 5G is still blurry on the approaches of implementation, or in other words, the key aspects necessary to implement such a system. However, several of them have been identified and those include mm-Waves, digital beam-forming, massive Multiple Input Multiple Output (mMIMO), micro-cells etc. mMIMO promises data rate improvements and link reliability as they use a greater number of amplifying sub-units in the base station than in the existing technologies. As the 5G standards use digital signals with high spectral efficiency, it is necessary that these signals are transferred with minimum power loss and the least possible signal degradation. This intrigues design of highly efficient RF Power Amplifiers (PA) operating in a transmitter front-end.

A Power Amplifier is one of the most important components in the RF front end and determines a variety of transmitter specifications like efficiency, transmitting range, gain, and linearity. PAs serve the purpose of boosting the power level of a modulated signal before launching it into free-space through an antenna. In this context it must be noted that the PA boosts the RF power level at the cost of DC power consumption. This is very important because PAs are the most power-hungry components in a transmitter front-end. Thus, it is necessary to design amplifiers that consume a minimum amount of DC power and at the same time, minimize the power dissipation at its output. To minimize the DC power consumption of a PA one has to focus on the biasing states of the transistor. Based on this, RFPAs can be classified into two broad categories as:

- Classical: These form the simple group of controlled conduction angle amplifiers whose behavior is defined by the length of the transistor's conduction state over a portion of the output waveform. In these cases, the transistor's operation lies somewhere between "fully ON" and "fully OFF". Typical examples include Classes- A, B, AB and C.

- Switched Mode: These are the classes of amplifiers in which the transistor behaves as a switch. They target high efficiencies by driving the device hard into saturation and the input signal is either fully "switched ON" or fully "switched OFF". These include Classes- D, E, F, G, S, T etc.

Fig. 6.1 illustrates the various classes of PA operating modes and their corresponding bias levels with respect to the conduction angle.

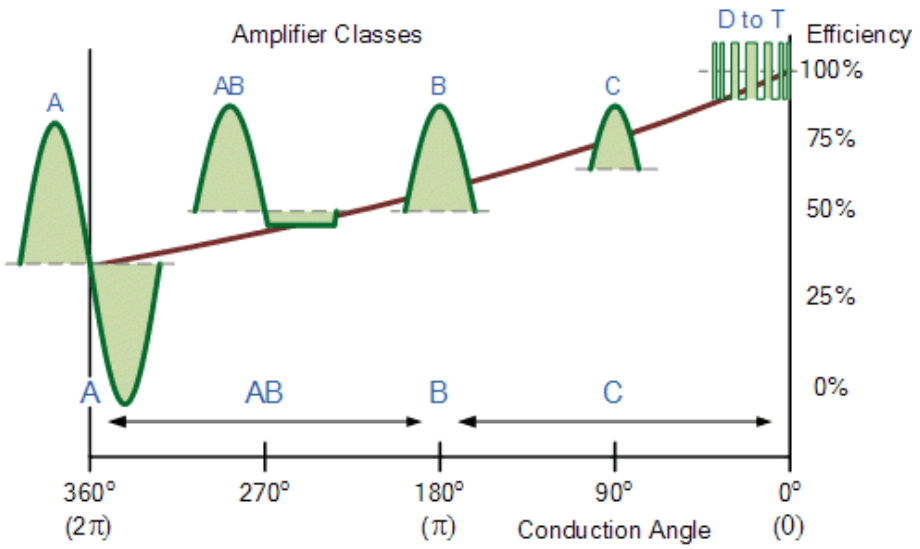

Figure 6.1: Classes of Operation of RFPAs and their Corresponding Transistor Bias States w.r.t Conduction Angle [4]

It can be readily inferred from the figure that while the transistors in Class- A amplifiers remain ON all the time, it consumes very high amount of DC power. On the other hand, as we shift the bias point more towards cut-off, the transistor conducts only in the presence of the input signal and remains OFF otherwise. While this saves a lot of DC power, near-cutoff amplifiers suffer from non-linearity (because of this transition from OFF to ON state and vice versa) and hence need additional pre-distortion circuitry for addressing that. On the other hand, Class-A is the best candidate in terms of linearity but can provide only up to 50% efficiency in theory. Thus real-life PA design is always a trade-off between linearity and efficiency, the choice of which depends upon the application that the PA would be used for. Another important factor behind the dissipation of power at the output of the PA is the overlap between the drain current (I) and voltages (V) of the transistor. The more the area of overlap, the more is the power dissipated. In other words, for an amplifier with 100% efficiency, theoretically there

should be no overlap between its drain voltage and current waveforms, as depicted in Fig. 6.2. However, this is not possible practically and therefore minimum overlap is targeted. A practical case of a PA drain I-V waveform is illustrated in Fig. 6.3. The area of I-V overlap is shaded in yellow and denotes the power dissipated in terms of heat, contributing to loss, and thereby, limiting the efficiency to reach 100%. There are a number of ways in which minimum current-voltage overlap can be achieved. One of them is waveform engineering in which either of the current or voltage waveforms is shaped to form a square wave whereas the other is a sinusoid.

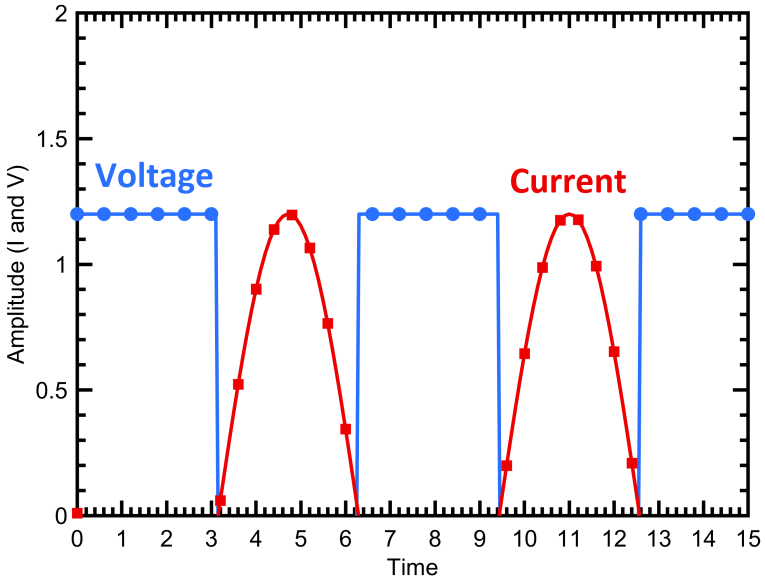

Figure 6.2: Ideal Case of Zero I-V Overlap Leading to 100% Efficiency

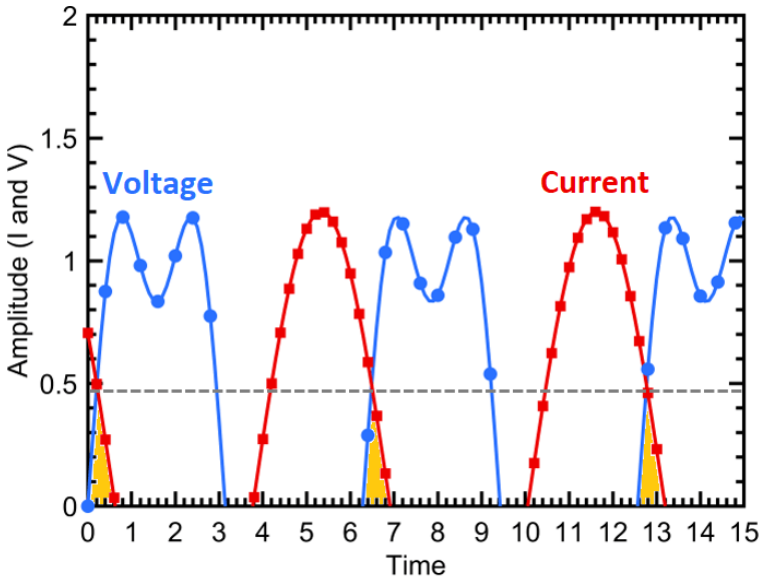

Figure 6.3: Practical Case where I-V Overlap Occurs leading to Power Dissipation (Yellow Shaded Region) and $< 100\%$ Efficiency

From Fig. 6.3 we can see that the voltage waveform has been engineered to form an "almost"-square wave while the drain current remains a sinusoid. This shaping is achieved by a technique widely known as harmonic tuning. Harmonic Tuning is the process of waveform shaping by either introducing harmonics or eliminating harmonics from a particular waveform. If we introduce odd harmonics in a sinusoidal voltage (or current) waveform, it would result in a square wave with ripples, as shown in Fig. 6.3. An infinite number of odd harmonic components would result is a perfect square window, however, in a real life scenario, only up to the third harmonic is considered. Thus, the near-square wave would spread into the adjacent sinusoidal wave leading to overlap, hence power dissipation. Classes- D, E, F and F^{-1} exhibit very high efficiencies but are limited in bandwidth. Because of their narrowband operation, different topologies for PA have been developed like the load-pull assisted PA, reactance compensation PA and the continuous mode PAs. Load-pull assisted PAs can be developed for higher bandwidth in an analytical way, reactance compensation PAs have sets design equations but lack output power and efficiency flatness whereas continuous class-B/J, F/F^{-1} etc. are designed based on harmonic tuning methods. As already discussed, the basic idea behind waveform shaping is harmonic tuning and that is achieved by providing a set of "proper" harmonic load impedances at the transistor's intrinsic drain plane. Fig. 6.4 illustrates the class-F PA with the harmonic load requirements at the intrinsic plane. The harmonic filter is responsible for shorting the even harmonic components and presenting an open circuit to the odd harmonics. The fundamental match is purely resistive. Similarly, in case of class-F^{-1}, the harmonic impedance conditions are opposite with shorted odd harmonics and open even harmonics.

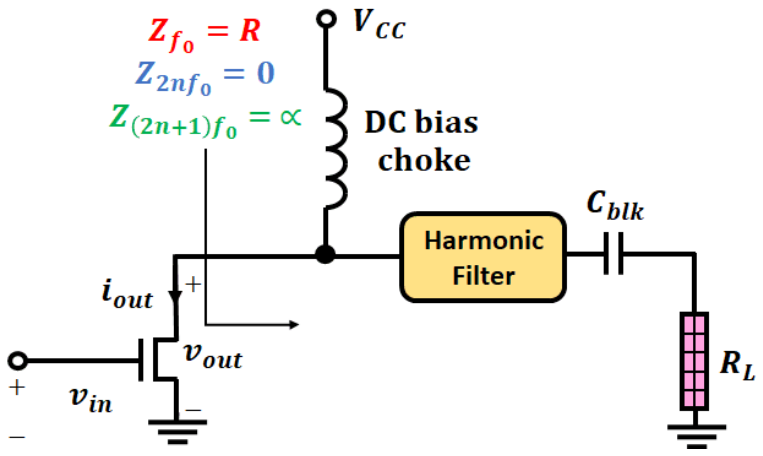

Figure 6.4: Classical Example of Class-F PA with Harmonic Load Conditions

It is important to note that all the impedances presented at the drain of the transistor is in respect to the intrinsic or current-generator plane and not the packaged plane. Commercial transistors are packaged devices that contain parasitics and thus, the harmonic impedances presented at the packaged plane would be different from what would actually be presented at the current-generator plane. Fig. 6.5 illustrates an example of class- F^{-1} harmonic impedance condition in which the open and short even and odd harmonic loads respectively would map into reactive harmonic impedances at the packaged plane. This mapping is important to design output matching networks and thereby absorbing the effect of the parasitics to a certain extent.

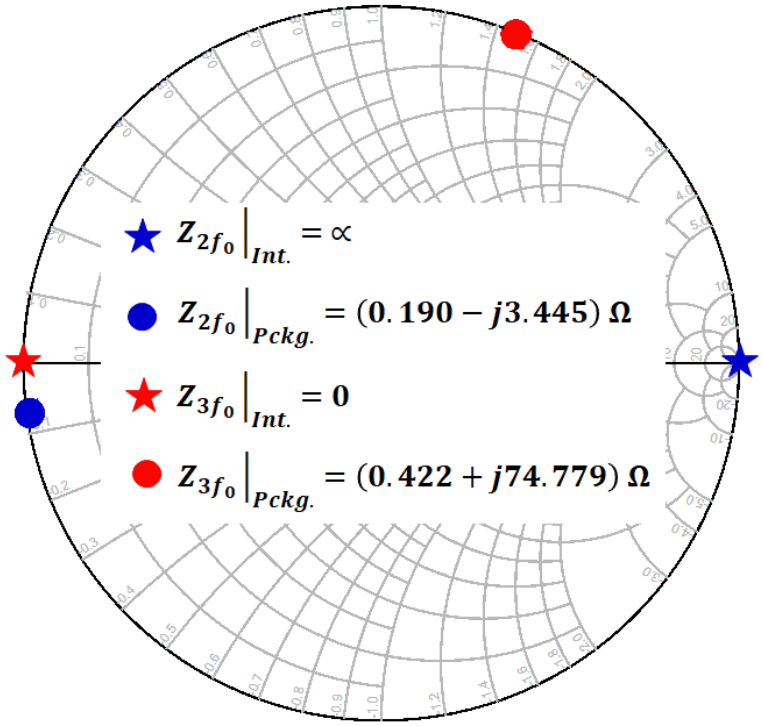

Figure 6.5: Mapping of Harmonic Impedances from the Intrinsic to the Packaged Drain Plane of the Transistor

6.2 PA Design Basics

PA design has long been considered an intelligent consideration of many factors and trade-offs that mostly depend upon the application to be served. Hence, there are various ways a PA can be designed, but certain steps are absolutely necessary and need to be followed irrespective of the type of PA being designed. In this section we will discuss the basics of PA design in a step-by-step way so that the reader gets a clear idea about the factors that should be considered. In this context, we will be using Keysight Advanced

Design System (ADS) as our computer-based design tool. Fig. 6.6 illustrates a complete step-wise PA design flow.

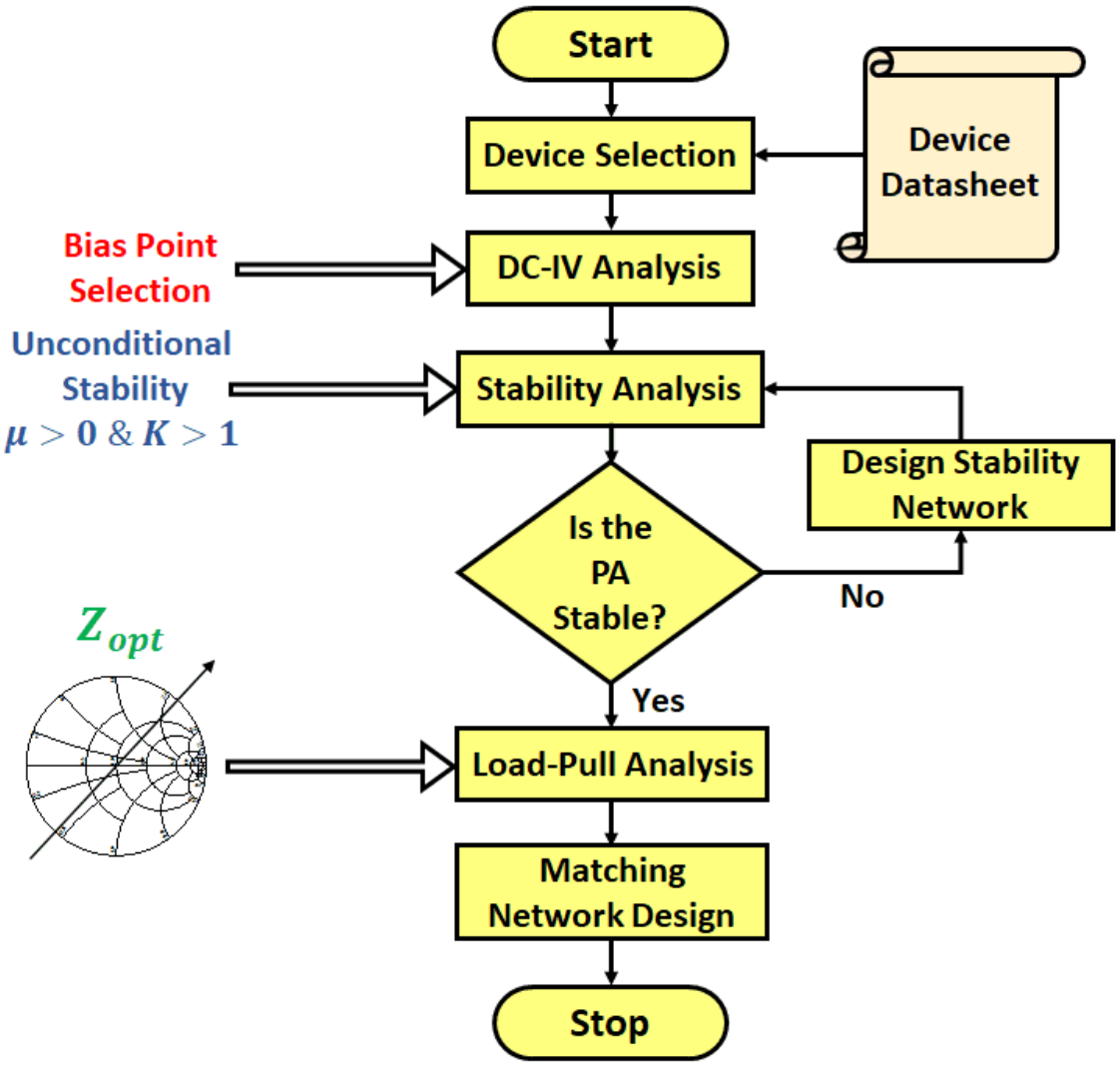

Figure 6.6: The RFPA Design Flow

Firstly, depending on the application (or link budget in case of RF system design), a set of specifications are obtained. Typical specification parameters are gain, efficiency, output power delivered, P1dB, IIP3, OIP3 etc. While efficiency and gain are very important, it is also of paramount importance to have a good linearity performance. An amplifier that would cause signal distortion and leakage is in no way of any practical utility. Based on the specifications of the PA to be deigned, a proper active device (transistor) is selected by carefully studying the vendor data sheets. In RFPAs, based on the substrate, three categories of active devices are mainly used- LDMOS (Laterally-Diffused Metal-

Oxide Semiconductor), GaAs (Gallium Arsenide) and GaN (Gallium Nitride). Out of them GaN HEMTs (High Electron Mobility Transistor) are widely used because of their high electron mobility, hence high speed and their ability to handle high power. Once the device is selected, we need to identify the DC operation point (quiescent point), i.e. the set of gate and drain voltages that need to be supplied to the transistor. The determination if the Q-point depends mainly upon two factors- the target efficiency and the linearity. As mentioned earlier, very high efficiency amplifiers are not linear and highly linear amplifiers are not efficient. Generally for space-unconstrained systems, high efficiency is given a priority because there are Digital Pre-Distortion (DPD) techniques to improve the linearity of a non-linear PA. Usually Class- B/AB operating points are chosen to target enhanced efficiency. As an example, Fig. 6.7 depicts the Keysight ADS window to determine the bias point obtained from the FET curve-tracer template. We can clearly choose from a set of I-V curves, obtain the corresponding drain current drawn by the transistor and have an idea about the DC power dissipation.

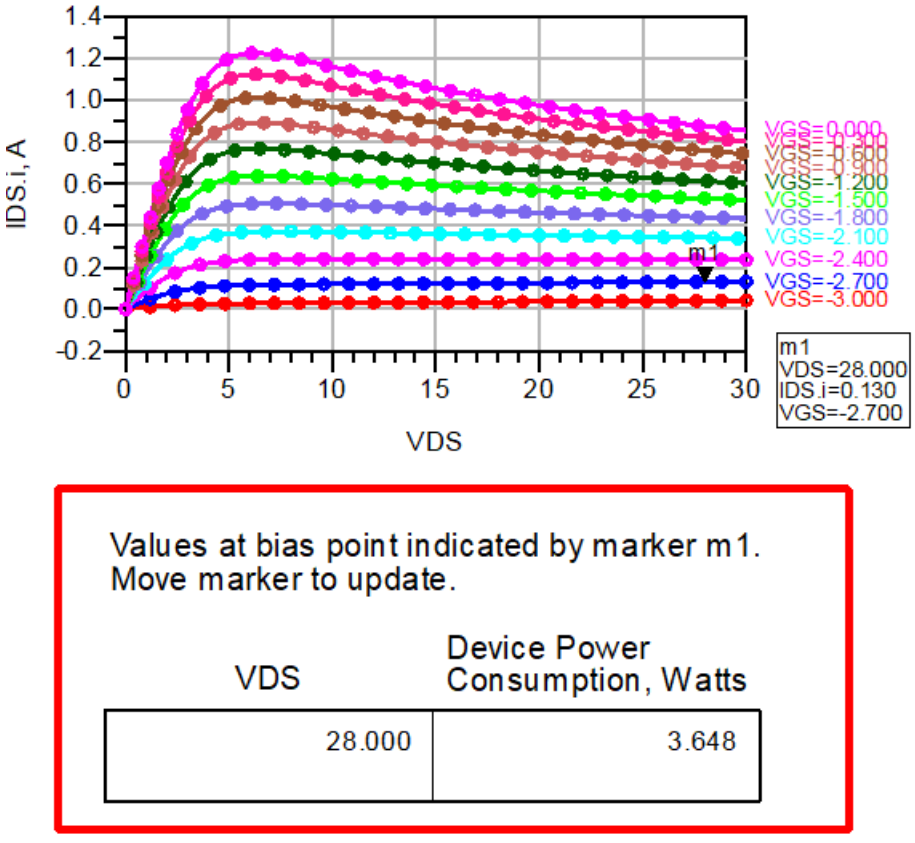

Figure 6.7: Determining DC I-V Q-Point in Keysight ADS

After obtaining the DC bias point, the next step is to stabilize the transistor unconditionally. This is very important because an unstable device would result in uncontrolled

oscillation that would not only damage the transistor (hence the PA) but also the next stages cascaded to it. Thus we must be certain that the transistor is stabilized over the entire operating frequency range. There are three ways to stabilize a transistor namely:

- High Pass Network: An RC parallel high pass network is the most common PA stabilizing agent. It is used mainly to suppress the low-frequency oscillations which are quite common in GaN PAs.

- Resistive Network: Another solution for stabilizing a transistor is to use a resistive network. On this regard, it is of utmost importance to note that a resistor in series to the input RF signal should be avoided because of the resistive loss. A series RC branch parallel to the input signal line is also quite common.

- Feedback Network: In analog electronic circuits it is very common to stabilize a transistor by feedback mechanism. In this, a part of the output from drain is fed-back to the transistors gate input. However, this topology is not so common in case of RFPAs because of their severe gain reductions.

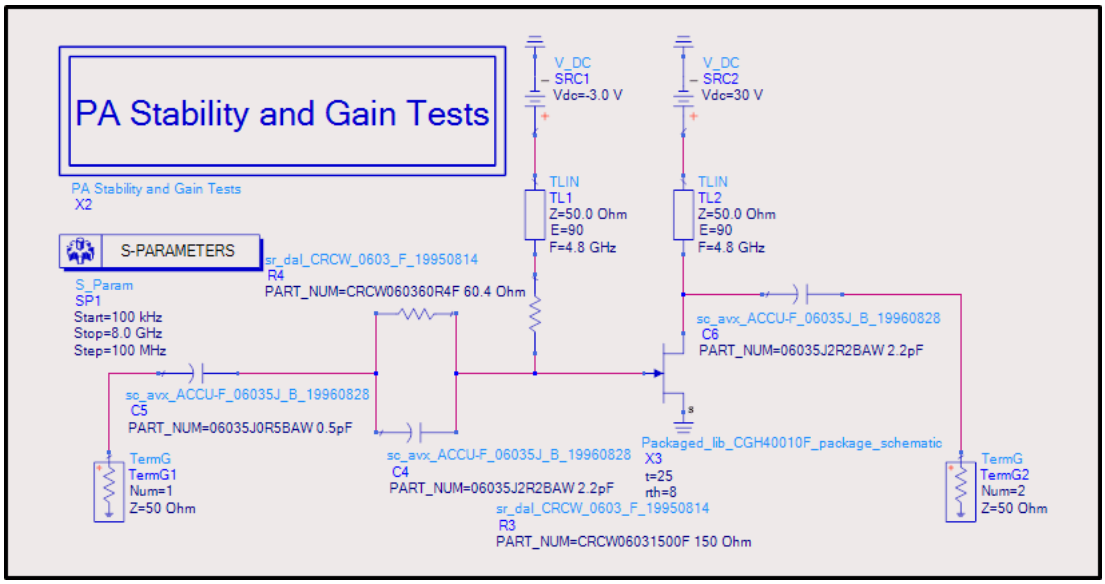

Figure 6.8: Example Setup- Setting up the Transistor for Unconditional Stability

Fig. 6.8 illustrates an example setup in Keysight ADS to demonstrate the unconditional stability criterion in PAs. As evident, the widely used Wolfspeed 10W transistor (CGH40010F) has been chosen and an RC parallel high-pass network is used to stabilize it. A resistor, followed by a quarter-wave transmission line in the gate bias path

prevents any RF leakage into the DC bias circuitry. The component values of the RC network are usually provided in the datasheet, or if not, they can be easily obtained by some basic maths and tuning.

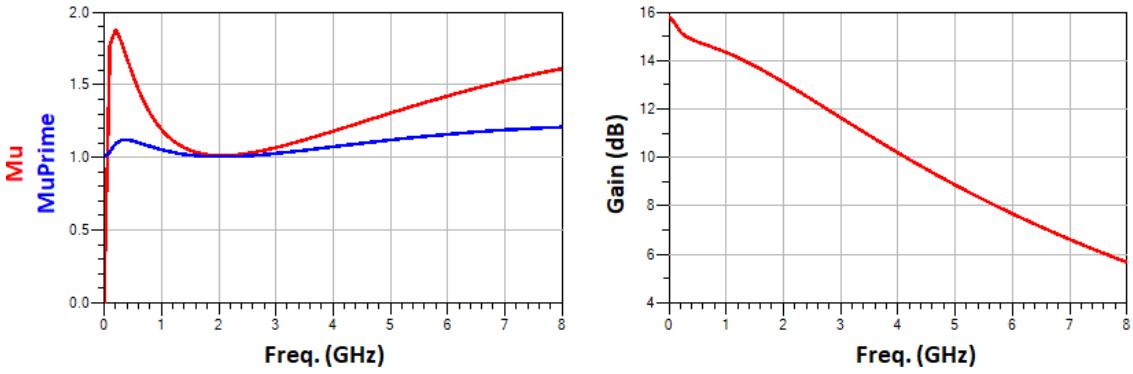

Figure 6.9: Stability Analysis Results

Fig. 6.9 illustrates an example result window for an unconditionally stabilized PA. We can see that the stability determiners, Mu and MuPrime in ADS are both greater than 1 over the entire range of operation. Moreover, the gain obtained around a selected design frequency of 2.4GHz is around 12. This network can then be proceeded with to perform the load-pull.

The optimum impedance to be presented at the drain of the transistor is determined by load-pull analysis. Load-pull is a method in which the transistor's load at the drain is varied across a particular region of the Smith Chart in order to find the appropriate impedance value that corresponds to the desired performance parameter specification. Generally maximum efficiency, gain and output power delivered are targeted in load-pull. A trade-off is made amongst the three to come up with an "optimum" load value, which satisfies these parameters. This is of prime importance in designing an output matching network. Load-pull analysis can be performed to determine the fundamental as well as the harmonic impedance terminations for a given transistor.

Fig. 6.10 illustrates a schematic for the load-pull analysis. The Smith-Chart with an arrow symbolizes the load tuner that varies the loads either across the entire Smith Chart or a specified region (shaded in yellow) across the Smith Chart. Fig. 6.11 presents the results for fundamental, second and third harmonic load-pull analyses for a 10W Wolfspeed GaN HEMT at 2.4GHz, without driving it into compression. As the load-pull is basically a sweep analysis, the results are obtained in form of contours. These

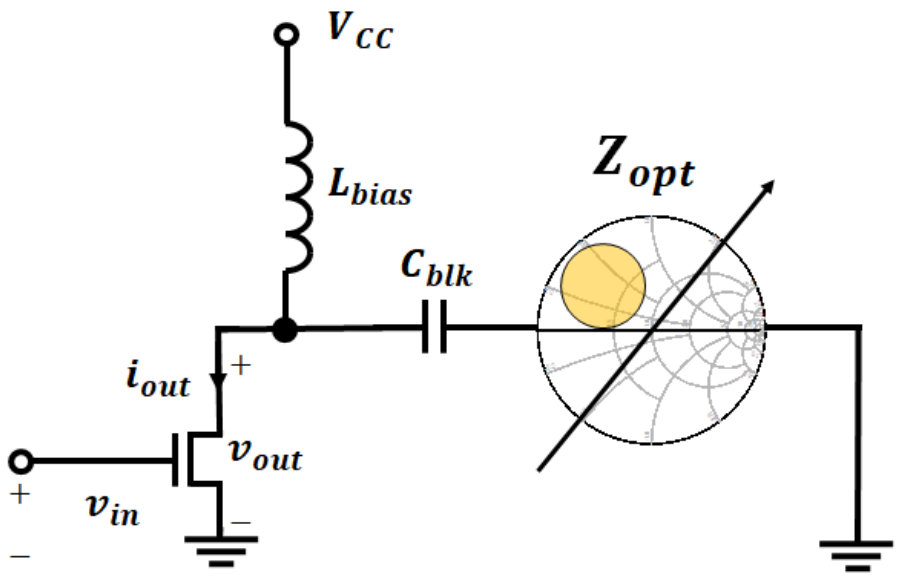

Figure 6.10: Load-Pull Analysis for Determining Z_{opt}

contours are lines joining the impedances that have the same value for a specification parameter. For example, in Fig. 6.11, the red contours join all the impedance points that correspond to the same value of power delivered (P_{del}) and the blue contours join all the impedance points corresponding to the same value of Power Added Efficiency (PAE). The lesser the size of the contour, the higher is the value of the Figure-of-Merit (PAE and Power Delivered in this case). We observe that the points of maxima for PAE and P_{del} are not the same point. This is the scenario where we should make a trade-off and choose an intermediate value that satisfies both requirements. Table- 6.1 shows the optimum impedances (Z_{opt}) and source impedances (Z_{src}) obtained from a typical fundamental and harmonic load pull analysis.

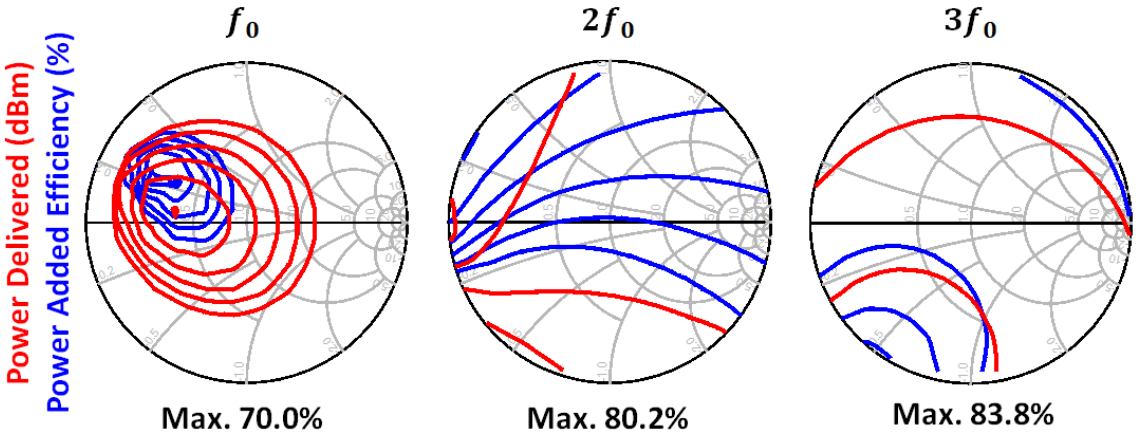

Figure 6.11: Fundamental and Harmonic Load-Pull Contours for Power Delivered and Power Added Efficiency

Table 6.1: Impedances Obtained from Load-Pull

	f_0	$2f_0$	$3f_0$
Z_{src}	(2.611-j4.077)	(2.322-j4.098)	(2.333-j4.104)
Z_{opt}	(17.623+j11.741)	(0.263+j10.997)	(2.634+j153.964)

The importance of harmonic tuning can be well observed from Fig. 6.11. We see that only a fundamental load pull can deliver a maximum PAE of up to 70%. Once the optimum second harmonic impedance is obtained and presented, the efficiency shoots up to 80%. The optimum third harmonic impedance, when presented, even shoots it further by around $3-4\%$. Thus we see that harmonic tuning is one of the key aspects of efficiency improvement in RFPAs and hence, has gained a lot of research attention.

Once the optimum impedance (Z_{opt}) and the source impedance (Z_{src}) values are obtained, the next step is to design output and input matching networks respectively, that match the same with the standard 50Ω port terminations. There are a number of ways to design a matching network- using the Smith Chart Utility, the impedance match utility or the analytical method. Generally for a wideband output matching network we choose a transmission line and stub ladder network. Detailed theoretical analysis on multi-band matching networks have already been presented in the earlier chapters. Readers are encouraged to go through the same. The design strategies are straightforward and depends mostly on the type of matching topology selected. Similarly, the input matching network also needs to be designed for conjugate matching, and hence, maximum power transfer. The idea remains the same, i.e. to match the transistor's input impedance obtained from the load pull with the standard 50Ω input termination.

6.3 Harmonic-Tuned Amplifiers- A Brief Introduction

The increasing demand of "wireless"-ly tied terminals have necessitated evolution and modernization of existing wireless standards. An important part of highly efficient wireless networks is efficient RF front-ends. The emerging trend in wireless technology is to develop RF front-ends that are highly efficient and linear. It is a well-established fact that the RF Power Amplifier (RFPA) is the key component that regulates the overall performance metric of RF front-end. Apparently, they play a vital role in RF transmitter circuits and determine figure of merits such as efficiency, output power, gain, linear-

ity, reliability, and transmission range. At this point, it is imperative to note that RF-PAs are the most power-hungry components but their efficient design can enhance the performance metrics significantly. The literature is replete with high efficiency RFPA architectures addressing various target specifications and performance parameters.

Here we have proposed a generalized methodology that targets efficiency enhancement by presenting proper reactive harmonic impedances at the intrinsic plane of the transistor. A passive two port network is introduced that facilitates independence between the fundamental, second and third harmonic matchings. The proposed network implements a tuned reactive 2nd harmonic load and a corresponding reactive 3rd harmonic load, thereby denoting the PA operation as an example of Class-X. The absence of lumped component in the design leads to its robustness and facilitates circuit simplicity and compactness.

6.4 The Proposed Theory

Fig. 6.12 depicts the internal parasitic model for the 10W Wolfspeed GaN HEMT. It is important to determine the value of the parasitic elements of the network in Fig. 6.12 in order to map the fundamental and harmonic impedance requirements from the packaged drain plane to the intrinsic (current generator) plane and vice versa.

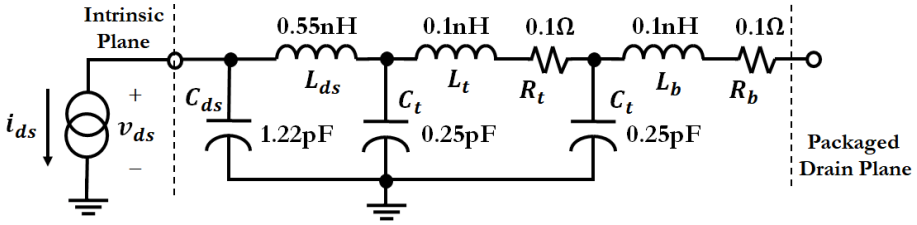

Figure 6.12: Parasitic Model of the Transistor used for Modelling Drain Impedances from the Intrinsic Plane to the Packaged Plane

We have extracted the values of the parasitic elements by de-embedding techniques from the device datasheet and the passive package model provided by the vendor. On this regard, it is important to note that de-embedding is essential for shifting the reference planes of analysis in a packaged transistor. In PA design, it is a process by which we obtain the values of the transistor's internal parasitic elements. This is essential for mapping the fundamental and harmonic impedances which are necessary to design the

output matching network. An internal reference model (Fig. 6.12) is provided by the transistor vendor which is used extensively to determine the parasite values. L_{ds} approximately represents the total bond wire inductance. The total number of bond wires as well as their dimensions being known, the total bond wire inductance was obtained by individually using the bond wire modeling component in Keysight ADS. The other elements include the packaged tab parasitics, namely L_t, C_t and R_t were modeled as a standard series-L/shunt-C network. The S-Parameter fit approach was then utilized to optimize the individual parasitic component values with reference to the S2P file from the datasheet. As the parasitic network consists of passive elements only, no non-linear behavior can be attributed to the same. Thus, all de-embedding operations carried out does not consider any non-linear element whatsoever.

Fig. 6.13 illustrates the proposed independent harmonic tuned two-port network along with the transistor model.

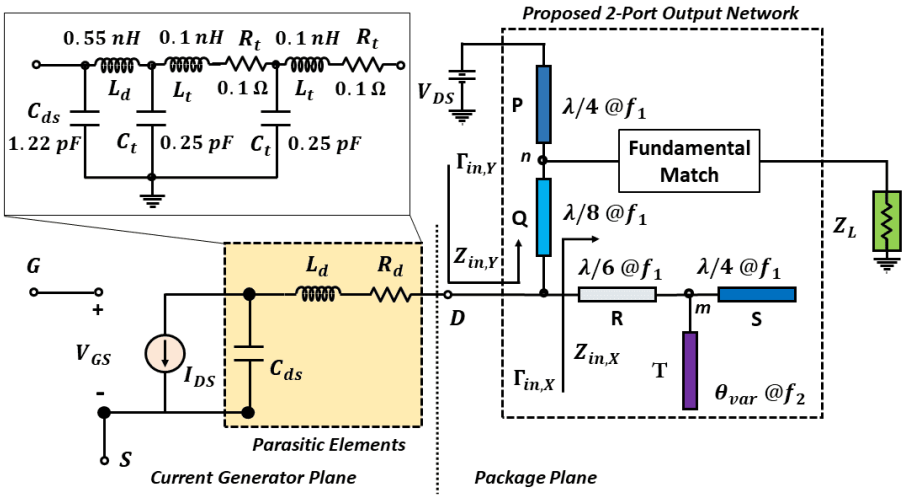

Figure 6.13: The Proposed Two-Port Harmonic Tuning Network

The proposed 2-port network is designed to provide separate paths for the fundamental and the 2nd harmonic signals while keeping the 3rd harmonic short at the packaged drain plane. To implement this, (6.1) need to be satisfied unconditionally:

$$Z_{in,X}(or\Gamma_{in,X}) > Z_{in,Y}(or\Gamma_{in,Y})@f_0 \tag{6.1a}$$

$$Z_{in,X}(or\Gamma_{in,X}) < Z_{in,Y}(or\Gamma_{in,Y})@2f_0 \tag{6.1b}$$

The fundamental, being Z_{opt} at node D, gets transformed into Z_{opt}^{Q} at node n as presented in (6.2). The impedance thus obtained is then matched to the load by the output matching network.

$$Z_{opt}^{Q} = \frac{Z_{opt} + jZ_Q \tan 45^\circ}{Z_Q + jZ_{opt} \tan 45^\circ} \tag{6.2}$$

On the other hand, the impedance faced by the fundamental at the 2nd harmonic signal path is $j\sqrt{3}Z_R$. The reflection coefficient $\Gamma_{in,Y}|_{f_0}$ being smaller on the upper branch ensures the fundamental to pass through it, thereby satisfying (6.1a). Node n being short for the 2nd harmonic, gets transformed into open at node D, thus satisfying (6.1b) and in turn isolating it from the fundamental branch. In the lower branch, the second harmonic impedance gets transformed into $Z_{in,X|2nd}$ as given in (6.3).

$$Z_{in,X|2nd} = Z_R \frac{-jZ_T \cot \theta_{var} + jZ_R \tan 120^\circ}{Z_R + Z_T \cot \theta_{var} \tan 120^\circ} \tag{6.3}$$

The electrical length of R is chosen as $\lambda/6@f_1$ to keep the third harmonic short at all times. The obtained impedance conditions are expressed in (6.4). The terms Z_R and Z_Q are the characteristic impedances of the lines R and Q respectively and θ_{var} is the electrical length of the transmission line T. It must be noted that the characteristic impedances of all the transmission lines are same and considered 50Ω for convenience.

$$Z_{in,X}|_{fund} = jZ_R\sqrt{3}; \qquad Z_{in,Y}|_{fund} = Z_Q \frac{Z_{opt} + jZ_Q}{Z_Q + jZ_{opt}} \tag{6.4a}$$

$$Z_{in,X}|_{2nd} = -jZ_R \frac{(Z_T \cot \theta_{var} + \sqrt{3}Z_R)}{\sqrt{3}Z_T \cot \theta_{var} - Z_R}; \quad Z_{in,Y}|_{2nd} = \propto \tag{6.4b}$$

$$Z_D|_{3rd} = 0 \tag{6.4c}$$

The design targets perfect fundamental match along with a tuned reactive load for the 2nd and the corresponding 3rd harmonic. While the proposed impedance conditions are presented at the packaged drain plane of the transistor, it must be noted that the 2nd harmonic impedance point can be tuned by varying the length θ_{var} of the transmission line T. This would not disturb the fundamental matching because the 2nd harmonic signal path is completely isolated, as evident from the conditions in (6.1). Tuning θ_{var} at the packaged drain plane presents a purely reactive 2nd harmonic impedance and correspondingly loads the 3rd harmonic with respect to the fixed value of the fundamental at the current generator plane of the transistor. This subsequently implements a subset

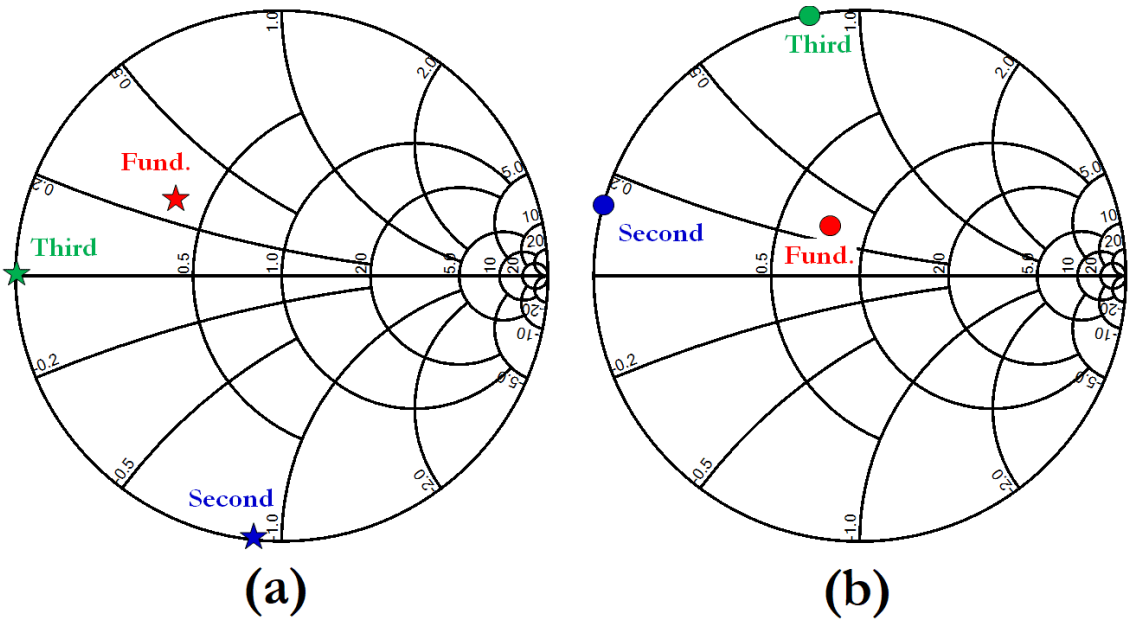

Figure 6.14: (a) Impedance Points of the Proposed Amplifier at the Packaged Drain Plane (b) Corresponding Impedance Points in the Intrinsic (Current Generator) Plane [Mentioned at the Design Frequency of 2.4GHz]

of Class-X operating conditions. The fundamental and harmonic loads thus obtained is illustrated in Fig. 6.14 both at the packaged drain and the current generator reference planes of the transistor.

6.5 Measurement Results

To validate the proposed theory, we have fabricated a Wolfspeed 10W GaN HEMT based PA on RO5880 substrate (ϵ_r=2.2, thickness 1.575mm, 1oz Cu). To further clarify the operation of the harmonic independence two-port network, the same has been fabricated separately and tested. The fabricated prototype of the two-port network along with the results are illustrated in Fig. 6.15. To satisfy the conditions in (6.1), the targeted S-Parameter results is presented in (6.5).

$$S_{21}@f_0 = 0; \qquad S_{21}@2f_0, 3f_0 = -\propto \tag{6.5a}$$

$$S_{31}@f_0, 3f_0 = -\propto; \quad S_{31}@2f_0 = 0 \tag{6.5b}$$

$$S_{23}@f_0, 2f_0, 3f_0 = -\propto \tag{6.5c}$$

From Fig. 6.15, the results clearly signify that the Port-2 allows only the fundamental signal while blocking the second and the third harmonics, whereas the Port-3

allows only the second harmonic and blocks all fundamental and third harmonic transmissions. It is worth noting that there is high isolation between ports 2 and 3 signifying no leakage of fundamental and second harmonic signals into each other's path. This clearly demonstrates harmonic isolation and thus finds usefulness in the output network of harmonically tuned PAs. The dimensions of the 2-port network are marked in the diagram for convenience. It must be noted that the separately designed 2-port network has slightly different dimensions than the one in the fabricated PA. This is because the standalone 2-port network does not consider the fundamental matching network at Port 2 and the optimum tuned length θ_{var} of the transmission line T as compared to the one assembled in the PA.

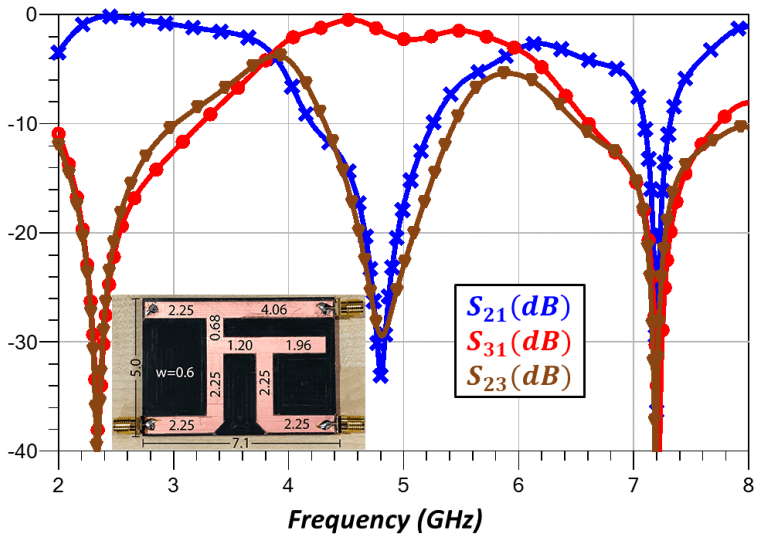

Figure 6.15: Fabricated 2-Port Network with Measured S-Parameter Results (Units in cm and default width = 0.6cm)

The fabricated PA, depicted in Fig. 6.16 was set up in the measurement test-bed in the order shown in Fig. 6.17. As a first step, DC Analysis and stability check was performed. At stability, the transistor draws a drain current of 65.32mA at a gate voltage of V_{GS}=-2.82V and drain voltage of V_{DS}=28V. This signifies deep Class-AB operation, and was chosen to avoid gain reduction as observed in Class-B bias conditions. Subsequently, we performed the large signal Continuous Wave (CW) measurement with an input power of 30dBm (1W). The measured results and I-V waveforms are plotted in Fig. 6.18. It is evident that the maximum power delivered by the PA is 41.1dBm and it is essentially a gain of >11dB. The maximum measured drain efficiency obtained is 82.3% at 2.4GHz. The corresponding Power Added Efficiency (PAE) is 77.8%. A com-

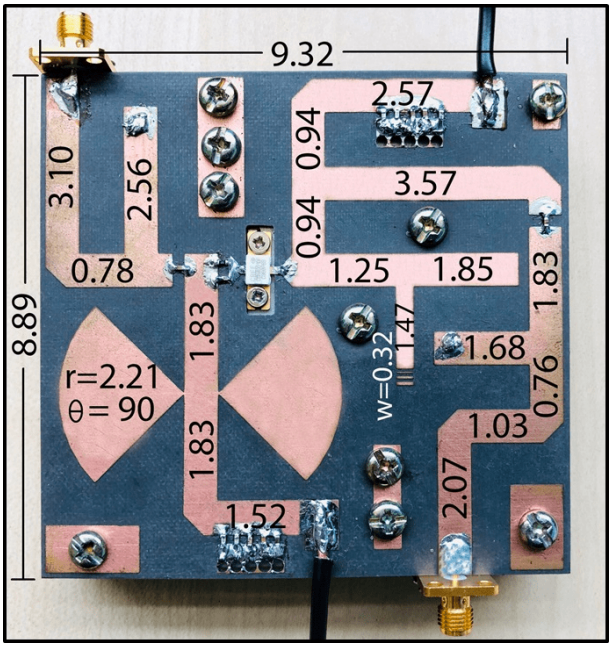

Figure 6.16: The Fabricated PA with all Dimension are in Centimeter (cm) and Default Line-Width of the PA is 0.6cm unless Otherwise Mentioned

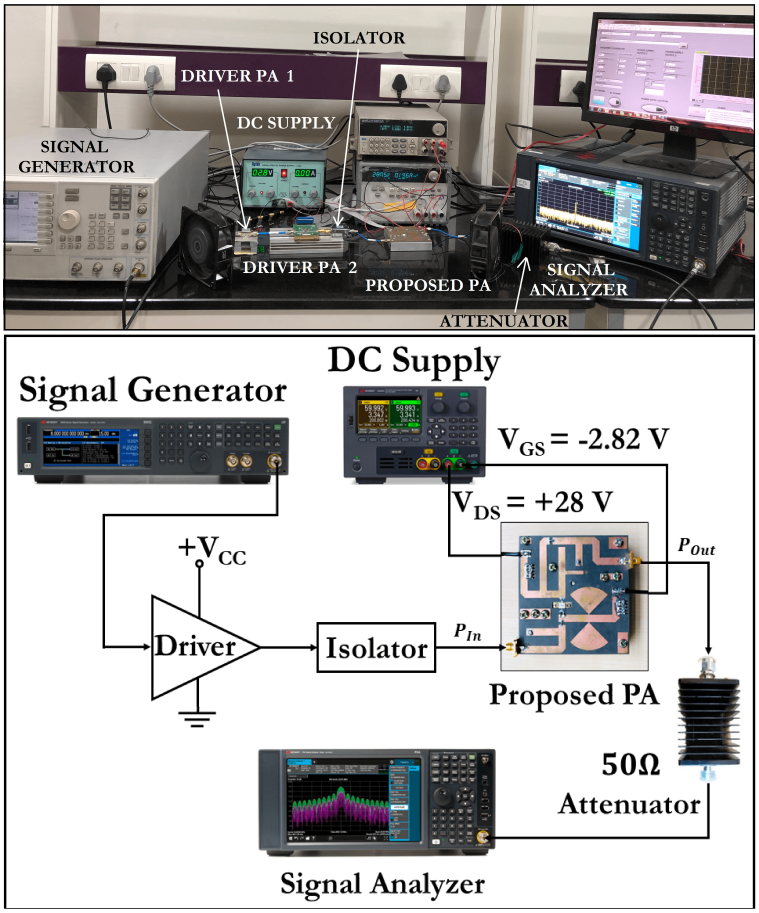

* Setup Courtesy: Dr. Karun Rawat, IIT Roorkee, India

Figure 6.17: The Measurement Chain with Schematic Representation

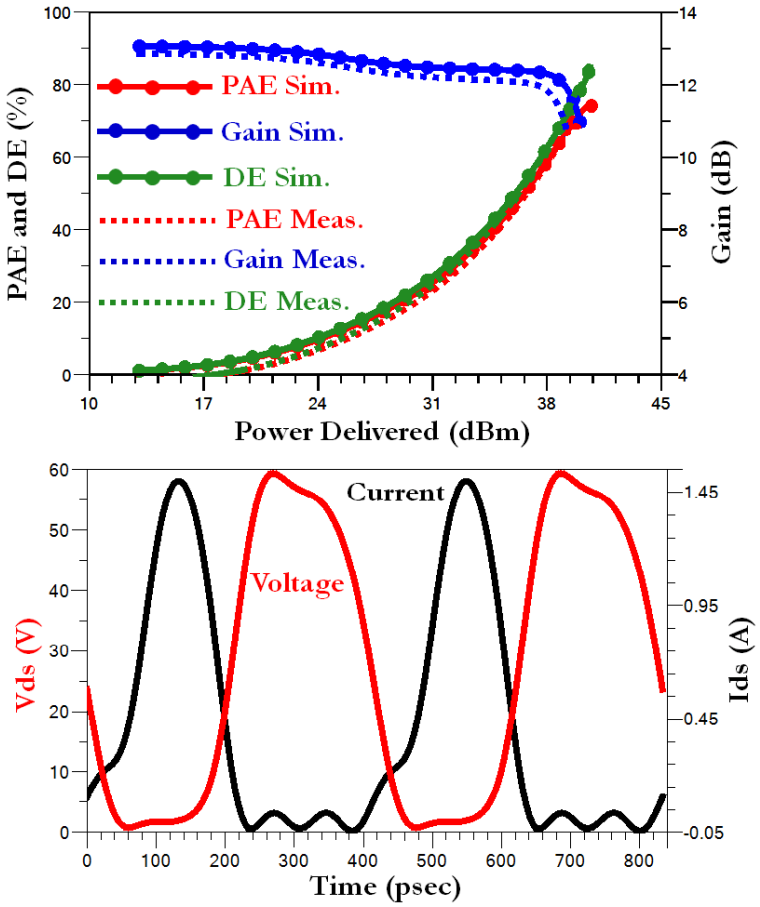

Figure 6.18: Simulated and Measured Results with IV Waveforms

parison of the proposed design with some of the recently reported designs are given in Table-6.2. It places the contribution of the proposed design appropriately in comparison to the existing state-of-the-art of the RFPA domain.

Table 6.2: Performance Comparison of the Designed PA With the State-of-the-Art

Ref.	**Freq. (GHz)**	η_{dr} **(%)**	P_{del} **(dBm)**	**Gain (dB)**
[140]$^{\$}$	1.0	80.6	35.9	15.5
[142]$^{\#}$	1.0	70 - 80	19.2	17.9
[149]$^{+}$	0.8 - 2.7	52 - 76	43 - 47	>10.0
[150]$^{+}$	1.7 - 3.0	67	43.8 - 44.4	10.7
This Work	**2.4**	**82.3**	**41.4**	**>11.0**

$\#$ using TriQuint a GaAs pHEMT transistor
$+$ using Wolfspeed 25W GaN (CGH40025F) transistor
$ using Wolfspeed 10W GaN (CGH40010F) transistor

6.6 A Three-Port Output Network-Based Harmonic Tuned PAs (Ongoing)

In the earlier sections we saw the utility of harmonic tuning on the overall performance of the PA. We also developed a 2-port output network that ensures independence between the harmonic impedances, thereby increasing the degree of freedom of the second harmonic design space. Moving forward, currently we are investigating the possibility of a 3-port output network for implementing the harmonic tuning operation. The hypothetical PA would consist of two transistors- carrier and harmonic generator. The carrier transistor would be biased in class-AB while the harmonic generator in deep class-AB or class-B. Input power would be fed in to these transistors by a WPD. The output of the harmonic generator would be fed into the output of the carrier in-phase or at a skew-phase. The schematic of the hypothetical PA under investigation is depicted in Fig. 6.19.

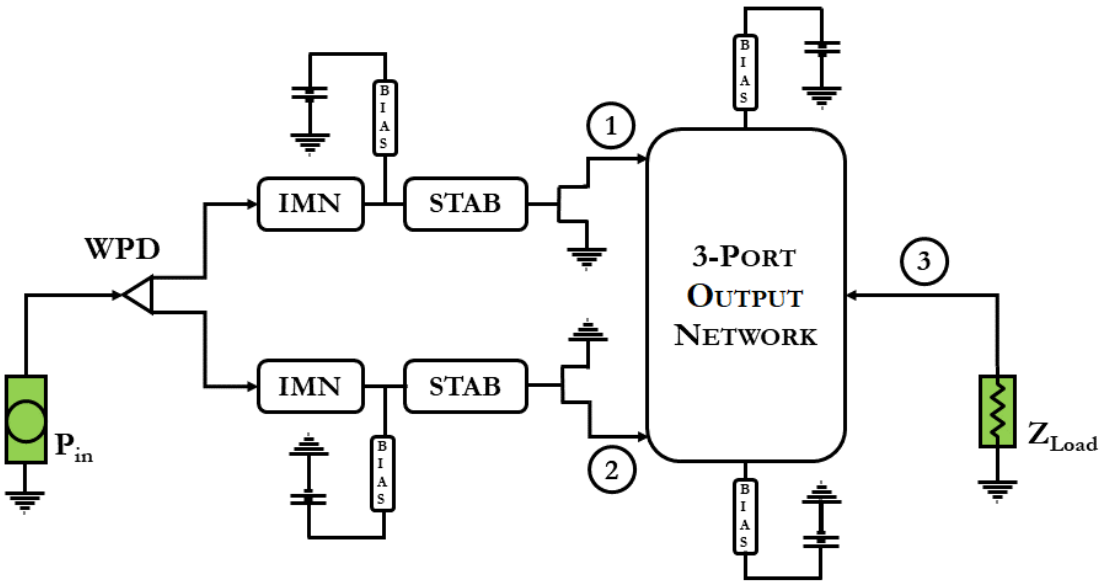

Figure 6.19: Schematic of the Hypothetical Harmonic Tuned PA

There are several things that need to be analyzed before a finalized circuit such as the type of WPD- equal or unequal split. It is a critical step in the entire circuit operation as the same would determine the amount of power entering each branch, and thereby the region of operation- in compression or linear. Another possibility that needs to be studied is the actual process by which waveform engineering would occur. In this regard, harmonic injection can be an option widely used in many cases [151–154].

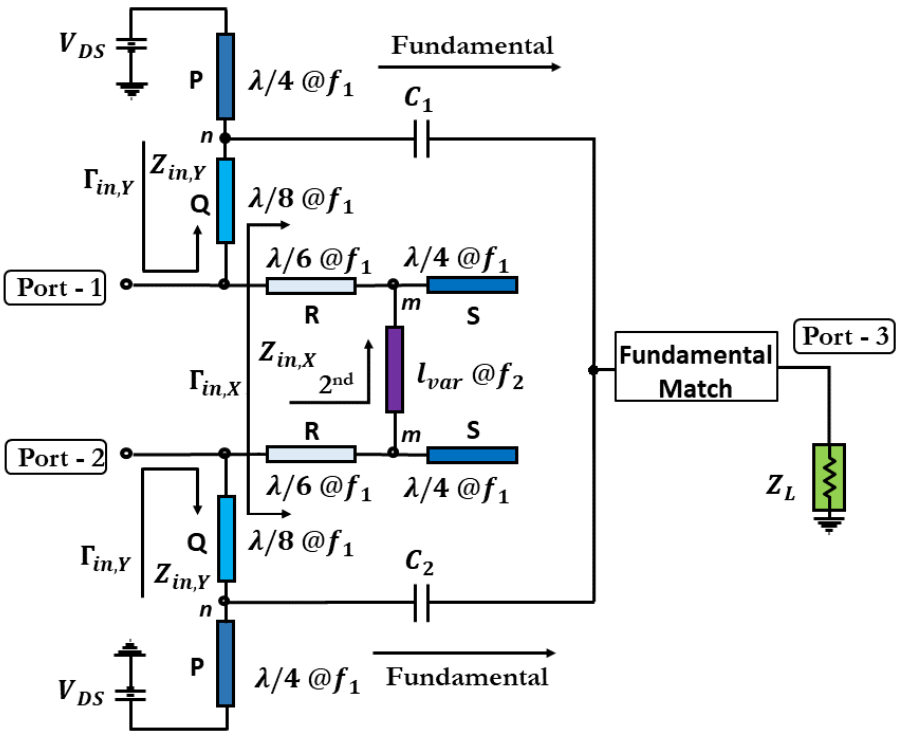

Figure 6.20: Circuit Under Investigation

Fig. 6.20 illustrates the circuit representation of the 3-port network under investigation. It is observed that this network is symmetrical on its X-axis and each equivalent half is same as the 2-port network developed earlier. Port-1 and Port-2 marked in the figure would be connected to the transistor drains of the main and the harmonic generator respectively. The harmonic tuning and the matching conditions that were developed in (6.1) through (6.4) would remain same. One major challenge that needs to be addressed is that owing to the circuit symmetry and the X-axis behaving as a magnetic mirror, there would be no current flowing from the harmonic generator to the main transistor, thereby diminishing the possibility of a straightforward harmonic injection.

There are several other considerations that need to be fully identified and investigated before coming up with a successful 3-port network that would facilitate harmonic tuning in the considered case.

6.7 Conclusion

We have reported a thorough study and analysis on parasitic power dissipation and its minimization within the RFPA regime. In essence, a novel technique using a two-port network to tune the harmonic loads has been proposed. Simulation results along with

case studies have been provided for the 10W Wolfspeed GaN HEMT model both at the intrinsic and the package plane. Finally, we fabricated a prototype and measured the same with continuous wave input power to evaluate the effectiveness of the proposed technique. The measurement results are in consonance with the EM simulations and thus demonstrate the viability of the proposed approach.

We have also discussed briefly about an ongoing project in which we are exploring the proposed theory to develop a three-port output network-based PA. The advantages would include increased bandwidth and better efficiency. The hypothetical network is under development and we are yet to come up with a finalized prototype.

CHAPTER 7

Conclusion and Future Work

With the rapid advancement of human standard of living and increase in the demand for a "high-speed" lifestyle, research in the domain of wireless communications has reached the zenith. The pressing needs of squeezing out every drop of performance over a large bandwidth has led to the exploration of broadband devices. At the same time designing devices that can operate on multiple frequencies concurrently also seems alluring because not always can a very wide bandwidth be practically possible. However, designing multi-frequency components and characterizing them properly based on the application requirements have also proved to be challenging on its own. On this note, it is of paramount importance to remember that regardless of broadband or multi-band, the key component of almost every RF circuits is an impedance transformer. Thus, a comprehensive analysis and design of impedance transformers are of utmost importance for the development of RF devices.

An important measure of performance for multi-band devices is the spacing between the bands of interest. In other words, it is a measure of how distantly can the devices operate on the frequency spectrum. A design with flexible frequency ratio is considered to be advantageous as there is a larger control over the choice of bands. This doctoral thesis was targeted to design dual and tri frequency impedance transformers as well as power dividers that address the limitation of frequency ratios in the literature. As the target application was sophisticated multi-band wireless systems, an important aspect to characterize the same is the measure of how efficiently can power be transmitted between the constituent wireless nodes. The design of an efficient RF power amplifier plays a very important role in this scenario and the same was developed as an integral part of the thesis.

In chapter 3, microstrip all-pass coupled-lines have been investigated. Two of their configurations- the floating arm type and the meandered line type has been thoroughly

analyzed. We have also demonstrated that the floating arm all-pass coupled-line can be utilized in the frequency ratio improvement of dual-band impedance transformers addressing frequency dependent complex loads. Secondly, the meandered all-pass coupled line has been used to design a dual-band impedance transformer on the light of slow wave structures. It was established that the presented configuration can improve the per-band bandwidth of a dual-band transformer addressing real loads. Finally, a highly flexible dual-band impedance transformer was proposed that has the ability to simultaneously improve frequency as well as impedance transformation ratios. Earlier it was seen that an improvement in frequency ratio led to a degradation in impedance transformation ratios. The theory presented in this thesis nullifies this inverse dependence and establishes a detailed mathematical model for high transformation ratio dual-band transformers. The utility of these types of transformers have been highlighted by designing a T-junction power divider that operates on high transformation ratios.

In chapter 4, a dual-band Wilkinson Power Divider utilizing coupled-line core has been proposed that exhibits high-frequency ratios. The design methodology is backed up with rigorous analyses and criteria for choice of transmission lines/stubs. Another important contribution of the proposed design strategy is the independence of isolation resistors on frequency band ratios. The theory is supported by design examples considering high-frequency ratios till 7. This was the first time when such a high operating frequency ratio was reported in WPDs.

Tri-band devices have gained recent research interests owing to the pressing demands in reducing circuit redundancy and compact size for next generation wireless standards. In chapter 5, we developed a new theory for designing tri-band impedance matching networks. The concept of a Virtual Impedance was established that forms a conjoining element between two dual-band transformers. Detailed mathematical analysis was provided along with a design example. A variant of the proposed concept has also been discussed in detail due to its ability to extend the upper and the lower frequency ratios. The same uses two dual-band meandered line impedance transformers conjoined by a quarter-wave line. The design strategy is simple and compact. Lastly, an Wilkinson Power Divider architecture is proposed that is generic and versatile in nature. The generalized WPD architecture uses a dual-band matching network as its constituent element. The transformer is extended to operate at three frequencies using

a dual to tri-band converter. The design theory is backed up with closed-form equations and a design flowchart. The speciality of the architecture lies in the fact that any kind of dual-band impedance transformer can be used in the design process. The choice would depend mostly on the application meant to be served. As an example, we fabricated a DC isolated WPD using the same architecture.

Needless to describe their importance in RF transceivers, the research domain of RF power amplifiers is huge and has attracted a lot of scientists to work on the same. Depending on the requirement there are plenty of amplifier configurations, specifically designed to serve high efficiency, gain or linearity. The relevance of power amplifiers in perspective of this doctoral thesis has already been explained in detail. A novel power amplifier configuration utilizing a specially designed harmonic independence output network was described in chapter 6. The proposed output network provides separate paths for the fundamental and the second harmonic matching, isolating the two from each other at the same time. Thus, for a fixed fundamental load, the second harmonic (and consequently the third harmonic) can be tuned in a reactive load space for maximized efficiency. The passive output network has been separately fabricated and tested along with the entire PA to demonstrate its operating principle.

Despite the addressing of many existing limitations in this thesis, still there are some shortcomings that need to be closely investigated and addressed. Moreover, the findings of this thesis opens doors to additional research problems that can be addresses as a part of future research. These can be listed as follows:

1. Increasing Stop-Band Spur Suppression: One of the major contributions of this thesis is the addressing of the frequency ratio and impedance transformation ratio limitations in dual-band impedance transformers. While the proposed theory is promising and extends the ratios to a vast extent, it must be noted that a high extension can prove to be troublesome. This is because, for two frequency bands of interest to be widely spaced apart, there must be high stop-band suppression as well. Often it is seen that for a high-frequency ratio transformer, low-level spurious transmission bands spike up in the spectrum leading to ghost channels. These channels can be identified as having return loss comparable to that of the actual bands of interest. Although this thesis focuses on the extension of frequency ra-

tios, the suppression of these stop-band spurs have not been analyzed. This could be an area of research in future works.

2. Increasing the Bandwidth of Power Amplifier: In the chapter on power amplifiers, we have proposed a two port output network that isolates the fundamental and the harmonic branches from each other. This network assures independence between the fundamental and harmonic impedances and implements a special case of Class-X amplifiers. However, the design is based on a single frequency and thus, the bandwidth provided by the network is severely limited. Therefore, achieving wideband performance with the proposed output network can prove to be useful over a number of applications.

3. Venturing into Substrate Integrated Waveguides: With the advent of 5G, a lot of research is being conducted on mmWaves. The sub-GHz and ISM bands being congested, it is now time to make the most out of mmWave bands. However, microstrip technology using transmission lines would not be efficient in such a scenario due to the constraints of substrate losses. This is when Substrate Integrated Waveguides (SIW) come into picture [155]. Fig. 7.1 illustrates the basic structure of an SIW. In brief, an SIW circuit makes use of rows of plated through-hole vias to emulate a waveguide structure on a PCB laminate. The via spacings, diameter and placements are determined mathematically according to many factors like frequency of operation, dielectric constant of the substrate used, substrate thickness etc.

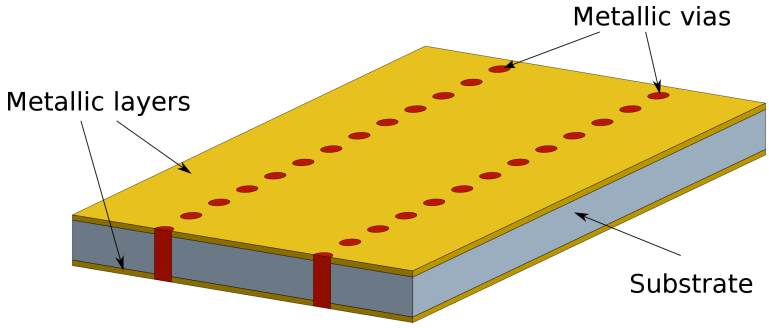

Figure 7.1: Substrate Integrated Waveguide Technology (Basic Structure) [5]

There has hardly been any research in the domain of multi-band SIW. This is mostly because designing SIWs is not only challenging but fabricating any complicated layout is even harder in case of SIWs than in microstrip technology. Designing dual-band passive circuits initially and then moving onto the more generalized multi-band scenario is an area worth considering for future research. On this regard, developing some kind of conversion theorem/method of dual-band microstrip circuits into SIW technology successfully would prove to be of paramount importance.

APPENDIX A

Fabrication of Transmission Lines

A very important aspect of designing RF and Microwave Circuits is to fabricate it for practical uses. In fact there are many interesting and idealistic results often obtained in theory but are not possible to fabricate in hardware. The critical factor determining the "fabricability" is the least possible width of the line that can be etched from the dielectric. Considering a transmission line with characteristic impedance Z_0, and the obtainable width W, to be fabricated in a material with dielectric thickness H, two cases are considered:

- If $(\frac{W}{H}) < 1$:

$$\epsilon_{eff} = \frac{\epsilon_r + 1}{2} + \frac{\epsilon_r - 1}{2}[\frac{1}{\sqrt{1 + 12\frac{H}{W}}} + 0.04(1 - \frac{W}{H})^2] \tag{A.1}$$

$$Z_0 = \frac{60}{\sqrt{\epsilon_{eff}}} \ln[8(\frac{H}{W}) + 0.25(\frac{W}{H})] \tag{A.2}$$

- If $(\frac{W}{H}) > 1$:

$$\epsilon_{eff} = \frac{\epsilon_r + 1}{2} + [\frac{\epsilon_r - 1}{2\sqrt{1 + 12(\frac{H}{W})}}] \tag{A.3}$$

$$Z_0 = \frac{120\pi}{\sqrt{\epsilon_{eff}}[\frac{W}{H} + 1.393 + \frac{2}{3}\ln(\frac{W}{H} + 1.444)]} \tag{A.4}$$

where, ϵ_{eff} is the effective dielectric constant and ϵ_r is the relative dielectric constant of the material. The above formulation can be implemented in MATLAB to determine W. However, it is imperative to note that the higher the value of impedance to be realized, the lower would be the transmission line thickness and vice versa. There are many moderate to low-cost fabrication technologies to etch out copper from the

laminates, such as chemical etching, mechanical CNC milling etc. However, the lowest possible limit they can achieve is around 8-12 mil, which corresponds to an impedance of around $170-180\Omega$, depending upon the substrate. However, with recently introduced laser milling technology, one can achieve a least count of 4 mil, corresponding to an impedance of $200 - 220\Omega$. This is a great improvement and would definitely broaden the spectrum of possibilities in the impedance matching domain. In this thesis, we have used our in-house fabrication facility- a mechanical CNC miller (LPKF Protomat), with a least count width of 8 mil. Therefore, the maximum line impedance that could be fabricated was 160Ω.

APPENDIX B

Losses Incurred During Measurements

One of the most important steps in the characterization of the performance of a device is its measurements. There are a broad category of measurements that can be performed on a device. This doctoral thesis mainly focuses on S-parameter measurements and PA large signal measurements. However, two types of losses that always find their way in are those due to connectors and cables.

- Connector Losses: Standard SMA connectors are the ports that act as an interface between the RF circuit and the input/output. While a 100% power transmission is idealistic and is not possible in practice, connector losses can be attributed to their overuse, improper soldering or simply oxide deposition over their leads. A typical N-type female connector reportedly has a -90dB leakage at 3.0GHz and an insertion loss of 0.15-0.20dB at 10.0GHz at first use [156].

- Cable Losses: Losses due to measurement cables usually increase with age and usage. In addition to it, long cables tend to be more lossy than short ones. It must be noted that measurement cables are attached to connectors at both ends, hence their overall loss contribution is the addition of the individual losses of the cable and the two connectors. Loss mainly depend on the quality of cables used, with expensive "space-grade" cables exhibiting very low values. Typical values for cable losses are 0.7-0.8dB per meter length. Added with the connector losses, the overall loss contribution for a cable is around 1.0-1.2dB at first use [156].

REFERENCES

[1] "Breaking down barriers for unmanned flight," *https://www.nasa.gov/sites/default/files/images/693260main_graphic1176_882.jpg*, Accessed Sept. 2020.

[2] "Drone types," *https://www.nextgov.com/emerging-tech/2018/03/drone-swarms-are-going-be-terrifying-and-hard-stop/146491/*, Accessed Sept. 2020.

[3] "Drone types," *https://c-drone-review.news/en/2019/01/05/uvify-to-launch-drone-swarm-lightshow-service-at-ces/*, Accessed Sept. 2020.

[4] "Amplifier classes," *https://www.electronics-tutorials.ws/amplifier/amplifier-classes.html*, Accessed Sept. 2020.

[5] "Substrate integrated waveguides," *https://en.wikipedia.org/wiki/Substrate_integrated_waveguide/media/File:SIW_sanstransparence.svg*, Accessed Sept. 2020.

[6] F. K. Jondral, "Software-defined radio—basics and evolution to cognitive radio," *EURASIP Journal on Wireless Communications and Networking*, vol. 2005, no. 3, p. 652784, 2005.

[7] H. Arslan, *Cognitive Radio, Software Defined Radio, and Adaptive Wireless Systems*. Springer, 2007.

[8] W. H. Tuttlebee, *Software Defined Radio: Enabling Technologies*. John Wiley & Sons, 2003.

[9] A. A. Abidi, "The path to the software-defined radio receiver," *IEEE Journal of Solid-State Circuits*, vol. 42, no. 5, pp. 954–966, 2007.

[10] J. Mitola, "Cognitive radio. an integrated agent architecture for software defined radio," *Doctoral Thesis*, 2002.

[11] J. Mitola and G. Q. Maguire, "Cognitive radio: Making software radios more personal," *IEEE Personal Communications*, vol. 6, no. 4, pp. 13–18, 1999.

[12] S. Haykin, "Cognitive radio: Brain-empowered wireless communications," *IEEE Journal on Selected Areas in Communications*, vol. 23, no. 2, pp. 201–220, 2005.

[13] E. Dahlman, P. Beming, J. Knutsson, F. Ovesjo, M. Persson, and C. Roobol, "Wcdma-the radio interface for future mobile multimedia communications," *IEEE Transactions on Vehicular Technology*, vol. 47, no. 4, pp. 1105–1118, 1998.

[14] H. Holma and A. Toskala, *WCDMA for UMTS: HSPA evolution and LTE*. john Wiley & sons, 2007.

[15] J. Ryynanen, K. Kivekas, J. Jussila, A. Parssinen, and K. A. Halonen, "A dual-band rf front-end for wcdma and gsm applications," *IEEE Journal of Solid-State Circuits*, vol. 36, no. 8, pp. 1198–1204, 2001.

[16] H. Harri, "Wcdma and wlan for 3g and beyond," *IEEE Wireless Communications Magazine*, 2002.

[17] J. Gubbi, R. Buyya, S. Marusic, and M. Palaniswami, "Internet of things (iot): A vision, architectural elements, and future directions," *Future Generation Computer Systems*, vol. 29, no. 7, pp. 1645–1660, 2013.

[18] S. D. T. Kelly, N. K. Suryadevara, and S. C. Mukhopadhyay, "Towards the implementation of iot for environmental condition monitoring in homes," *IEEE Sensors Journal*, vol. 13, no. 10, pp. 3846–3853, 2013.

[19] Q. Zhu, R. Wang, Q. Chen, Y. Liu, and W. Qin, "Iot gateway: Bridging wireless sensor networks into internet of things," in *2010 IEEE/IFIP International Conference on Embedded and Ubiquitous Computing*. IEEE, 2010, pp. 347–352.

[20] X. Jia, Q. Feng, T. Fan, and Q. Lei, "Rfid technology and its applications in internet of things (iot)," in *2012 2nd International Conference on Consumer Electronics, communications and networks (CECNet)*. IEEE, 2012, pp. 1282–1285.

[21] M. Centenaro, L. Vangelista, A. Zanella, and M. Zorzi, "Long-range communications in unlicensed bands: The rising stars in the iot and smart city scenarios," *IEEE Wireless Communications*, vol. 23, no. 5, pp. 60–67, 2016.

[22] D. Gregory, "From a view to a kill: Drones and late modern war," *Theory, Culture & Society*, vol. 28, no. 7-8, pp. 188–215, 2011.

[23] D. Byman, "Why drones work: The case for washington's weapon of choice," *Foreign Aff.*, vol. 92, p. 32, 2013.

[24] A. Cavoukian, *Privacy and Drones: Unmanned Aerial Vehicles*. Information and Privacy Commissioner of Ontario, Canada Ontario, 2012.

[25] M. Nikravan and Z. Atlasbaf, "T-section dual-band impedance transformer for frequency-dependent complex impedance loads," *Electronics Letters*, vol. 47, no. 9, pp. 551–553, 2011.

[26] Y. Chow and K. Wan, "A transformer of one-third wavelength in two sections-for a frequency and its first harmonic," *IEEE Microwave and Wireless Components Letters*, vol. 12, no. 1, pp. 22–23, 2002.

[27] C. Monzon, "A small dual-frequency transformer in two sections," *IEEE Transactions on Microwave Theory and Techniques*, vol. 51, no. 4, pp. 1157–1161, 2003.

[28] Y. Wu, Y. Liu, S. Li, and C. Yu, "New coupled-line dual-band dc-block transformer for arbitrary complex frequency-dependent load impedance," *Microwave and Optical Technology Letters*, vol. 54, no. 1, pp. 139–142, 2012.

[29] M. A. Maktoomi, M. S. Hashmi, and F. M. Ghannouchi, "A t-section dual-band matching network for frequency-dependent complex loads incorporating coupled-line with dc-block property suitable for dual-band transistor amplifiers," *Progress in Electromagnetics Research*, vol. 54, pp. 75–84, 2014.

[30] O. Manoochehri, A. Asoodeh, and K. Forooraghi, "π -model dual-band impedance transformer for unequal complex impedance loads," *IEEE Microwave and Wireless Components Letters*, vol. 25, no. 4, pp. 238–240, 2015.

[31] M. A. Maktoomi, R. Gupta, and M. S. Hashmi, "A dual-band impedance transformer for frequency-dependent complex loads incorporating an l-type network," in *2015 Asia-Pacific Microwave Conference (APMC)*, vol. 1. IEEE, 2015, pp. 1–3.

[32] M. A. Maktoomi, M. S. Hashmi, and F. M. Ghannouchi, "Improving load range of dual-band impedance matching networks using load-healing concept," *IEEE Transactions on Circuits and Systems II: Express Briefs*, vol. 64, no. 2, pp. 126–130, 2016.

[33] M.-L. Chuang and M.-T. Wu, "General dual-band impedance transformer with a selectable transmission zero," *IEEE Transactions on Components, Packaging and Manufacturing Technology*, vol. 6, no. 7, pp. 1113–1119, 2016.

[34] X. Wang, Z. Ma, and M. Ohira, "Dual-band design theory for dual transmission-line transformer," *IEEE Microwave and Wireless Components Letters*, vol. 27, no. 9, pp. 782–784, 2017.

[35] M.-L. Chuang and M.-T. Wu, "Transmission zero embedded dual-band impedance transformer with three shunt stubs," *IEEE Microwave and Wireless Components Letters*, vol. 27, no. 9, pp. 788–790, 2017.

[36] L. Jiao, Y. Wu, Z. Zhuang, M. Li, and Y. Liu, "Multiband dc-block impedance transformer for extreme complex impedances," *Electronics Letters*, vol. 54, no. 2, pp. 105–107, 2018.

[37] R. Gupta, O. Shaikenov, S. Kairatova, K. Dautov, and M. Hashmi, "Dual-frequency impedance transformer with ultra-high impedance transformation," in *2019 IEEE Asia-Pacific Microwave Conference (APMC)*. IEEE, 2019, pp. 458–460.

[38] K. Rawat, M. S. Hashmi, and F. M. Ghannouchi, "Dual-band rf circuits and components for multi-standard software defined radios," *IEEE Circuits and Systems Magazine*, vol. 12, no. 1, pp. 12–32, 2012.

[39] K.-K. M. Cheng and C. Law, "A novel approach to the design and implementation of dual-band power divider," *IEEE Transactions on Microwave Theory and Techniques*, vol. 56, no. 2, pp. 487–492, 2008.

[40] M.-J. Park, "Two-section cascaded coupled line wilkinson power divider for dual-band applications," *IEEE Microwave and Wireless Components Letters*, vol. 19, no. 4, pp. 188–190, 2009.

[41] Y. Wu, Y. Liu, and Q. Xue, "An analytical approach for a novel coupled-line dual-band wilkinson power divider," *IEEE Transactions on Microwave Theory and Techniques*, vol. 59, no. 2, pp. 286–294, 2010.

[42] M. Bemani and S. Nikmehr, "Dual-band n-way series power divider using crlh-tl metamaterials with application in feeding dual-band linear broadside array antenna with reduced beam squinting," *IEEE Transactions on Circuits and Systems I: Regular Papers*, vol. 60, no. 12, pp. 3239–3246, 2013.

[43] N. Gao, G. Wu, and Q. Tang, "Design of a novel compact dual-band wilkinson power divider with wide frequency ratio," *IEEE Microwave and Wireless Components Letters*, vol. 24, no. 2, pp. 81–83, 2013.

[44] X. Wang, I. Sakagami, Z. Ma, A. Mase, M. Yoshikawa, and M. Ichimura, "Miniaturized dual-band wilkinson power divider with self-compensation structure," *IEEE Transactions on Components, Packaging and Manufacturing Technology*, vol. 5, no. 3, pp. 389–397, 2015.

[45] Y. Wu, Y. Liu, Y. Zhang, J. Gao, and H. Zhou, "A dual band unequal wilkinson power divider without reactive components," *IEEE Transactions on Microwave Theory and Techniques*, vol. 57, no. 1, pp. 216–222, 2008.

[46] X. Liu, Y. Liu, S. Li, F. Wu, and Y. Wu, "A three-section dual-band transformer for frequency-dependent complex load impedance," *IEEE Microwave and Wireless Components Letters*, vol. 19, no. 10, pp. 611–613, 2009.

[47] Y. Wu, L. Cui, Z. Zhuang, W. Wang, and Y. Liu, "A simple planar dual-band bandpass filter with multiple transmission poles and zeros," *IEEE Transactions on Circuits and Systems II: Express Briefs*, vol. 65, no. 1, pp. 56–60, 2017.

[48] M. A. Maktoomi, A. P. Yadav, M. S. Hashmi, and F. M. Ghannouchi, "Dual-frequency impedance matching networks based on two-section transmission line," *IET Microwaves, Antennas & Propagation*, vol. 11, no. 10, pp. 1415–1423, 2017.

[49] M. A. Maktoomi, M. S. Hashmi, and V. Panwar, "A dual-frequency matching network for fdcls using dual-band λ/4-lines," *Progress In Electromagnetics Research*, vol. 52, pp. 23–30, 2015.

[50] M. A. Maktoomi and M. S. Hashmi, "A performance enhanced port extended dual-band wilkinson power divider," *IEEE Access*, vol. 5, pp. 11 832–11 840, 2017.

[51] A. Saxena, D. Banerjee, M. Hashmi, and F. Ghannouchi, "Design of compact dual-band matching network with single unequal susceptance cancellation stub," in *2018 Asia-Pacific Microwave Conference (APMC)*. IEEE, 2018, pp. 300–302.

[52] D. Rano, D. Banerjee, and M. Hashmi, "A miniaturized three-stage dual-frequency matching network," in *2017 IEEE MTT-S International Microwave and RF Conference (IMaRC)*. IEEE, 2017, pp. 1–5.

[53] D. Banerjee, A. Saxena, and M. Hashmi, "A novel design of a bandwidth enhanced dual-band impedance matching network with coupled line wave slowing," in *2019 IEEE 69th Electronic Components and Technology Conference (ECTC)*. IEEE, 2019, pp. 1770–1773.

[54] D. Banerjee, A. Saxena, M. Hashmi, and F. Ghannouchi, "A compact dual-band impedance matching network based on all-pass coupled lines," in *2018 IEEE 61st International Midwest Symposium on Circuits and Systems (MWSCAS)*. IEEE, 2018, pp. 937–939.

[55] A. Saxena, D. Banerjee, M. Hashmi, and M. Auyenur, "A dual-band impedance transfomer for matching frequency dependent complex source and load impedances," in *2019 15th Conference on Ph. D Research in Microelectronics and Electronics (PRIME)*. IEEE, 2019, pp. 173–176.

[56] L. Wu, Z. Sun, H. Yilmaz, and M. Berroth, "A dual-frequency wilkinson power divider," *IEEE Transactions on Microwave Theory and Techniques*, vol. 54, no. 1, pp. 278–284, 2006.

[57] Y. Wu, Y. Liu, and S. Li, "Unequal dual-frequency wilkinson power divider including series resistor–inductor–capacitor isolation structure," *IET Microwaves, Antennas & Propagation*, vol. 3, no. 7, pp. 1079–1085, 2009.

[58] M.-J. Park and B. Lee, "Dual-band design of single-stub impedance matching networks with application to dual-band stubbed t-junctions," *Microwave and Optical Technology Letters*, vol. 52, no. 6, pp. 1359–1362, 2010.

[59] M.-J. Park, "Dual-band unequal power divider with simplified structure," *IET Microwaves, Antennas & Propagation*, vol. 5, no. 15, pp. 1891–1896, 2011.

[60] X. Wang, I. Sakagami, K. Takahashi, and S. Okamura, "A generalized dual-band wilkinson power divider with parallel $l, c,$ and r components," *IEEE TRANSACTIONS on microwave theory and Techniques*, vol. 60, no. 4, pp. 952–964, 2012.

[61] Y. Liu, W. Chen, X. Li, and Z. Feng, "Design of compact dual-band power dividers with frequency-dependent division ratios based on multisection coupled line," *IEEE Transactions on Components, Packaging and Manufacturing Technology*, vol. 3, no. 3, pp. 467–475, 2013.

[62] G. Wu, L. Yang, Y. Zhou, and Q. Xu, "Wilkinson power divider design for dual-band applications," *Electronics Letters*, vol. 50, no. 14, pp. 1003–1005, 2014.

[63] Z. Bedar Khan, Z. Huiling, and Z. Yimin, "Simplified approach for design of dual-band wilkinson power divider with three transmission line sections," *Microwave and Optical Technology Letters*, vol. 58, no. 10, pp. 2374–2377, 2016.

[64] M. Maktoomi, D. Banerjee *et al.*, "An enhanced frequency-ratio coupled-line dual-frequency wilkinson power divider," *IEEE Transactions on Circuits and Systems II: Express Briefs*, vol. 65, no. 7, pp. 888–892, 2017.

[65] R. Gupta, V. V. Singh, and M. S. Hashmi, "High impedance transforming dual-band wilkinson power divider," in *2018 IEEE MTT-S International Microwave and RF Conference (IMaRC)*. IEEE, 2018, pp. 1–4.

[66] M. Chongcheawchamnan, S. Patisang, M. Krairiksh, and I. D. Robertson, "Tri-band wilkinson power divider using a three-section transmission-line transformer," *IEEE Microwave and Wireless Components Letters*, vol. 16, no. 8, pp. 452–454, 2006.

[67] A. Genc and R. Baktur, "Dual-and triple-band wilkinson power dividers based on composite right-and left-handed transmission lines," *IEEE Transactions on Components, Packaging and Manufacturing Technology*, vol. 1, no. 3, pp. 327–334, 2011.

[68] H.-H. Chen and Y.-H. Pang, "A tri-band wilkinson power divider utilizing coupled lines," in *2011 IEEE International Symposium on Antennas and Propagation (APSURSI)*. IEEE, 2011, pp. 25–28.

[69] H.-J. Zhou, H.-F. Wu, G.-Z. Lei, and Y.-Z. Ma, "Design of a compact tri-band power divider with unequal outputs," *Progress In Electromagnetics Research*, vol. 41, pp. 255–265, 2013.

[70] X. H. Wang, L. Zhang, Y. Xu, Y. F. Bai, C. Liu, and X.-W. Shi, "A tri-band impedance transformer using stubbed coupling line," *Progress In Electromagnetics Research*, vol. 141, pp. 33–45, 2013.

[71] B. M. Abdelrahman, H. N. Ahmed, and A. Nashed, "A novel tri-band wilkinson power divider for multiband wireless applications," *IEEE Microwave and Wireless Components Letters*, vol. 27, no. 10, pp. 891–893, 2017.

[72] R. K. Barik, T. Laxman Deep, and S. Karthikeyan, "An equal split triple-band wilkinson power divider employing extended cross-shaped microstrip line," *Microwave and Optical Technology Letters*, vol. 60, no. 10, pp. 2488–2492, 2018.

[73] Y. Yang, N. Hu, W. Xie, W. Wang, and Y. Wu, "A compact tri-band impedance-transforming power divider with independent controllable power division ratios and enhanced bandwidths," *IEEE Access*, vol. 7, pp. 25 185–25 194, 2019.

[74] Y.-F. Bai, X.-H. Wang, C.-J. Gao, Q.-L. Huang, and X.-W. Shi, "Design of compact quad-frequency impedance transformer using two-section coupled line," *IEEE Transactions on Microwave Theory and Techniques*, vol. 60, no. 8, pp. 2417–2423, 2012.

[75] D. Banerjee, A. Saxena, and M. Hashmi, "A novel compact tri-band matching network utilizing two dual-band transformers at a common reference frequency," in *2017 IEEE Asia Pacific Microwave Conference (APMC)*. IEEE, 2017, pp. 1080–1083.

[76] D. Banerjee, A. Saxena, and M. S. Hashmi, "A novel compact tri-band impedance matching network with enhanced frequency ratios," in *2017 IEEE MTT-S International Microwave and RF Conference (IMaRC)*. IEEE, 2017, pp. 1–4.

[77] D. Banerjee, M. Hashrni, and F. Ghaanouchi, "A novel design of a tri-band impedance matching network based on the concept of an impedance bridge," in *2018 Asia-Pacific Microwave Conference (APMC)*. IEEE, 2018, pp. 318–320.

[78] D. Banerjee, A. Saxena, and M. S. Hashmi, "A novel concept of virtual impedance for high frequency tri-band impedance matching networks," *IEEE Transactions on Circuits and Systems II: Express Briefs*, vol. 65, no. 9, pp. 1184–1188, 2018.

[79] A. Saxena, D. Banerjee, and M. Hashmi, "A novel meandered coupled-line tri-band impedance matching network," in *2018 Twenty Fourth National Conference on Communications (NCC)*. IEEE, 2018, pp. 1–4.

[80] D. Banerjee, A. Saxena, and M. Hashmi, "A simple robust equal-split t-junction power divider at three frequencies," in *2018 Twenty Fourth National Conference on Communications (NCC)*. IEEE, 2018, pp. 1–4.

[81] "Drone types," *https://www.google.co.in*, Accessed Sept. 2020.

[82] "Veil of secrecy lifted on pentagon office planning "Avatar" fighters and drone swarms," *https://www.washingtonpost.com/news/checkpoint/wp/2016/03/08/inside-the-secretive-pentagon-office-planning-skyborg-fighters-and-drone-swarms/*, Accessed Sept. 2020.

[83] "China launches drone swarm of 119 fixed-wing unmanned aerial vehicles," *https://www.business-standard.com/article/international/china-launches-drone-swarm-of-119-fixed-wing-unmanned-aerial-vehicles-117061100388_1.html*, Accessed Sept. 2020.

[84] "Record-breaking drone swarm sees 50 uavs controlled by a single person," *https://www.popularmechanics.com/flight/drones/news/a17371/record-breaking-drone-swarm/*, Accessed Sept. 2020.

[85] Q. Wu, G. Y. Li, W. Chen, D. W. K. Ng, and R. Schober, "An overview of sustainable green 5g networks," *IEEE Wireless Communications*, vol. 24, no. 4, pp. 72–80, 2017.

[86] M. Piñuela, P. D. Mitcheson, and S. Lucyszyn, "Ambient rf energy harvesting in urban and semi-urban environments," *IEEE Transactions on Microwave Theory and Techniques*, vol. 61, no. 7, pp. 2715–2726, 2013.

[87] C. Gray, R. Ayre, K. Hinton, and L. Campbell, "'smart'is not free: Energy consumption of consumer home automation systems," *IEEE Transactions on Consumer Electronics*, vol. 66, no. 1, pp. 87–95, 2019.

[88] H. Jabbar, Y. S. Song, and T. T. Jeong, "Rf energy harvesting system and circuits for charging of mobile devices," *IEEE Transactions on Consumer Electronics*, vol. 56, no. 1, pp. 247–253, 2010.

[89] Z. Liu, Z. Zhong, and Y.-X. Guo, "Enhanced dual-band ambient rf energy harvesting with ultra-wide power range," *IEEE Microwave and Wireless Components Letters*, vol. 25, no. 9, pp. 630–632, 2015.

[90] Y. Liu, Y. Zhang, R. Yu, and S. Xie, "Integrated energy and spectrum harvesting for 5g wireless communications," *IEEE Networks*, vol. 29, no. 3, pp. 75–81, 2015.

[91] A. Ö. Ercan, M. O. Sunay, and I. F. Akyildiz, "Rf energy harvesting and transfer for spectrum sharing cellular iot communications in 5g systems," *IEEE Transactions on Mobile Computing*, vol. 17, no. 7, pp. 1680–1694, 2017.

[92] D. I. Kim, S. W. Jung, and Y. Yun, "A high performance transformer-type wilkinson power splitter with compensating circuit for catv transmission system and optimal design method," *IEEE Transactions on Consumer Electronics*, vol. 50, no. 3, pp. 934–940, 2004.

[93] C. Shao, H. Roh, T. Kim, and W. Lee, "Multisource wireless energy harvesting-based medium access control for rechargeable sensors," *IEEE Transactions on Consumer Electronics*, vol. 62, no. 2, pp. 119–127, 2016.

[94] W. Duan, Y. F. Cao, Y.-M. Pan, Z. X. Chen, and X. Y. Zhang, "Compact dual-band dual-polarized base-station antenna array with a small frequency ratio using filtering elements," *IEEE Access*, vol. 7, pp. 127 800–127 808, 2019.

[95] M. Sun, Z. Zhang, F. Zhang, and A. Chen, "L/s multiband frequency-reconfigurable antenna for satellite spplications," *IEEE Antennas and Wireless Propagation Letters*, vol. 18, no. 12, pp. 2617–2621, 2019.

[96] D. M. Pozar, *Microwave engineering*. John wiley & sons, 2009.

[97] S. J. Orfanidis, "A two-section dual-band chebyshev impedance transformer," *IEEE Microwave and Wireless Components Letters*, vol. 13, no. 9, pp. 382–384, 2003.

[98] G. Castaldi, V. Fiumara, and I. Gallina, "An exact synthesis method for dual-band chebyshev impedance transformers," *Progress In Electromagnetics Research*, vol. 86, pp. 305–319, 2008.

[99] M. A. Maktoomi and M. S. Hashmi, "A coupled-line based l-section dc-isolated dual-band real to real impedance transformer and its application to a dual-band t-junction power divider," *Progress In Electromagnetics Research*, vol. 55, pp. 95–104, 2014.

[100] M. Maktoomi, M. Maktoomi, A. P. Yadav, M. S. Hashmi, and F. M. Ghannouchi, "Dual-frequency admittance property of two sections transmission-line and application," in *2016 IEEE 59th International Midwest Symposium on Circuits and Systems (MWSCAS)*. IEEE, 2016, pp. 1–4.

[101] P. Colantonio, F. Giannini, and L. Scucchia, "A new approach to design matching networks with distributed elements," in *15th International Conference on Microwaves, Radar and Wireless Communications (IEEE Cat. No. 04EX824)*, vol. 3. IEEE, 2004, pp. 811–814.

[102] Y. Wu, Y. Liu, and S. Li, "A dual-frequency transformer for complex impedances with two unequal sections," *IEEE Microwave and Wireless Components Letters*, vol. 19, no. 2, pp. 77–79, 2009.

[103] Y. Wu, Y. Liu, S. Li, C. Yu, and X. Liu, "A generalized dual-frequency transformer for two arbitrary complex frequency-dependent impedances," *IEEE Microwave and Wireless Components Letters*, vol. 19, no. 12, pp. 792–794, 2009.

[104] M.-L. Chuang, "Dual-band impedance transformer using two-section shunt stubs," *IEEE Transactions on Microwave Theory and Techniques*, vol. 58, no. 5, pp. 1257–1263, 2010.

[105] K. Rawat and F. Ghannouchi, "Dual-band matching technique based on dual-characteristic impedance transformers for dual-band power amplifiers design," *IET Microwaves, Antennas & Propagation*, vol. 5, no. 14, pp. 1720–1729, 2011.

[106] M.-L. Chuang, "Analytical design of dual-band impedance transformer with additional transmission zero," *IET Microwaves, Antennas & Propagation*, vol. 8, no. 13, pp. 1120–1126, 2014.

[107] X. Fu, D. T. Bespalko, and S. Boumaiza, "Novel dual-band matching network for effective design of concurrent dual-band power amplifiers," *IEEE Transactions on Circuits and Systems I: Regular Papers*, vol. 61, no. 1, pp. 293–301, 2013.

[108] Y. Wu, W. Sun, S.-W. Leung, Y. Diao, and K.-H. Chan, "A novel compact dual-frequency coupled-line transformer with simple analytical design equations for frequency-dependent complex load impedance," *Progress In Electromagnetics Research*, vol. 134, pp. 47–62, 2013.

[109] S. Li, B. Tang, Y. Liu, S. Li, C. Yu, and Y. Wu, "Miniaturized dual-band matching technique based on coupled-line transformer for dual-band power amplifiers design," *Progress In Electromagnetics Research*, vol. 131, pp. 195–210, 2012.

[110] H.-X. Zhu, P. Cheong, S.-K. Ho, K.-W. Tam, and W.-W. Choi, "Realization of extremely high and low impedance transforming ratios using cross-shaped impedance transformer," *IEEE Transactions on Circuits and Systems II: Express Briefs*, 2019.

[111] B.-T. Moon and N.-H. Myung, "A dual-band impedance transforming technique with lumped elements for frequency-dependent complex loads," *Progress In Electromagnetics Research*, vol. 136, pp. 123–139, 2013.

[112] Z. Wang and C.-W. Park, "Concurrent tri-band gan hemt power amplifier using resonators in both input and output matching networks," in *WAMICON 2012 IEEE Wireless & Microwave Technology Conference*. IEEE, 2012, pp. 1–4.

[113] M. A. Maktoomi, M. S. Hashmi, A. P. Yadav, and V. Kumar, "A generic tri-band matching network," *IEEE Microwave and Wireless Components Letters*, vol. 26, no. 5, pp. 316–318, 2016.

[114] K.-K. M. Cheng and F.-L. Wong, "A new wilkinson power divider design for dual-band application," *IEEE Microwave and Wireless Components Letters*, vol. 17, no. 9, pp. 664–666, 2007.

[115] M.-J. Park and B. Lee, "Wilkinson power divider with extended ports for dual-band operation," *Electronics Letters*, vol. 44, no. 15, pp. 916–917, 2008.

[116] M. Park and B. Lee, "A dual-band wilkinson power divider," *IEEE Microwave and Wireless Components Letters*, vol. 18, no. 2, pp. 85–87, 2008.

[117] I. Sakagami, X. Wang, K. Takahashi, and S. Okamura, "Generalized two-way two-section dual-band wilkinson power divider with two absorption resistors and its miniaturization," *IEEE Transactions on Microwave Theory and Techniques*, vol. 59, no. 11, pp. 2833–2847, 2011.

[118] Q. Wang, C. Bao, B. Wu, and X. Wang, "Multiple design approach of dual-band wilkinson power divider with arbitrary transmission line ratio," *International Journal of RF and Microwave Computer-Aided Engineering*, vol. 30, no. 4, p. e22109, 2020.

[119] R. Gomez-Garcia, R. Loeches-Sanchez, D. Psychogiou, and D. Peroulis, "Single/multi-band wilkinson-type power dividers with embedded transversal filtering sections and application to channelized filters," *IEEE Transactions on Circuits and Systems I: Regular Papers*, vol. 62, no. 6, pp. 1518–1527, 2015.

[120] F. H. Raab, "Class-f power amplifiers with maximally flat waveforms," *IEEE Transactions on Microwave Theory and Techniques*, vol. 45, no. 11, pp. 2007–2012, 1997.

[121] V. Radisic, Y. Qian, and T. Itoh, "Broad-band power amplifier using dielectric photonic bandgap structure," *IEEE Microwave and Guided Wave Letters*, vol. 8, no. 1, pp. 13–14, 1998.

[122] P. Colantonio, F. Giannini, R. Giofre, E. Limiti, A. Serino, M. Peroni, P. Romanini, and C. Proietti, "A c-band high-efficiency second-harmonic-tuned hybrid power amplifier in gan technology," *IEEE Transactions on Microwave Theory and Techniques*, vol. 54, no. 6, pp. 2713–2722, 2006.

[123] T. Sharma, R. Darraji, F. Ghannouchi, and N. Dawar, "Generalized continuous class-f harmonic tuned power amplifiers," *IEEE Microwave and Wireless Components Letters*, vol. 26, no. 3, pp. 213–215, 2016.

[124] K. Bathich and G. Boeck, "Wideband harmonically-tuned gan doherty power amplifier," in *2012 IEEE/MTT-S International Microwave Symposium Digest*. IEEE, 2012, pp. 1–3.

[125] T. Sharma, E. Srinidhi, R. Darraji, D. G. Holmes, J. Staudinger, J. K. Jones, and F. M. Ghannouchi, "High-efficiency input and output harmonically engineered power amplifiers," *IEEE Transactions on Microwave Theory and Techniques*, vol. 66, no. 2, pp. 1002–1014, 2017.

[126] T. Sharma, R. Darraji, and F. Ghannouchi, "A methodology for implementation of high-efficiency broadband power amplifiers with second-harmonic manipulation," *IEEE Transactions on Circuits and Systems II: Express Briefs*, vol. 63, no. 1, pp. 54–58, 2015.

[127] A. Saxena and M. S. Hashmi, "A tri-band impedance transformer based output network for efficient rf power amplifiers," *Progress In Electromagnetics Research*, vol. 106, pp. 177–186, 2020.

[128] X. Li, M. Helaoui, and X. Du, "Class-x—harmonically tuned power amplifiers with maximally flat waveforms suitable for over one-octave bandwidth designs,"

IEEE Transactions on Microwave Theory and Techniques, vol. 66, no. 4, pp. 1939–1950, 2018.

[129] S. C. Cripps, P. J. Tasker, A. L. Clarke, J. Lees, and J. Benedikt, "On the continuity of high efficiency modes in linear rf power amplifiers," *IEEE Microwave and Wireless Components Letters*, vol. 19, no. 10, pp. 665–667, 2009.

[130] P. Wright, J. Lees, J. Benedikt, P. J. Tasker, and S. C. Cripps, "A methodology for realizing high efficiency class-j in a linear and broadband pa," *IEEE Transactions on Microwave Theory and Techniques*, vol. 57, no. 12, pp. 3196–3204, 2009.

[131] S. Rezaei, L. Belostotski, F. M. Ghannouchi, and P. Aflaki, "Integrated design of a class-j power amplifier," *IEEE Transactions on Microwave Theory and Techniques*, vol. 61, no. 4, pp. 1639–1648, 2013.

[132] J. Moon, J. Kim, and B. Kim, "Investigation of a class-j power amplifier with a nonlinear c_{out} for optimized operation," *IEEE Transactions on Microwave Theory and Techniques*, vol. 58, no. 11, pp. 2800–2811, 2010.

[133] S. K. Dhar, T. Sharma, R. Darraji, D. G. Holmes, S. V. Illath, V. Mallette, and F. M. Ghannouchi, "Investigation of input–output waveform engineered continuous inverse class f power amplifiers," *IEEE Transactions on Microwave Theory and Techniques*, vol. 67, no. 9, pp. 3547–3561, 2019.

[134] S. K. Dhar, T. Sharma, N. Zhu, R. Darraji, R. McLaren, D. G. Holmes, V. Mallette, and F. M. Ghannouchi, "Input-harmonic-controlled broadband continuous class-f power amplifiers for sub-6-ghz 5g applications," *IEEE Transactions on Microwave Theory and Techniques*, 2020.

[135] M. T. Arnous, Z. Zhang, S. E. Barbin, and G. Boeck, "A novel design approach for highly efficient multioctave bandwidth gan power amplifiers," *IEEE Microwave and Wireless Components Letters*, vol. 27, no. 4, pp. 371–373, 2017.

[136] P. Saad, M. Thorsell, K. Andersson, and C. Fager, "Investigation of push-pull microwave power amplifiers using an advanced measurement setup," *IEEE Microwave and Wireless Components Letters*, vol. 23, no. 4, pp. 220–222, 2013.

[137] M. T. Arnous, K. Bathich, S. Preis, and G. Boeck, "Harmonically-tuned octave bandwidth 200w gan power amplifier," in *2012 7th European Microwave Integrated Circuit Conference*. IEEE, 2012, pp. 429–432.

[138] T. Sharma, D. G. Holmes, R. Darraji, E. R. Srinidhi, J. Staudinger, J. K. Jones, and F. M. Ghannouchi, "On the second-harmonic null in design space of power amplifiers," *IEEE Microwave and Wireless Components Letters*, vol. 28, no. 7, pp. 600–602, 2018.

[139] T. Sharma, S. K. Dhar, D. G. Holmes, R. Darraji, S. E. Ramanujan, J. Staudinger, J. K. Jones, and F. M. Ghannouchi, "Simplified first-pass design of high-efficiency class-f^{-1} power amplifiers based on second-harmonic minima," *IEEE Transactions on Microwave Theory and Techniques*, vol. 67, no. 7, pp. 3147–3161, 2019.

[140] V. Carrubba, R. Quay, M. Schlechtweg, O. Ambacher, M. Akmal, J. Lees, J. Benedikt, P. J. Tasker, and S. C. Cripps, "Continuous-classf3 power amplifier mode varying simultaneously first 3 harmonic impedances," in *2012 IEEE/MTT-S International Microwave Symposium Digest*. IEEE, 2012, pp. 1–3.

[141] T. Canning, P. J. Tasker, and S. C. Cripps, "Continuous mode power amplifier design using harmonic clipping contours: Theory and practice," *IEEE Transactions on Microwave Theory and Techniques*, vol. 62, no. 1, pp. 100–110, 2013.

[142] V. Carrubba, M. Akmal, R. Quay, J. Lees, J. Benedikt, S. C. Cripps, and P. J. Tasker, "The continuous inverse class-f mode with resistive second-harmonic impedance," *IEEE Transactions on Microwave Theory and Techniques*, vol. 60, no. 6, pp. 1928–1936, 2012.

[143] M. Roberg and Z. Popovic, "Analysis of high-efficiency power amplifiers with arbitrary output harmonic terminations," *IEEE Transactions on Microwave Theory and Techniques*, vol. 59, no. 8, pp. 2037–2048, 2011.

[144] P. Colantonio, F. Giannini, G. Leuzzi, and E. Limiti, "Multiharmonic manipulation for highly efficient microwave power amplifiers," *International Journal of RF and Microwave Computer-Aided Engineering*, vol. 11, no. 6, pp. 366–384, 2001.

[145] D. Banerjee, A. Saxena, and M. Hashmi, "A novel independent harmonic tuned two-port output network for efficiency enhanced rf power amplifiers," *Microwave and Optical Technology Letters*, 2020.

[146] R. K. Mongia, J. Hong, P. Bhartia, and I. J. Bahl, *RF and Microwave Coupled-Line Circuits*. Artech house, 2007.

[147] M. Jamshidi, A. Lalbakhsh, S. Lotfi, H. Siahkamari, B. Mohamadzade, and J. Jalilian, "A neuro-based approach to designing a wilkinson power divider," *International Journal of RF and Microwave Computer-Aided Engineering*, vol. 30, no. 3, p. e22091, 2020.

[148] E. Jedkare, F. Shama, and M. A. Sattari, "Compact wilkinson power divider with multi-harmonics suppression," *AEU-International Journal of Electronics and Communications*, vol. 127, p. 153436, 2020.

[149] Z. Cheng, X. Xuan, H. Ke, G. Liu, Z. Dong, and S. Gao, "Design of 0.8–2.7 ghz high power class-f harmonic-tuned power amplifier with parasitic compensation circuit," *Active and Passive Electronic Components*, vol. 2017, 2017.

[150] A. S. Sayed and H. N. Ahmed, "Wideband high efficiency power amplifier design using precise high frequency gan-hemt parasitics modeling/compensation," in *2019 IEEE Topical Conference on RF/Microwave Power Amplifiers for Radio and Wireless Applications (PAWR)*. IEEE, 2019, pp. 1–4.

[151] A. Dani, M. Roberg, and Z. Popovic, "Pa efficiency and linearity enhancement using external harmonic injection," *IEEE transactions on microwave theory and techniques*, vol. 60, no. 12, pp. 4097–4106, 2012.

[152] A. Dani, M. Coffey, and Z. Popović, "4w x-band high efficiency mmic pa with output harmonic injection," in *2014 9th European Microwave Integrated Circuit Conference*. IEEE, 2014, pp. 389–392.

[153] A. Dani, M. Roberg, and Z. Popovic, "Efficiency and linearity of power amplifiers with external harmonic injection," in *2012 IEEE/MTT-S International Microwave Symposium Digest*. IEEE, 2012, pp. 1–3.

[154] Y. M. A. Latha, K. Rawat, M. Helaoui, and F. M. Ghannouchi, "Broadband continuous mode power amplifier with on-board harmonic injection," *IET Microwaves, Antennas & Propagation*, vol. 13, no. 9, pp. 1402–1407, 2019.

[155] "Surfing millimeter waves with siw technology," *https://www.microwavejournal.com/blogs/1-rog-blog/post/25359-surfing-millimeter-waves-with-siw-technology*, Accessed Oct. 2020.

[156] "Typical losses in coaxial cables and connectors," *https://www.qsl.net/vk5bar/AHARS-Resources/typical_coax_cable_losses.htm*, Accessed Dec. 2020.

LIST OF PAPERS BASED ON THESIS

Journal Articles

1. **D. Banerjee**, A. Saxena and M.S. Hashmi, "A Novel Concept of Virtual Impedance for High-Frequency Tri-Band Impedance Matching Networks", IEEE Transactions on Circuits and Systems- II: Express Briefs, Vol. 65, Iss. 9, pp. 1184 - 1188, Sept. 2018.

2. **D. Banerjee**, A. Saxena and M.S. Hashmi, "A Novel Independent Harmonic Tuned Two-Port Output Network for Efficiency Enhanced RF Power Amplifiers", Wiley Microwave and Optical Technology Letters, Vol. 63, Iss. 2, p.p. 426 - 431, Feb. 2021.

3. **D. Banerjee**, M.S. Hashmi and F.M. Ghannouchi, "Generalized Design Scheme of a Versatile Tri-Frequency Wilkinson Power Divider", Wiley International Journal of RF and Microwave Computer Aided Engineering, Vol. 31, Iss. 5, e22578, May 2021.

4. **D. Banerjee**, M.S. Hashmi and F.M. Ghannouchi, "A Flexible Ultra-High Transformation Ratio Based Dual-Band Impedance Transformer and its Applications in a T-Junction Power Divider", IET Microwaves, Antennas and Propagation *(Accepted: May 2021)*.

5. M. H. Maktoomi, **D. Banerjee** and M. S. Hashmi, "An Enhanced Frequency-Ratio Coupled-Line Dual-Band Wilkinson Power Divider", IEEE Transactions on Circuits and Systems- II: Express Briefs, Vol. 65, Iss. 7, pp. 888 - 892, Jul. 2018.

Conference Proceedings

1. **D. Banerjee**, A. Saxena and M.S Hashmi, "A Novel Compact Tri-band Matching Network Utilizing Two Dual-Band Transformers at a Common Reference Frequency", 29th IEEE Asia-Pacific Microwave Conference (APMC), Nov. 13 - 16, 2017, Kuala Lumpur, Malaysia.

2. **D. Banerjee**, A. Saxena and M.S Hashmi, "A Novel Compact Tri-band Matching Network With Enhanced Frequency Ratios", IEEE-MTTS International Microwave and RF Conference (IMaRC), Dec. 11 - 13, 2017, Ahmedabad, India.

3. **D. Banerjee**, A. Saxena and M.S Hashmi, "A Simple Robust Equal-Split T-Junction Power Divider at Three Frequencies", 24th IEEE National Conference on Communication (NCC), Feb. 25 - 28, 2018, Hyderabad, India.

4. **D. Banerjee**, A. Saxena, M.S Hashmi and F.M Ghannouchi, "A Compact Dual-Band Impedance Matching Network Based on All-Pass Coupled Lines", 61st IEEE Mid-West Symposium on Circuits and Systems (MWSCAS), Aug. 06 - 08, Windsor, Ontario, Canada.

5. **D. Banerjee**, A. Saxena, M.S Hashmi and F.M Ghannouchi, "A Novel Design of a Tri-Band Impedance Matching Network Based on the Concept of an Impedance Bridge", 30th IEEE Asia-Pacific Microwave Conference (APMC), Nov. 6 - 9, 2018, Kyoto, Japan.

6. **D. Banerjee**, A. Saxena and M.S Hashmi, "A Novel Design of a Bandwidth Enhanced Dual-Band Impedance Matching Network With Coupled Line Wave Slowing", IEEE 69th Electronic Components and Technology Conference (ECTC), May 28 - 31, 2019, Las Vegas, USA.

Papers Not Included in this Thesis

1. D. Rano, **D. Banerjee** and M.S Hashmi, "A Miniaturized Three-Stage Dual-Frequency Matching Network", IEEE-MTTS International Microwave and RF Conference (IMaRC), Dec. 11 - 13, 2017, Ahmedabad, India.

2. A. Saxena, **D. Banerjee**, and M.S Hashmi, "A Novel Meandered Coupled-Line Tri-Band Impedance Matching Network", 24th IEEE National Conference on Communication (NCC), Feb. 25 - 28, 2018.

3. A. Saxena, **D. Banerjee**, and M.S Hashmi, "Design of Compact Dual-Band Matching Network with Single Unequal Susceptance Cancellation Stub", 30th IEEE Asia-Pacific Microwave Conference (APMC), Nov. 6 - 9, 2018, Kyoto, Japan.

4. A. Saxena, **D. Banerjee**, and M.S Hashmi, "Design of π-Structure Dual-Band Matching Network With Unequal Susceptance Cancellation Stubs", IEEE-MTTS International Microwave and RF Conference (IMaRC), Nov. 28 - 30, 2018, Kolkata, India.

5. A. Saxena, **D. Banerjee**, M.S Hashmi and M. Auyenur, "A Dual-Band Impedance Transformer for Matching Frequency Dependent Complex Source and Load Impedances", IEEE 15th Conference on Ph.D Research in Microelectronics and Electronics (PRIME), Jul. 15 - 18, 2019, Laussane, Switzerland.

BIOGRAPHY

DEEPAYAN BANERJEE (S'16) was born in Durgapur, West Bengal, India. He completed his Bachelors in Electronics and Communication Engineering from the West Bengal University of Technology, Kolkata and Masters in Microwave Engineering from the Indraprastha Institute of Information Technology, Delhi (IIIT-D) and is currently working towards his Ph.D. degree at the Advanced High Speed Electronics Research Group at IIIT Delhi. He was also associated with the iRadio Lab., Schulich School of Engineering, at the University of Calgary, Canada, where he was a Visiting Research Scholar during May 2018–19.

He works primarily on multi-band passive and active RF Circuits for Wireless Applications. Research interests include GaN Power Amplifiers, MMIC based amplifiers for Space Communications, Dual/Tri-band RF Circuits and Energy Harvesting for 5G. Mr. Banerjee was the recipient of the IEEE Travel Grant for Outstanding Research Work at the 69th Electronics Components and Packaging Conference (ECTC), held at Las Vegas, Nevada, USA. He was also the winner of the Student Design Competition at the IEEE International Microwave and RF Conference (IMaRC) organized by the Space Application Center of the Indian Space Research Organization (SAC-ISRO).

Besides research he enjoys photography, globe-trotting, Indian Classical Music and playing Chess.